Quantifying the importance of ocean-atmosphere exchange for atmospheric chemistry

Ryan Joseph Pound

Doctor of Philosophy

University of York

Chemistry

June 2021

Abstract

Ocean atmosphere interactions are a vital part of the Earth system, especially for the composition of the atmosphere which impacts climate, and air quality. Our understanding of this system comes from numerical models, observations and laboratory studies. The representation of ocean-atmosphere interactions in these models is often simplistic. This work aims to extend our understanding of some of these interactions by improving their representation in the chemistry transport model GEOS-Chem.

A more complete representation of oceanic ozone dry deposition results in a 50% reduction in ozone deposition velocity to the ocean, bringing measured and modelled ozone fluxes into better agreement. The resulting increase in tropospheric ozone is limited to the marine boundary layer (MBL), especially over the Southern Ocean where modelled ozone concentrations are brought closer to observations.

Oceanic emissions of alkenes (ethene and propene) are parameterized based on observations and laboratory studies. An emission inventory is tuned to observations and extrapolated globally. The resulting increase of alkenes in the MBL improves model comparisons. Model predictions overestimate remote observations from aircraft over open ocean, implying further development is needed to better capture differences between coastal and open ocean emissions. Oceanic emissions of ethene and propene have a negligible impact on tropospheric oxidative capacity.

Spatial resolution is an important consideration for marine environments. Representation of local emissions from islands and shipping plumes, transport and vertical mixing, and steep gradients in concentration can all contribute to differences between the predictions of models at different spatial resolution. Although there are some species which show large differences (likely when the chemical and dynamical timescales are comparable) the impact of spatial resolution on OH and O_3 is small. When comparing model predictions and observations for remote islands the nearest grid box to the island might not be the most appropriate comparison for some species.

Contents

List of Tables

List of Figures

Acknowledgements

I thank NERC SPHERES DTP (NE/L002574/1) for funding this PhD project.

I thank WMO GAW and the individual sites that make up this network, for the availability of the surface ozone data.

I thank Kelvin Bates of the Atmospheric Chemistry Modelling group in Harvard for the use of a currently unpublished ethene chemistry scheme.

This work was undertaken on the Viking Cluster, which is a high-performance computing facility provided by the University of York. I am grateful for computational support from the University of York High Performance Computing service, Viking and the Research Computing team.

Finally I would like to thank all those at the Wolfson Atmospheric Chemistry Laboratories for the help and advice I have received throughout my PhD as well as making my PhD such an enjoyable experience.

Authors Declaration

I declare that this thesis is a presentation of original work and I am the sole author. This work has not previously been presented for an award at this, or any other, University. Chapter 3 (Oceanic Ozone Deposition) contains the published work from Pound et al. (2020). All sources are acknowledged as references.

1 Introduction

1.1 The Earth system

Humanity has changed the energy balance of the Earth's natural systems and hence climate ([IPCC] et al., 2014). Anthropogenic emissions of greenhouse gasses, driven by the growth of economies and an increasing global population, have caused the atmosphere and oceans to warm, reduced the amount of ice and snow covering the planet and caused sea levels to rise. This has increased the occurrences of extreme weather events, causing irreversible damage to ecosystems and without mitigation will cause further damage to the earth system.

Air pollution has also increased. Globally, pollution of the air was responsible for 7 million deaths in 2016 and it is estimated that 90% of people in urban areas are exposed to fine particulate matter (PM2.5) that exceeds WHO air quality guidelines (WHO, 2019). Exposure to poor air quality increases the risk of heart disease, lung disease and increases the risks of cancer.

Although both of these problem originate in terrestrial, populated regions, the oceans play keys roles in mitigating their impact. Oceans cover more than 70% of the surface of the planet and the transfer of compounds from the atmosphere to the ocean and from the ocean to the atmosphere plays a key role in regulating the Earth system. Improving our understanding of these ocean-atmosphere interactions with respect to the chemical composition of the atmosphere is the theme of this thesis. In this introduction, previous work on the exchange of tracer gases between the ocean and the atmosphere is discussed (Section 1.2). Then the structure of the atmosphere above the ocean (Section 1.3) and the chemical processing within the lowest most part of the atmosphere (Section 1.4) are outlined. Atmospheric observatories based on islands or coast regions have been central to our understanding of ocean-atmosphere interactions and some of these studies are highlighted in Section 1.6. Finally, the unresolved scientific questions

which are the focus of this thesis are outlined in Section 1.7.

1.2 Ocean atmosphere exchange

The largest exchanges between Earth's oceans and its atmosphere, and as a result have the largest impacts on both atmospheric composition and climate is that of water vapour and heat (Jacob, 1999). Anthropogenic activity and emissions of these are minimal compared to the natural emissions of the ocean, however, warming caused by anthropogenic emissions can trigger a strong positive feedback of water vapour emissions further increasing the greenhouse effect (Jacob, 1999).

Another substantial exchange between the ocean and atmosphere is CO_2. The oceans help regulate atmospheric CO_2 concentrations, with CO_2 dissolving in sea-water and ultimately being converted into carbonate compounds which form rocks. This removes the carbon from the atmosphere-ocean system. Between 1.85 to 2.81 Pg C yr^{-1} of anthropogenic of CO_2 is removed from the atmosphere by the ocean each year, with the Southern Ocean representing the largest single sink (23% of global total) but with the tropics also playing a considerable role (Mikaloff Fletcher et al., 2006). Thus, around 48% of all anthropogenic CO_2 emitted into the atmosphere from fossil-fuel use and the manufacturing of cement between 1880 and 1994 (Sabine et al., 2004) has been taken up by the ocean. However, the increased uptake of CO_2 since the beginning of the industrial era has caused the acidification of oceans ([IPCC] et al., 2014) which has impacted biological processes.

Depending on the concentrations of a compound in the ocean or atmosphere, the exchange of gases can be seen in multiple ways. From an atmospheric perspective, the transfer of compounds from the atmosphere to the ocean is seen as a deposition, with the transfer from the ocean to the atmosphere as an emission. An oceanic perspective would see this differently. In reality the transfer is

bi-directional depending upon the concentrations of compound at the interface in the ocean and the atmosphere and the physical processes controlling the exchange. In this section an atmospheric perspective is taken to describe previous work controlling the exchange of trace gasses from the atmosphere to the ocean (deposition, Section 1.2.1), from the ocean to the atmosphere (emissions, Section 1.2.2) and for those compounds which are thought to do both depending up on the conditions (bi-directional, Section 1.2.3).

1.2.1 Deposition

Ammonia, sufuric and nitric acid are important for the generation of aerosol particles. They play a critical role in the climate system (Haywood and Boucher, 2000). They are also highly water soluble, with loss to the ocean surface by dry and wet deposition being important global sinks for the species (Behera et al., 2013). The transfer of both oxidized and reduced nitrogen to the ocean by these species can have large influences on biological activity within the ocean surface, and influence the biogeochemical cycle of carbon. This can cause alterations to the life-cycles of phytoplankton (Krishnamurthy et al., 2007; Duce et al., 2008; Mahowald et al., 2017) which could ultimately impact biodiversity (Behera et al., 2013). Sulfur dioxide (necessary to produce sulfutric acid) is another highly water soluble species with approximately half of the total loss being dry deposition to the ocean (Chin et al., 2000; Sheng et al., 2015).

Another critical depositions process in the atmosphere, is the loss of O_3 from the atmosphere to the ocean. This processes represents approximately a third of the global total O_3 loss to dry deposition (Ganzeveld et al., 2009) and thus is an important sink for the significant climate gas and air pollutant. Once transferred into the ocean, O_3 is lost through chemical reactions with iodide, dissolved organic carbon (DOC), dimethyl sulfide (DMS) and bromide (Martino et al., 2012; Shaw and Carpenter, 2013; Sarwar et al., 2016; Carpenter et al., 2021). Reactions with DMS and bromide are negligible (Sarwar et al., 2016), and the

mechanisms of the reactions with DOC are not well understood (Martino et al., 2012; Shaw and Carpenter, 2013). The reaction of O_3 with I^- is thought to be sufficient to describe observed O_3 fluxes to the ocean surface (Luhar et al., 2017, 2018; Garland et al., 1980).

1.2.2 Emissions

From a climate perspective, the most important transfer of a trace gas from the ocean to the atmosphere is DMS. This is generated in the ocean from biological activity in the ocean surface an subsequently emitted into the atmosphere. This is the main source of sulfur in the marine boundary layer (Yang et al., 2011; Sinha et al., 2007). In remote areas, far from anthropogenic sources of sulfur, the oxidation of DMS in the atmosphere is the dominant route to the production of sulfur aerosol which directly scatters solar radiation and forms products acting as cloud condensation nuclei (Shaw, 1983; Andreae and Crutzen, 1997; Ayers and Gillett, 2000). Simó and Dachs (2002) predicted global emissions of DMS from the ocean surface are between 23–35 Tg S yr^{-1}. Using more advanced climatology and including more recent observations from the Indian Ocean, Lana et al. (2011) estimate global oceanic emissions of DMS to be 28.1 (17.6–34.4) Tg S yr^{-1}. Historically, it was suggested that this emission created a self regulating system as a decrease in sunlight reaching the ocean surface (due to increased DMS sourced aerosol scattering and cloud albedo) results in a decrease in plankton activity (the biological source for DMS), this then will result in a reduction of DMS emissions (Charlson et al., 1987; Simó and Dachs, 2002). However more recently, an evaluation of this feedback suggests isn't strong enough to have this influence (Woodhouse et al., 2010).

The emission of sea salt aerosol in the atmosphere occurs due to physical rather than chemical processes. For much of the ocean surface, sea-salt is the dominant aerosol (by mass), thus having important roles in earths energy bal-

ance and climate change (Ma et al., 2008; Jaeglé et al., 2011). Emission of sea-salt from the ocean is driven by turbulence at the ocean surface caused by wind (O'Dowd and de Leeuw, 2007) and also correlates with sea surface temperature (Liu et al., 2021). As well as offering a source of primary particles, the emission of sea-salt allows for the secondary emission of inorganic chlorine and bromine compounds from the ocean. Reactions on the surface of sea-salt leads to the conversion of chemically inert chloride and bromide into more reactive chlorine and bromine species (Sherwen et al., 2016b) which can then influence the oxidation of compounds in marine environments. Organo-halogen compounds are also emitted from the oceans through compounds such as CH_3Br, $CHBr_3$, and CH_2Br_2 for bromine and CH_3Cl, $CHCl_3$, and CH_2Cl_2 for chlorine (Ordóñez et al., 2012; Parrella et al., 2012; Schmidt et al., 2016). These compounds have some influence on the troposphere but play a significant role in determining the loss of stratospheric O_3 (Solomon, 1999).

The emission of iodine from the ocean into the atmosphere follows a different route. Our current understanding of the mechanisms behind iodine emission from the ocean is explored by Carpenter et al. (2021). Iodine is thought to be primarily emitted in the form of I_2 and HOI, driven by the oxidation of ocean iodide by O_3 (Garland and Curtis, 1981; Sakamoto et al., 2009; Hayase et al., 2010; Carpenter et al., 2013). This is the same process that causes the deposition of O_3 to the ocean. Iodinated organic compounds are also emitted (CH_3I, CH_2I_2, CH_2ICl, CH_2IBr) but are a small fraction of the total source (Ordóñez et al., 2012). The majority of iodine emissions occurs in the tropics, decreasing towards the poles (Sherwen et al., 2016b).

Isoprene is a volatile organic compound (VOC) that plays a dominant role in the atmospheric chemistry of forested terrestrial ecosystems (Guenther et al., 2012). It also emitted from the ocean surface, with production linked to the biological activity of phytoplankton in the ocean surface (Lewis et al., 2001; Shaw

et al., 2003). As well as impacts on key atmospheric oxidation, isoprene has been suggested as a source of secondary organic aerosol (SOA) in the marine troposphere (Gantt et al., 2009a; Arnold et al., 2009; Shaw et al., 2010). However model analysis shows that marine emissions of isoprene plays an insignificant role in remote marine aerosol production, with an aerosol from isoprene contributing between 0.01–1.4% of total aerosol mass (Arnold et al., 2009).

Other alkenes (notably ethene and propene) have also been observed in the ocean surface and the marine boundary layer. Both supersaturation in the ocean surface and relatively high atmospheric mixing ratios are indicative of an ocean source (Bongsang et al., 1988, 1990; Koppmann et al., 1992; Plass-Dulmer et al., 1993).

1.2.3 Two-way interactions

Some species exhibit two-way interactions with with ocean acting as a source under some situations and a sink under others. Acetaldehyde and acetone are abundant in remote marine air, combined with methanol, they contribute 85% of the total mass of non-methane volatile organic compounds (NMVOCs) and 80% of the OH sink in some oceanic locations (Lewis et al., 2005). Oceanic sources of acetaldehyde represents the second largest global source of the species, with the first being chemical production from hydrocarbon oxidation (Millet et al., 2010). Production of acetaldehyde in the ocean surface is thought to occur from the degradation of dissolved organic matter (DOM) by UV light (Kieber et al., 1990; Sinha et al., 2007; Zhou and Mopper, 1997). Globally, the oceans provide an important control over atmospheric acetone concentrations, with tropical oceans being a net source and northern oceans being a net sink. Overall the ocean concentrations are in near-equilibrium with the atmosphere (Fischer et al., 2012). Acetone is produced in the ocean surface from biological and photochemical processes (Sinha et al., 2007; Zhou and Mopper, 1997; Nemecek-Marshall et al., 1995).

1.2.4 Summary

Overall the ocean provides a critical constraint on the concentration of compounds in the atmosphere acting as a source for some species and a sink for others. Although significant previous work has been undertaken to understand the role of these emissions for some compounds (e.g. CO_2 or DMS), much less work has been done on others despite its potential importance.

To further understand this chemistry from an atmospheric perspective, there is a necessity to understand the structure of the atmosphere above the ocean and the chemistry that occurs in the air over the ocean.

1.3 Structure of the atmosphere

Vertically, the atmosphere is divided into layers by the reversal of the temperature gradient (Jacob, 1999). From the surface the temperature reduces over 8-18 km until a minimum is reached at the tropopause. The temperature then increases, driven by the absorption of high energy solar photons by the ozone layer, until the mesopause is reached (at around 50km), when again the temperature drops through the mesosphere. Whilst the majority of the atmospheric volume is within the mesosphere, by mass over 99% of the atmosphere is contained within the troposphere and stratosphere, with around 90% in the troposphere alone. The troposphere thus is area of most interest for air quality and pollution. The lowest section of the troposphere ($\sim$1km) is most influenced by the Earths surface. This region responds rapidly to changes in surface temperature and turbulence, resulting in a well mixed layer known as the boundary layer. Above the boundary layer the atmosphere is often mode stable.

Over oceanic regions the changes in surface temperature are small compared to those over land due to the heat capacity and thermal conductivity of the water. This results in relatively small changes in atmospheric temperatures. This surface thermal stability leads to boundary layers which are more stable than those found

over land. This often means that mixing between the marine boundary layer and the air above is lower than might be considered typical for terrestrial or polluted environments.

1.4 Chemistry of the marine boundary layer

The fate of compounds emitted from the ocean, and the concentration of compounds deposited into the ocean, is strongly linked to the chemistry occurring within the marine boundary layer. This chemistry is driven by oxidation processes, moderated by the concentration of oxides of nitrogen and organic compounds. Halogens can also play a significant role. This chemistry is extensive, complex and is still subject to significant current research.

1.4.1 Oxidation

In the clean marine boundary layer, the dominant oxidant is the OH radical (Atkinson, 2000; Logan et al., 1981). This initiates the destruction of many compounds in the atmosphere such as methane, carbon monoxide, organic compounds, oxides of nitrogen etc.

$$CH_4 + OH \rightarrow CH_3 + H_2O \quad (1)$$

$$CO + OH + O_2 \rightarrow CO_2 + HO_2 \quad (2)$$

$$RH + OH + O_2 \rightarrow RO_2 + H_2O \quad (3)$$

$$NO_2 + OH \rightarrow HNO_3 \quad (4)$$

Chlorine radicals can play a similar role, but their concentrations are significant lower than those of OH and so they are thought to play a significantly smaller role (Sherwen et al., 2016b).

Primary OH is predominately produced from the photolysis of ozone by higher energy UV photos and subsequent reaction of the electronically exited oxygen

atom ($O(^1D)$) with water vapour (reactions 5 & 6) (Atkinson, 2000).

$$O_3 + h\nu \rightarrow O(^1D) + O_2 \tag{5}$$

$$O(^1D) + H_2O \rightarrow 2OH \tag{6}$$

Secondary OH is formed from the reaction of the peroxy radicals (HO_2 and RO_2), which are from reactions of OH with CO and organic compounds (reactions 2 and 1). Peroxy radicals can react with nitrogen oxide (NO) to regenerate OH, either directly in the case of the hydroxy-peroxy radical (HO_2) (reaction 7) or indirectly for ogranic-peroxy radicals (RO_2) (reaction 8).

$$NO + HO_2 \rightarrow NO_2 + OH \tag{7}$$

$$NO + RO_2 \rightarrow\rightarrow NO_2 + OH \tag{8}$$

Thus the concentration of OH in the marine boundary layer depends on the strength of the sunlight to photolyse O_3, the concentration of O_3 and the the water vapour concentration to determine the primary production of OH; the concentration of oxides of nitrogen and peroxy radicals to determine its secondary production; and the concentration of the species OH can react with destroying OH.

1.4.2 Ozone chemistry

Ozone is made in the stratosphere from the photolysis of O_2 by very high frequency UV radiation. This ozone can be transported into the troposphere, but within the troposphere the appropriately high energy photons are not available, hence this production route does not occur.

Instead, O_3 in the troposphere is made through the oxidation of organic compounds in the presence of oxides of nitrogen (Logan, 1985). The oxidation of organic compounds by OH leads to the production of peroxy radicals (Reaction 2,

1, 3). These peroxy radicals can then react with nitrogen oxide (Reaction 7, 8 to generate nitrogen dioxide (NO_2). This readily photolyses, regenerating a nitrogen oxide and creating a ground state oxygen atom (Reaction 9).

$$NO_2 + h\nu \rightarrow NO + O(^3P) \tag{9}$$

This ground state oxygen atom reacts rapidly with an oxygen molecule to generate O_3.

$$O(^3P) + O_2 \rightarrow O_3 \tag{10}$$

Thus the production of O_3 in the marine boundary layer is determined to a large extent by the concentration of oxides of nitrogen. Their emission in the atmosphere is dominated by high temperature anthropogenic combustion, and so their concentration in the remote atmosphere is often very low, leading to ozone production being slow. Very often in the marine boundary layer, O_3 destruction processes dominate.

The chemical destruction of O_3 occurs through a number of reaction. Largest is the same reaction that causes the primary production of OH (Reactions 5 and 6) through O_3 photolysis and the reaction of the excited oxygen atom produced with H_2O. O_3 can also be destroyed through its reaction with HO_2 and OH.

$$O_3 + OH \rightarrow O_2 + HO_2 \tag{11}$$

$$O_3 + HO_2 \rightarrow 2O_2 + OH \tag{12}$$

Halogens (Br, Cl, I) can also lead to O_3 destruction within the marine boundary layer through a series of catalytic cycles (for example Reactions 13 - 16 in low NO_x concentrations, where X is Br, Cl, I, Chameides and Davis (1980)).

$$O_3 + X \rightarrow XO + O_2 \tag{13}$$

$$HO_2 + XO \rightarrow HOX + O_2 \tag{14}$$

$$HOX + hv \rightarrow OH + X \tag{15}$$

$$OH + O_3 \rightarrow HO_2 + O_2 \tag{16}$$

Overall, this chemistry leads to O_3 mixing ratios in the marine boundary layer being at their lowest in the tropical marine boundary layer notably around the location of the inter-tropical convergence zone (ITCZ). High humidity, intense sunshine, remoteness from human activity, and emission of halogens in this region all lead to rapid O_3 loss and so low concentrations (Kley, 1997).

1.4.3 Volatile organic compounds

Volatile Organic Compounds (VOCs) form an important group of compounds in the atmosphere, they drive ozone production and their reaction with OH can reduce the rate of methane oxidation. Transport of VOCs from terrestrial sources into the marine boundary layer is often the dominant source, as their direct sources are typically limited to emissions from ships and from human or biogenic activity on islands.

Their oxidation in the marine boundary is dominated by the reaction with OH (Lewis et al., 2005), but oxidation by the Cl radical can also be important (Sherwen et al., 2016b). After this initial oxidation, the oxidation products may then go on to form aerosol and cloud condensation nuclei (Gantt et al., 2009a; Arnold et al., 2009; Shaw et al., 2010).

1.5 Modeling the troposphere

The complexity of this chemistry, coupled with atmospheric transport (meteorology), the emissions of a wide range of compounds from a number of different sources in to the air, and the loss of species both through contact with the surface (dry deposition) and clouds (wet deposition) makes understanding the chemistry of the atmosphere hugely complex. Making predictions of the composition of the atmosphere for the past, present or future without a systematic, numerical representation of these processes is impossible. Atmospheric chemistry transport models represent the tools that allows for this numerical representation.

One of the first efforts to describe the chemistry of the troposphere in such a way was Logan et al. (1981). This developed a model for photo-chemistry in the troposphere, constrained by observations of H_2O, O_3, CO, CH_4, NO, NO_2, and HNO_3. This only considered the two dimensional zonal (latitude-altitude) transport of the atmosphere and was then used to predict a range of tropospheric trace gasses, including HO_x, as functions of altitude, latitude and season. This derived top-down budgets for key species (CO, CH_4, NOx) and a budget for the tropospheric production of O_3.

Over time these models have got increasingly more complex. Where Logan et al. (1981) only considered the 2D zonal atmospheric flow (latitude and altitude), models were subsequently developed based on 3D flow (latitude, longitude and altitude Chipperfield et al. (1993); Wang et al. (1998); Langner and Rodhe (1991)). These models were either driven by meteorological information calculated elsewhere and read into the model (offline models, see for example Bey et al. (2001)) or calculated within a model designed for weather forecasting or climate research (online models, see for example Shindell et al. (2001)).

As well as increased complexity in the physical representation of these models (improved meteorology, boundary layer mixing etc), the complexity of the chem-

istry also increased. Initially only the oxidative chemistry of methane, carbon monoxide, oxides of nitrogen, oxides of hydrogen were considered (Logan et al., 1981). However, over the subsequent decades the complexity of the chemistry has increased to represent the oxidation of many organic compound such as alkanes, alkenes, akynes, di-aklenes, alcohols, organic acids, organic nitrates, organic peroxides etc (see for example Emmons et al. (2020)). The chemistry of DMS oxidation was included in these models in the mid 2000s (e.g. Kloster et al. (2006)).

Halogen chemistry had always been considered important in the stratosphere, and a parallel track of model development for stratospheric applications occurred. However, until the 2010s, halogens were not typically considered in atmospheric chemistry transport models, von Glasow et al. (2004) being a notable exception. A number of models developed representation of halogen chemistry in this time (Parrella et al., 2012; Schmidt et al., 2016; Sherwen et al., 2016b; Ordóñez et al., 2012; Saiz-Lopez et al., 2012). This chemistry now covers the emission of organic halogens from the ocean and terrestrial ecosystems, the direct emission of iodine compounds from the oceans, the emission of sea-salt and the subsequent liberation of reactive halogens and the gas phase chemistry of Cl, Br and I.

As well as gas phase chemistry, the aerosol composition of the atmosphere needs to be modelled. Aerosols are liquid or solid particles suspended in the air (Seinfeld and Pandis, 2012). Aerosols consist of a large number of different compounds, with a range of sizes and different degrees of mixing. Different modelling approaches have tended to emphasise either the size distribution of the aerosols (Spracklen et al., 2005), their composition (Kim et al., 2015) or a combination (Kaiser et al., 2019). A full representation of aerosol size distribution, composition, mixing state and phase in a chemistry transport model is current a challenge for the research community.

Although there have been significant developments in the ability to simulate the composition of the troposphere and the marine boundary layer over the last decades, these models need to be tested and evaluated before they are used. For the marine boundary layer, ship and aircraft born observations can provide some information but it has been long term monitoring from island and coastal atmospheric observatories which have provided most knowledge as discussed in section 1.6.

1.6 Observations

The longest running atmospheric in the world is at Mauna Loa, Hawaii. Located on the northern side of the Mauna Loa volcano, it was established in 1957 (NOAA, 2021). Over the years it has produced key long-term observational datasets notably to show the increasing CO_2 concentrations in the atmosphere (Thoning et al., 1989; Bacastow et al., 1985). A wide range of trace gasses have been and continue to be made at the side, however with the observatory situated at an altitude of 3397m, this station and its long term observations are not useful in providing models with a constraint for the marine boundary layer.

A relatively small number of sites are located close to the ocean surface, within the marine boundary layer. Many of these form part of the World Meteorological Organization's Global Atmosphere Watch network (WMO-GAW, `https://public.wmo.int/en/programmes/global-atmosphere-watch-programme`). These are distributed around the world often in the marine boundary layer (Figure 1).

Figure 1: Locations of the WMO Global Atmosphere Watch station. Taken from http://community.wmo.int/activity-areas/gaw/research-infrastructure/gaw-stations (WMO-GAW, 2021)

From a European perspective, the Mace Head observatory on the western coast of Ireland has provided significant utility as it represents the concentration of pollutants flowing into Europe on the prevailing wind flowing from the west. Studies have highlighted the trends in O_3 concentrations over the 30 year of observation (Derwent et al., 2018), and it has been the scene of a number of intensive field campaigns (Heard et al., 2006; Evans et al., 2000).

Although not part of the GAW network, Trinidad head, located on the northern coast of California, USA (41.0541° N, 124.151° W) (NOAA, 2021) provides similar role for measuring the concentration of pollutants transported from the Pacfic over North America. Surface observations began at the site in 2002 and expanded over the years to include ozone, halocarbons, climate gasses and VOCs (Millet et al., 2004; Li et al., 2005; Oltmans et al., 2008). In 2017 the site was downgraded from observatory to a sampling site, however observations still continue for some instruments and species.

Observations are in the Southern hemisphere are more sparse than in the North, but Cape Grim has provided continuous observations background air since

1976 (CSIRO, 2021). Long term observations have shown the increase of important climate gases (Fraser et al., 1981) and aerosols (Crawford et al., 2017). This observatory has also been the location of field campaigns studying fundamental ozone photochemistry (SOAPEX Monks et al. (1998)), free-radical chemistry (SOAPEX-2 Sommariva et al. (2004)) and methyl halides (AGAGE Cohan et al. (2003); Simmonds et al. (2004)).

Remote South Pacific marine air has been observed at the Samoa Observatory, Tutuila, American Samoa since 1974 (NOAA, 2021). This site has, and continues to make long term observations showing increasing concentrations of CO_2 (Waterman et al., 1989) as well as trends in trace atmospheric gases such as ozone (Harris and Oltmans, 1997).

Cape Verde Atmospheric Observatory (CVAO), part of the (WMO-GAW) network making long term observations of meteorology, greenhouse gases, aerosols and shot-lived reactive gasses (Carpenter et al., 2010). Located north-east facing lava field on Sao Vincente (16° 51' 49 N, 24° 52' 02 W), 50m from the coastline and an elevation of 10m. Its location allows observations of clean Atlantic marine air and has been continuously making observations since 2006 (Carpenter et al., 2010; AMOF, 2021). Observations include ozone, halocarbons, VOCs, NO_x and aerosols (Carpenter et al., 2010; Andersen et al., 2021; Fomba et al., 2014; Read et al., 2008).

Instruments on board ships and aircraft can also provide information about the composition of the marine boundary layer. For example ships have measured the fluxes of compounds from the oceans into the atmosphere (such as DMS, Huebert et al. (2004)) and from the atmosphere to the ocean (such as CO_2, McGillis et al. (2001)). Similarly, aircraft observations can measure the composition of the marine boundary layer far from land (Travis et al., 2020; Bates et al., 2021; Wang et al., 2020) but they give an extreme snapshot of the environment.

These long term measurement sites, together with ship and aircraft platforms have driven our understanding of the marine environment over the last decades. These observations can be used to challenge models, ensuring that they give a useful representation of the processes occurring in the marine boundary layer, and to constrain models where physical, chemical or biological processes are uncertain.

1.7 Summary

The exchange of material between the ocean and the atmosphere and the subsequent chemistry of the marine boundary layer is critical for the climate and air pollution. Although decades of research has been undertaken to better understand these processes, questions remain. This thesis aims to address three of these problems using an atmospheric chemistry transport model as a tool to represent our understanding. Firstly, what level of complexity do we need to represent the deposition of O_3 to the ocean surface (Chapter 3)? Secondly, what are the global oceanic emissions of alkenes (Chapter 4)? Thirdly, what role does the resolution of the model play in our understanding of the chemistry of the marine boundary layer and how we evaluate the model against observation (Chapter 5)?

This thesis will also pose a final question, what should the future development priorities be modelling ocean-atmosphere interactions in global chemistry transport models (Chapter 6)?

The central tool for this evaluation is the GEOS-Chem model and this is described in more detail in Chapter 2.

2 The GEOS-Chem model

As described in the introduction, numerical models of the chemistry, transport, emissions and deposition of compounds form one of the pillars supporting in our ability to explore the processes controlling the composition of the marine boundary layer and the exchange of material between the ocean and atmosphere. These models have developed over the years until they provide an extensive computational framework for developing this understanding. A number of models are available for this supported by groups around the world (Emmons et al., 2020; Archibald et al., 2020; Huijnen et al., 2010; Menut et al., 2021).

These models essentially split the atmosphere into a number of finite grid-boxes. Within each grid box, properties (temperature, pressure, concentration etc) are considered uniform at any one time. By solving a series of differential equations which represent processes such as advection, convection, diffusion, emissions, deposition, and chemistry, the concentration of trace gases in a grid box can be calculated for a short period into the future. By continually solving these equations, the future the temporal variation in the concentration of trace gases can be calculated. As well as calculating the concentration of trace gases, the flux of material into each grid box whether from transport, emissions, deposition or chemistry can also be achieved, allowing for insight into why the model is calculating those trace gas concentrations.

For this work, the 3-D global chemical transport model, GEOS-Chem model is used. It was first described by (Bey et al., 2001). GEOS-Chem is an offline model (meteorological parameters are calculated by a different model and then input into this model) driven by assimilated meteorology from the NASA Global Modeling and Assimilation Office. There are currently two available meteorological product, GEOS Forward Processing (GEOS-FP, Molod et al. (2012)) which is the operational product, reflecting the most up to date version of the GEOS meteorology and physics. GEOS-FP has data archived from 2012 on-wards and

is available at a spatial resolution of 0.25°x0.3125°. The second product is the MERRA-2 reanalysis (Gelaro et al., 2017) which offers a consistent meteorology and physics product from 1979 on-wards at a spatial resolution of 0.5°x0.625°. Both meteorological products contain 72 vertical levels.

2.1 Transport and Vertical structure

Advection within in the model uses the semi-Lagrangian scheme from Lin and Rood (1996). Convective transport is computed from the convective mass fluxes in the meteorological archive (GEOS-FP or MERRA2) as described by Wu et al. (2007). For boundary layer mixing either the non-local scheme (Lin and McElroy, 2010) or full mixing up to the GEOS mixing depth (from the GEOS-FP or MERRA2 meteorology) is used.

The GEOS-Chem model can be run with a reduced vertical grid (47 vertical levels instead of 72) and full chemistry in the troposphere only (TROPCHEM). A simple linear representation of stratospheric chemistry is then used (McLinden et al., 2000; Murray et al., 2012) with the reduced veritcal grid. The main advantage of this is a decrease in model run time when the main focus of the model run is on troposphere, as this work focuses on tropospheric chemistry and impacts only, the TROPCHEM option is used for GEOS-Chem model runs throughout.

Whilst vertical levels exit for the troposphere in GEOS-Chem, oceanic layers do not and there are limited treatments for ocean-atmosphere interactions.

2.2 Chemistry

GEOS-Chem includes HOx-NOx-VOC-ozone-halogen-aerosol tropospheric chemistry, following the JPL/IUPAC recommendations
(GEOS-Chem Steering Committee, 2021). Gas-phase tropospheric oxidant chemistry was first implemented by Bey et al. (2001). Aerosol chemistry was first im-

plemented by Park et al. (2004). Isoprene chemistry (for model versions before to 12.8.0) is from Travis et al. (2016) and Fisher et al. (2016), Criegee chemistry from Millet et al. (2015), and peroxyacetyl nitrate (PAN) is from Fischer et al. (2014). Halogen chemistry (for model versions before 12.9.0) is from Sherwen et al. (2016b) and Chen et al. (2017). The chemistry solver in GEOS-Chem is FlexChem (`https://kpp.readthedocs.io/en/latest/`) which is an implementation of the Kinetic Pre Processor (KPP, Damian et al. (2002)). Photolysis rates are calculated using the Fast-JX code developed by Bian and Prather (2002) with implementations in GEOS-Chem for the troposphere developed by Mao et al. (2010) and the stratosphere developed by Eastham et al. (2014).

2.3 Aerosol

GEOS-Chem models the composition of aerosols. Sulfate, nitrate and ammonia was first implemented and coupled into tropospheric chemistry by Park et al. (2004) with the thermodynamics of these species computed using the ISORROPIA model (Fountoukis and Nenes, 2007). Carbon based aerosols in GEOS-Chem include black carbon (Wang et al., 2014), organic aerosol (Pai et al., 2020) and complex SOA (Pye et al., 2010; Marais et al., 2016). Dust aerosol is included as four bin sizes (Fairlie et al., 2007) and sea salt in two size bins (Jaeglé et al., 2011).

2.4 Emissions and Deposition

Dry deposition is based on the resistance-in-series scheme of Wesely (1989) following the implementation of Wang et al. (1998). Aerosol deposition as a whole is from Zhang et al. (2001), with the case of deposition to snow and ice following that of Fisher et al. (2011). Ozone deposition to the ocean was recently updated to capture ocean surface interactions and is discussed at greater detail in chapter 3 (version 12.8.0 on-wards, Pound et al. (2020)). The wet deposition scheme in GEOS-Chem for water soluble aerosols is based on Liu et al. (2001a) and

trace gas wet deposition from Amos et al. (2012). Henrys law values used are from Sander (2015), where water-soluble organics are from Safieddine and Heald (2017).

Emissions in the model are handled by Harvard–NASA Emission Component (HEMCO, Keller et al. (2014)). At runtime HEMCO provides emissions to the model based on user preferences and has the capability to combine, overlay, mask or scale GEOS-Chem default emissions or user supplied inventories. For times outside of the emission inventories provided, the user can choose to repeat the last available year. For example if the emission inventory ends in 2017, model results from 2018 will use emissions from that inventory from 2017.

By default, global anthropogenic emissions and shipping emissions are from the CEDS inventory (Hoesly et al., 2018), apart from ethane and propane which are from Tzompa-Sosa et al. (2017) and Xiao et al. (2008). Alternatively, anthropogenic emission inventory EDGAR (Crippa et al., 2018) may be used instead of CEDS. Diurnal cycles and weekday scale factors applied to the anthropogenic emissions are from van Donkelaar et al. (2008). Anthropogenic emissions can also be used to forecast for future, following the RCP scenarios (Holmes et al., 2013). Aircraft emissions are from the AEIC inventory (Stettler et al., 2011).

Biogenic emissions of VOCs use the off-line, resolution independent, MEGAN inventory (Weng et al., 2020; Guenther et al., 2012; Hu et al., 2015), apart from acetaldehyde which is from Millet et al. (2010). Soil NO_x emissions also use a resolution independent inventory (Weng et al., 2020; Hudman et al., 2012). By default biomass burning emissions are from GFED (Giglio et al., 2013), however alternative exit in the emissions repository. Lightning NO_x emissions are from (Murray et al., 2012).

The default time steps for chemistry, transport, emissions, and deposition at

each model spatial resolution have been optimised for accuracy and speed by Philip et al. (2016).

2.5 Ocean-atmosphere interactions in GEOS-Chem

Although in reality a two way process, ocean atmosphere exchange in GEOS-Chem is (in general) treated as a number of independent emissions and deposition processes.

For most species, emissions from the ocean to the atmosphere assume a distribution of concentrations across the ocean surface. The emission is then calculated using an exchange function which can depend on factors such as wind speed and ocean temperature. Emissions from the ocean of DMS are based on Lana et al. (2011) (28.1 [17.6–34.4] Tg S yr^{-1}) which was implemented in GEOS-Chem by Breider et al. (2017). Sea salt emissions from the ocean surface are from resolution independent inventory from Weng et al. (2020). Ammonia emissions are from Bouwman et al. (1997). Acetaldehyde emissions from the ocean are from Millet et al. (2010). Ocean atmosphere exchange of acetone in GEOS-Chem assumes fixed ocean concentrations and implemented in GEOS-Chem by Fischer et al. (2012). Oceanic emissions of most halogens (Sherwen et al., 2016b; Chen et al., 2017) follow this pattern. However, the emissions of I_2 and HOI involve a parameterization which uses the surface O_3 concentration (Carpenter et al., 2013).

Dry deposition to the ocean surface follows the resistance in series scheme (Wesely, 1989). The Wesely (1989) scheme considers both transport through the marine boundary layer towards the ocean surface as well as uptake at the ocean surface in the deposition calculation. Gases that are highly soluble (like SO_2) readily deposit to the ocean surface, hence atmospheric transport towards the ocean surface is the limiting factor. Less soluble gases (such as O_3) are limited

by the surface uptake term, hence capturing physical, chemical and biological processes at the ocean surface which control this loss is key to understanding their ocean deposition. The Wesely (1989) scheme, which is used in most atmospheric chemistry models (Hardacre et al., 2015), prescribes constant values for the surface uptake component of the deposition to the ocean surface. As the surface uptake is the rate limiting factor, this results in uniform oceanic deposition velocities globally.

Whilst not an ocean-atmosphere interaction, shipping emissions of NO_x play an important role in marine boundary layer chemistry and representation of the plume at course resolution (Charlton-Perez et al., 2009). NO_x shipping emissions are from CEDS Hoesly et al. (2018) and then processed by PARANOX (Vinken et al., 2011; Holmes et al., 2014) to account for plume chemistry, this results in a reduction of the emission of NOx, but leads to a direct emissions of O_3 and HNO_3. This aims to mitigate the spatial resolution effects of ship plume representation.

3 Oceanic Ozone Deposition

3.1 Introduction

Tropospheric ozone is an important secondary pollutant. Globally it causes one million premature deaths a year (Malley et al., 2017), degrades ecosystems (The Royal Society, 2008) and is a greenhouse gas (IPCC Stocker et al., 2013). Transport from the stratosphere and in-situ chemical production are balanced by chemical destruction and dry deposition to the surface. Total dry deposition of ozone is thought to amount to $\sim$978 Tg y^{-1} (Hardacre et al., 2015) compared to $\sim$500 Tg y^{-1} transported from the stratosphere, $\sim$5000 Tg y^{-1} for chemical production, and $\sim$4500 Tg y^{-1} for chemical loss (Young et al., 2018). Whilst dry deposition velocity to the ocean is thought to be slow ($\sim$0.05 cm s^{-1}) compared to vegetation ($\sim$0.1 cm s^{-1}), the larger area of the ocean compared to the land results in ozone deposition to the ocean representing approximately one third of the total deposition (Ganzeveld et al., 2009).

The ultimate sink of ozone to the ocean is due to chemical reactions as discussed in section 1.2. The focus of this chapter is reaction of ozone with iodide ($[I^-]$) in the surface layer of the ocean via the simplified reaction 17 (Garland and Curtis, 1981; Sakamoto et al., 2009; Hayase et al., 2010; Carpenter et al., 2013) as the dominant mechanism (Garland et al., 1980) of ozone in dry deposition. The transport of ozone within the ocean surface also plays an important role in this process, a simplified version of the relevant processes is shown in Fig. 2.

$$O_3 + I^- + H^+ \rightarrow HOI + O_2 \tag{17}$$

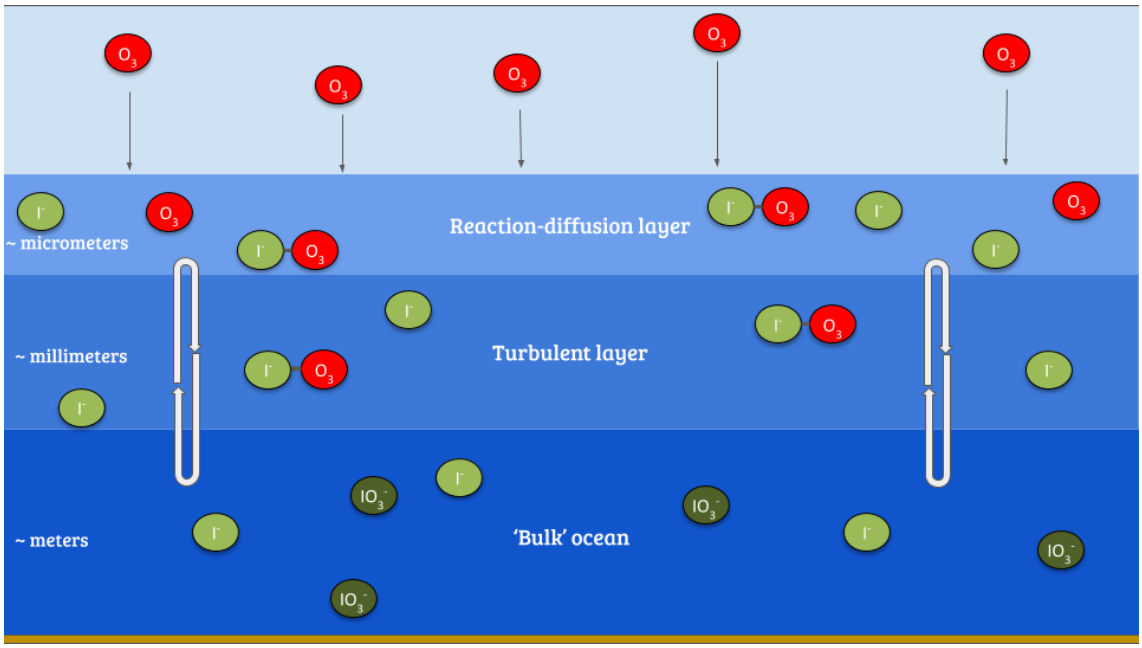

Figure 2: Illustration of the reaction of ozone with I^- in the sea-surface also demonstrating a simplified version of the surface structure where the reaction occurs

The net flux of a gas to a surface F is calculated as the atmospheric concentration at the ocean surface C multiplied by the deposition velocity, v_d, shown in equation 18.

$$F = -v_d C \tag{18}$$

The deposition velocity (v_d) in many models is calculated using the resistance-in-series scheme (Wesely and Hicks, 1977) shown in equation 19. This describes the different limiting factors of the deposition: transport to the ocean surface through turbulent transport (r_a); transport through the quasilaminar sub-layer, which is the air directly in contact with a surface (r_b); and the physical, chemical or biological loss of the molecule at the surface (the ocean in this case) (r_c).

$$v_d = \frac{1}{r_a + r_b + r_c} \tag{19}$$

The relative importance of the different resistances is dependent primarily on the gas being considered. Gases that are highly soluble (such as sulfur dioxide) will have a small r_c, so their limiting factors are the atmospheric resistances (r_a and r_b). Less soluble gases such as ozone are limited by the chemical loss at the surface (r_c). Wesely (1989) gives a value of $r_c = 2000$ s m^{-1} for ozone in both fresh and salt water, and this is used in most atmospheric chemistry models (Hardacre et al., 2015; Luhar et al., 2017, 2018). This chemical loss of ozone, is the limiting factor for ozone deposition (95% of the sum of the resistances is the value of r_c (Chang et al., 2004) and so yields an almost constant (0.05 cm s^{-1}) overall deposition velocity, with only small variation due to meteorological variation in r_a and r_b.

Observations of ozone deposition show significant variability. From the observations collated by Ganzeveld et al. (2009), fresh water deposition velocities range from 0.01 to 0.1 cm s^{-1}, with ocean observations ranging from 0.01 to 0.15 cm s^{-1}. The higher values of ocean observations are likely influenced by coastal footprints containing both land, vegetation and water such as described

by Bariteau et al. (2010), with the open ocean observations being substantially lower (0.009 - 0.065 cm s^{-1}) (Helmig et al., 2012). Given this observed variability, the fixed r_c approach appears overly simple.

Based on Fairall et al. (2007) and Luhar et al. (2017), Luhar et al. (2018) formulated a new scheme for calculating r_c which explicitly takes into account the simultaneous effects of chemical reactions in the ocean with iodide and the physical processes of molecular diffusion and turbulent transfer in the ocean surface. This considers three oceanic layers (Fig. 2); a very shallow "surface reaction-diffusion" layer, that represents the region of the ocean through which the O_3 can diffuse from the atmosphere before it reacts in the ocean. This lies above a thicker turbulent layer which is mixed by wind-stress driven turbulence, which in turn, lies above the the 'bulk' ocean. The loss of O_3 is determined by the chemical reactivity within the reaction-diffusion layer, which is supplied by I^- from below. The resulting scheme derived by Luhar et al. (2018), is based on solving the fundamental equation for the conservation of mass of a reacting and diffusing substance in water (Fairall et al., 2007), yields equation 3

$$r_c = \frac{1}{\alpha\sqrt{aD}}\left[\frac{\Psi K_1(\xi_\delta)\sinh(\lambda) + K_0(\xi_\delta)\cosh(\lambda)}{\Psi K_1(\xi_\delta)\cosh(\lambda) + K_0(\xi_\delta)\sinh(\lambda)}\right] \tag{20}$$

where α is the dimensionless solubility of O_3, a the chemical reactivity of O_3 with sea-surface iodide (the product of $[I^-]$ and the second order rate-coefficient, k), D the diffusivity of O_3 in water, Ψ is defined in equation 22 where u_w^* is the water-side friction velocity, δ_m is the thickness of the reaction-diffusion layer of the sea-surface microlayer, κ the von Kármán constant (≈ 0.4), ξ_δ defined in equation 21, λ defined in equation 23 and K_0, K_1 are modified Bessel functions of the second kind with order zero and one respectively. where,

$$\xi_\delta = \left[\frac{4a}{\kappa u_w^*}\left(\delta_m + \frac{D}{\kappa u_w^*}\right)\right]^{\frac{1}{2}} \tag{21}$$

$$\Psi = \left[1 + \left(\frac{\kappa u_w^* \delta_m}{D}\right)\right]^{\frac{1}{2}} \tag{22}$$

$$\lambda = \delta_m \sqrt{\frac{a}{D}} \tag{23}$$

This representation of the chemical loss of O_3 in the ocean surface is now incorporated into the chemical transport model GEOS-Chem.

3.2 Model setup

Version 12.1.1 (GC12.1.1, 2018) of the 3-D global chemical transport model GEOS-Chem Classic (Bey et al., 2001) (`www.geos-chem.org`) is used. More details on the GEOS-Chem model are available in section 2. In this work global simulations run at a spatial resolution of 2°x2.5° with meteorological data from MERRA-2 (Gelaro et al., 2017). Whilst 2°x2.5° is a relatively coarse model resolution, an assumption is made of no significant sub-grid scale correlation between tropospheric ozone concentration and sea-surface I^- concentration, therefore there should not be a resolution dependence. Resolution impacts are described in more detail in chapter 5. Simulations are run for 2006-2008, 2013 and 2014 so that field observations are compared with the appropriate meteorology. Analysis of the sensitivity of the ozone deposition velocity to its controlling factors uses model runs for 2014. For the analysis of the impact on atmospheric composition, a one year 'spin-up' was used to allow the tropospheric composition to reach equilibrium before the subsequent analysis year.

As with many other atmospheric chemistry and transport models, the dry deposition in GEOS-Chem uses a resistance-in-series scheme based on that of Wesely (1989). The details of this implementation are described by Wang et al. (1998). For terrestrial land types, the dry deposition in GEOS-Chem is generally consistent with observations (Silva and Heald, 2018).

This work follows the Luhar et al. (2018) methodology, and as shown in Equation 20, requiring the calculation of $\alpha, D, k, [I^-]$ and δ_m. Where these require the sea surface temperature (K), T, the skin temperature from the MERRA-2 meteorolog-

ical fields is used.

The dimensionless solubility of ozone in water α from Morris (1988)

$$\alpha = 10^{-0.25-0.013(T-273.16)} \tag{24}$$

the diffusivity D (m^2 s^{-1}) from Johnson and Davis (1996).

$$D = 1.1 \times 10^{-6} exp\left(\frac{-1896}{T}\right) \tag{25}$$

the temperature dependent k (M^{-1} s^{-1}) for the aqueous phase reactions between ozone and iodide from Magi et al. (1997)

$$k = exp\left(\frac{-8772.2}{T} + 51.5\right) \tag{26}$$

the reaction-diffusion sublayer thickness (m) is defined as

$$\delta_m = \sqrt{\frac{D}{a}} \tag{27}$$

and the global ocean iodide concentration distribution [I^-] (M) is taken from the most recent global climatology (Sherwen et al., 2019).

The waterside friction velocity u_w^* (m s^-1) can be calculated from the MERRA-2 atmospheric friction velocity u^* using equation 28 where ρ_a and ρ_w are the density of the atmosphere and seawater respectively. This assumes that drivers of atmospheric stress result in an equivalent oceanic stress (Fairall et al., 2007).

$$u_w^* = \sqrt{\frac{\rho_a}{\rho_w}} u^* \approx 0.0345 u^* \tag{28}$$

Three significant differences exist in our choice of parameters compared to the work of Luhar et al. (2018). Firstly, this work uses the Sherwen et al. (2019) ocean iodide distributions, whereas they use MacDonald et al. (2014). Sherwen et al. (2019) is based on a recent collation of sea surface iodide observations

(Chance et al., 2019) which are interpolated using a machine learning approach. MacDonald et al. (2014) is based on a more restrictive observational dataset and uses a simple temperature based parameterization. Sherwen et al. (2019) calculates a global average sea-surface [I^-] of 105.8 ± 45.6 nM which is a significant increase from the global mean of 58.9 ± 34.9 nM found by MacDonald et al. (2014). Secondly, the inclusion of a variable thickness for the reaction-diffusion sublayer (Equation 27). Luhar et al. (2018) explore various options for this parameter and decide upon a fixed value of δ_m (3.0×10^{-6} m) as this gave the best fit of v_d to observations from Helmig et al. (2012). The variable definition is used in this work as it is more physically based and produces comparable results in our simulations. However, it should be noted that using this definition of δ_m results in terms cancelling in equation 23 such that $\lambda = 1$. This thus simplifies equation 20 somewhat as $sinh(1) \approx 1.175$ and $cosh(1) \approx 1.543$. Some of the implications for different choices for δ_m are explored in Luhar et al. (2018). The final implementation differentiates between salt and fresh water, using a salinity map from the World Ocean Atlas 2013 (Zweng et al., 2013). The new ozone deposition scheme is only applied to ocean water. Anywhere with water and a salinity below 20 PSU or no salinity value (fresh water) is assigned a constant $r_c = 2000$ s m^{-1} as is the case in the Wesely (1989) scheme. One further difference between this work and that of Luhar et al. (2018) is in the global chemistry transport model and its chemistry scheme, GEOS-Chem includes halogen chemistry which has a notable effect on tropospheric ozone (Sherwen et al., 2016b).

Any additional computational expense of implementing this improved r_c calculation will be small as the deposition velocity calculation remains a two dimensional problem, unlike the chemistry or transport calculations which are three dimensional problems. It would be possible to apply this method of calculating r_c to other chemical species. If the appropriate sink processes were understood, chemical kinetics and rate constants available, and concentrations of reactant species known. For this to be useful, the species would need to have a high de-

pendence on r_c (rather than the physical resistances ,hence not highly water soluble), but also for dry deposition to form a substantial part of the species budget. It is not clear whether any species, other than O_3, would meet these requirements.

It would also be possible to to include additional loss reactions of O_3 to species such as DOC, which would increase the rate of oceanic O_3. For this to be possible the rate and form of the loss reactions would need to be known and any competing reactions between I^- and DOC also known. Currently there is insufficient understanding of these reactions for their inclusions.

3.3 Impact of new parameterization on deposition

3.3.1 Change in global distribution of deposition velocities

Figure 3 shows the annual average global distribution of oceanic ozone deposition velocity for both the standard model and the updated surface resistance scheme, along with the percentage difference between the two. Table 1 gives a statistical description of global ozone dry deposition in the model. The near uniform value of v_d with the standard uniform surface resistance can be observed in Fig. 3 (top). The small variability in deposition velocity seen is driven by differences in the meteorology which impacts the r_a and r_b terms. This contrasts with the variability calculated with the new scheme (middle). The two schemes also differ in the magnitude of the deposition velocities. The largest change occurs in the coolest waters towards the poles, with the Southern Ocean having a reduction of over 90% compared to the standard scheme, whereas the tropics can have as little as a 10% reduction. The distribution of v_d is similar to that shown in Luhar et al. (2018), despite our use of the variable thickness for the reaction-diffusion sublayer and the use of the Sherwen et al. (2019) iodide. On an area-weighted basis, the deposition of ozone to the ocean surface is reduced from 0.0464 cm s^{-1} (25^{th} and 75^{th} percentiles of 0.0461 cm s^{-1} and 0.0471 cm s^{-1} respectively), to 0.0231 cm s^{-1} (25^{th} and 75^{th} percentiles of 0.0121 cm s^{-1} and 0.0303 cm s^{-1} respectively). This amounts to a halving of the mean ocean deposition ve-

locity. The reduction of deposition velocity to the ocean results in a reduction of 17% in the global average deposition velocity (Table 1). The total annual loss of tropospheric ozone to dry deposition decreases by 104 Tg yr^{-1} to 758 Tg yr^{-1}, substantially lower than the average of 978 $\pm$ 127 Tg yr^{-1} from the multi-model comparison found by Hardacre et al. (2015) but comparable to the value obtained by Luhar et al. (2018) of 722 $\pm$ 87.3 Tg yr^{-1}.

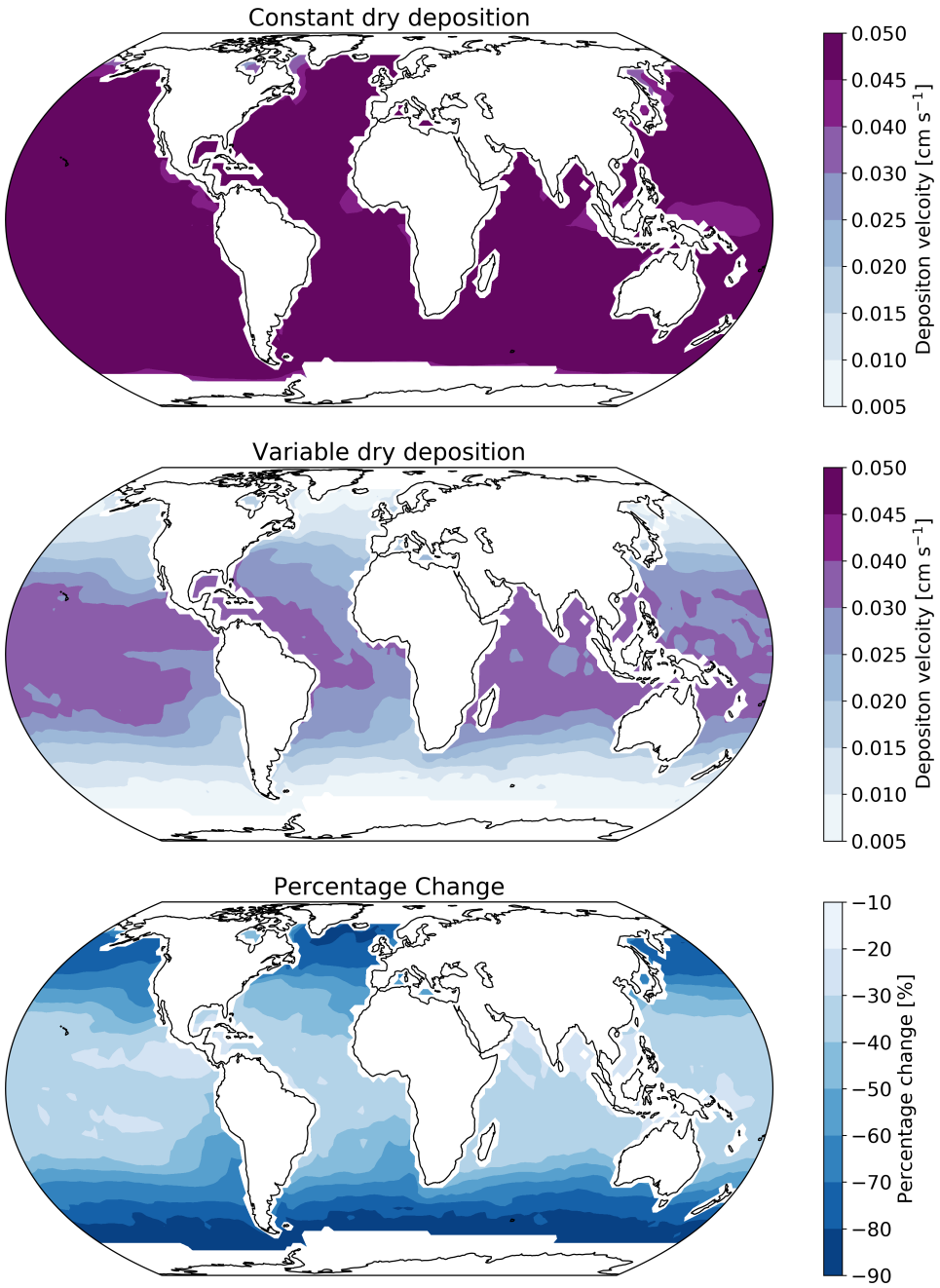

Figure 3: Annual average ozone deposition velocities for 2014 as calculated by GEOS-Chem using the default deposition scheme (top), the new parameterization (middle) and the percentage change between the two schemes (bottom). A 2°x2.5° land mask has been applied to the deposition velocities to show only the deposition velocity to the ocean.

Table 1: Area-weighted annual average deposition velocity and deposition flux for 2014 by land type for ozone in GEOS-Chem using the default (constant) and new (variable) scheme for calculating r_c. The 25^{th} and 75^{th} percentiles are the subscripts and superscripts respectively for each land types deposition velocity. The average deposition velocities, 25^{th} and 75^{th} percentiles were calculated from monthly average model values for grid boxes containing 100% of the land type specified unless otherwise stated.

Land type	Constant r_c		Variable r_c	
	O_3 v_d [cm s^{-1}]	O_3 deposition flux [Tg yr^{-1}]	O_3 v_d [cm s^{-1}]	O_3 deposition flux [Tg yr^{-1}]
Land	$0.2370^{0.2612}_{0.1486}$	383	$0.2370^{0.2612}_{0.1486}$	386
Ocean	$0.0464^{0.0471}_{0.0461}$	222	$0.0231^{0.0303}_{0.0121}$	122
Mixed*	$0.1501^{0.1785}_{0.0489}$	255	$0.1426^{0.1755}_{0.0332}$	248
Ice	$0.0098^{0.0100}_{0.0094}$	2	$0.0098^{0.0100}_{0.0094}$	2
All	$0.0937^{0.0582}_{0.0319}$	862	$0.0781^{0.0460}_{0.0124}$	758

*Where mixed is defined as any grid box containing less than 100% water and less than 100% land

The seasonal changes in ozone oceanic deposition velocities from the new annual mean are shown in Fig. 4. This shows the response of the ozone deposition velocity to changes in sea-surface temperature with the highest value in the summer for each hemisphere and the lowest values occurring in the winter. In the extra-tropical oceans, deposition velocities are predicted to vary by roughly 50% between summer and winter. Deposition velocities in the tropics remain relatively constant over the year.

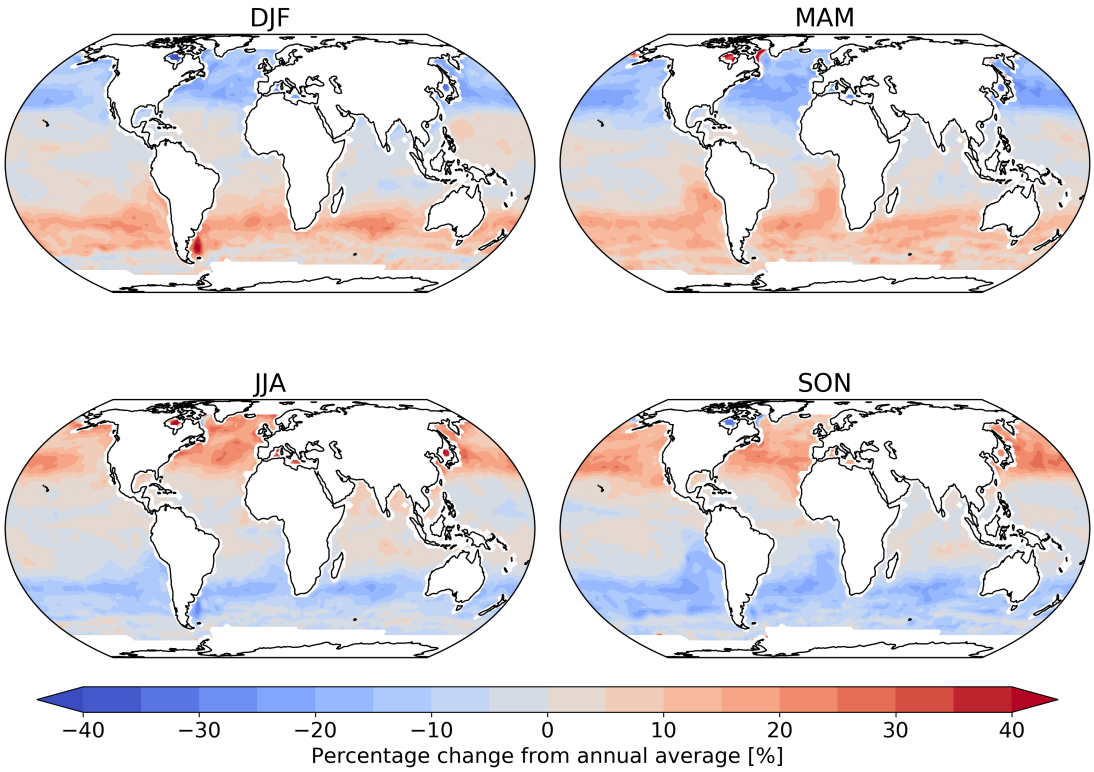

Figure 4: Percentage change from the annual mean deposition velocity for 2014 in December, January, Febuary (DJF) March, April, May (MAM) June, July August (JJA) and September, October, November (SON) for the new parameterization (shown in figure 3) demonstrating the deposition velocity responding to changes in sea-surface temperature and ocean I^- concentration with the lowest values of deposition velocity seen in the winter of each hemisphere. Land and ice grid boxes have been masked out.

3.3.2 Comparison to observations

Here the modelled deposition velocities are evaluated against the open ocean measurements from Helmig et al. (2012) who measured ozone fluxes to the

ocean surface using eddy covariance. These measurements are from a series of five cruises between 2006 to 2008 that took place in the Gulf of Mexico, eastern Pacific Ocean, western Atlantic Ocean and Southern Ocean (Fig. 5). These cruises were made in waters of significantly different sea surface temperature (SST) and show a trend between deposition velocity and the SST. The comparisons between observations and model were made using daily average values with model output selected from grid boxes that the ship track passed through in that 24 hour period. The old scheme (grey line) overestimates the rate of dry deposition substantially and fails to capture any of the temperature dependencies seen in the observations. The new scheme (black line) is a significant improvement, agreeing more with the magnitude and the temperature dependence of the observations. It should be noted that there are significant uncertainties in the measured deposition velocities at low values (Helmig et al., 2012). Combining all the measurements made by Helmig et al. (2012) and comparing to the model predictions for deposition velocity, the root mean square error for the model agreement was reduced from 0.04 cm s^{-1} using the default scheme to 0.01 cm s^{-1} using the new scheme. Whilst the overall agreement of the model with the observations has been improved, the model still fails to capture all of the variability of the deposition velocity measurements. This may be an issues with the resolution of the model (2°x2.5°) which may fail to capture local conditions. Uncertainties in sea-surface iodide concentration or the lack of other sea-surface reactions (reaction between ozone and DOC) may also contribute.

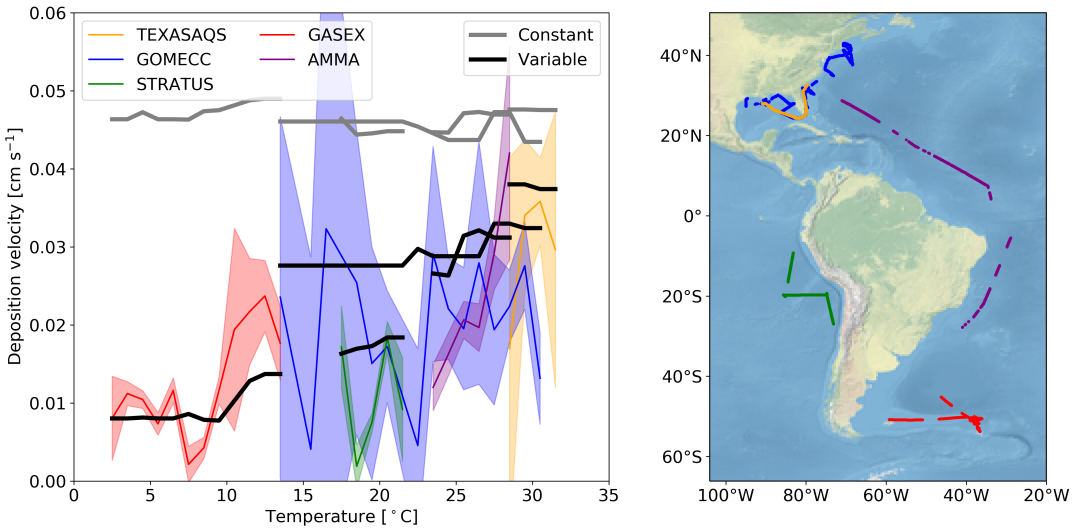

Figure 5: (left) The deposition velocities predicted by the model using the default (Constant) value for r_c and the new (Variable) parameterization of r_c compared against the 5 open ocean cruise data-sets of ozone deposition by Helmig et al. (2012). The solid lines representing the median of the deposition velocity for a one degree temperature window, with the shaded region representing the 25^{th} to 75^{th} percentiles. (right) The locations along the cruise tracks where the ozone deposition has been compared.

3.3.3 Sensitivity of new scheme

This section will now explore the sensitivity of the new scheme to our choice of parameterization for u_w^*, I^-,k,D and α. Five model simulations were each run for a year with only one of the parameters allowed to vary. When constrained, the value of each parameter was set to a representative value of the global average (α, D, k calculated with an SST of 289 K, sea-surface iodide concentration of 106 nM, and u_w^* of 0.01 m s^{-1}). A sixth model simulation was run with all r_c parameters kept constant at these representative values. The resulting dependence of deposition velocity for each simulation is shown in Fig. 6 as a function of sea surface temperature. If all of the terms needed to calculate r_c are kept constant (top left) the oceanic deposition velocity does not vary with temperature. Similarly, if only the water side friction velocity is allowed to vary, no dependence on temperature is seen. Surprisingly the temperature dependence of the iodide concentration is not large, reflecting its square root dependence in the calculation of r_c. The two most important factors for giving the observed temperature dependence are k and α. Of these two terms, the dependence on rate coefficient carries the most uncertainty.

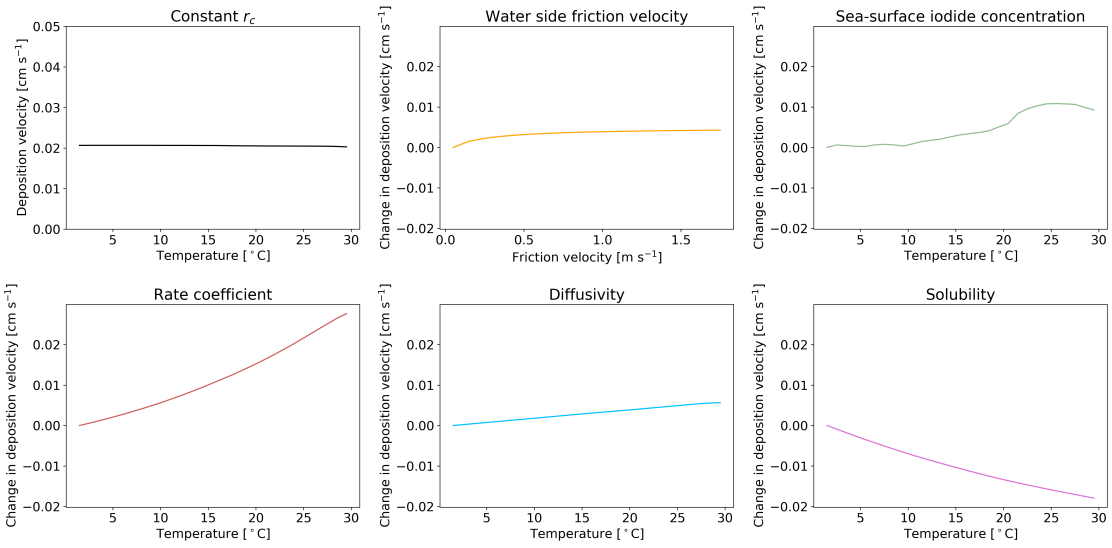

Figure 6: The response of deposition velocity to the variation of only a single parameter with other parameters set to global average values. Sea-surface iodide concentration [I^-], rate coefficient k, diffusivity D and solubility α are produced from global values averaged into 1 K temperature bins. Water side friction velocity u_w^* is averaged into 0.1 m s^{-1} friction velocity bins.

Magi et al. (1997) is the only temperature dependent rate constant in the literature. Other studies are at single temperatures and show differences (Luhar et al., 2018). The impact of these differences is explored by running a number of simulations with different values of the rate constants (Fig. 7). This includes the single temperature rate constants given by Garland et al. (1980) (2.0×10^9 M^{-1} s^{-1} at 298K), Liu et al. (2001b) (1.2×10^9 M^{-1} s^{-1} at 298K) and Hu et al. (1995) (4.0×10^9 M^{-1} s^{-1} at 277K) as well as the upper (equation 29) and lower (equation 30) estimates of Magi et al. (1997) (based on the reported error of the series of measurements).

$$k = exp\left(\frac{-9261.6}{T} + 53.6\right) \tag{29}$$

$$k = exp\left(\frac{-8796.2}{T} + 50.8\right) \tag{30}$$

Figure 7 shows that the uncertainties in k can substantially impact the modeled deposition velocity, with the difference between a temperature invariant and temperature dependent k most notable. Differences in values for k result from experimental setup and I^- concentration. At low I^- and O_3 concentrations (representative of the ocean surface) the reaction occurs in the aqueous-phase, whereas at higher concentrations the surface reaction is the preferred route (Moreno et al., 2018), this results in additional uncertainty in values for k. The temperature independent rate constants don't correctly simulate the observed temperature variability in deposition velocity. The higher estimate from Magi et al. (1997) over estimates the deposition velocity in warm waters, with the lower estimate underestimating in cold waters.

As discussed in section 3.1, iodide is the dominant but not only removal mechanism for ozone at the ocean surface. Given the upper and mid value of the Magi et al. (1997) rate constants there does not appear to be much potential role for other oceanic components to play an important role. On the other hand if the lower values of the Magi et al. (1997) rate constant were correct, this would allow

for inclusion of additional reactions (such as that of ozone with dissolved organic carbon) in the model parameterization without overestimating deposition velocities.

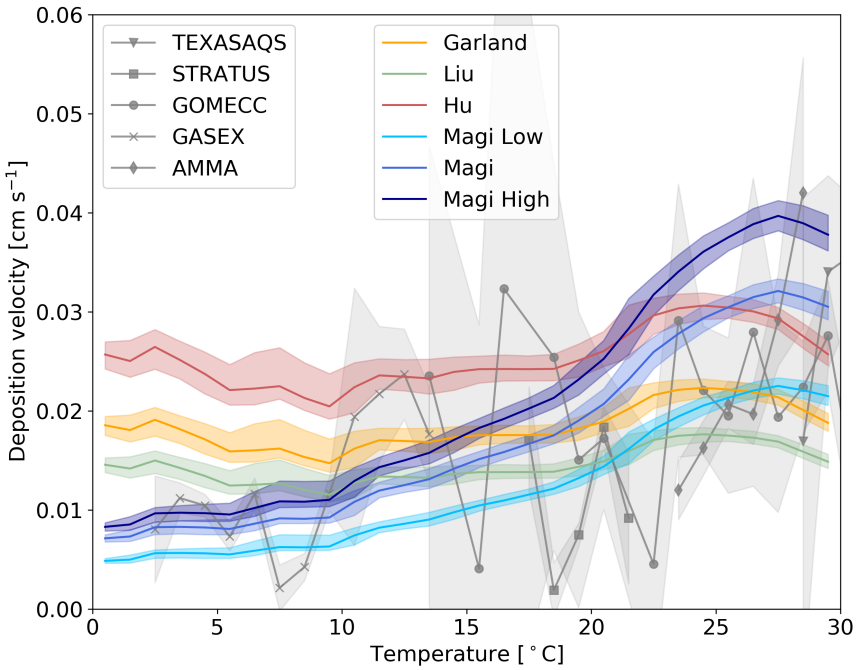

Figure 7: The response of deposition velocity to different different laboratory measurements of k. Three are constant with respect to temperature Garland et al. (1980); Liu et al. (2001b); Hu et al. (1995) and the temperature dependent parameterization of Magi et al. (1997) with two additional cases of k based on the error range of the Magi et al. (1997) measurements (shown in equation 30 and 29). Each function is produced from global values averaged into 1 K temperature bins with the shaded region representing the 25^{th} to 75^{th} percentiles.

3.4 Atmospheric impact

3.4.1 Global impacts

The net decrease in deposition of ozone to the surface results in an increase in both modelled surface and column ozone mixing ratio (Fig. 8). The greatest increase in ozone concentration occurs in the boundary layer with the magnitude of the change decreasing with altitude through the troposphere. The largest increases in ozone mixing ratio is above the oceans, most notably the extra-tropics with the Southern Hemisphere extra-tropics being the area of greatest increase.

The increase in surface ozone concentration becomes small over land. Surface grid boxes that experience a 10% increase or greater in ozone mixing ratio represent 34% of the total surface grid box count. Table 2 gives diagnostics on the oxidative capacity of the troposphere for both the old and new schemes. The increase in ozone mixing ratio shown in Fig. 8 equates to an increase in the tropospheric ozone burden of 4 Tg yr^{-1} (1.2%). This effects the global chemical production and loss of O_3, however these changes are globally minimal at -0.6% and 1.2%, respectively.

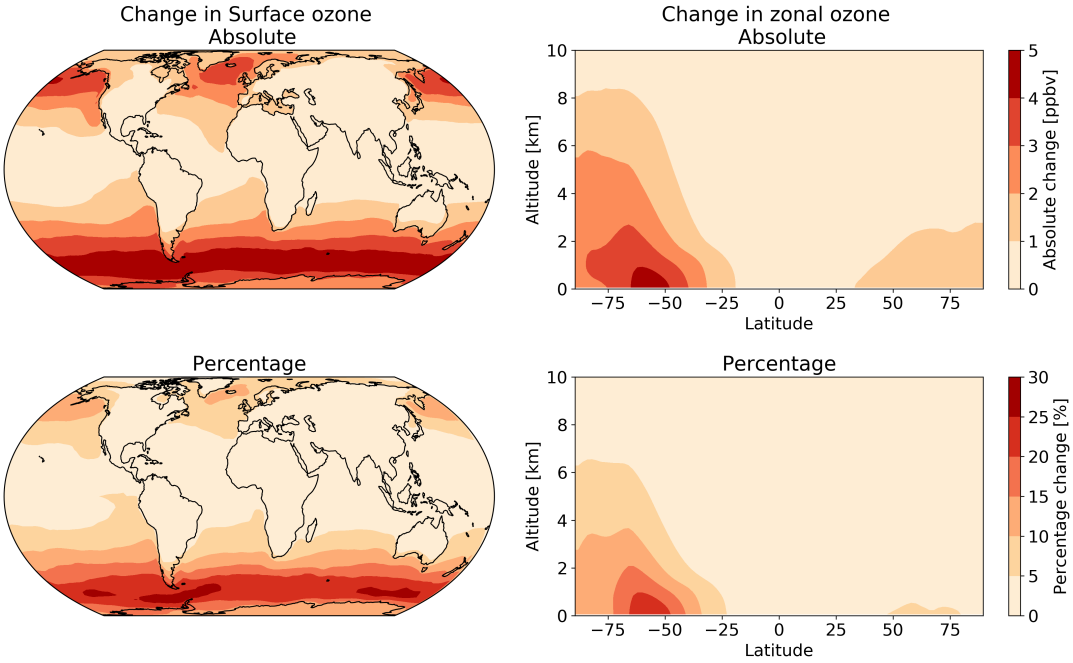

Figure 8: The annual absolute (first row) and percentage (second row) change in surface and column ozone mixing ratios for 2014 between the model using the default (constant) and new (variable) parameterization for r_c. The largest changes occur in the surface levels of the model, especially in higher latitudes with the Southern Ocean boundary layer representing the area experiencing the most annual average change between the two model runs.

Table 2: Summary of change to atmospheric oxidative capacity for GEOS-Chem using default (constant) scheme for calculating r_c and the new scheme (variable) for 2014

	Constant	**Variable**
Troposphere O_3 burden [Tg]	324	328
Net chemical O_3 rate [Tg yr^{-1}]*	450	363
O_X production rate [Tg yr^{-1}]*	5048	5017
O_X loss rate [Tg yr^{-1}] *	4598	4654
O_3 loss to deposition [Tg yr^{-1}]	862	758
Stratospheric O_3 flux [Tg yr^{-1}]	412	395
Global annual mean OH [10^6 molec cm^{-3}]	1.17	1.18
Global CH_4 lifetime [years]	8.3	8.2

*with O_X defined as O_3 + NO_2 + NO_3 + HNO_4 + HNO_3 + N_2O_5 + BrO + HOBr + $BrNO_2$ + $BrNO_3$ + IO + HOI + IONO + $IONO_2$ + OIO + I_2O_2 + I_2O_3 + I_2O_4 + ClO + HOCl + $ClNO_2$ + $ClNO_3$ + Cl_2O_2 + OClO + PAN (peroxyacetylnitrate) + PMN (Peroxymethacryloylnitrate) + PPN (Peroxypropionylnitrate) + MPN (Methyl peroxy nitrate) + ETHLN (Ethanal nitrate) + R_4N_2 ($\geq$ C_4 alkylnitrates) + R4N1 (RO2 from R_4N_2) + Isoprene Nitrate (ISN1, ISOPNB, ISOPND, ISNP) + Peroxy radical from isoprene (ISNOOA, ISNOOB, ISNOHOO) + MACRN (Methacrolein nitrate) + MVKN (nitrate from methly vinyl keytone) + PROPNN (propanone nitrate) + $O_2NOCH_2C(OO)(CH_3)CH = CH_2$ INO2 + $O_2NOCH_2C(OOH)(CH_3)CH = CH_2$ (INPN) + $HOCH_2C(ONO_2)(CH_3)CHO$ (MAN2) + PRN1 (RO2 from propene + NO_3) + PRPN (Peroxide from PRN1) + MACRNO2 (result of $HOCH_2C(ONO_2)(CH_3)CHO$ + OH). For further details on this tagging see the GEOS-Chem wiki `http://wiki.seas.harvard.edu/geos-chem/index.php/FlexChem`

Another consequence of the increased ozone mixing ratio is a small increase in global mean OH concentration of 0.9% (table 2), resulting in a decrease in the tropospheric methane lifetime from 8.3 years to 8.2 years.

Seasonal variations are also observed in the changes in surface ozone mixing ratio due to the new scheme (Fig. 9). The largest increase is observed over the oceans during the winter of each hemisphere due to both the lower deposition velocity that occurs in colder waters and due to the dry deposition playing a larger role in the ozone budget when photolysis is at a seasonal low.

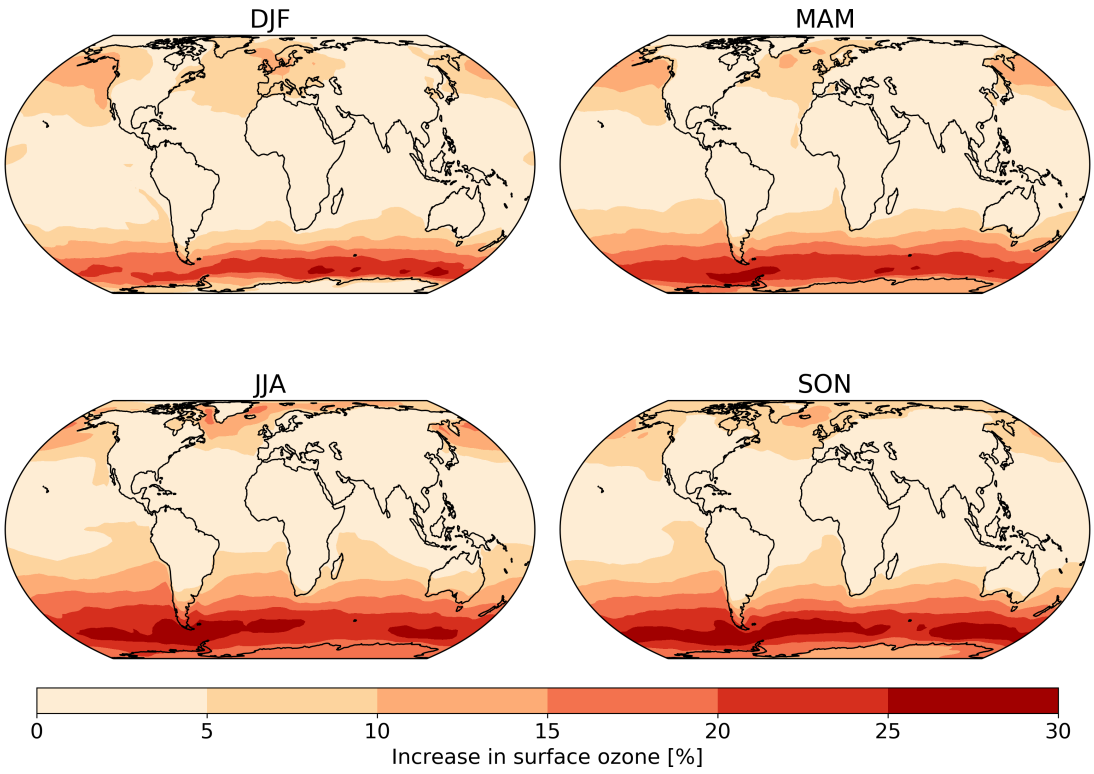

Figure 9: The absolute seasonal surface ozone mixing ratio change for 2014 between the model runs using the default (constant) and new (variable) parameterization for r_c.

3.4.2 Regional impacts

To assess the predictions of surface ozone mixing ratios in the model, comparisons were made with surface ozone measurements from a number of World Meteorological Organization (WMO) Global Atmosphere Watch (GAW; `http://www.wmo.int/pages/prog/arep/gaw/gaw_home_en.html`, accessed through EBAS `http://ebas.nilu.no/`, the database infrastructure operated by NILU – Norwegian Institute for Air Research) sites around the world (Fig. 10, shown south to north).

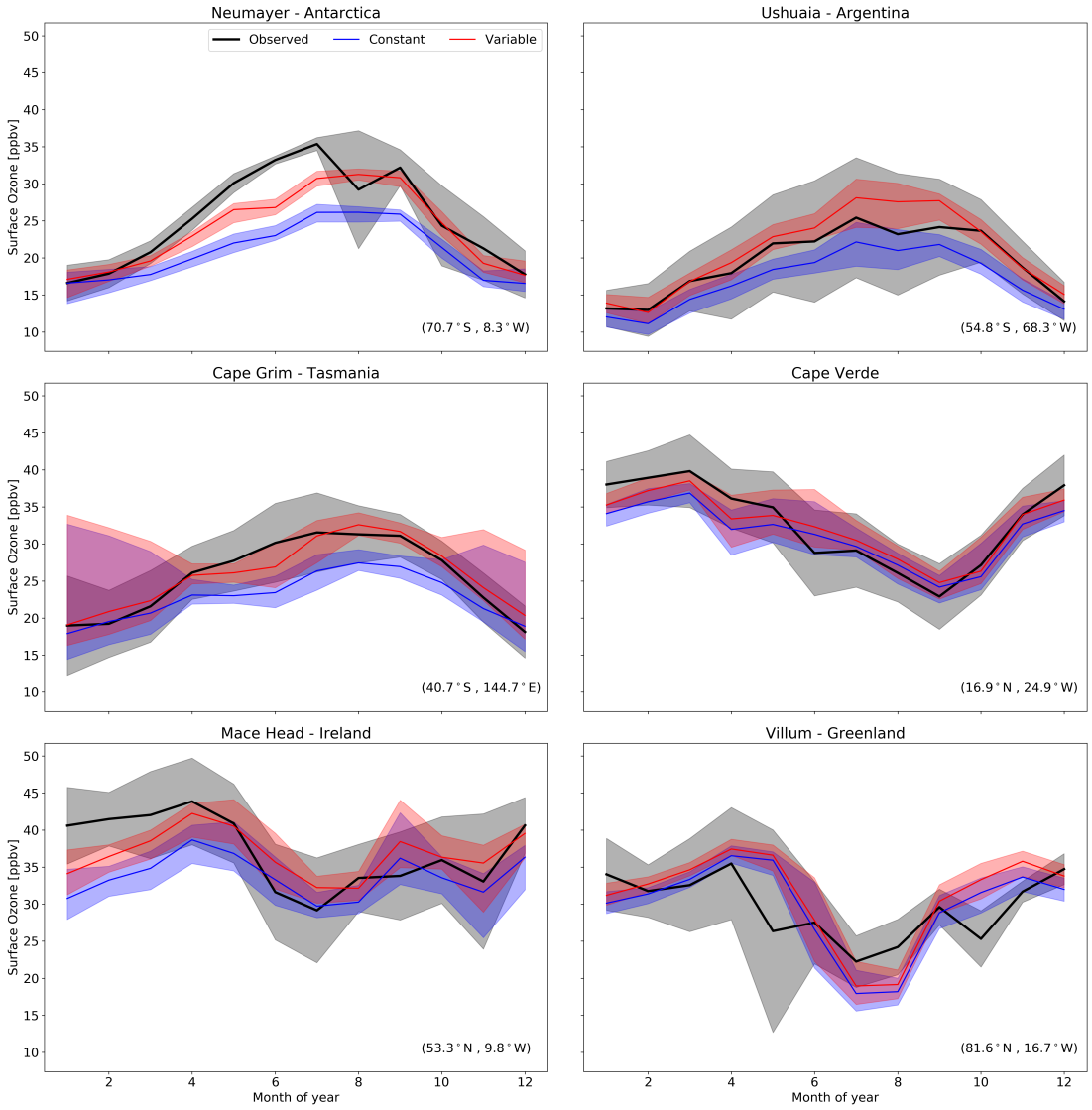

Figure 10: Predictions and observations of monthly average surface ozone mixing ratio for 2014 from the model using the default (Constant) and new (Variable) parameterization for r_c for six GAW stations (with the latitude and longitude for each station at the bottom right) with the shaded region representing the 25^{th} to 75^{th} percentiles.

The largest area of change in surface ozone in the model is in the Southern Ocean. GAW sites in this region (Cape Grim, Ushuaia and Neumayer) show increases in ozone prediction during their winter/spring with the increase most notable in the Antarctic site of Neumayer. Previous work in GEOS-Chem by Schmidt et al. (2016) and Sherwen et al. (2016a) as well as inter-model comparison with ozonesonde observations by Young et al. (2013) show a low bias of GEOS-Chem and other models in the Southern Ocean and Antarctic region. The increased surface ozone mixing ratio brings the model predictions closer to the observations in the Southern Ocean region (Fig. 10), as well as the reductions in root mean square error (RMSE), a measure of disagreement between the model and observations, (table 3) which is reduced by an average of 44% across these three locations. Whilst there are considerable improvements in the Antarctic location of Neumayer, surface ozone demonstrate a 'lag' in responding to Antarctic spring/summer. The model also fails to capture the spring time halogen induced ozone depletion events that are observed at Neumayer.

Table 3: Root mean square error (RMSE) of the model with the default (constant) scheme for r_c and the new scheme (variable) when compared to the observations at GAW sites calculated from monthly mean values of observations and model predictions.

GAW site	Constant RMSE [ppbv]	Variable RMSE [ppbv]
Villum	4.2	4.5
Mace Head	5.0	3.4
Cape Verde	2.6	2.0
Cape Grim	3.5	1.5
Ushuaia	2.7	2.0
Neumayer	5.6	2.8

A comparison to a clean tropical location is made using the GAW site in Cape Verde. Tropical waters are where there has been the least change in ozone deposition velocity, as well as the least increase in ozone mixing ratio both annually and seasonally. Whilst there is a slight increase in predicted ozone compared to the observations at Cape Verde both the model using the old and new schemes for ozone deposition are within the error of the observations, and there is a small reduction in RMSE.

Mace Head, Ireland offers an evaluation of model performance in a mid-latitude inflow region, the inflow of air from the North Atlantic at this site is the dominant component into Europe. Comparing the increase to the observations at Mace Head the improvement is notable with the models error reduced by approximately 30%.

The most northerly of the GAW sites in this comparison is the Villum research station in Greenland. There is a minimal increase in predicted surface ozone ($\sim$1 ppbv) at this site and the resulting RMSE (table 3) shows for Villum an increases of 0.3 ppbv with the new parameterization. The observations at Villum also show spring time ozone depletion events and, as with Neumayer, the model fails to capture this.

Overall, the majority of GAW sites show an improved comparisons with observations due to the implementation of the new r_c scheme and supporting that this change is an improvement to the model.

3.5 Conclusions

This work has implemented a new scheme for the deposition of ozone to the ocean into the GEOS-Chem chemistry transport model based on the work of Luhar et al. (2018). This considers the physical and chemical controls of ozone loss in the sea surface. In contrast to Luhar et al. (2018), our work has used

a variable surface micro-layer depth and the higher ocean iodide concentrations from Sherwen et al. (2019). The new scheme results in a halving of the global mean ozone deposition velocity to the ocean, leading to a small increase in the global tropospheric ozone burden and some regional increases in ozone mixing ratios of up to 30% in the high latitude boundary layer, notably around the Southern Ocean. The new scheme improves comparisons between the model and observations in oceanic regions. The increase in tropospheric ozone concentration also has a minor effect on the global mean OH and CH_4 lifetimes.

The new parameterization improves comparisons between the model and observed oceanic dry deposition velocities. However, no account has been made of potential additional processes such as the reaction of O_3 with DOC, DMS and bromide at the ocean surface. Uncertainties in the rate constant for the reaction between I^- and O_3 could allow room for such additional reactions to play a role. Reduced uncertainty in the temperature dependent rate constant for this reaction would be useful. In addition it seems likely that the interaction between DOC and ozone would be complex. It seems likely that some compounds will act as deposition enhancers, whilst others may act as inhibitors (Martino et al., 2012; Shaw and Carpenter, 2013). Further lab, field and modeling studies will be required to better constrain this.

4 Oceanic Sources of Alkenes

4.1 Introduction

Chapter 3 focused on the transfer from the atmosphere through the air-sea interface in the form of the dry deposition of O_3. Chemistry and mixing at the air sea interface also gives rise to emission of compounds from the ocean into the atmosphere as discussed in section 1.2. This chapter will focus on emissions from the ocean surface of alkenes into the marine boundary layer as an ocean emission that is not currently extensively considered in global chemistry transport models.

Ocean emissions play a key role in understanding the marine atmosphere. Emissions of some species from the ocean are known to play a significant role in determining atmospheric composition. A large number of studies have been conducted on these species (such as DMS discussed in section 1.2). However other species are much less well explored, non-methane volatile organic compounds (NMVOCs) are an example of these. There is a range of work that has observed evidence of oceanic emissions NMVOCs (Bongsang et al. (1988, 1990); Koppmann et al. (1992); Plass-Dulmer et al. (1993), etc), with alkenes (hydrocarbons containing a carbon-carbon double bond) being a dominant component of this emission. The limited studies on oceanic emissions of NMVOCs have found they impact the oxidative environment (Plass-Dulmer et al., 1995; Lewis et al., 2005). Isoprene and monoterpenes are also a source of organic aerosol in the marine boundary layer (Shaw et al., 2010; Arnold et al., 2009; Gantt et al., 2009b), however there is no evidence to support alkenes also being a source of organic aerosol.

In section 4.1.1 observations of alkenes in the marine boundary layer from both ship and land based observatories are discussed, while laboratory experiments exploring the production mechanisms of alkenes in the ocean surface are then discussed in section 4.1.2 in order to explore processes that might play a

role in alkene emission. Subsequent sections trial functional forms for this emission which are scaled to observations at Cape Verde Atmospheric Observatory. The best fit form of oceanic emissions are then compared to surface and plane flight observations globally. Finally this is implemented into the model to assess the global impacts on ethene, propene and atmospheric oxidants.

4.1.1 Previous observations

Measurements of the ocean surface by Bongsang et al. (1988) from a cruise in the Indian Ocean found the ocean surface was supersaturated with NMVOCs compared to contemporaneous air samples. Ethene was the most abundant of the NMVOCs in both sea and air samples, with all NMVOCs demonstrating a consistent relative abundance in sea and air. Continental sources and contamination from the ships plume were removed. Observations of the marine boundary layer made on Amsterdam island (Indian Ocean) by Bongsang et al. (1990) found the relative ratio of NMVOCs concentrations similar to previously published data, again eliminating continental and local sources. In both of these studies it was concluded that the ocean surface was the source for the observed NMVOCs.

Koppmann et al. (1992) performed measurements of atmospheric NMVOCs concentrations above the ocean from Atlantic cruises. They then applied a simple one dimensional model to calculate ocean emission fluxes. Amongst the NMVOCs, ethene showed the best agreement between the model and observations. Observations found that the NMVOCs (including ethene) tended to have lower emissions in the Southern Hemisphere than the Northern Hemisphere. Further cruises in the Atlantic from Plass-Dulmer et al. (1993) also measured NMVOCs in the sea surface. Budget analysis based on those measurements showed the sea surface as a NMVOCs reservoir and NMVOCs in surface waters down to $20m$ were homogeneously mixed. The main loss mechanism for oceanic NMVOCs was thought to be emission into the atmosphere. Plass-Dulmer et al. (1993) also found that emissions (based on the budget analysis) were dominated

by alkenes, with ethene being the largest. No enhancement of ocean surface alkene concentrations were found in regions of high phytoplankton abundance, however in less phytoplankton abundant areas alkene concentrations were higher.

Collecting together a large sample of oceanic NMVOCs observations, Plass-Dulmer et al. (1995) analysed NMVOCs correlations with other available measurements. Ethene was found to have a strong anti-correlation with the transfer velocity of sea-air exchange, implying ethene emissions increasing in turbulent conditions. No correlation was found with solar radiation, chlorophyll-a or sea surface temperature. The dominant loss mechanism of sea-surface alkenes was thought to be emission into the atmosphere. Plass-Dulmer et al. (1995) extrapolated estimates of oceanic emissions of NMOVCs globally, finding ethene alone contributing 40% of NMVOC oceanic emissions (between 0.89 - 1.40 Tg yr^{-1} of ethene). However compared to continental sources, the ocean source played a minor role.

Super saturation of NMVOCs in ocean surface waters was also found by Broadgate et al. (1997) in the North sea. Here a weak correlation was found between chlorophyll and ethene concentrations. Many of the NMVOCs, including alkenes, showed a seasonal cycle in ocean surface concentrations with a minimum in February and maximum in May. Broadgate et al. (1997), like previous studies, found that estimates of NMVOCs emissions from the ocean surface was dominated by C_2-C_4 alkenes.

Cruise based observations of of the marine boundary layer made in the north Pacific and east Indian Ocean by Saito et al. (2000) found ethene and propene shared mostly constant latitudinal profiles with some high observations likely from continental influence. These alkene mixing ratios were substantially higher than in-situ measurements, as with other measurements from lab analysis of gas cylinder samples (Plass-Dulmer et al., 1995). Using back trajectories, Saito et al.

(2000) conclude that the majority of ethene and propene observations were from an oceanic rather than continental source.

More recently Tripathi et al. (2020) studied the atmospheric mixing ratios of NMVOCs above the Arabian sea. Alkenes ethene and propene were the dominant NMVOCs observed, showing a comparable ethene/propene ratios ($\sim$2.6 ppb ppb^{-1}) to other marine boundary layer studies ($\sim$1.96 ppb ppb^{-1} from Bongsang et al. (1988), $\sim$2.27 ppb ppb^{-1} from (Plass-Dulmer et al., 1995)). Here ethene and propene had higher mixing ratios (by as much as 2 orders of magnitude) than other previously studied regions, although an ocean emission was still thought to be the source of these alkenes. Tripathi et al. (2020) attribute the higher ethene and propene mixing ratios to high levels of biological activity in the region. There was also a great deal of variability in the observed alkene concentrations, with coastal regions being $\sim$40% higher than open water.

4.1.2 Laboratory studies

While there is substantial observational evidence to support an ocean surface source of alkenes, the production route is less clear. Laboratory experiments conducted by Ratte et al. (1998) studied the production of many NMVOCs in seawater samples. Ethene and propene were found to be photochemically produced from dissolved organic carbon (DOC). DOC is one of the largest organic carbon reservoirs on the planet (Druffel et al., 1992) and is primarily produced by biological activity in the ocean by phytoplankton. The production of alkenes was greatest with exposure to UV light with a wavelength of 300-420nm. Almost complete removal of ethene and propene from the samples was achieved through de-gassing but was later replenished by further UV exposure. Further studies of biological links to NMVOCs production in ocean surface waters was performed by Shaw et al. (2003). This laboratory study took five different phytoplankton and throughout their life cycle observed NMVOCs concentrations in the samples. Strong correlations were found to phytoplankton metabolism, cell size, and expo-

sure to light for isoprene emissions. However little to no effect for any of these factors was had on other NMVOCs concentrations, including the alkenes.

4.1.3 Summary

Whilst there is uncertainty on the exact routes of production for NMVOCs in seawater, several assumptions can be made. The dominant component of non-methane hydrocarbon (NMHC) ocean emissions are alkenes, notably ethene (C_2H_4) and propene (C_3H_6). Ethene and propene have relatively short lifetimes of 1.4 days and 5.3 hours respectively (at a mean OH concentration of 2x10^6 molec cm^{-1}, Atkinson (2000)), making them more comparable to isoprene with lifetime of 1.4 hours than propane with lifetime of approximately 10 days (under the same conditions). The production route likely starts from or is correlated to DOC. Sunlight in the form of UV also seems to play a role in the creation or emission of the alkenes. This will be the basis of developing an emissions framework for ethene and propene within an atmospheric chemistry transport model.

4.1.4 Developing a global and observationally constrained estimate for oceanic alkene emissions

In this chapter, oceanic emissions of ethene and propene are to be introduced into a chemistry transport model, based on the factors considered important from the observational and laboratory studies discussed in section 4.1.2. Several trial functions representing different production methods will be evaluated and constrained against observations of ethene and propene made at the Cape Verde Atmospheric Observatory (CVAO). Once constrained the impact of these emissions on marine tropospheric composition will be eventuated. The predictions of the model will be assessed against other observations made in other locations to further evaluate the ocean emissions on a global scale.

4.2 Model setup

In this work version, 12.6.0 of the 3-D global chemical transport model GEOS-Chem Classic (Bey et al., 2001; GC12.6.0, 2019) (www.geos-chem.org) is used. More details about the model can be found in section 2. The model is driven by assimilated meteorology (GEOS-FP (Molod et al., 2012)) from the NASA Global Modeling and Assimilation Office. Global simulations are run at a spatial resolution of 2°x2.5°, justification of the selection of this resolution is given in section 5.7. Simulations span a total of 18 months with a 6 month 'spin-up' period to allow the tropospheric composition to reach equilibrium before any subsequent analysis of model outputs between 2017-01-01 and 2018-01-01. When comparing to observations outside of the model run period, equivalent dates in 2017 are selected from the model to compare to observations.

4.2.1 Alkene Chemistry

GEOS-Chem by default includes a HOx - NOx - VOC - ozone - halogen - aerosol tropospheric chemistry, however, propene is the only alkene. The propene tracer is designed to represent propene and larger alkenes. Loss reactions involving the propene tracer in GEOS-Chem include; OH from JPL (2015), O_3 from Millet et al. (2015), NO_3 from Canosa-Mas et al. (1991) and halogens from Sherwen et al. (2016b). Chemical production occurs from the reactions of isoprene and limonene with O_3 (Marais et al., 2016; Atkinson and Arey, 2003), and from reactions involving RO_2 from the oxidation of limonene by OH (Roberts and Bertman, 1992), however, these are of small global importance.

Ethene is not (as of version 12.6.0) included in the GEOS-Chem chemistry scheme. An unpublished ethene oxidation scheme (Per. Comm. Kelvin Bates, Harvard University) has been implemented in the model chemistry scheme along the inclusion of additional reactions with Halogens (Br and Cl) and NO_3 for completeness. Primary loss pathways for ethene are shown in equations 31 to **??**.

These use rate constants found in the Master Chemical Mechanism (MCM) (Saunders et al., 2003) or IUPAC Task Group on Atmospheric Chemical Kinetic Data Evaluation data sheets (IUPAC, 2021). The products from the primary oxidation step are chemically coherent for reactions with OH, O_3 and NO_3 but are simplified for the halogens by assuming the same product for OH chemistry as for halogen chemistry. These halogen channels account for a negligible amount ethene loss ($< 0.3\%$) and so this approximation is unlikely to be significant. Secondary chemistry is a simplification of the MCM chemistry scheme (Saunders et al., 2003) but is designed to be computationally efficient and contains both low and high NOx pathways.

Loss reactions:

$$C_2H_4 + OH \rightarrow HOC_2H_4OO \tag{31}$$

$$C_2H_4 + O_3 \rightarrow CH_2O + CH_2OO \tag{32}$$

$$C_2H_4 + NO_3 \rightarrow O_2C_2H_4NO_3 \tag{33}$$

First generation reactions:

$$HOC_2H_4OO + HO_2 \rightarrow HOCH_2CH_2OOH \tag{34}$$

$$C_2H_4OOH + NO \rightarrow 0.995 \times HOCH_2CH_2O + 0.995NO_2 + 0.005 \times HOCH_2CH_2ONO2 \tag{35}$$

$$C_2H_4OOH + NO3 \rightarrow HOCH_2CH_2O + NO_2 \tag{36}$$

$$\begin{aligned} C_2H_4OOH + MO2 \rightarrow & 0.6 \times HOCH_2CH_2O + 0.6 \times HO_2 + 0.8 \times CH_2O \\ & + 0.2 \times MOH + 0.2 \times C_2H_4O_2 \\ & + 0.2 \times HOC_2CHO \end{aligned} \tag{37}$$

$$HOCH_2CH_2O \rightarrow HO_2 + 2 \times CH_2O \tag{38}$$

$$HOCH_2CH_2O + O_2 \rightarrow HOC_2CHO + HO_2 \tag{39}$$

Second generation reactions:

$$HOCH_2CH_2ONO_2 + OH \rightarrow HOC_2CHO + NO_2 \tag{40}$$

$$HOCH_2CH_2OOH + OH \rightarrow ETOO \tag{41}$$

$$HOCH_2CH_2OOH + OH \rightarrow OH + HOC_2CHO \tag{42}$$

$$HOCH_2CH_2OOH + hv \rightarrow HOCH_2CH_2O + OH \tag{43}$$

Ethene and propene from the ocean will be emitted into separate tracers from the existing terrestrial tracers, but with duplicate chemistry. This allows the independent analysis of the new ocean source without influence from existing emission sources. Combining the individual tracers allows for the total mixing ratio of ethene or propene to be calculated and compared to observations.

4.2.2 Alkene Emission Inventories

The base global inventory used in this work for anthropogenic alkene emissions is the community emissions data systems (CEDS) described by Hoesly et al. (2018). The most recent year available for use in GEOS-Chem is 2014, after which the last available year is used for all subsequent years. Following the standard emissions settings for GEOS-Chem, regional inventories will replace the global default CEDS where available. Regional inventories superseding the global CEDS inventory are national emissions inventory (NEI) for the United States implemented in GEOS-Chem by Travis et al. (2016), for East Asia the mix inventory Li et al. (2014), the DICE inventory for Africa Marais and Wiedinmyer (2016). Additionally global aircraft emissions are from the AEIC inventory described by Stettler et al. (2011). Global shipping emissions are from CEDS (Hoesly et al., 2018).

Biogenic emissions of ethene and propene come for the biogenic VOC's inventory MEGAN v2.1 described in Guenther et al. (2012) and implemented into GEOS-Chem by Hu et al. (2015). Emissions of ethene and propene from biomass

burning sources come from global fire emissions database (GFED) 4.1 Giglio et al. (2013). The global yearly average total emissions of ethene and propene by sector are shown in table 4.

Sector	Ethene [Tg]	Propene [Tg]
Biogenic	20.4	19.3
Biomass burning	3.57	3.80
Anthropogenic	5.18	6.45
Shipping	0.16	0.18
Aircraft	0.00	0.01
Total	29.3	29.8

Table 4: Yearly global emissions of ethene and propene in GEOS-Chem by emissions sector for 2017. Biogenic emissions are from MEGAN (Guenther et al., 2012), biomass burning from GFED (Giglio et al., 2013), shipping emissions are from (Hoesly et al., 2018) and aircraft emissions are from Stettler et al. (2011). Anthropogenic emissions are from CEDS (Hoesly et al., 2018), NEI (Travis et al., 2016) and DICE (Marais and Wiedinmyer, 2016)

For both ethene and propene, biogenic emissions dominate the global source. However, very little emphasis has been placed on a rigorous evaluation of this source. For example a SCOPUS (www.scopus.com) search of ”ETHENE AND MEGAN” only identifies 2 papers. The first is the original MEGAN descriptor paper (Guenther et al., 2012), the second describes the implementation of MEGAN into a CTM (Henrot et al., 2017). A SCOPUS search for ”PROPENE AND MEGAN” only identifies Guenther et al. (2012). Thus although the biogenic source dominates the global emissions in the model, evaluations of its accuracy are hard to find.

4.3 Current model comparisons at Cape Verde

The Cape Verde Atmospheric Observatory, located on eastern side of Sao Vicente in Cape Verde, is positioned to monitor clean mid-Atlantic background air (AMOF, 2021) (see section 1.6). Long term observations of VOC’s have been made since 2006 using a dual channel gas chromatograph with flame ionisation detector (GC-FID) with a detection limit of 2-3 pptv (AMOF, 2021). Included in the long term observations made by GC-FID at this location are measure-

ments of atmospheric ethene and propene (NCAS et al., 2010). Observed ethene and propene, due to prevailing wind direction and the relatively short lifetime of both species (1.4 days and 5.3 hours respectively at 2x10^6 molec cm^{-3}, Atkinson (2000)), originates relatively locally and with minimal contributions from Anthropogenic sources. All model values compared to CVAO observations from the 2°x2.5° global runs in following sections will use the more representative grid box, marked with the yellow border in figure 11 (see Section 5.7) which unlike the model grid box over CVAO (shown in red) does not contain land.

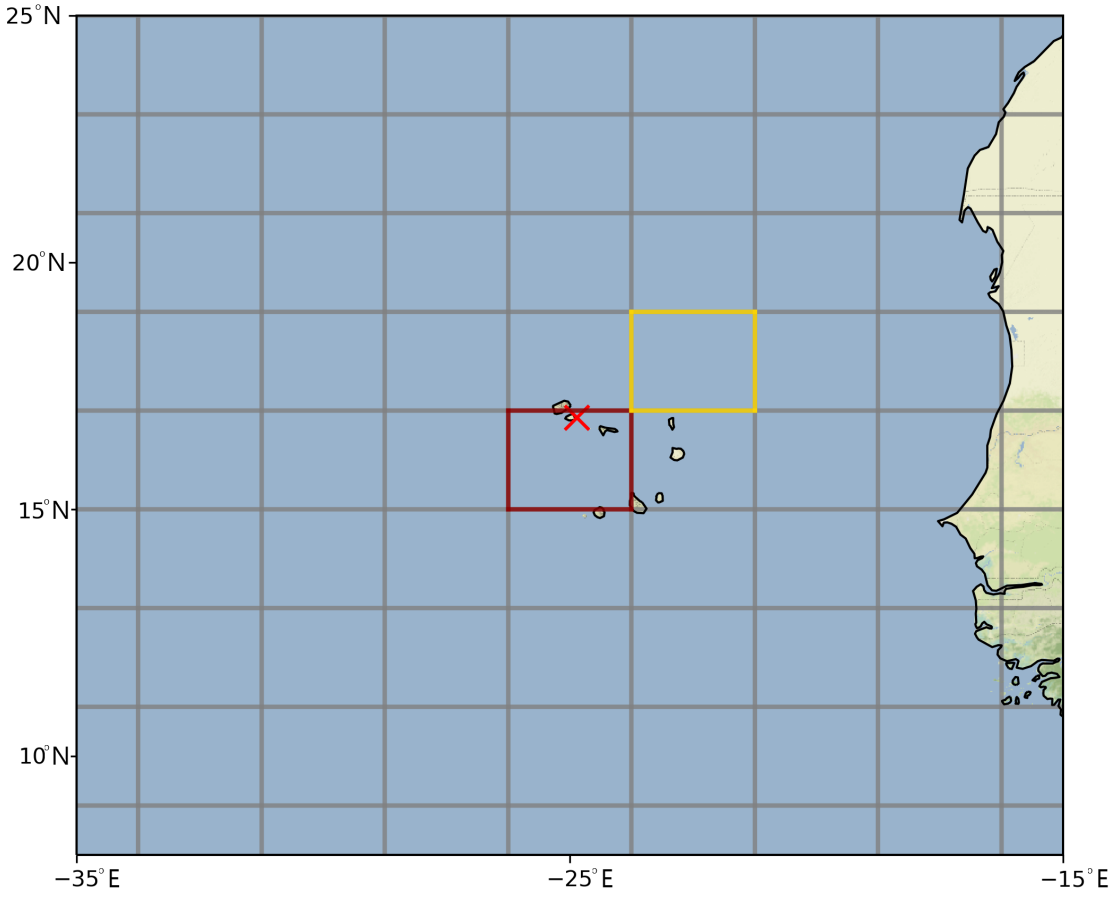

Figure 11: Local region surrounding CVAO (marked with red cross) with surface grid boxes for 2°x2.5° (grey), with grid box over CVAO marked with red edges. Grid box selected as most representative of CVAO observed airmass marked with yellow edges.

For this work observations of ethene and propene made in 2017, that are shown in figure 12 along with the model predictions for the same period. Observations of these alkenes show minimal seasonal dependence likely indicating a

local source and a relatively unchanging local oxidative environment, typical of that found in the tropics. Compared to the model, observations are between approximately five and ten times larger (mean difference of 21 $\pm$ 6 pptv for ethene and 8 $\pm$ 3 pptv for propene).

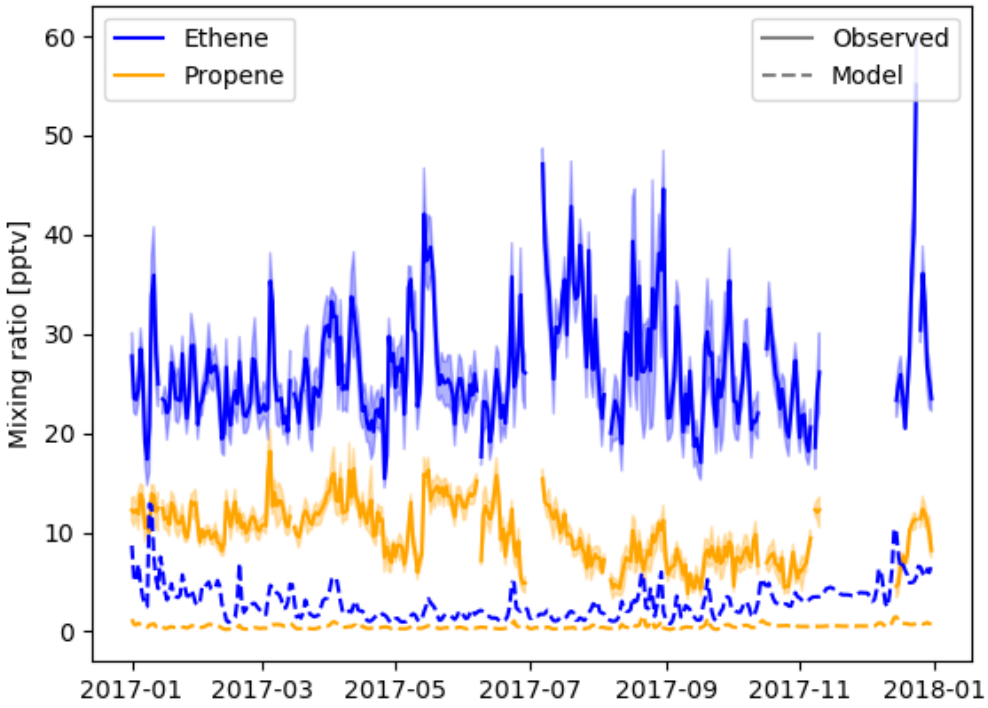

Figure 12: Daily average observed timeseries of ethene and propene from CVAO with shaded region representing two sigma standard deviation (solid line, shaded region showing) and corresponding default model predictions (dashed line).

As observations filtered to remove the influence of local terrestrial influences, and the relatively short lifetimes of both ethene and propene, a substantial increase terrestrial emissions from Europe and Western Africa would be required and there is no evidence to support emissions from these regions are systematically wrong. Additionally there is no evidence to support systematic errors in model transport or vertical mixing, further supporting the need for a localised source. Finally loss of ethene and propene to higher than real world OH is unlikely as this would also be evident in other NMVOC species. Hence an oceanic emission source, supported by previous observations and laboratory studies (sections

4.1.1 and 4.1.2) would be the remaining most likely explanation for the ethene and propene observations at CVAO.

The focus of this work is to find an emission source able to describe the observed diurnal and seasonal cycles for ethene and propene, not the model's ability to replicate fine structure of the observed timeseries. Hence the focus of the model evaluation will be on the average diurnal and seasonal cycles.

Figures 13 and 14 compare the model to the measurements for both the mean diurnal and seasonal cycle. In both cases the model is substantially lower than the observations. Transport of terrestrial biogenic or antroprogenic sources alone are unable to replicate observed alkene concentrations in the model. A substantial increase in existing continental emissions would be needed to reach observed concentrations. However, an ocean source, as indicated by cruise and laboratory experiments, could reconcile the model and the measurements. The question now is how to best represent that source.

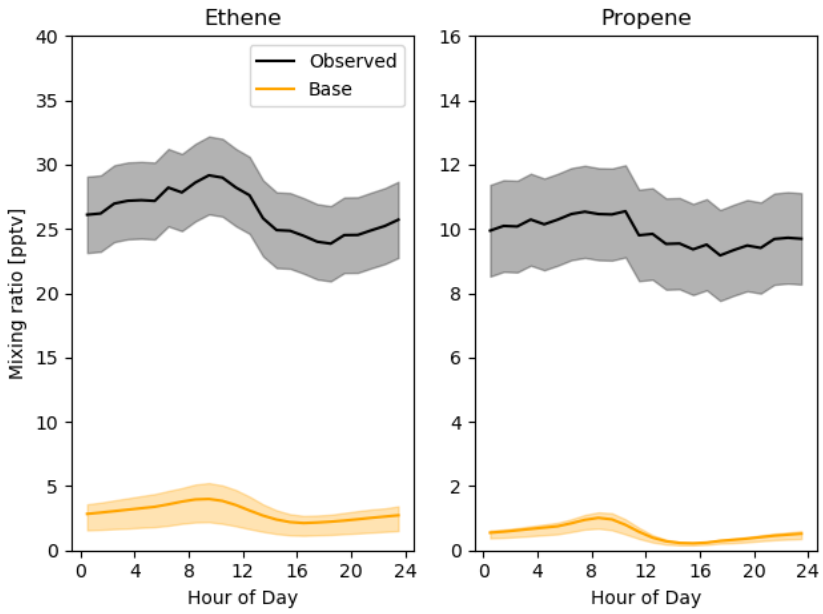

Figure 13: Average diurnal from CVAO observations (black, shaded region two sigma standard deviation) and from the model (orange) using default emission settings for 2017.

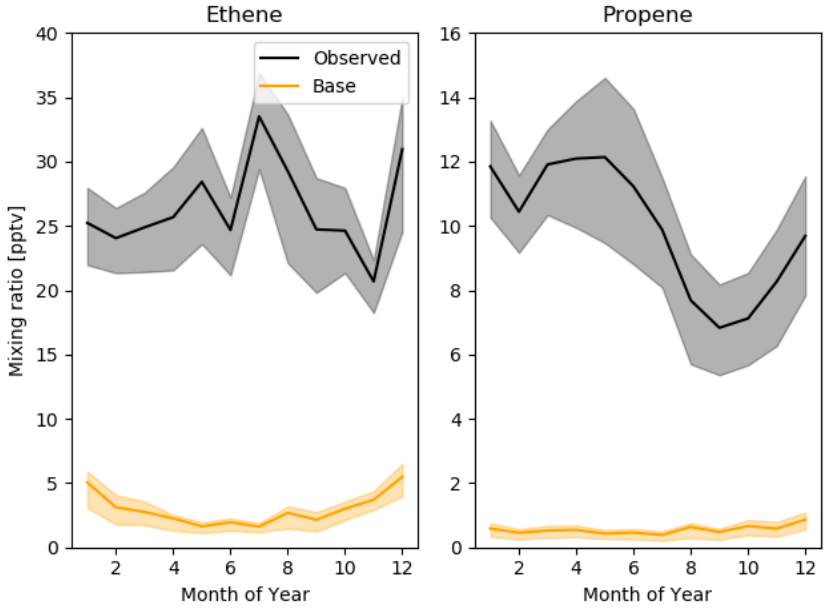

Figure 14: Seasonal cycle of monthly mean mixing ratios from CVAO observations (black, shaded region two sigma standard deviation) and from the model (orange) using default emission settings for 2017.

4.4 Evaluating different forms of ocean emission

There are several possible forms the ocean alkene emission could take. Whilst there is significant uncertainty on the exact routes of production for alkenes (section 4.1.2), some assumptions about the type of ocean source can be made. The production route likely starts from dissolved organic carbon (DOC) in the ocean surface (Ratte et al., 1998) and a photolytic component also seems important (Shaw et al., 2003). Various options are now explored to see how they impact the concentrations of ethene and propene simulated at Cape Verde.

4.4.1 An out-gassing emission ocean source

The simplest implementation would be an emission that just depends on the DOC concentration in the ocean surface. The DOC field developed by Roshan and DeVries (2017) is used here. This was developed using a combination of observations, a neural network and constraint from ocean circulation to give an annual average DOC concentration (figure 15). Globally the lowest values occur in the Southern ocean, increasing toward the central Pacific and Atlantic, and decreasing again at higher latitudes, although Arctic waters have greater DOC concentrations than the Southern ocean. The highest values occur in coastal waters and inland seas where there is higher biological activity.

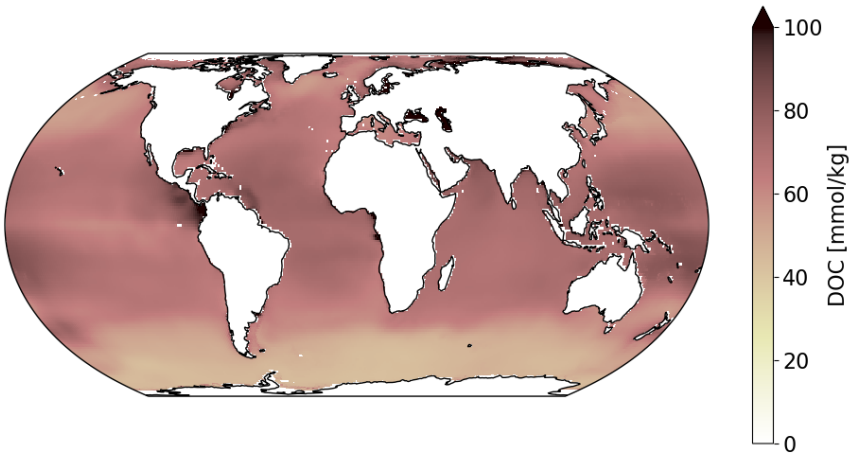

Figure 15: Annual mean ocean surface DOC concentrations from Roshan and DeVries (2017).

Seasonal fluctuations of sea-ice is taken into account by using the sea-ice field from the GEOS-FP meteorology to scale the emission from grid boxes which contain sea ice. The assumption of no emission from sea ice is made, hence emissions in a grid box are reduced by the percentage of sea-ice coverage. The DOC field is then multiplied by a scale factor ($k = 2.0x10^{-15}$ kg^{2}m^{-2}s^{-1}mmol^{-1}) to give an emission flux of alkenes which does not perturb the atmospheric oxidative environment. The emission value for the grid-box representing Cape Verde is 1.4x10^{-13} kgm^{-2}s^{-1}. Assuming steady state, no horizontal or vertical mixing, a boundary layer height of 1000m and a mean OH concentration of 5x10^6 molec cm^{-3}, a ethene and propene mixing ratios of 4 pptv and 0.6 pptv is the result of this emission.

The calculated mixing ratio for the ocean emitted ethene and propene tracers are then compared to the observations. An emissions scaling factor is calculated by minimizing the least squares fit between the hourly observations and the modelled mixing ratios for 2017. This assumes a linear relationship with emissions and surface mixing ratios; the emissions of ethene and propene are assumed to not impact the concentration of atmospheric oxidants. A Python curve fitting function (SciPy community, 2021) is used to optimise the model timeseries. The

resultis a single, temporally constant, scale factor for ethene and propene that can be applied to both the modelled surface mixing ratios and the emissions to gives the best fit to observations.

The diurnal and seasonal cycle for the optimized model mixing ratio are shown in figures 16 and 17 respectively. Whilst the new tuned, out-gassing ocean source does substantially increase both ethene and propene concentrations, it fails to capture the diurnal profile of the observations. There is a much more muted diurnal in the observations compared to the model diurnal, which would imply the need for an emission that peaks at the solar maximum, when loss processes (via OH) are at their peak. The seasonal cycles for ethene and propene, whilst again much closer in magnitude to the observations, does not demonstrate the same trend as the observations.

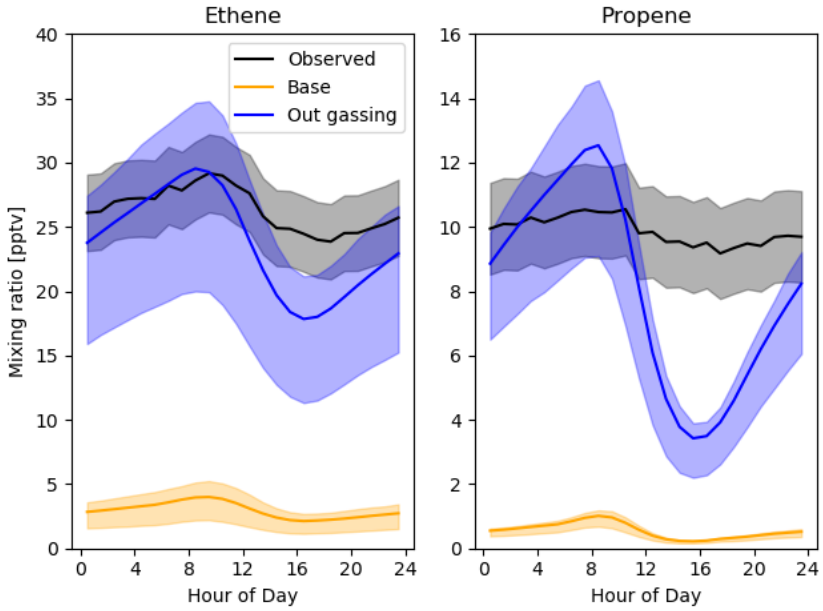

Figure 16: Mean diurnal cycle in alkene concentrations for 2017 at CVAO. Observed in black, with 2 sigma interval as the shaded region, the model using default emission settings in orange, and the combination of default terrestrial emissions and the optimized out-gassing ocean source in blue.

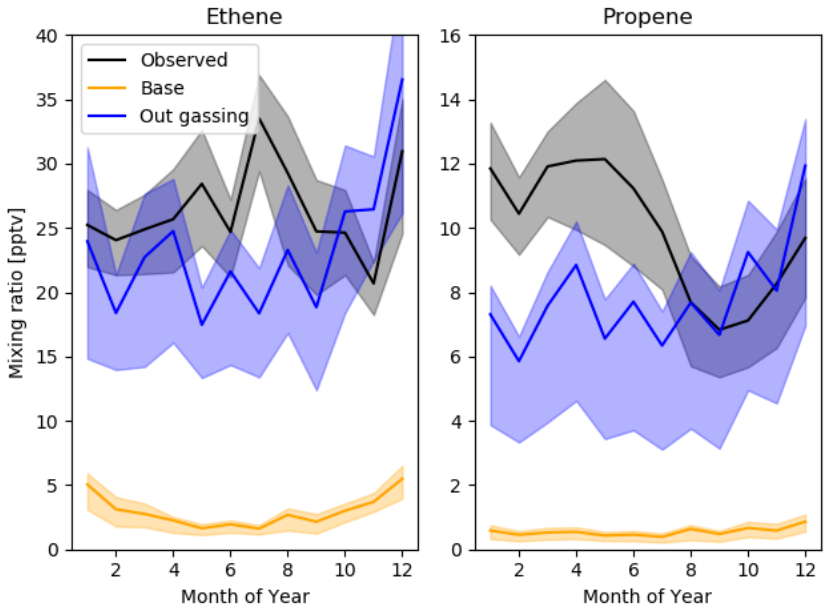

Figure 17: Monthly mean seasonal cycle in alkene concentrations for 2017 at CVAO. Observed in black, with 2 sigma interval as the shaded region, the model using default emission settings in orange, and the combination of default terrestrial emissions and the optimized out-gassing ocean source in blue.

4.4.2 A photolytically driven ocean emission source

An alternative to simple out-gassing from a super-saturated ocean surface is production and emission being closely linked to the photolytic environment. This would be a system where photochemical or photobiological production is the rate limiting factor and emissions are closely correlated to this. The ocean surface alkene concentration quickly reaches equilibrium with the production.

Two possibilities for the photolytic link are now be tested. The first of these uses lower energy photons (towards the red end in the visible spectrum). These photons have a stronger link to the ocean biological activity, which in laboratory experiments has shown strongest correlation with isoprene concentration, but did have a weak correlation with ethene concentration (Shaw et al., 2003). For this the emission source follows the values of photolytically active radiation (PAR) from the meteorological model inputs.

The second option is the higher energy photon (blue end of visible into low

UV). These higher energy photons combined with DOC were found in laboratory experiments to have a strong correlation with alkene production (Ratte et al. (1998)). The Photolysis rate of $O_3 \rightarrow O(^1D)$ ($J(O^1D)$) was selected as the proxy in this case, with values calculated by the model during run time.

In the same way as the previous constant out gassing, the photolytic component of the emissions emissions for ethene and propene are calculated by multiplying the DOC by k and then by either PAR or $J(^1D)$. As before the scale factors are then calculated by comparing the mixing ratio of the tracer against that observed and finding the optimal fit.

The diurnal and seasonal cycle of the optimized model mixing ratios are shown in figures 18 and 19. Again optimization achieves the right magnitude of mixing ratio, but the average diurnal cycle is both offset to, and more pronounced than, the observations. At night there is no emission (as there are no solar photons) so the mixing ratio of both ethene and propene drop as air from aloft with low concentrations is mixed down. Thus at dawn the model is at its minimum, whereas the observations are at their maximum. During the day, modelled concentrations increase rapidly as photons land on the ocean surface. The modelled mixing ratio maximizes at dusk whereas observations show a minimum here. The modelled seasonal cycle shows improvements with the ethene showing little seasonality (as observed) and the propene showing higher concentrations during the spring than the summer.

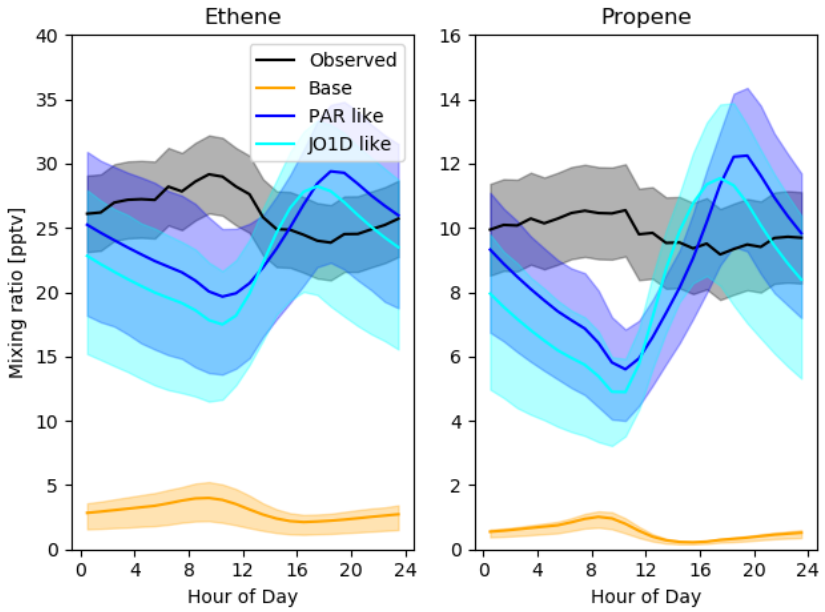

Figure 18: Mean diurnal cycle in alkene concentrations for 2017 at CVAO. Observed in black, with 2 sigma interval as the shaded region, the model using default emission settings in orange, and the combination of default terrestrial emissions and the optimized PAR like ocean source in blue, and the combination of default terrestrial emissions and the J(O^1D) like ocean source in cyan.

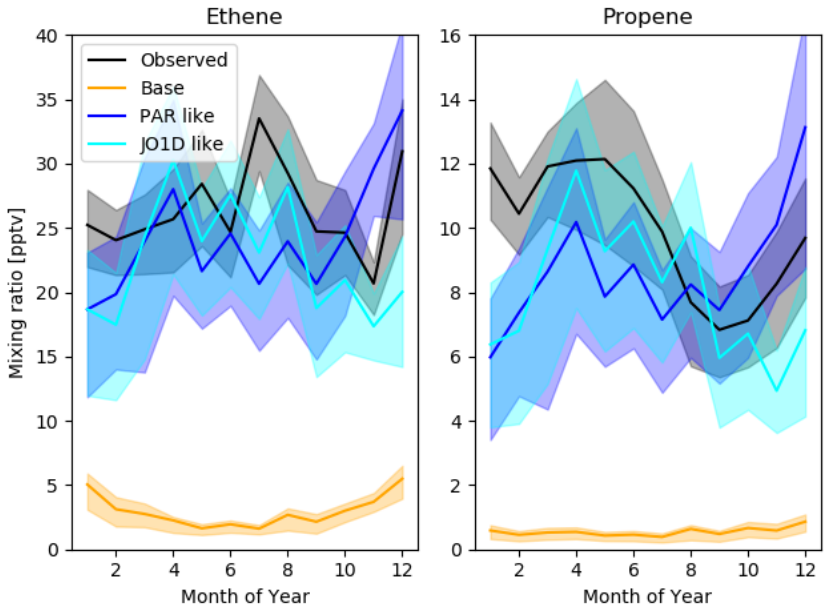

Figure 19: Monthly mean seasonal cycle in alkene concentrations for 2017 at CVAO. Observed in black, with 2 sigma interval as the shaded region, the model using default emission settings in orange, and the combination of default terrestrial emissions and the optimized PAR like ocean source in blue, and the combination of default terrestrial emissions and the J(O^1D) like ocean source in cyan.

4.4.3 Combination of out-gassing and photolytically driven emission sources

An out-gassing source or a photolytic driven source alone are unable to fully replicate the observed seasonal and diurnal cycle of ethene and propene at CVAO.

Here a combination of both an out-gassing and photolytic source, describing an ocean surface that is supersaturated with alkenes, that is continually out-gassing with an increase in emissions occurring when ocean surface concentrations increase from photolytic production alkenes.

Two tracers each with the initial oxidation chemistry are used for ethene and propene. One which is subject to the continuous emissions, and one which is subject to the photolytic emissions (for both PAR and J(O^1D). The optimization then attempts to linearly scale the tracers from both emissions types to give the best fit. The resulting optimised diurnal and seasonal cycle for both the PAR and J(O^1D) like ocean emission are shown in figures 20 and 21. Both a PAR like and a J(O^1D) like plus out-gassing ocean emission source result in a model diurnal cycle that more closely resembles the observations for ethene and a significantly reduces error for propene.

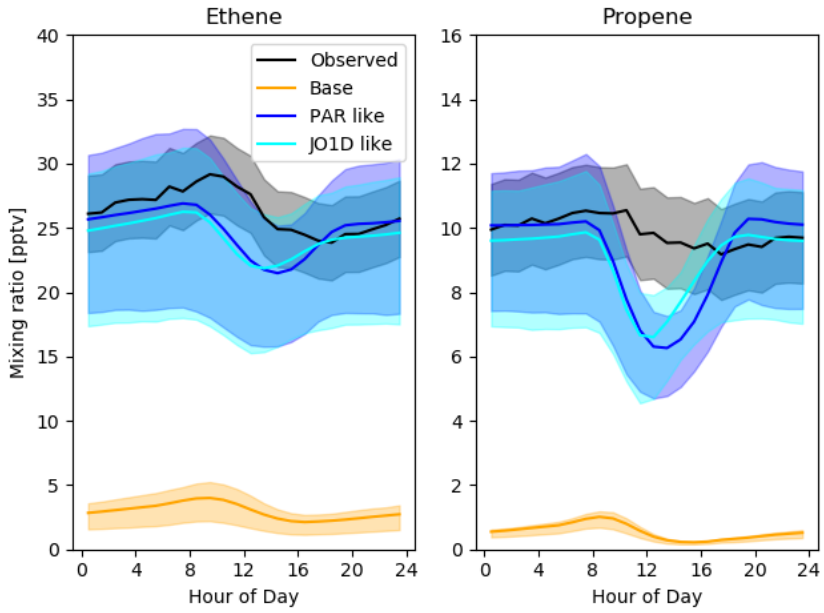

Figure 20: Mean diurnal cycle in alkene concentrations for 2017 at CVAO. Observed in black, with 2 sigma interval as the shaded region, the model using default emission settings in orange, the combination of default terrestrial emissions with optimized PAR like and outgassing ocean source in blue, and the combination of default terrestrial emissions with J(O^1D) like and outgassing ocean source in cyan.

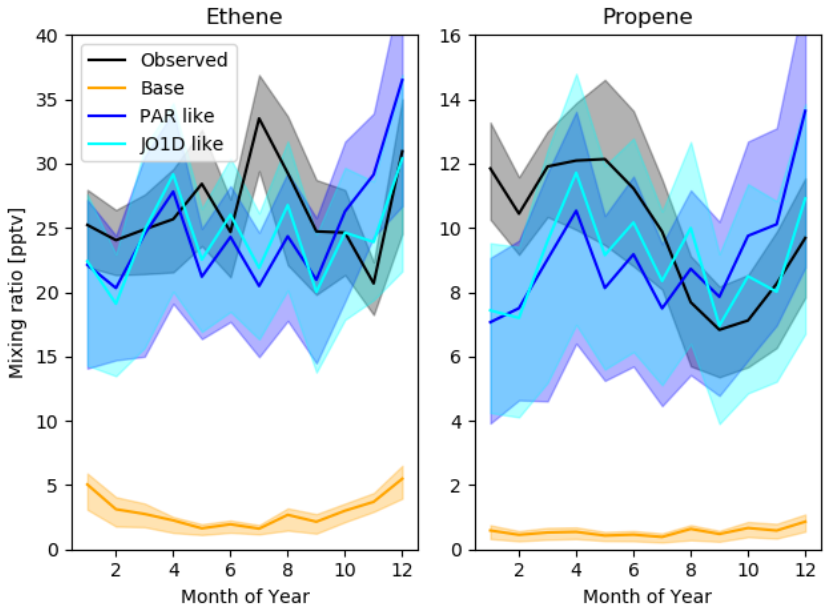

Figure 21: Monthly mean seasonal cycle in alkene concentrations for 2017 at CVAO. Observed in black, with 2 sigma interval as the shaded region, the model using default emission settings in orange, the combination of default terrestrial emissions with optimized PAR like and outgassing ocean source in blue, and the combination of default terrestrial emissions with J(O^1D) like and outgassing ocean source in cyan.

A quantitative comparison of the model and measured root mean square errors (RMSE) for all of the optimized emission possibilities is shown in table 5. The combination of an out-gassing source and a J(O^1D) like photolytic source has the lowest RMSE for both diurnal and seasonal cycles for propene, but leads to a slight reduction in performance compared to the PAR like photolytic source for the ethene diurnal. The reduction in RMSE for the model diurnal is more notable than that of the seasonal cycle, which even in the best case, still shows significant differences to that of the observations. However, the J(O^1D) parameterization is preferred.

	Ethene [pptv]		Propene [pptv]	
	Diurnal RMSE	Seasonal RMSE	Diurnal RMSE	Seasonal RMSE
Base	20.4	20.9	8.24	8.53
Base + Out-gassing	3.52	6.68	3.24	3.38
Base + PAR	5.04	5.87	2.66	3.01
Base + J(O^1D)	6.25	5.96	3.14	2.70
Base + Out-gassing + PAR	2.30	5.73	1.60	2.83
Base + Out-gassing + J(O^1D)	2.55	4.61	1.40	2.17

Table 5: Root mean square error between observations and model predictions for

To further assess the best fit case of out-gassing and J(O^1D), it is now evaluated globally. This will use the same scaling on the out-gassing and J(O^1D) like tracers derived for CVAO but reflects local changes in DOC and J(O^1D).

4.5 Global comparisons to CVAO like ocean alkene source

4.5.1 Cape Grim, Tasmania, Australia

Lewis et al. (2001) made observations of ethene and propene from Cape Grim (-40.7,144.7), located on the island of Tasmania off the south east coast of Australia. This observational data set only spans one month (between January 14^{th} - February 19^{th} 1999) with a subset of that being measurements made of clean marine background, determined by back trajectories performed as part of the data analysis. Similar considerations of model spatial resolution were made for this site as they were for CVAO as discussed in section 5.7. Thus the model grid box west of the one containing Cape Grim is used to mitigate for the influence of land. Figure 22 compares those clean marine background periods for that time, with the average diurnal for standard model and with the additional ocean source. There are between eight to ten observations per hour for ethene and propene from which the diurnal cycles are constructed. Unlike the model comparisons made to observations at CVAO, the base case for both ethene and propene is substantially higher than the observations. The addition of the new ocean source further exacerbates this difference.

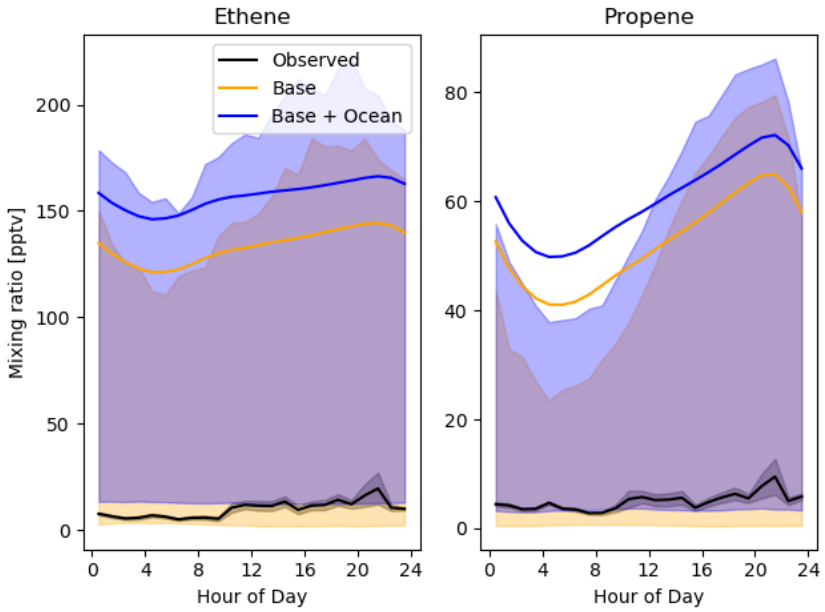

Figure 22: Mean diurnal cycle (UTC) in alkene concentrations at Cape Grim during marine boundary layer origin airmass. Observed in black, the model using default emission settings in orange, and the combination of default terrestrial emissions ocean source in blue. Shaded regions representing 25^{th} and 75^{th} for model and 2 sigma standard deviation for observations.

The dominant emission source for ethene and propene in Australia, as with much of land based emissions in the southern hemisphere, is biogenic. Figure 23 shows the fraction of emissions in the model which are biogenic for ethene and propene. Emissions of both ethene and propene in MEGAN v2.1 (Guenther et al., 2012) are based on measurements of canopy scale fluxes from a temperate deciduous forest in Massachusettes, US (Goldstein et al., 1996). It would seem likely that vegetation in a very different ecosystem could emit different amounts of these VOCs. For example, Garraway (2018) showed that GEOS-Chem substantially overestimated propene compared to observations made in the tropical rain forest environment of Malaysia. Garraway (2018) did not make comparisons for ethene as this was not in the model. Biogenic emissions from MEGAN needed to be reduced by a factor of 10 to bring the model and measurements into better agreement. It would seem therefore that the model could overestimate the biogenic emissions of ethene and propene from Australia.

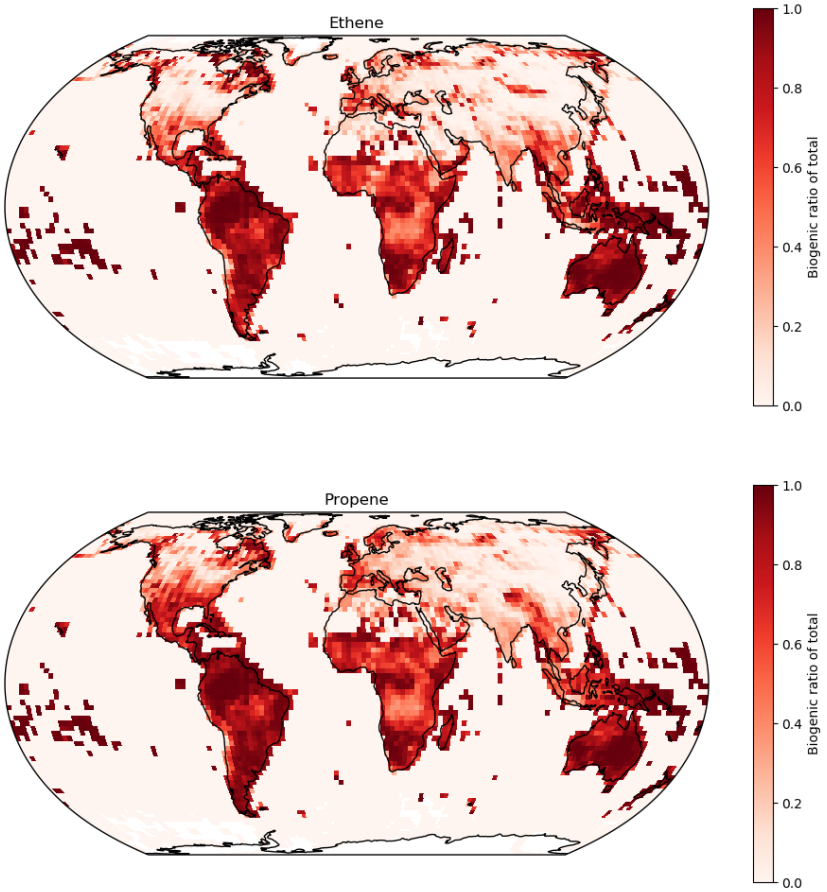

Figure 23: Ratio of biogenic emissions to the total emissions from all anthrorpogenic, biogenic and biomass burning sectors for ethene and propene.

Removing the effects of the biogenic emissions overestimate by making the comparison between the observations and the tracers from the model ocean source alone results in a substantially improved agreement (figure 24). This is different to model predictions at Cape Verde, where terrestrial sources of ethene and propene contribute < 4 and < 1 pptv to model predictions. The ocean source of ethene and propene alone results in a comparable order of magnitude to the observed average diurnal but does not capture the diurnal cycle of these observations. The short period of time used combined with the exclusion of observations marked as continental in origin makes the interpretation of the model failure in this situation difficult.

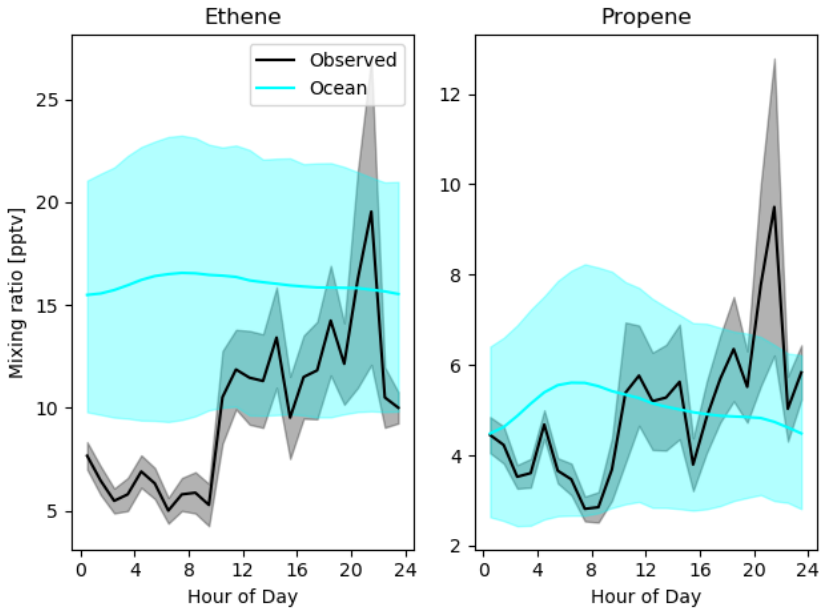

Figure 24: Mean diurnal cycle (UTC) in alkene concentrations at Cape Grim during marine boundary layer origin airmass. Observed in black and the alkenes from an ocean source in blue. Shaded regions representing 25^{th} and 75^{th} for model and 2 sigma standard deviation for observations.

4.5.2 Halley base, Antarctica

A year worth of ethene and propene observations made as part of the CHABLIS experiment (Read et al., 2007) at Halley base, Antarctica (-75.3,-26.7). This provides another point of comparison for southern ocean ethene and propene. To be more representative of the air mass observed at Halley the grid box to the north of the box containing the Halley observations is used here. The annual average diurnal and seasonal cycle for both ethene and propene are shown in figures 25 and 26 respectively. The average diurnal for model ethene is close to the magnitude of the average observed diurnal, however a strong seasonal cycle is present in the model base case for ethene which does not reflect observations. This is due to the large biogenic emissions in the Southern Hemisphere coupled with the very low oxidation rates that occur in Southern Hemisphere winter. The model fails to capture both seasonal and diurnal trends observed for propene. Whilst the additional ocean source does result in an increase in modelled propene, a more substantial increase in the ocean emissions would be required to replicate the observed diurnal and seasonal cycle. Increasing oceanic emissions of ethene

by ∼56% and propene by 153% would result in a model more comparable to observations.

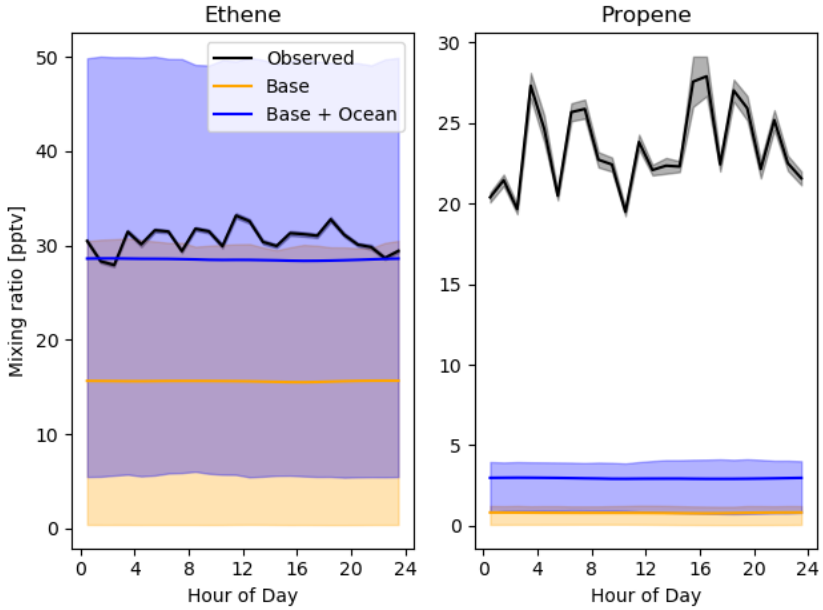

Figure 25: Mean diurnal cycle (UTC) in alkene concentrations at Halley. Observed in black, the model using default emission settings in orange, and the combination of default terrestrial emissions ocean source in blue. Shaded regions representing 25^{th} and 75^{th} for model and 2 sigma standard deviation for observations.

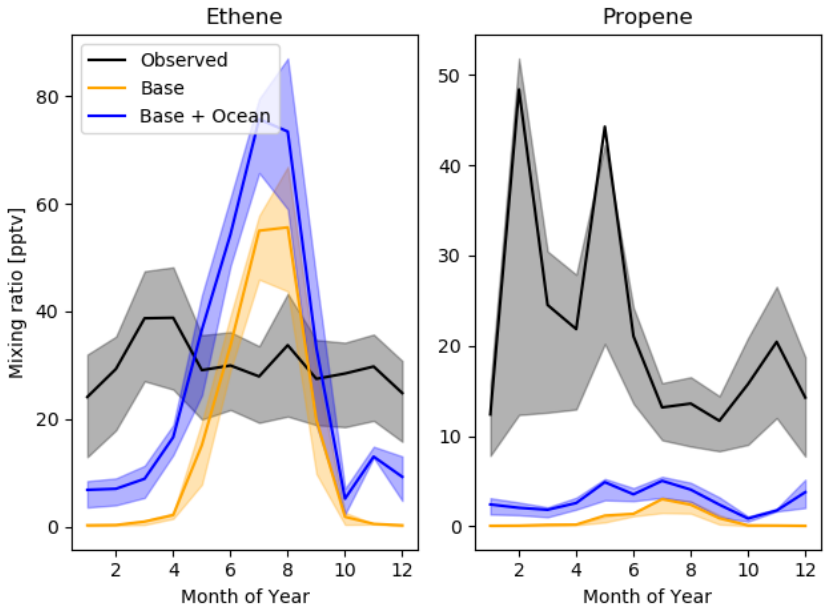

Figure 26: Monthly mean seasonal cycle in alkene concentrations at Halley. Observed in black, the model using default emission settings in orange, and the combination of default terrestrial emissions with the ocean alkene source in blue. Shaded regions representing 25^{th} and 75^{th} for model and 2 sigma standard deviation for observations.

4.5.3 ATom

The comparisons between observations and models have so far been made at stationary observatories. This allows for analysis of the diurnal profile of the emissions but little information about the global distribution of ethene and propene over the ocean. The NASA ATom campaign (Wofsy and ATom Science Team, 2018) aimed to measure the composition of the remote atmosphere by flying an aircraft from the Northern polar regions to the Southern polar regions down the middle of the Pacific and the Atlantic ocean, profiling from the surface to the lower stratosphere, during spring, summer, autumn and winter. Whole air sampled (WAS) were taken and the air subsequently analysed for hydrocarbons (Barletta et al., 2019). Within the model the concentrations along the aircraft flight track are sampled, but only grid boxes that contain only ocean (no land) are used to reduce the effects of terrestrial emissions. Any points that are within a plume from anthropogenic or biomass burning source are also removed. CO mixing ratios greater than 100 ppb used as a flag for this. Only comparisons between modeled and observed ethene are made as there is insufficient propene observations in the

ATom dataset above the limit of detection (404 observations for ethene, 15 observations for propene).

Figure 27 shows the comparison between the base model, the ocean source alone, their sum and the AToM observations of ethene. The highest concentrations in the base model are found around the southern ocean. This is due to biogenic emissions from South America, South Africa and Australia building up in the low oxidation region above the Southern ocean. However, ignoring terrestrial sources and just comparing to the oceanic source, the model significantly overestimates the observations at all latitudes. Reducing ocean ethene emissions by $\sim$60% results in the model being more comparable to the ATom observations (figure 28).

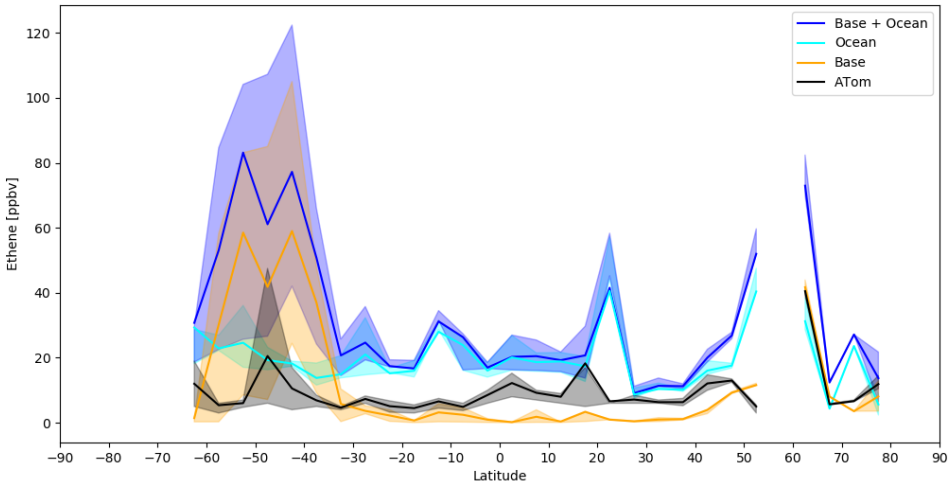

Figure 27: CLatitude average (5° bins) of ethene from the four ATom campaigns in the remote marine troposphere and the equivalent model predictions of ethene using a mix of the default emissions and the scaled oceanic components.

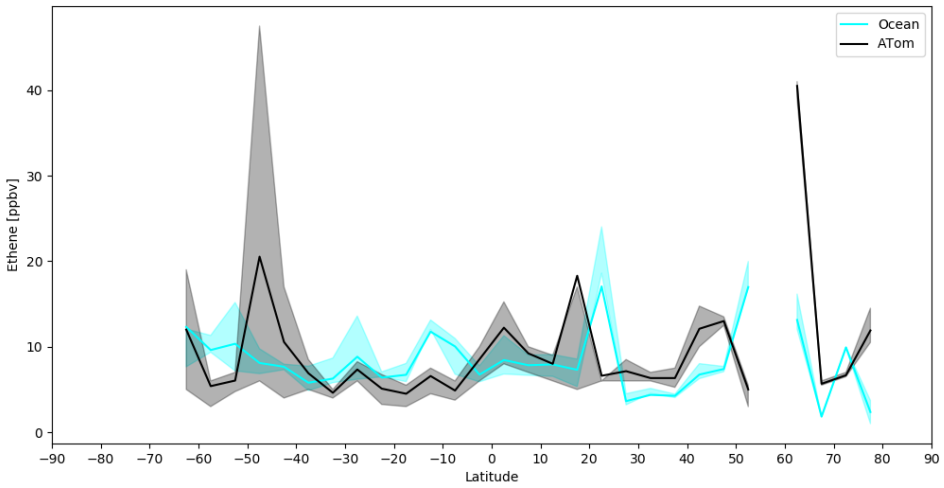

Figure 28: Latitude average (5° bins) of ethene from the four ATom campaigns in the remote marine troposphere and the equivalent model predictions of ethene using the CVAO style oceanic emission source reduced by 60%.

4.5.4 Summary of model observation comparisons

A combination of an out-gassing and photolytic emission sources has been shown in section 4.4.3 to provide the best fit to observations. Comparisons between observations made at Cape Grim found that the models ocean source was able to replicate the magnitude of the observations but failed to capture the diurnal cycle. However, the ocean emissions were not able to replicate mean diurnal and seasonal trends in Halley, with the ocean emission source needing to be increased by 56% for ethene and 153% for propene to make the model comparable to the observations. In both Halley and Cape Grim high biogenic emissions of ethene and propene results in the model base predictions presenting substantially different trends to observations. Finally comparisons were made to the global observations from ATom further highlighted the high predictions for ethene in the low oxidation region above the Southern Ocean. The oceanic source for ethene would require a 60% reduction to improve comparisons to observations. The ocean emission source developed for CVAO and extended globally using DOC field and J(O^1D) values over estimates open ocean emissions, captures the magnitude of coastal observations and substantially underestimates in the Antarctic region.

Two model runs will now be run feeding in the scale factors found for the ocean source to asses atmospheric impacts on oxidants and other species. The first will be the CVAO form of emissions from section 4.4.3. The second reduces these emissions by 60% to better reflect the ATom observations.

4.6 Global impacts of oceanic emission of alkenes

In this section the global impacts of the addition of the oceanic source of ethene and propene will be explored. In the previous version the model reflected the resulting prediction from a trial emission which was scaled to fit observations. Now the emissions will be scaled and then the model run with these scaled emissions. Emissions based on the CVAO observations using the constant out-gassing and photolytically dependent (JO1D like) emission source (section 4.4.3) are used as well as a version reduced by 60% to reflect the ATom observations (section 4.5.3). The 60% reduction in emissions to better reflect ATom ethene observations will also be applied to oceanic propene emissions despite the lack of propene observations. First the model predictions will be validated to show the impact of emissions on mixing ratios of ethene and propene. Then the effect this has on atmospheric oxidants is assessed.

4.7 Validation against observations

Model predictions for the mean observed diurnal cycle for CVAO, Cape Grim and Halley are shown in figure 29. At CVAO, the model predictions has a diurnal cycle much closer to the observations than previously (figure 20), implying either a change in OH concentration or the assumption of perfect scaling between emissions and mixing ratio is flawed. However there is an underestimation by the model still by approximately 3 pptv for ethene and propene.

Both ethene and propene at Cape Grim using the CVAO style emission replicate the magnitude of observations but still lacks the diurnal profile. Model predictions from Halley using CVAO style emissions remain unable to replicate ob-

servations. In all three locations, the ATom style emissions are substantially lower than observation.

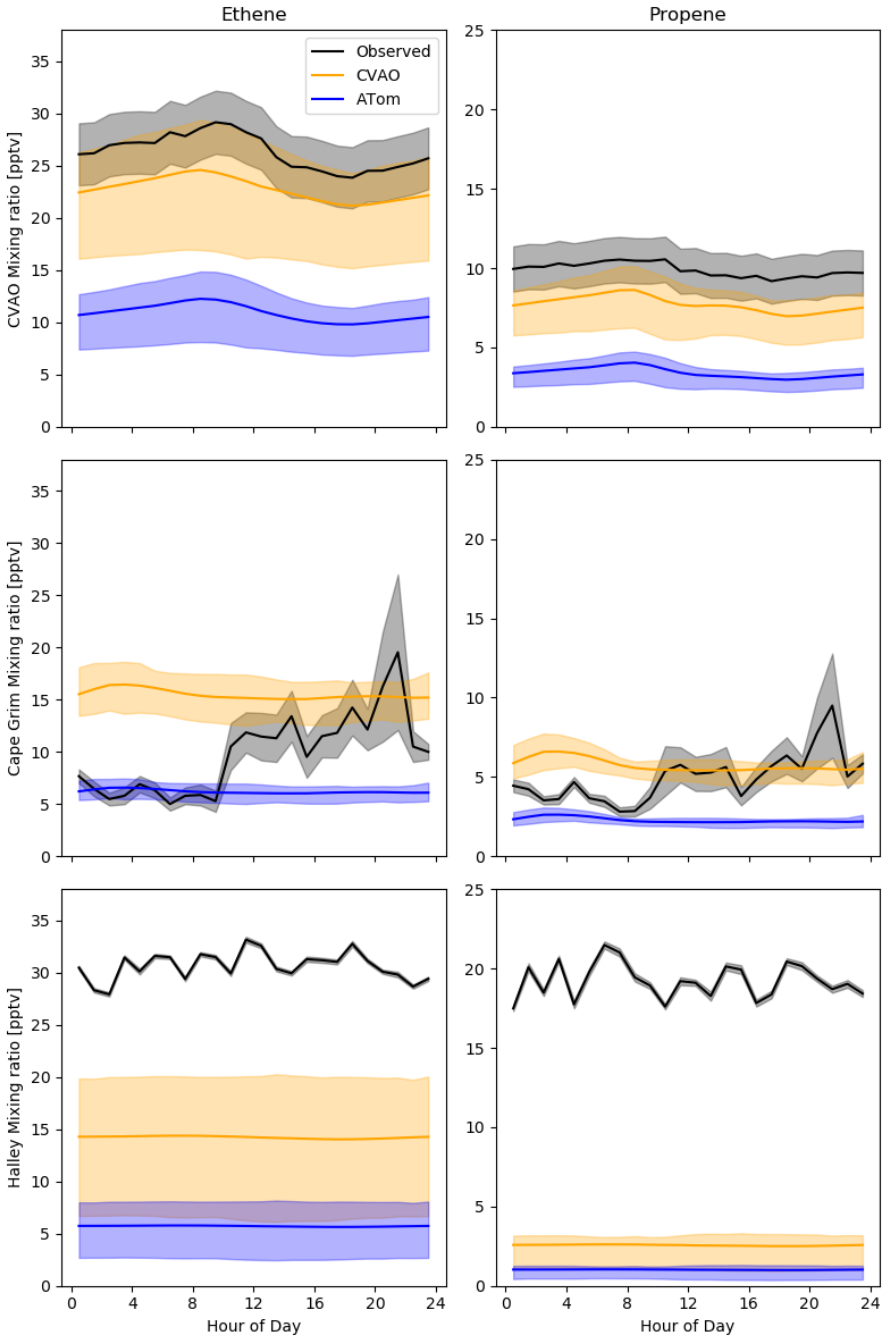

Figure 29: 2017 annual average diurnal for ethene and propene at CVAO, Cape Grim and Halley. Observed average diurnal (black), shaded region representing 2-sigma range. Model average diurnal using CVAO style emissions (orange) and ATom style emissions (blue). CVAO model predictions are a combination of default alkene emissions and oceanic emissions, while Cape Grim and Halley are from ocean emissions only.

Repeating the comparison to ATom observations (figure 30) show again a 60%

reduction in the CVAO like oceanic results in model predictions of approximately the right magnitude (as they did in figure 28). The CVAO like emissions overestimate these observations.

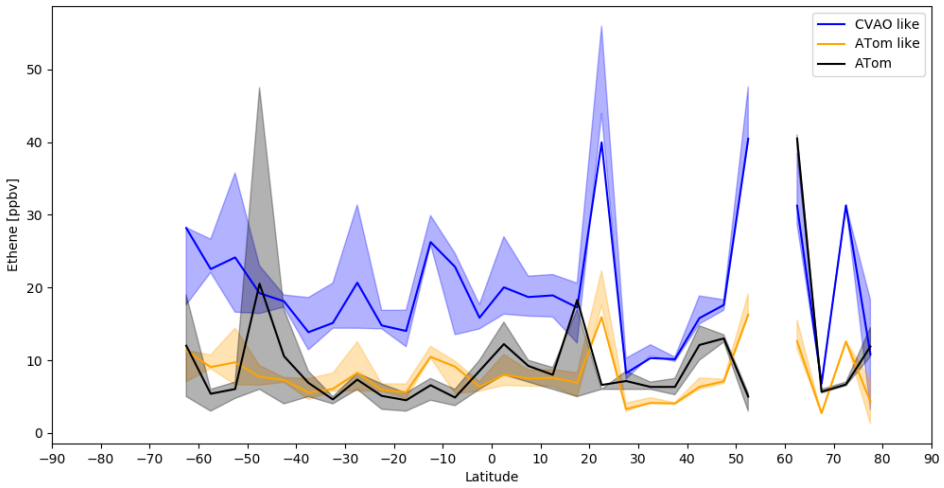

Figure 30: Latitude average (5° bins) of ethene from ATom observations (black) of remote marine tropospheric ethene and the equivalent model predictions of ethene using the CVAO style oceanic emission source (orange) and ATom style emissions (blue).

4.7.1 Global ethene and propene distribution

The change in annual average surface mixing ratio for ethene and propene from the new ocean emissions is shown in figures 31 and 32. The ocean source has negligible impact on ethene and propene mixing ratios over land. Antarctica, northern Canada, Greenland, and northern Russia see the largest over land mixing ratio increase of < 5 pptv of ethene in the CVAO like case. Globally remote marine environments see very large percentage increases ($\sim$10,000%) in ethene and propene for both emission scenarios due to negligible ethene and propene in these environments with the default GEOS-Chem emissions.

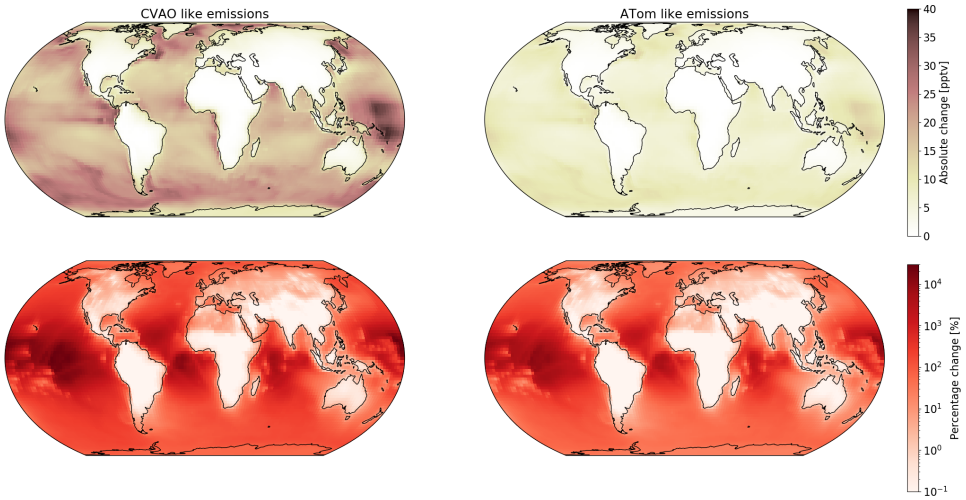

Figure 31: Absolute (top) and percentage (bottom) increase in average surface mixing ratio for ethene with the addition of CVAO (left) and ATom (right) like oceanic emissions.

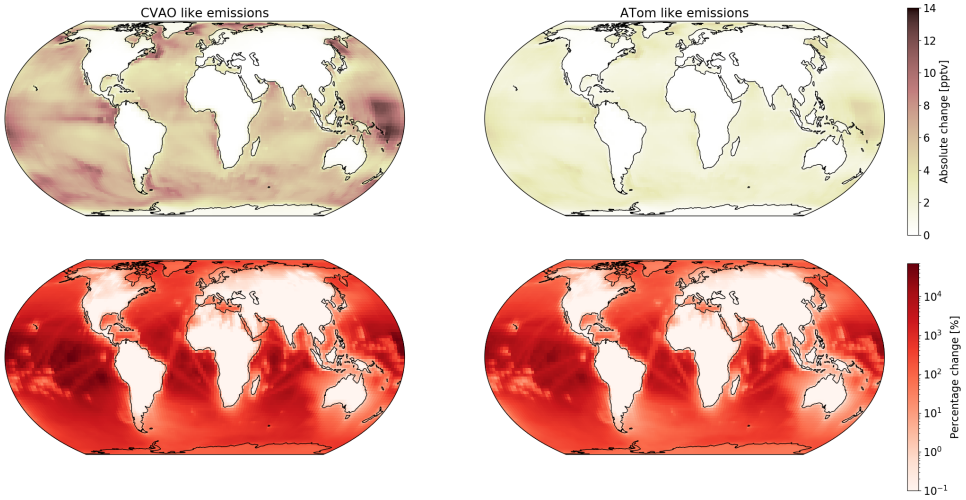

Figure 32: Absolute (top) and percentage (bottom) increase in average surface mixing ratio for propene with the addition of CVAO (left) and ATom (right) like oceanic emissions.

The oceanic alkene emissions increase the tropospheric burden of ethene by 0.019 - 0.026 Tg yr^{-1} and propene by 0.005 - 0.013 Tg yr^{-1} (table 6). This represents a percentage increase of 6.5 - 8.9% in tropospheric ethene and 2.4 - 6.3% in tropospheric propene. Global oceanic alkene emissions are approximately 20-50% of the total global anthropogenic emissions (figure 33).

Simulation	Global annual average tropospheric burden					
	Ethene [Tg]	Propene [Tg]	Ozone [Tg]	OH [x10^5 molec cm^{-3}]	Cl [kg]	Br [Gg]
Base	0.291	0.206	318.59	10.72	142.3	0.575
CVAO	0.317	0.219	318.87	10.71	141.4	0.569
ATom	0.310	0.211	318.70	10.72	141.9	0.572

Table 6: Global annual average tropospheric burdens of ethene, propene, O_3 and mass weighted mean OH concentration in troposphere. Without ocean emissions (base), with CVAO style ocean emissions (CVAO) and reduced CVAO style ocean emissions to ATom levels (ATom).

Oceanic alkene emissions as a percentage of total emissions by hemisphere are roughly equal (table 7). However due to uncertainty in terrestrial biogenics, a reduction in this would increase the relative importance of oceanic emissions in the Southern Hemisphere.

Emission Source	Northern Hemisphere		Southern Hemisphere	
	Ethene [%]	Propene [%]	Ethene [%]	Propene [%]
Oceanic	3-8	4-10	3-8	5-11
Biogenic	51-54	47-49	75-80	71-77

Table 7: Percentage contribution of oceanic and biogenic emissions of total emissions for alkenes by hemisphere.

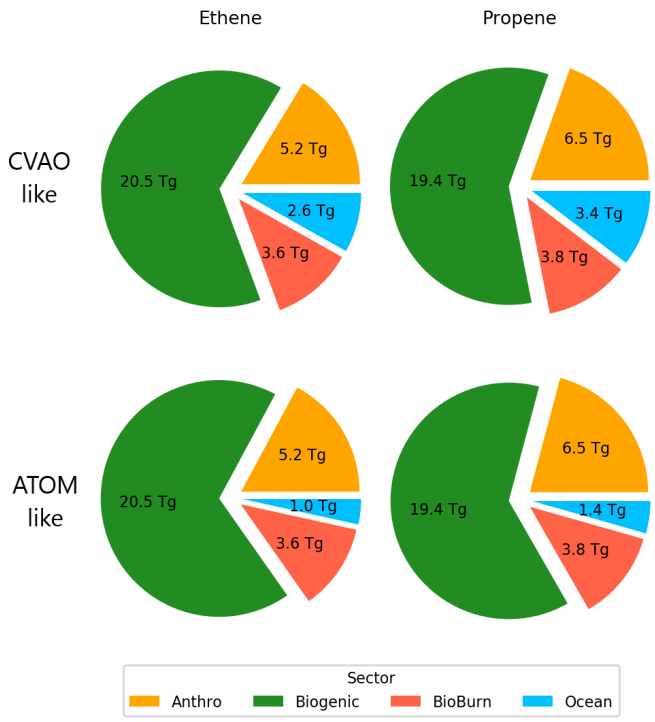

Figure 33: Percentage contribution by sector (Anthropogenic [Anthro], Biogenic [Biogenic], Biomass Burning [BioBurn], Ocean surface [Ocean], emissions from shipping and aviation are negligible) of total global annual ethene and propene emissions for CVAO like oceanic alkene source and the reduced ATom like emissions.

4.7.2 Tropospheric oxidative capacity

The increase in ethene and propene from the addition of an oceanic source has minimal impacts on the global oxidative capacity of the troposphere (table 6). Annual average surface concentrations of OH are shown in figure 34. Globally there are minimal decreases in OH, this is close to zero over land and $\sim$3% over the ocean. There are slight increases in surface OH around the polar coast, due to the small increase in radical production during high latitude winters from alkene reactions with O_3, although this is also $\sim 3\%$. Annual average mass weighted surface OH decreases from 10.17x10^5 molec cm^{-3} to 10.14x10^5 molec cm^{-3} with ATom like oceanic alkene emissions and to 10.10x10^5 molec cm^{-3} with CVAO like oceanic alkene emissions.

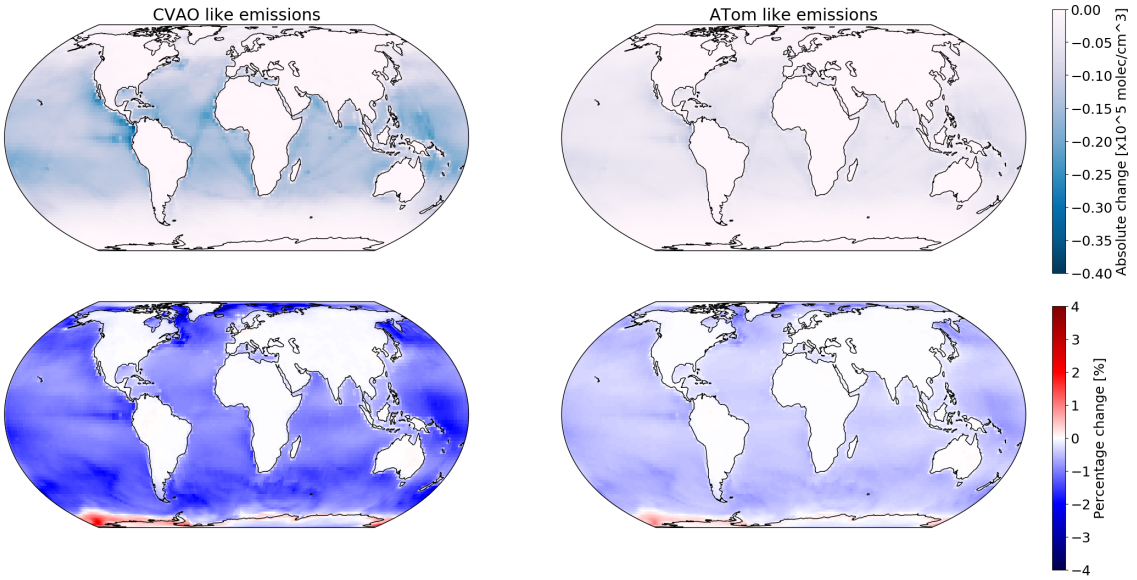

Figure 34: Comparisons between base (default emissions) and new annual average OH surface concentration with absolute (top) and percentage (bottom) change for both CVAO and ATom like ocean alkene emissions.

4.8 Conclusions

A combination of out-gassing and UV photolytically linked ocean emission of alkenes substantially improves model performance at predicting the observed ethene and propene diurnal cycle at CVAO. Model seasonal cycles for both ethene and propene still struggles to capture observed trends. Extending the CVAO ocean alkene emissions globally produces concentrations of ethene and propene much greater than those made by the ATom campaign in the marine boundary layer. Additionally the emissions biogenic emissions of ethene and propene from South America, Southern parts of Africa and Australia were found to be substantial. Limited work exists characterising this, however it has been noted previously that the biogenic emissions of propene in tropical forests were a factor of 10 greater than observations (Garraway, 2018). The magnitude of mean diurnal observations made at Cape Grim were replicated well when considering ethene and propene from the ocean source only. Observations at Halley were substantially higher than model predictions. This work has not considered if there are alkene emissions from sea-ice. Read et al. (2007) found evidence that a snow pack source at Halley may explain summer alkene observations however the magnitude and mechanisms behind this are not explored.

One possible cause of the difference between observed and modelled seasonal cycles in ethene and propene may be due to seasonality in DOC. The DOC inventory from Roshan and DeVries (2017) presents a single annual average estimate for DOC concentration, however there is evidence from previous work for seasonality in DOC. Thomas et al. (1995) found that DOC concentrations in surface waters above upwelling regions in the Atlantic were higher during warmer seasons than cooler ones. Total organic carbon (of which DOC is a constituent) correlates with the onset of the spring bloom in north east Atlantic waters with values peaking in summer, however summer and autumn values do not show the same strong relationship to biological activity (Sohrin and Sempéré, 2005). Additionally DOC shows more seasonal variability in coastal waters and fresh water outlets than more open waters (Del Vecchio and Blough, 2004). DOC distributions derived from satellite observations shows enhancement at the coast as well as accumulation during spring and summer (Mannino et al., 2008). The difficulty in capturing seasonal ethene and propene trends in coastal environments may be due this seasonality in surface DOC concentrations.

Based on this work, global emissions of ethene and propene from the ocean surface are between 1.04 - 2.59 Tgyr^{-1} and 1.37 - 3.42 Tgyr^{-1} respectively. This is a roughly comparable for previous predictions for ethene (0.89 - 1.40 Tg yr^{-1}) but a substantial increase on previous estimates for propene (0.52 - 0.82 Tg yr^{-1}) (Plass-Dulmer et al., 1995). The range of ocean emission values are substantially smaller than biogenic sources (20.4 Ggyr^{-1} of ethene and 19.3 Ggyr^{-1} of propene) but these are poorly constrained outside of temperate environments. The relative importance of oceanic alkene emissions could likely increase, especially in the Southern Hemisphere if terrestrial biogenic emissions were reduced. The maximum prediction for global oceanic emissions are approximately half of total model anthropogenic emissions of ethene and propene and comparable to biomass burning model emissions.

It is likely that the ocean emissions around CVAO are influenced by coastal process. Higher concentrations of DOC and greater ocean surface turbulence due to wave breaking could result in a higher rate of emissions than in open oceans. Ocean emissions based on ATom observations are more likely to be representative of the open ocean and act as a minimum bound to the total ocean emission source. In this work the oceanic only annual average DOC concentration and photolytic activity were used to constrain the oceanic flux we calculate. This could be further extended to account for seasonality in DOC, composition of DOC, and ocean surface turbulence such as wave breaking. This would give a more representative set of physical and biological conditions which may better reflect the real world processes across all marine environments. Additionally, further marine boundary layer observations of alkene mixing ratios could also be used to further constrain the oceanic source.

There is minimal change in global tropospheric oxidative capacity. Surface OH concentration decreases by $\sim$3%. Tropospheric OH has a negligible change of $\sim$0.1% (10.72x10^5 molec cm^{-3} to 10.71x10^5 molec cm^{-3}). Tropospheric burdens of O_3, Cl and Br have similarly small changes of $< 1\%$.

5 Importance of Spatial Resolution in Remote Marine Environments

5.1 Introduction

In chapter 3 the effects of spatial resolution on oceanic ozone dry deposition is briefly discussed. Whilst there is no significant sub-grid scale correlation between tropospheric ozone concentration and sea-surface I^- concentration, the effects of spatial resolution may effect oceanic ozone deposition in coastal areas. Also when comparing to observations, coarser model spatial resolution is unable to capture local meteorological variability. The effects of spatial resolution were also discussed in 4, with the effects of local emissions becoming more pronounced at higher model spatial resolution.

The remote marine troposphere plays an important role in determining the concentration of long lived pollutants such as methane and ozone. Over polluted regions when considering questions such as air quality, high resolution regional models (grid resolutions of less than 1° latitude and 1° longitude) are often used to simulate the composition to reflect the heterogeneity of emissions and of the populations being exposed to these pollutants. Over the remote atmosphere when climate is the aim of the study, it is usually thought that coarser resolution models (greater than 1°) are suitable, due to more homogeneous emissions. This chapter expands on the previous considerations of model spatial resolution and evaluate how this impacts, and what considerations should be made for, marine environments.

5.2 Previous Work

When considering the effects of model spatial resolution in atmospheric models, the majority of previous work has focused on densely populated regions, such as

mega-cities. The inhomogeneous emissions from populated regions and nonlinear HO_x-NO_x-O_x chemistry are the key motivations behind understanding spatial resolution impacts in these regions.

Three high spatial resolution (36km, 12km, and 4km) model runs were evaluated over North Carolina, using a range of meteorological and chemical conditions (Arunachalam et al., 2006). They found that differences in predicted O_3 between 4km and 12km resolutions in almost all cases were statistically insignificant. Statistically significant differences were found between 36km and 4km, with spatial resolution contributing an uncertainty of 1-3ppbv in O_3.

Stock et al. (2013) considered the effects of megacities on tropospheric ozone at local, regional, and global scales. Emissions from the grid cells containing the mega city we're perturbed by removing the emissions entirely, increasing by 25% and redistributing 25% and 100% of the emissions to the surrounding region. Redistributing emissions to a wider area at a fixed model spatial resolution (1.25° x 1.875°) in effect degrades resolution of emissions. There was little effect found to global annual ozone burden (0.12%) when NO_x emissions were redistributed, hence local emission distribution has little effect on model predictions on a global scale (Stock et al., 2013). However at local scales, in northern hemisphere megacities, over 30% (at 100% redistribution) increase in ozone was found as the chemistry scheme shifted towards NO_x-limited conditions. Stock et al. (2013) conclude that higher model spatial resolutions would be better suited to assess megacity effects on local scales.

Stock et al. (2014) compared O_3 at two model spatial resolutions (150 km and 40 km) also on local, regional, and global scales. This work again found small differences on a global scale (5% change in ozone burden), however O_3 from the coarser resolution presented greater differences to the higher resolution predictions when compared with observations. Emission resolution was deter-

mined to be an important factor during winter months in very polluted areas. The model was unable to capture the transition between NO_x and VOC limited environments, which due to the non-linearity in the chemistry, results in either an O_3 production or titration environment depending on resolution (Stock et al., 2014). During summer months representation of boundary layer height played a greater role in polluted local environments and vertical mixing of lightning NO_x in tropical environments. Higher resolution model predictions were generally better than lower resolutions compared to observations in polluted urban areas.

A study in GEOS-Chem across spatial resolutions found that degrading the model spatial resolution from 2°x2.5° to 4°x5° increased error substantially more than alterations to the time step frequency (Philip et al., 2016).

The effects of spatial resolution in GEOS-Chem have also been considered by Yu et al. (2016). They compared the global course resolutions of 4°x5° and 2°x2.5° to the nested domain over north America at 0.25°x0.3125° (using 0.25°x0.3125° as boundary conditions). For the south eastern US, the differences in NO_x between resolutions was most pronounced in areas of highest concentration but that on the whole the models were in agreement. Comparisons to observations improved going from 4°x5° to 2°x2.5°, but decreased when comparing 2°x2.5° to 0.25°x0.3125°. This decrease was attributed to effects of NO_x chemistry. Overall they conclude that 2°x2.5° is adequate for global modelling purposes. Further work by Yu et al. (2018) in GEOS-Chem compared the 2°x2.5° and 0.25°x0.3125° resolutions with GEOS-5 GCM at cubed-sphere c360. The c360 model run is a similar spatial resolution to 0.25°x0.3125° but has online rather than archived meteorology. Comparisons between ^{222}Rn in the c360 and 0.25°x0.3125° found errors of up to 20% in vertical transport due to the temporal averaging of archived meteorology. When the archived meteorology was further degraded in resolution from 0.25°x0.3125° to 2°x2.5° a further bias of 40% was introduced to vertical transport. Methods to mitigate the effects of archived meteorology on the effec-

tiveness of vertical transport were discussed and are planned for introduction into future model versions.

Fenech et al. (2018) compared a 140 km and 50 km model with a domain covering Europe. This work primarily focused on O_3 and PM 2.5 and found that both species experienced a seasonal resolution dependence. O_3 from the course model was up to 10% greater than the high resolution in winter and spring, whereas it was up to 4% lower in summer and autumn. This was believed to be due to NO_2 differences between the two resolution runs as well as differences in the boundary layer height. The opposite trend was found for PM 2.5 with this also being attributed to differences in boundary layer height as well as convective rainfall.

Mertens et al. (2020) considered effects of spatial resolution on O_3 over Europe with a nested model, comparing global results to a nested domain over continental Europe and then a further nest at a higher spatial resolution over Germany. Their comparisons between global and continental scale found minimal differences caused by emissions spatial resolution, however differences in surface ozone was found to be due to stratospheric ozone transport. Differences of up to 30% in surface ozone transported from the stratosphere was found to be from two resolutions having differences in vertical mixing efficiency. Greater differences were found in comparisons between regional and global scales. This was believed to be due to differences in emissions. Coarse emissions in the lower resolutions would not accurately capture the transport of emissions around coastal areas, resulting in a more dilute emission than in higher resolutions. Furthermore, Mertens et al. (2020) also speculate that differences in biogenic emissions and dry deposition will also have contributed to the differences at this scale.

The motivations of in-homogeneous emissions and nonlinearities in HO_x-NO_x-O_x chemistry is also true for marine environments with finely structured emissions

from coastal, island, and shipping lanes are conducive to the same nonlinear chemistry. Furthermore spatial resolution and meteorology as as important over urban as well as marine environments, with the ability to resolve cloud, convection, and wind speed all having possible impacts on tropospheric chemistry.

Model resolution effects on shipping emissions in the tropical marine boundary layer has been found to increase OH concentration by 8%, decrease NO_x lifetime by 32%, and increase O_3 production efficiency by 31% (between lowest and highest spatial resolution, Charlton-Perez et al. (2009)). Charlton-Perez et al. (2009) found that the chemistry impacts of shipping NO emissions were highly dependent on model spatial resolution and estimates that there is likely a 59% overestimation in ozone production from shipping emissions in CTMs. Charlton-Perez et al. (2009) also found a that as model spatial resolution increases, the model predictions begin to converge towards a single value, however it was unclear if this was due to the spatial resolution itself or the resolution of input meteorology.

To account for plume chemistry from shipping emissions, PARANOX (Vinken et al., 2011; Holmes et al., 2014) is used in GEOS-Chem. This chemically ages the plume for 5 hours before being released into the model gridbox. This reduces the NO_x emission and releasing a proportion of that as O_3 and HNO_3.

This chapter will now explore the impact on the composition of the remote tropical Atlantic Ocean boundary layer by running the GEOS-Chem model at resolutions of 4°x5°, 2°x2.5°, 1°x1.25° and 0.5°x0.625° over the same domain. The same emissions, meteorology and timesteps are used to control for factors other than spatial resolution. Custom idealised tracers are used to explore the effects of spatial resolution on specific aspects of the GEOS-Chem model and diagnose the causes of differences between the resolutions. Comparisons will are then made between the resolutions for species of interest in the troposphere. Finally considerations will be made for comparing coarse global spatial resolutions (4°x5°,

2°x2.5°, 1°x1.25°) to observations made in the marine environment of CVAO.

5.3 Model Setup

Version 12.6.0 of the 3-D global chemical transport model GEOS-Chem Classic (Bey et al., 2001; GC12.6.0, 2019) driven by meteorological data from GEOS-FP (Molod et al., 2012) is used. This work uses the model nesting capability first implemented by Wang et al. (2004). Boundary conditions are produced from 4°x5° global model runs, which are then used to constrain the user defined nested domain (shown in figure 35, latitude range -10.0° to 24.0°, longitude range -60.0° to -5.0°). The boundary conditions model run had a spin up period from 2016-01-01 to 2016-10-01 before the nested regions were then initialised. The nested domain is then run at spatial resolutions of 4°x5°, 2°x2.5°, 1°x1.25°, and 0.5°x0.625° with all model runs using the same boundary conditions. The nested regions were given their own spin up time from the end state of the boundary conditions initialisation from 2016-10-01 to 2017-01-01. The analysis period was then run for the six month period between 2017-01-01 to 2017-07-01. As recommended in GEOS-Chem documentation (`www.geos-chem.org`), a buffer region of 3 boxes is used between the domain and boundary conditions as recommended by the model documentation `http://wiki.seas.harvard.edu/geos-chem/index.php/FlexGrid`.

All nested domains use the same time steps which are set at the recommended values for 0.5°x0.625° (300 seconds for chemistry and 600 seconds for emissions). This contrasts to the previous work of Yu et al. (2016) where different chemical and emission timesteps were used for each resolution. The offline emissions for dust aerosol, lightning NO_x, biogenic VOCs, soil NO_x, and sea salt aerosol are used for consistency between resolutions (Weng et al., 2020). All other model inputs which have multiple resolutions available are set to use the same resolution files to control for emission resolution as a contributing factor to

any differences between model predictions, thus, the same emissions are used in all simulations.

5.3.1 Changes to horizontal grid definition

GEOS-Chem classic horizontal grids are defined with a centre starting at -180° for longitude and -90° for latitude, a process that is consistent across all horizontal grid resolutions in both global and nested model runs. Plotting horizontal grid edges from these resolutions, such as in figure 35, for 4°x5°, 2°x2.5°, and 1°x1.25°, shows that this style of grid definition gives coordinates of common grid centres across the horizontal domain but with grid box edges out of phase.

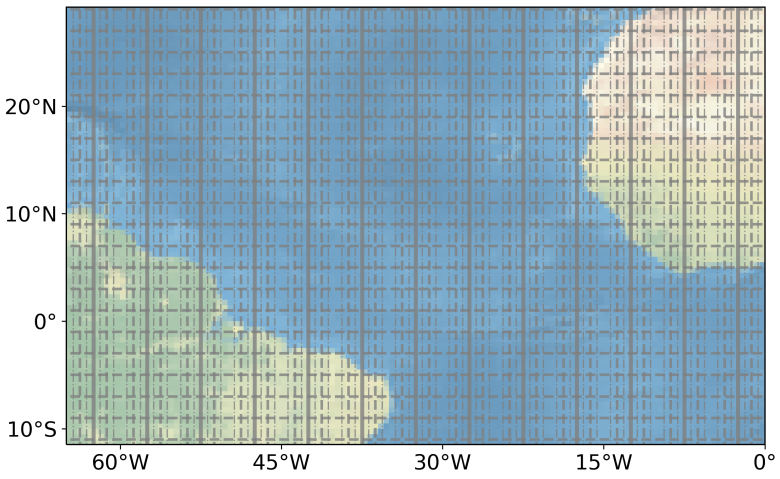

Figure 35: Horizontal Grid edges for resolutions for 4°x5° (solid line), 2°x2.5° (dashed line), 1°x1.25° (dotted-dashed line) over the mid-Atlantic region to be modelled.

For this work the grid definition is updated such that all horizontal grids are defined with the left edge of the grid starts at -180° longitude and the bottom edge at -90° latitude. This results in horizontal grids with common edges rather than common centres with the example of this shown in figure 36. This change to the horizontal grid definition allows for the same nested domain to be selected across all resolutions, along the common edges, allowing for a direct comparison between the resolutions. The matching domain between resolutions will also al-

low for the same boundary conditions for each mode resolution run.

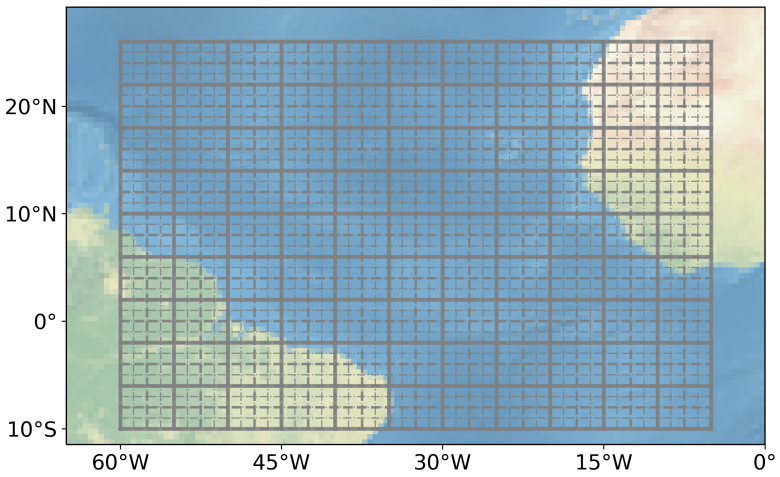

Figure 36: Horizontal Grid edges for resolutions for 4°x5° (solid line), 2°x2.5° (dashed line), 1°x1.25° (dashed-dotted line) over the mid-Atlantic region to be modelled.

5.3.2 Regridding model output

To compare between resolutions model outputs were regrid onto the same resolution to allow for direct comparison. This is achieved using the universal regridder for geospatial data, *xESMF* python package (`https://xesmf.readthedocs.io/en/latest/`). In this work the *conservative* regridding method is used as it is designed to conserve the original structure of the data when increasing resolution and averaging over the source grid boxes when decreasing resolution. This is also the recommended method when considering real world data.

5.3.3 Addition of idealised tracers

A further change made for this work was the addition of idealised tracers. These new tracers are intended to highlight specific aspects of GEOS-Chem. The idealised tracers are listed in table 5.3.3. The only source of idealised tracer 1 is a constant value in the boundary conditions. It has no loss mechanism and the nested grid is initialised with no tracer present. This tracer thus acts as a measure

of the ”spin-up” time of the nested grid. Such that when the nested region is the same mixing ratio as the boundary conditions, the nested region has thoroughly mixed with the boundary conditions and can be seen as initialised.

The effects of spatial resolution on emissions is explored using idealised tracers 2 and 3. These tracers have no chemical production or loss, no values from the boundary condition and will not dry or wet deposit. A uniform surface emission of tracer 2 will test if emissions are consistently emitted between resolutions. A point source emission of tracer 3 (from the location of CVAO) will be used to determine how the spatial resolution effects the mixing and chemistry of the point source.

The only source of idealised tracers 4,5 and 6 is from the boundary conditions and the only sink being a chemical loss with a lifetime of five days, one day and one hour respectively. These tracers will show any effects of resolution on chemistry and tracer lifetime as well as how tracers of various lifetimes are transported from boundary conditions at each of the spatial resolutions.

Finally wet deposition is studied through tracers 7, 8, and 9. Each of these tracers only have sources from the boundary condition and only loss is through wet deposition, with each idealised tracer behaving like an existing tracer in the model (HNO_3, Sea Salt, NH_3^+).

Tracer	Boundary conditions	Emissions	Chemical loss	Wet deposition
1	1 ppbv	None	None	None
2	0 ppbv	Uniform 1 kg m^{-2} s^{-1}	None	None
3	0 ppbv	1 kg m^{-2} s^{-1} point source	None	None
4	1 ppbv	None	t=5 days	None
5	1 ppbv	None	t=1 day	None
6	1 ppbv	None	t=1 hour	None
7	1 ppbv	None	None	Like HNO_3
8	1 ppbv	None	None	Like Sea Salt (SALC)
9	1 ppbv	None	None	Like SNA (NH_3^+)

Table 8: Definition and parameters for idealised tracers being added to GEOS-Chem to analyse resolution dependence of individual components.

5.4 Idealised tracers

A timeseries of the domain average for idealised tracer 1 is shown in figure 37 for each spatial resolution. Whilst there are differences in the progression from zero to equilibrium with the boundary conditions, all model runs take approximately 30 days of simulation to reach equilibrium. This tracer can be used infer the minimum initialisation time for the nested domain from start and with the similarities between model resolution showing that this initialisation time is likely a function of domain size rather than model spatial resolution. It takes the lowest resolution $\sim$10.67 days to exceed a domain average of 0.9, which is a minimal difference to the highest resolution, which takes $\sim$10.28 days.

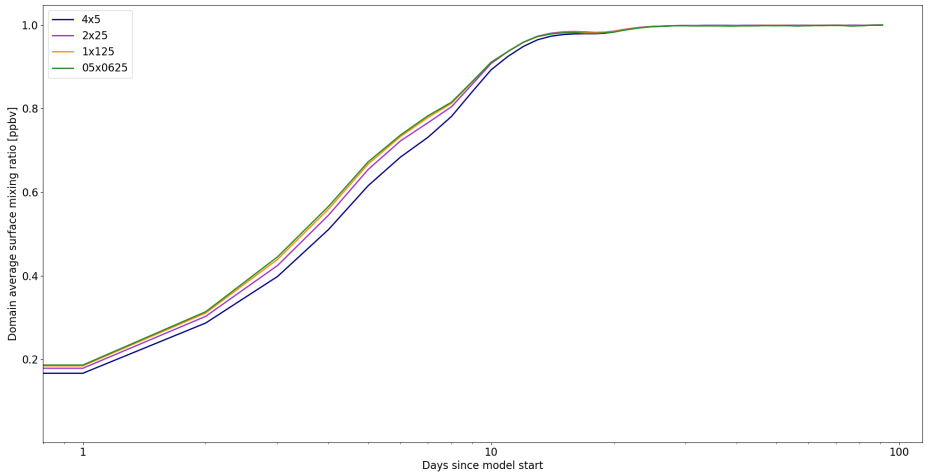

Figure 37: Domain average timeseries (days since model start) of surface mixing ratio for the idealised tracer with infinite lifetime for model spatial resolutions 4°x5°, 2°x2.5°, 1°x1.25° and 0.5°x0.625°.

5.4.1 Idealised emission tracers

The uniform emission tracer (tracer 2) surface average mixing ratio is shown in figure 38. Approximately a 10% difference in average surface mixing ratio exists between spatial resolutions. However emission diagnostics (figure 39) show that there is no difference in emission between spatial resolutions.

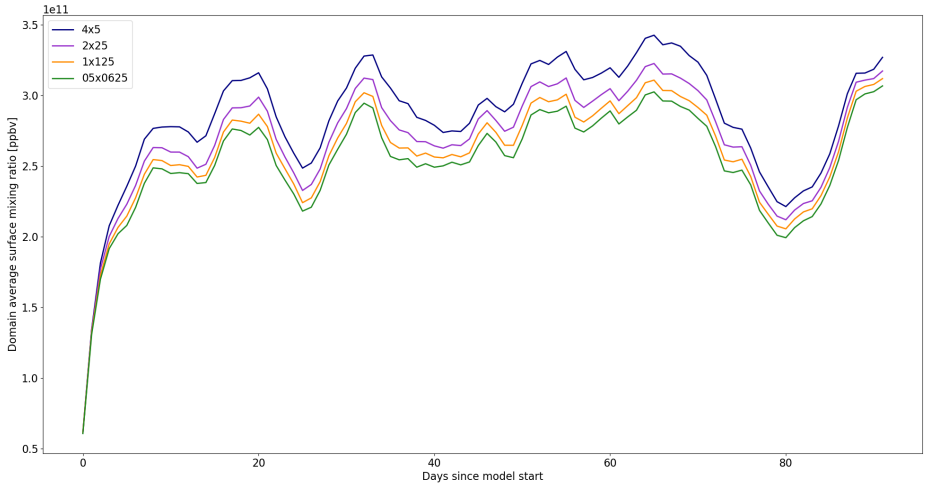

Figure 38: Domain average timeseries (days since model start) of surface mixing ratio for the idealised tracer with uniform 1 kg m^{-2} s^{-1} emissions across the domain for model spatial resolutions 4°x5°, 2°x2.5°, 1°x1.25° and 0.5°x0.625°.

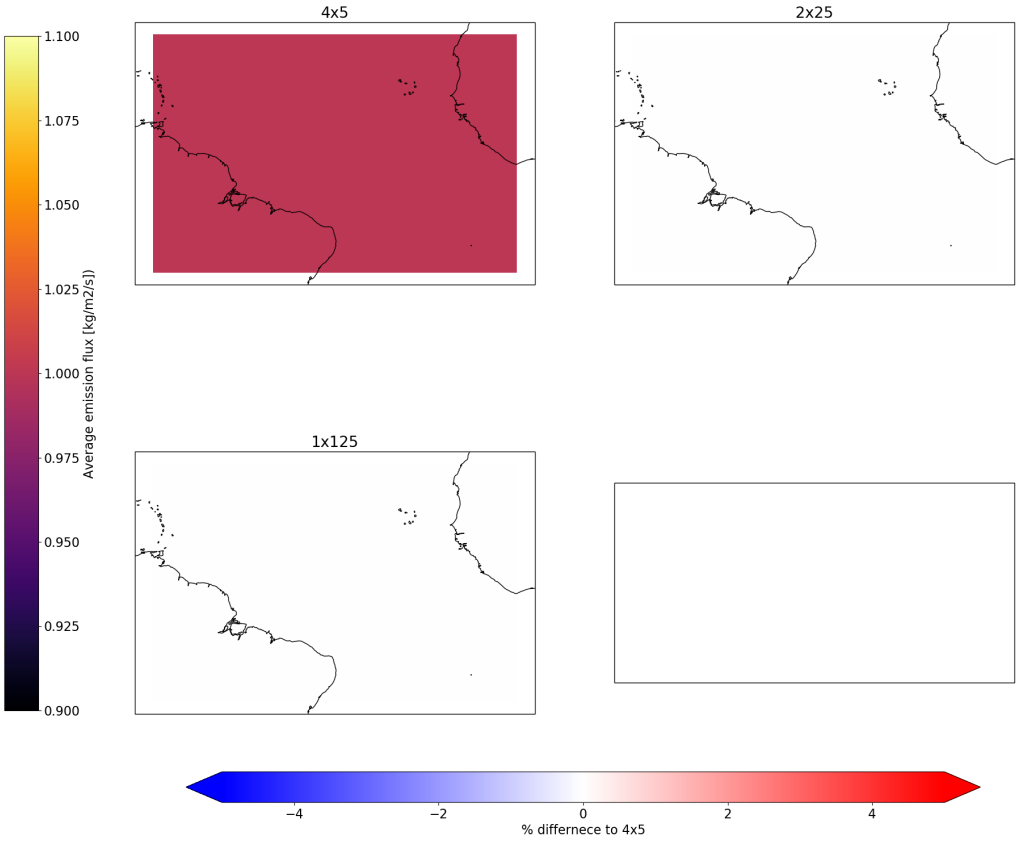

Figure 39: Average emission of idealised tracer of 1 kg m^{-2} s^{-1} emissions across the domain for 4°x5° (top left). Percentage difference of emissions compared to 4°x5° at 2°x2.5° (top right), 1°x1.25° (bottom left), and 0.5°x0.625° (bottom right) downscaled to 4°x5°.

With no chemical or deposition loss, removal of this tracer from the domain only occurs via transport. Hence this is the driving force between differences in spatial resolutions. Figure 40 shows the average surface mixing ratio for the idealised emission tracer along with average surface wind speed and average vertical pressure velocity. The distribution of the idealised tracer is larger controlled by these two meteorological factors, with the tracer accumulating in areas where there is low wind speed and down-welling. At the boundary of the domain and in areas of up-welling the tracer is at its lowest. Whilst both model runs shown in figure 40 have the same input resolution meteorology, the averaging of this across the model spatial resolutions results in the differences observed between model spatial resolutions.

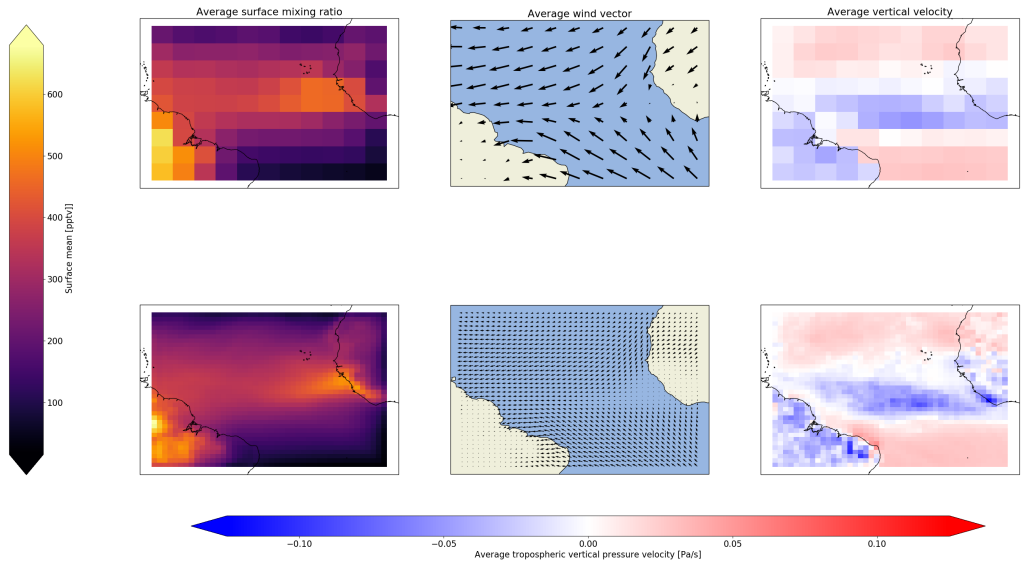

Figure 40: Average surface mixing ratio of idealised tracer with 1 kg m^{-2} s^{-1} emissions across the domain (left), average surface wind vectors (mid) and average vertical transport velocity (right) for model spatial resolutions of 4°x5° (top) and 1°x1.25°

(bottom).

Figure 41 shows the progressive difference between model spatial resolutions. The average surface mixing ratio is shown for 4°x5° (top left). Following this, 2°x2.5° shows the percentage difference between 4°x5° and 2°x2.5°,

1°x1.25° shows the percentage difference between 2°x2.5° and 1°x1.25°, finally 0.5°x0.625° shows the percentage difference between 1°x1.25° and 0.5°x0.625°. On the top right of this figure is the total difference between model spatial resolutions (difference between 4°x5° and 0.5°x0.625°). The average surface mixing ratio at 0.5°x0.625° is shown at the bottom right.

Errors across the domain from horizontal and vertical transport show 4°x5° generally over estimates surface mixing ratios compared to other model spatial resolutions and that the largest change between spatial resolutions is the step between 4°x5° and 2°x2.5°.

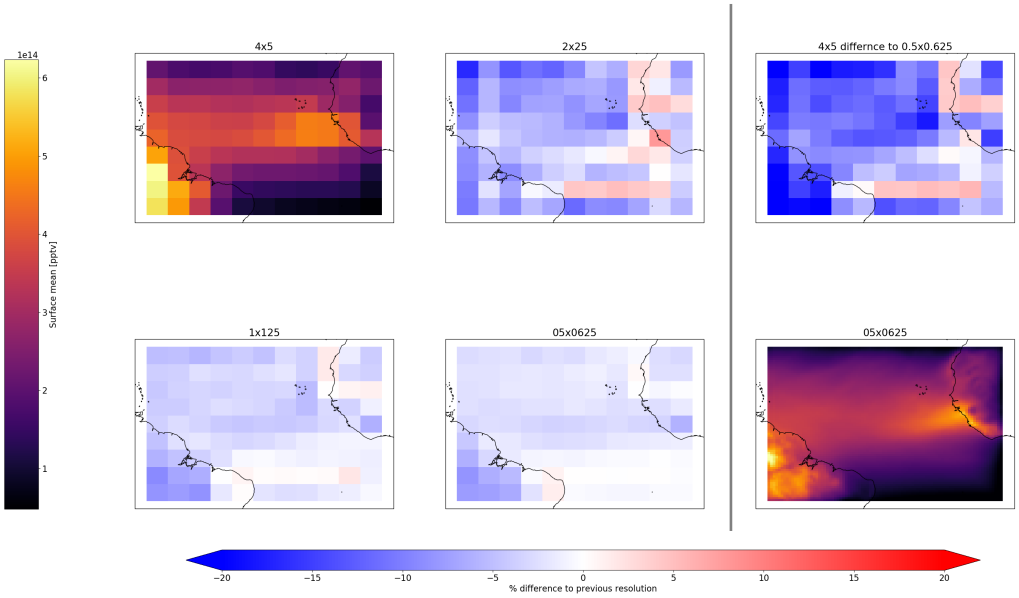

Figure 41: Average surface mixing ratio of idealised tracer with 1 kg m^{-2} s^{-1} within the nested domain for 4°x5° and 0.5°x0.625°. Percentage difference between 2°x2.5° and 4°x5°, percentage difference between 1°x1.25° and 2°x2.5°, percentage difference between 1°x1.25° and 0.5°x0.625°, and total percentage difference between 4°x5° and 0.5°x0.625°.

The differences between spatial resolutions persist when considering the sum of the uniform emission tracer between the surface and 10km (figure 42), further showing areas of high convection contribute to spatial resolution differences but borders of the nested region (inflow and outflow) are also a source of differences. While convection does play a role, transport in to the nested region of airmass'

not containing the uniform emission tracer and loss of this tracer from the domain across the troposphere are key processes in spatial resolution differences.

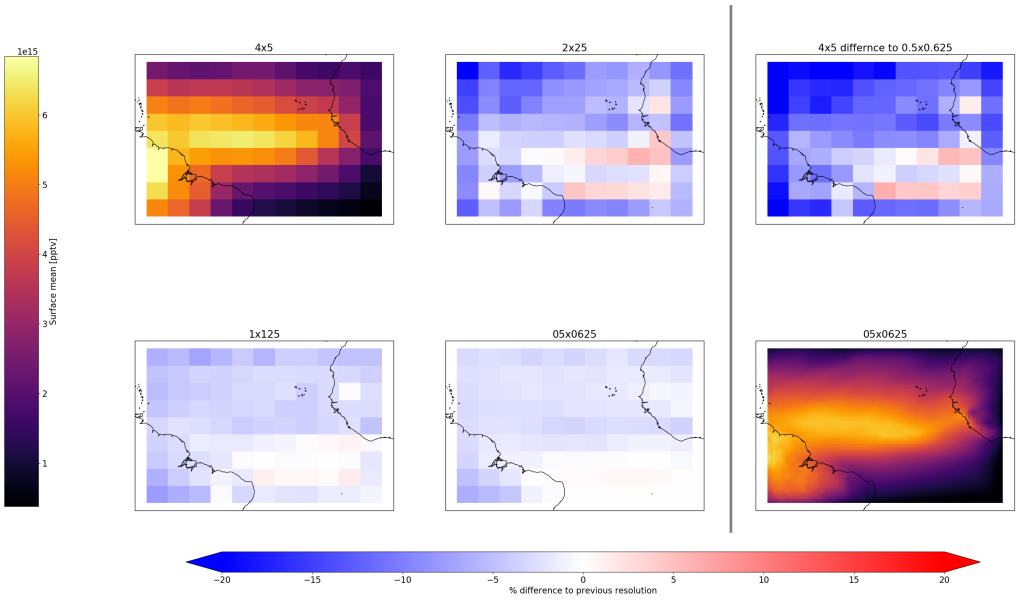

Figure 42: Average sum of mixing ratios between the surface and 10km altitude of idealised tracer with 1 kg m^{-2} s^{-1} within the nested domain for 4°x5° and 0.5°x0.625°. Percentage difference between 2°x2.5° and 4°x5°, percentage difference between 1°x1.25° and 2°x2.5°, percentage difference between 1°x1.25° and 0.5°x0.625°, and total percentage difference between 4°x5° and 0.5°x0.625°.

Figure 43 shows the surface average mixing ratio for the point source tracer, emitted from CVAO. There is general agreement in the plume size and direction, however the representation of this in the model is subject to the spatial resolution, with greater detail in the plume structure achieved at higher resolution compared to low spatial resolution as expected. The domain average timeseries for the point source idealised tracer is shown in figure 44. The idealised point source presents greater agreement in surface domain average timeseries than the uniform emission source (figure 41).

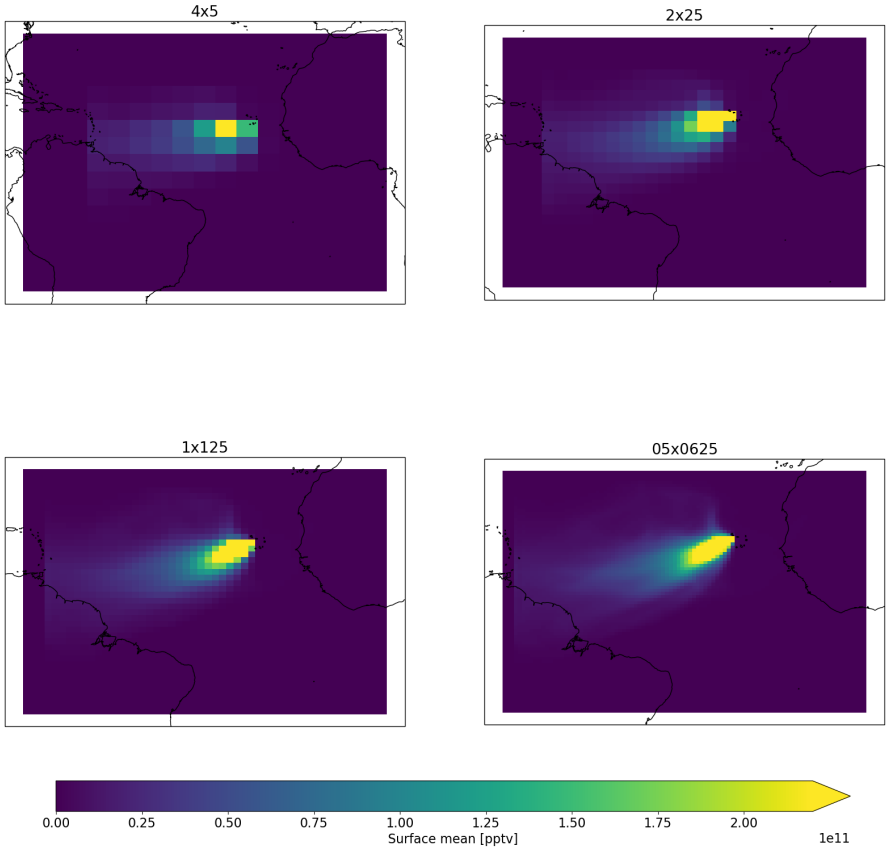

Figure 43: Surface average mixing ratio for the idealised tracer with point source 1 kg m^{-2} s^{-1} emissions across the domain for model spatial resolutions 4°x5°, 2°x2.5°, 1°x1.25° and 0.5°x0.625°.

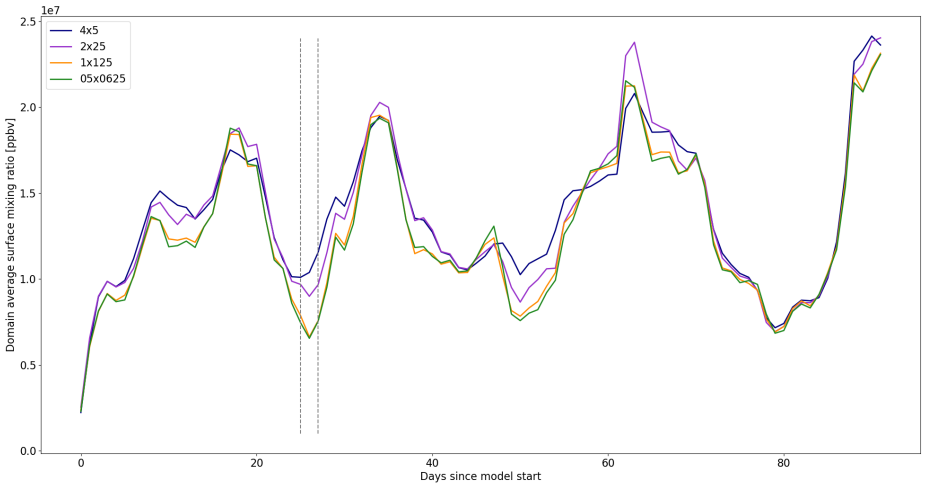

Figure 44: Domain average timeseries of days since model start for the idealised tracer with point source 1 kg m^{-2} s^{-1} emissions across the domain for model spatial resolutions 4°x5°, 2°x2.5°, 1°x1.25° and 0.5°x0.625°. Dashed grey lines covers days 25,26 and 27 since model spin-up which are shown in figure 46

Figure 45 shows the average surface mixing ratio of the idealised point source tracer from figure 43, but in $\log_{10}$ space. This also shows strong agreement between spatial resolutions and the overall structure within the domain is consistent between resolutions.

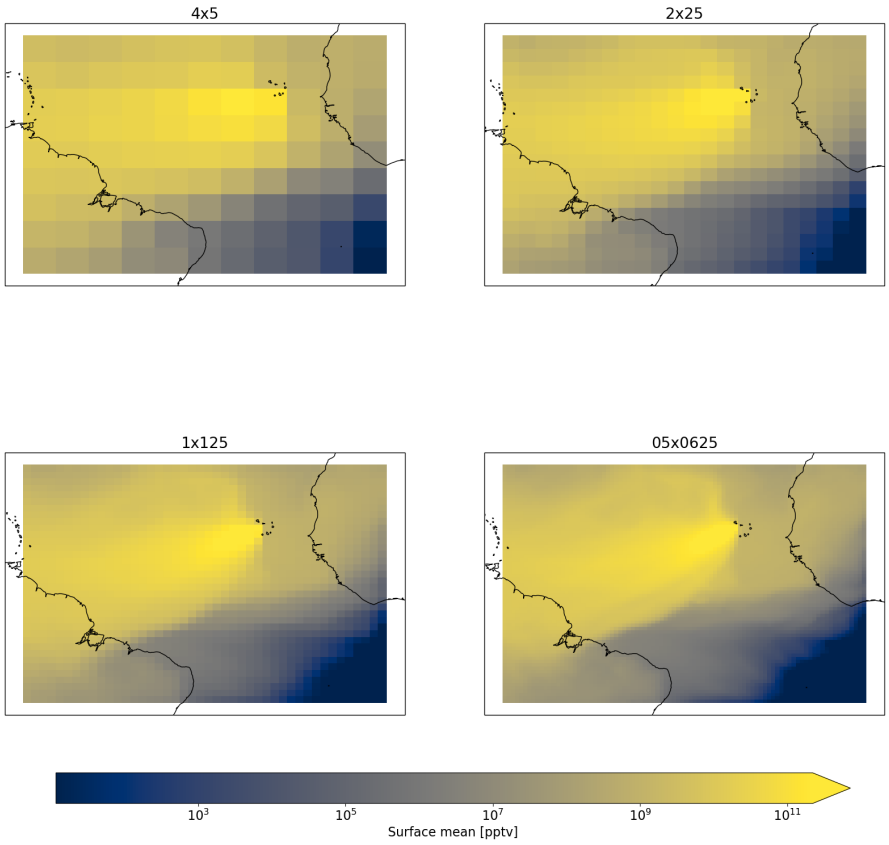

Figure 45: Log_{10} of domain surface average mixing ratio for the idealised tracer with point source 1 kg m^{-2} s^{-1} emissions across the domain for model spatial resolutions 4°x5°, 2°x2.5°, 1°x1.25° and 0.5°x0.625°.

As shown in figure 44, there are periods in which there is greater differences between the spatial resolutions, such as that shown in figure 46. During this period (days 25-27 on figure 44) a change in meteorology drives differences between the spatial resolutions with these being particularly notable north of Cape Verde, where air pulled into the domain from outside the nested region, being low in the idealised tracer, has very high resolution dependence.

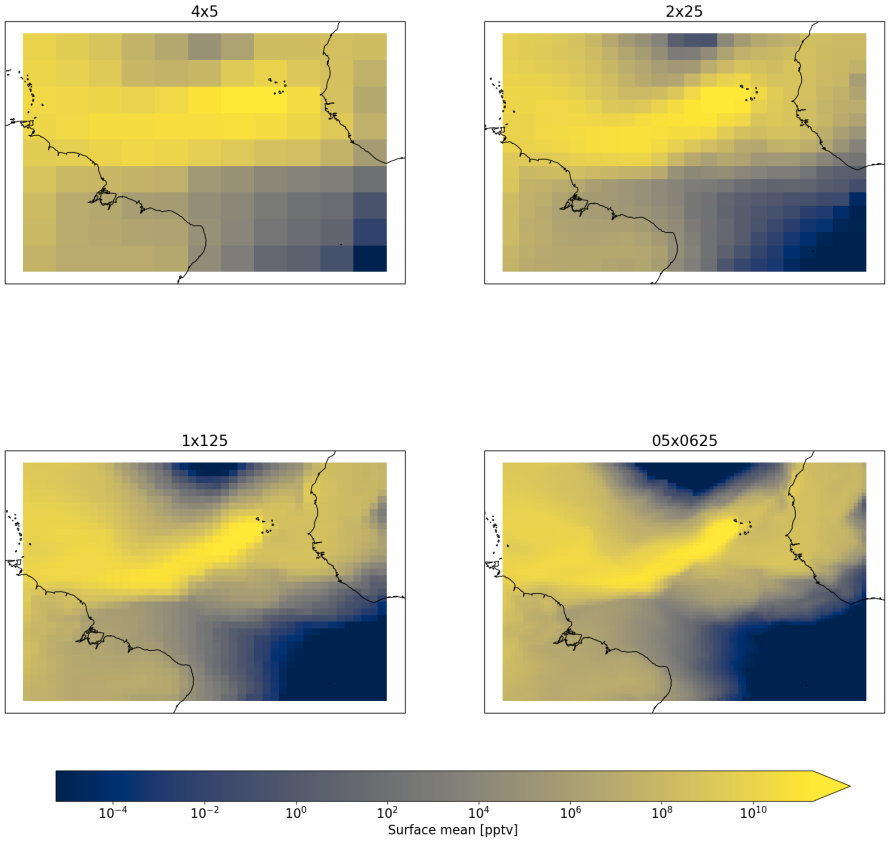

Figure 46: Log_{10} surface average mixing ratio for the idealised tracer with point source 1 kg m^{-2} s^{-1} emissions for model days 25,26,27 since start across the domain for model spatial resolutions 4°x5°, 2°x2.5°, 1°x1.25° and 0.5°x0.625°.

The progressive differences in average surface mixing ratio for the idealised point source tracer (figure 47) further shows that representation of the plume and its boundaries within the domain are subject to spatial resolution dependence and inflow of 'clean' airmasses (not containing the idealised emission tracer) are subject to large percentage differences. These differences are visible in the transition from all resolutions.

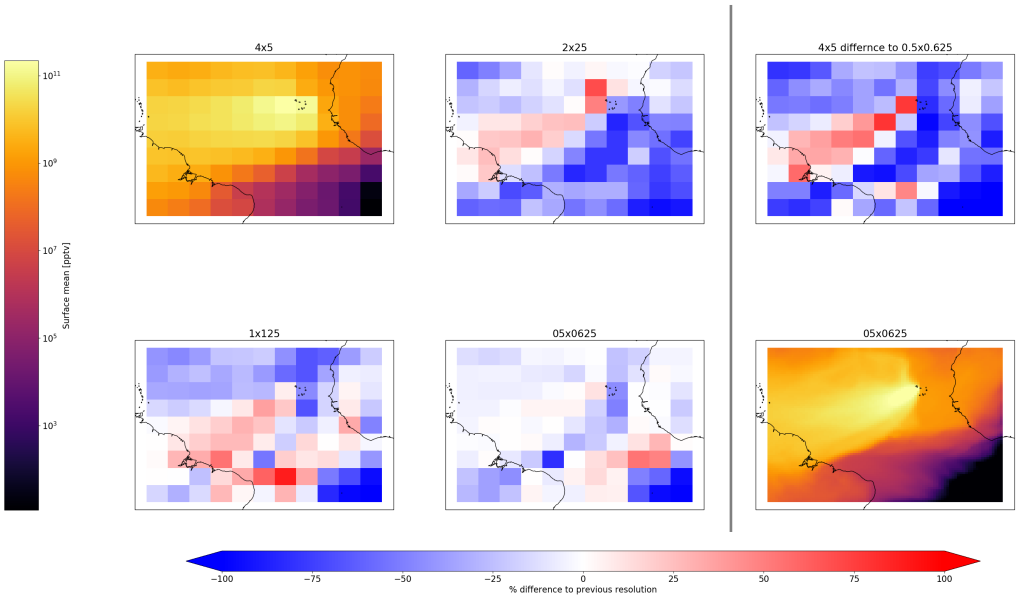

Figure 47: Average surface mixing ratio of idealised tracer with 1 kg m^{-2} s^{-1} within the nested domain for 4°x5° and 0.5°x0.625°. Percentage difference between 2°x2.5° and 4°x5°, percentage difference between 1°x1.25° and 2°x2.5°, percentage difference between 1°x1.25° and 0.5°x0.625°, and total percentage difference between 4°x5° and 0.5°x0.625°.

5.4.2 Idealised chemical tracers

Timeseries of domain average surface mixing ratios for each of the idealised chemistry tracers are shown in figures 48 - 50. The only source for these tracers is the boundary conditions and the tracers have a lifetime of approximately 5 days, 1 day and 1 hour respectively. For the three different lifetimes, each resolution broadly predicts similar trends and features, however the spread of differences between the resolutions increases as lifetime of the tracer decreases and higher resolutions predict higher grid average mixing ratios. The longest lifetime of five days (figure 48 demonstrates minimal spread between resolutions apart from 4x5 which is more obvious difference to other resolutions. As lifetime decreases to one day (figure 49) and one hour (figure 50) there is further divergence between resolutions, however throughout 4x5 remains the lowest predictions and the greatest difference from other resolutions.

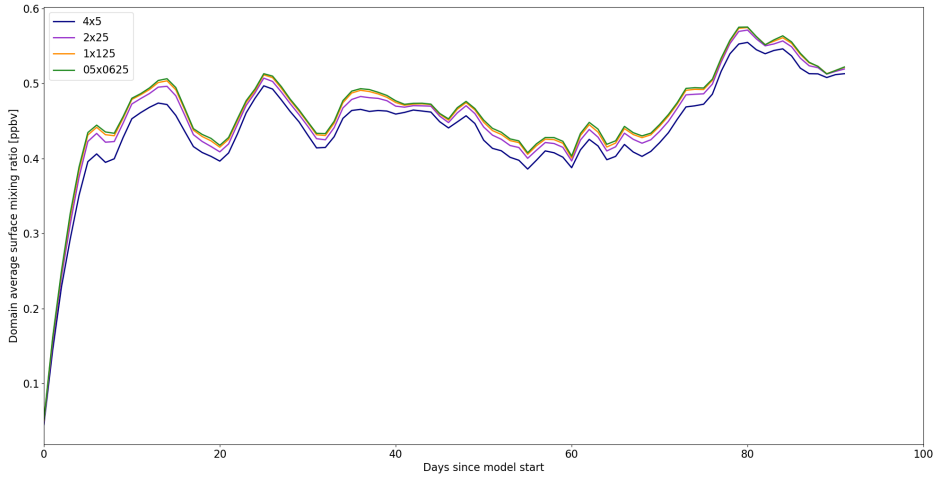

Figure 48: Domain average timeseries of days since model start for the idealised tracer with five day lifetime for model spatial resolutions 4°x5°, 2°x2.5°, 1°x1.25° and 0.5°x0.625°.

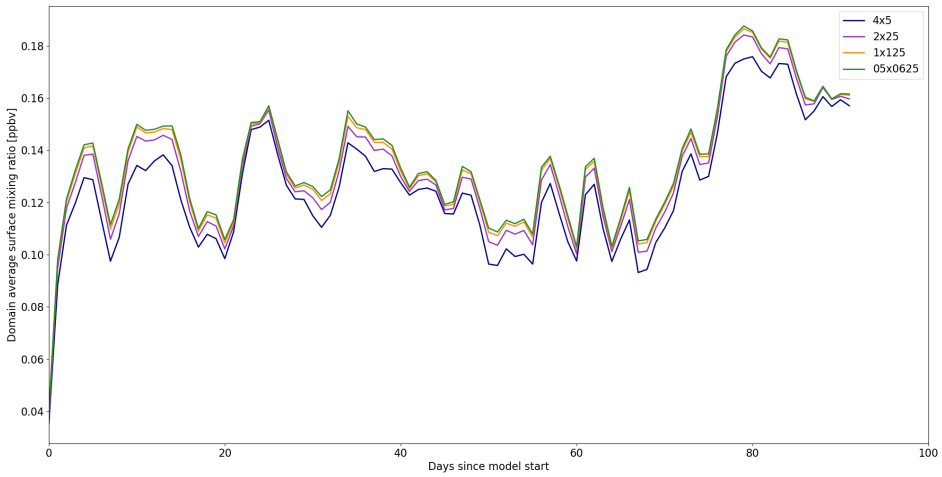

Figure 49: Domain average timeseries of days since model start for the idealised tracer with one day lifetime for model spatial resolutions 4°x5°, 2°x2.5°, 1°x1.25° and 0.5°x0.625°.

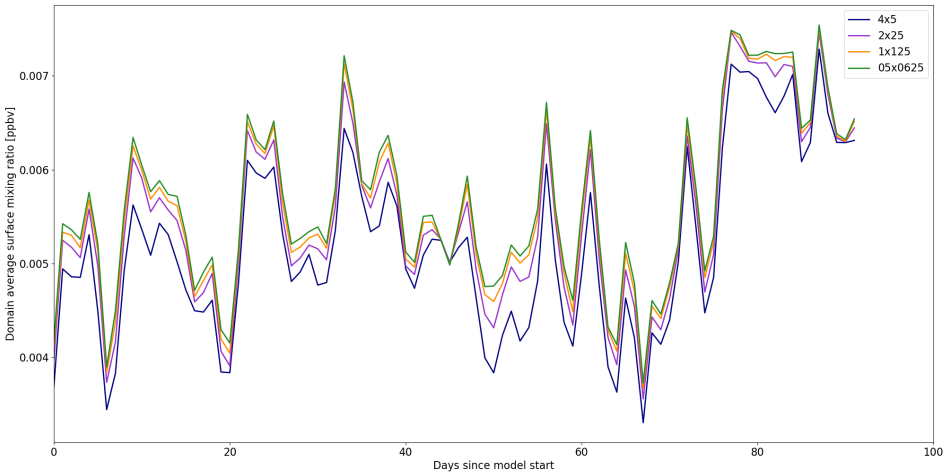

Figure 50: Domain average timeseries of days since model start for the idealised tracer with one hour lifetime for model spatial resolutions 4°x5°, 2°x2.5°, 1°x1.25° and 0.5°x0.625°.

5.4.3 Idealised wet deposition tracers

Finally the timeseries for idealised tracers for wet deposition are shown in figure 51. The only source for these tracers is the boundary conditions and wet deposit like nitric acid, sea salt and ammonia. These tracers show similar trends to the idealised chemistry tracers, with higher resolutions predicting higher average mixing ratios but with broadly similar trends across resolutions. All three idealised tracers display similar timeseries with the rate of wet deposition having very little impact. However all three wet deposition tracers across all resolutions have values somewhere within the domain that exceed the boundary condition source (> 1 ppbv, figure 52) despite not having any additional sources or a production mechanism. The reasons behind this are currently unknown and are topics of discussion with the GEOS-Chem support team and user community.

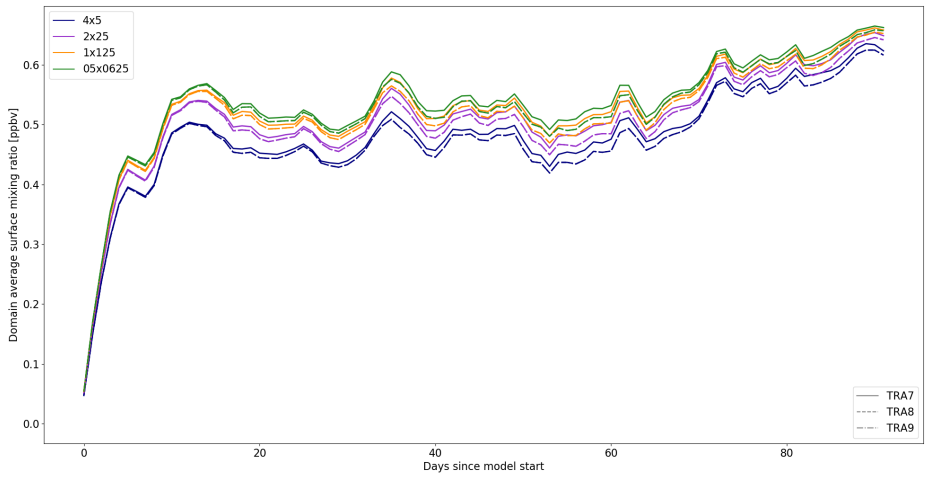

Figure 51: Domain surface mean hourly timeseries since model start for idealised tracers with uniform 1 ppbv boundary condition source and wet deposition as the only loss mechanism. TRA7 wet deposits like HNO_3, TRA8 like sea salt and TRA9 like ammonia.

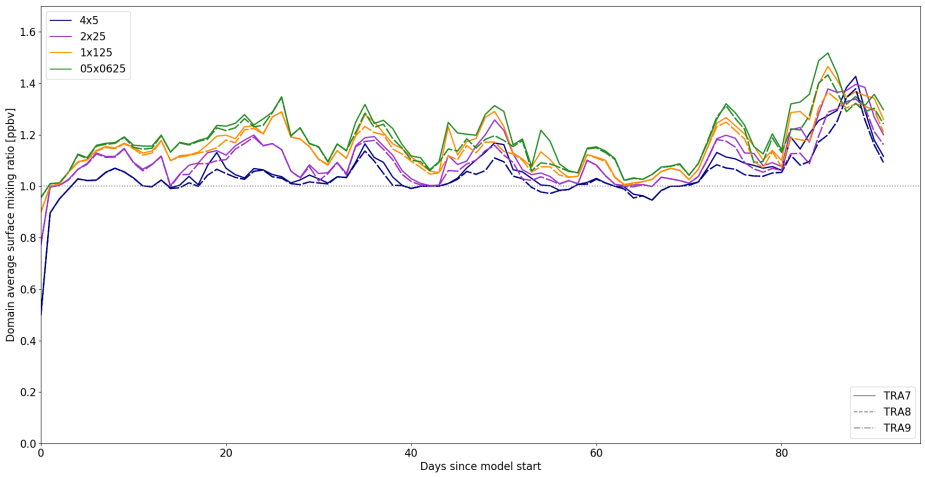

Figure 52: Domain surface maximum hourly timeseries since model start for idealised tracers with uniform 1 ppbv boundary condition source and wet deposition as the only loss mechanism. TRA7 wet deposits like HNO_3, TRA8 like sea salt and TRA9 like ammonia.

5.4.4 Summary of idealised tracers

The idealised tracers have shown that negligible error between spatial resolutions results from spin-up. Furthermore emissions are uniform between resolutions. The representation of transport and convection at different spatial resolutions seems to be a key contributor to error between them. These errors appear to be largest in tracers with short atmospheric lifetime ($\sim$1hr). Idealised tracers representing wet deposition show inconsistent behaviour with tracers within the domain at all resolutions exceeding the boundary condition source with no other source existing. The reasons behind this, and implications for other wet-depositing species within the model are unclear.

5.5 Comparison of key atmospheric species between spatial resolutions

This section will now focus on exploring the impact of the spatial resolution differences (found in section 5.4) across a range of model tracers.

5.5.1 Tropospheric oxidants

To analyse spatial distributions of the differences between resolutions, the progressive difference between model spatial resolutions is used. This is shown for O_3 in figure 53. The top left plot shows the mean surface concentration over the 6 months (2017/01/01 to 2017/07/01) of the simulation at 4°x5°resolution. The bottom left plot shows the same simulation but run at 0.5°x 0.625°. The top right shows the ratio of the concentrations calculated by the 4°x5°simulation divided by the 0.5°x 0.625°averaged onto the 4°x5°grid. This represents the "error" in the 4°x5°simulation. The top middle shows the equivalent plot calculated with the 2°x2.5°simulation instead of the 4°x5°. The bottom left is the same plot but compares the 1°x1.25°to the 2°x2.5°simulation and the bottom middle compares the 0.5°x 0.625°with the 1°x1.25°. Multiplying the top middle by the bottom left and the bottom middle plots gives the top right.

The region of greatest change between resolutions for O_3 is above the Amazon where emissions and chemistry are their most complex in the domain. However even here the maximum changes between the highest and lowest resolution are less than 10%. Across the marine environment, smaller percentage differences ($<$3%) remain, decreasing with each increase in spatial resolution. An area around the African coast shows a different tendency, in that O_3 decreases with increasing resolution (notably from 2x2.5 to 4x5). This may be due to the non-linear relation between shipping emissions and NO_x chemistry and that this region has transitioned from a net O_3 production, to net loss environment due to changes in the NO_x mixing ratio by representation of their emissions.

The inter-tropical convergence zone (ITCZ) (located on average between the most southerly part of West Africa in the domain and the the most westerly coast of South America) shows a persistent difference at each resolution. The resolution step from 4°x5° to 2°x2.5° with greatest spatial distribution across the domain and largest single change (10-15%, over the Amazon). Generally the lower spa-

tial resolutions are underestimating O_3 compared to higher spatial resolutions.

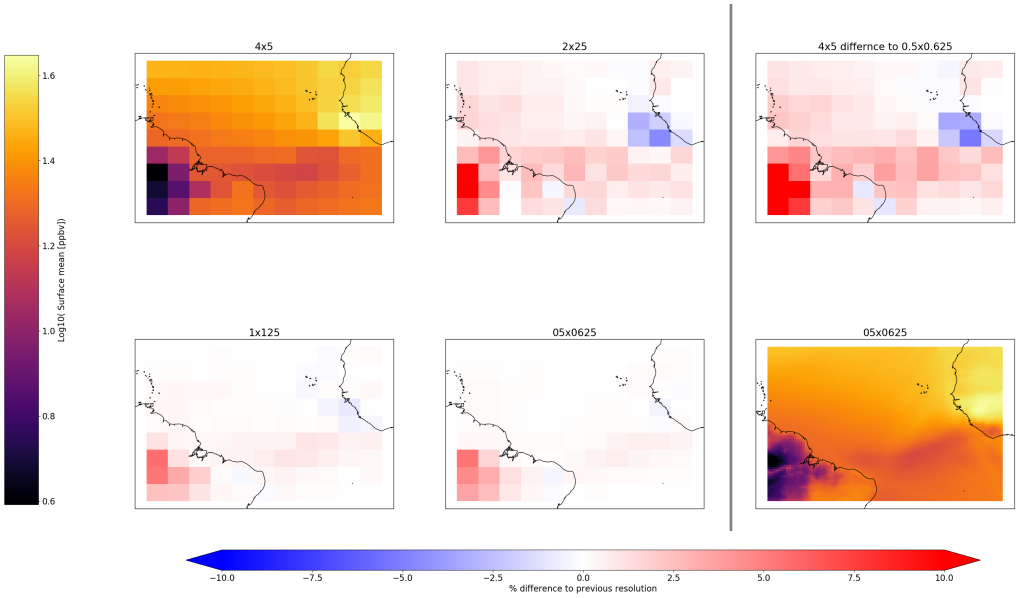

Figure 53: Average surface mixing ratio of O_3 within the nested domain for 4°x5° (top left) and 0.5°x0.625° (bottom right). Percentage difference between 2°x2.5° and 4°x5° (middle top), percentage difference between 1°x1.25° and 2°x2.5° (bottom left), percentage difference between 1°x1.25° and 0.5°x0.625° (bottom middle), and total percentage difference between 4°x5° and 0.5°x0.625° (top right).

Similar trends are observed in OH (figure 54). The largest differences are seen going from 4°x5° to 2°x2.5° and subsequent resolution differences showing increasingly smaller changes for increases in spatial resolution. Unlike O_3, OH shows a much stronger split in the domain differences with OH reducing over the amazon region as resolution increases, but mostly increasing over western Africa, Cape Verde and along shipping tracks as resolution increases. Both O_3 and OH demonstrate notable localised changes in surface mixing ratio.

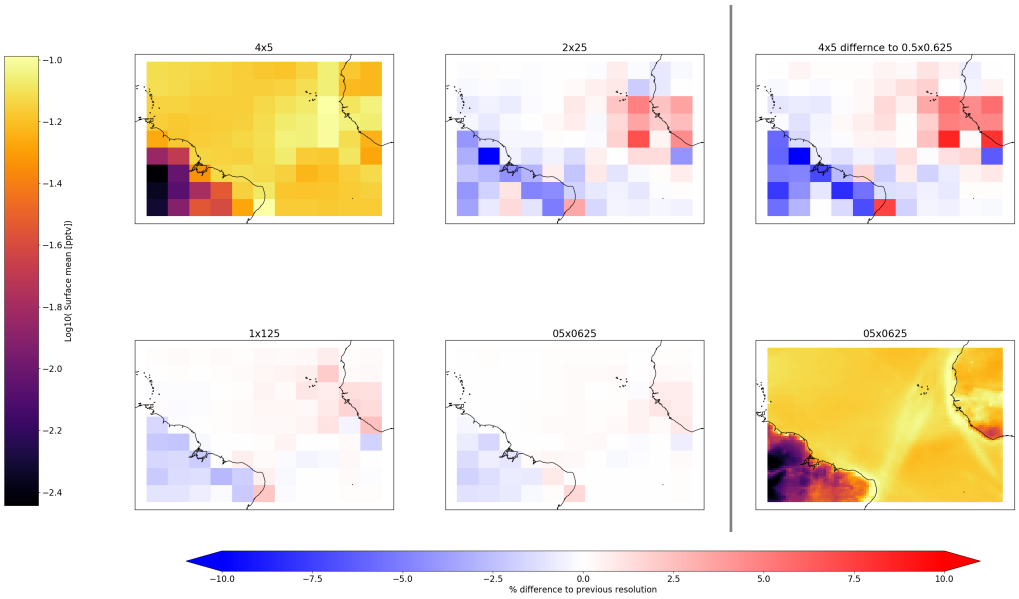

Figure 54: Average surface mixing ratio of OH within the nested domain for 4°x5° and 0.5°x0.625°. Percentage difference between 2°x2.5° and 4°x5°, percentage difference between 1°x1.25° and 2°x2.5°, percentage difference between 1°x1.25° and 0.5°x0.625°, and total percentage difference between 4°x5° and 0.5°x0.625°.

5.5.2 NO_x

The progressive percentage differences between spatial resolutions for NO_x is shown in figure 55. Unlike the structures shown at difference resolutions for O_3 and OH, NO_x presents a less structured response case. This difference may reflect the very strong gradients seen in the concentration calculated in the model. NO_x mixing ratios over land and coastal regions which can be over 3 orders of magnitude greater than those seen over the remote ocean. Secondly, effects of shipping emissions will also likely play a role, with well defined ship plumes at the highest resolution being effectively washed out at lower resolutions. Although the PARANOX module (Vinken et al., 2011; Holmes et al., 2014) might mitigate some of these effects, there appears to be the lowest oxides of nitrogen concentration in the ship tracks at higher resolution compared to lower. As with O_3 and OH, increasing resolution results in reducing differences between the spatial resolutions and the greatest differences observed between 4x5 and 2x2.5.

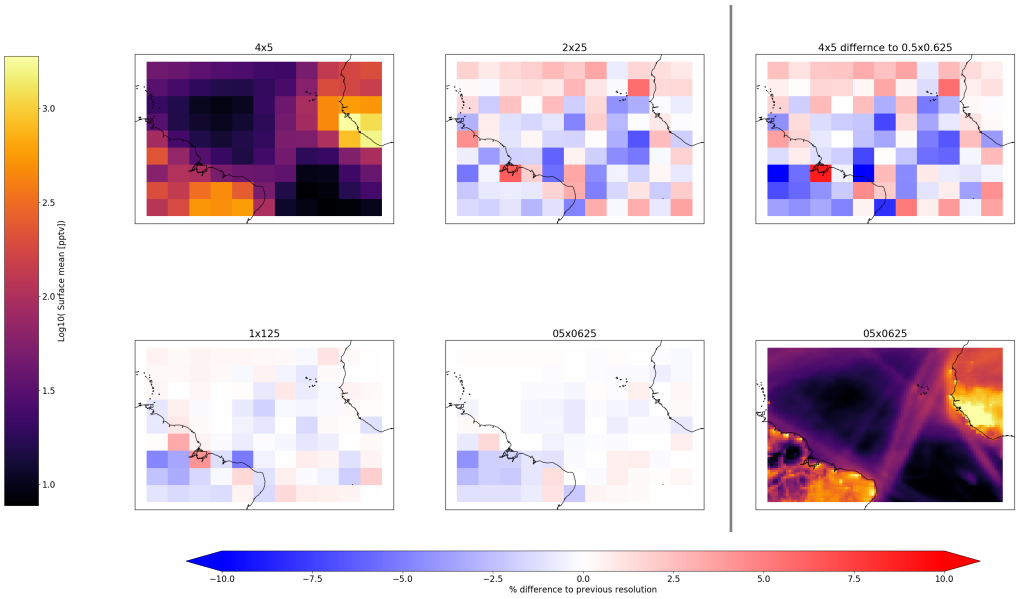

Figure 55: Average surface mixing ratio of NO_x within the nested domain for 4°x5° and 0.5°x0.625°. Percentage difference between 2°x2.5° and 4°x5°, percentage difference between 1°x1.25° and 2°x2.5°, percentage difference between 1°x1.25° and 0.5°x0.625°, and total percentage difference between 4°x5° and 0.5°x0.625°.

5.5.3 Volatile organic compounds

The progressive percentage difference is shown for the propene (which represents propene and $>$ C_4 alkenes, approximate lifetime of 5.3 hours (Atkinson, 2000)) in figure 56. Similar to NO_x, propene presents a highly structured set of differences between spatial resolutions. However unlike the previous cases of O_3, OH, and NO_x, high percentage differences remain between the highest resolutions around coastal regions, Cape Verde archipelago and along shipping lanes.

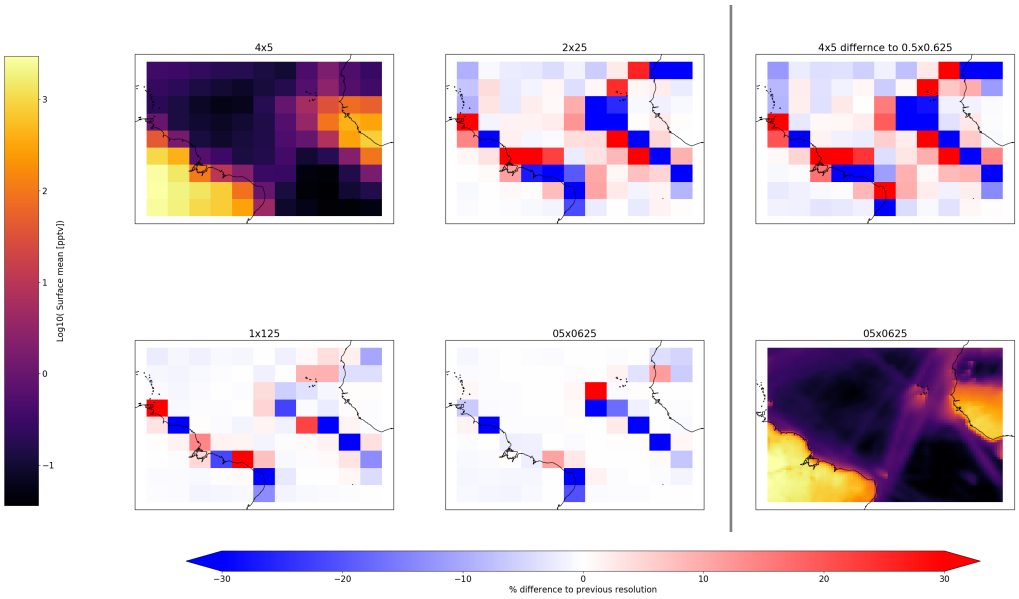

Figure 56: Average surface mixing ratio of propene within the nested domain for 4°x5° and 0.5°x0.625°. Percentage difference between 2°x2.5° and 4°x5°, percentage difference between 1°x1.25° and 2°x2.5°, percentage difference between 1°x1.25° and 0.5°x0.625°, and total percentage difference between 4°x5° and 0.5°x0.625°.

The comparatively longer lived propane (with lifetime of approximately 10 days (Atkinson, 2000)) presents a different trend again (figure 57. The increase in spatial resolution from 4°x5° to 2°x2.5° results in a 5% increase in mixing ratio for most surface grid boxes. This trend does not continue to higher resolutions where the remaining differences persist as decreases over the amazon region. One factor in the remaining differences between resolutions could be attributed to the emissions used for propane (Xiao et al., 2008). They were developed at 2°x2.5° and then up-scaled to 1°x1°, subsequently they are then interpolated to the 0.5°x0.625° resolution used here. The surface mixing ratio's at 0.5°x0.625° demonstrate that the coarse structure of the emissions translate to the surface mixing ratios with substantial emissions occurring over the coastal regions due to the coarse resolution of the emissions .

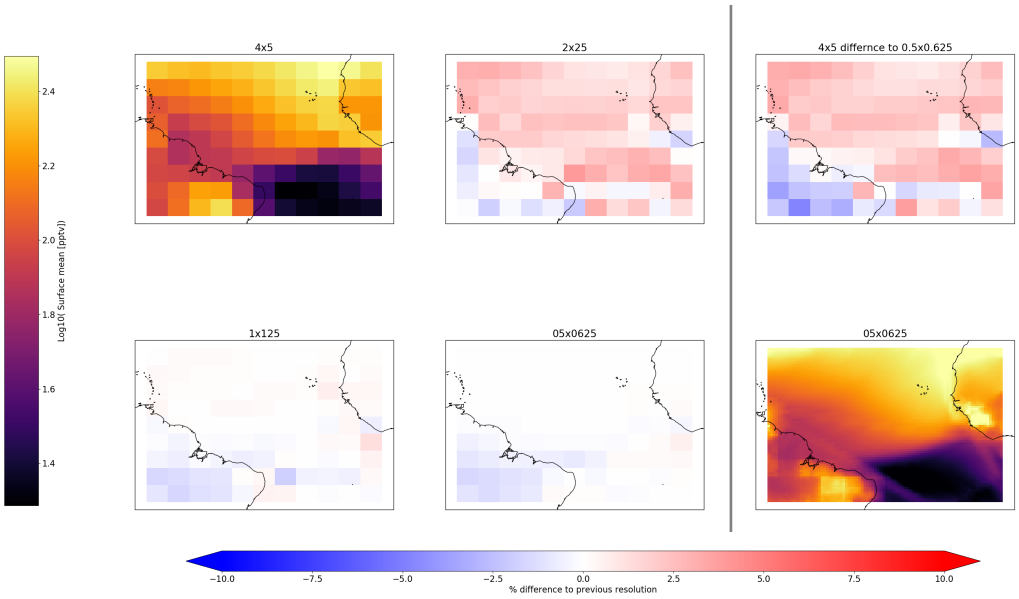

Figure 57: Average surface mixing ratio of propane within the nested domain for 4°x5° and 0.5°x0.625°. Percentage difference between 2°x2.5° and 4°x5°, percentage difference between 1°x1.25° and 2°x2.5°, percentage difference between 1°x1.25° and 0.5°x0.625°, and total percentage difference between 4°x5° and 0.5°x0.625°.

Alkanes with C_4 and greater are lumped in the model in the ALK4 tracer, with the resolution differences for this shown in figure 58. Whilst having a broadly similar surface distribution and structure of mixing ratios, there are differences between ALK4 and propane. Firstly, as ALK4 does not use the Xiao et al. (2008) emission inventory. Hence the coarse structure observed over South America for propane is not present in the 0.5°x0.625° surface mixing ratios. Secondly the differences between resolutions have a substantially different structure. Whereas propane has an almost uniform increase in surface mixing ratio with increasing resolution, ALK4 has a more complex picture. Predictions for the plume leaving Africa and Cape Verde heading to south America, decrease with the first resolution increase and remaining fairly constant thereafter, while elsewhere in the grid a more variable picture in resolution differences is present. As with previous species, the initial increase from 4°x5° to 2°x2.5° seems to offer the greatest return for change in model predictions.

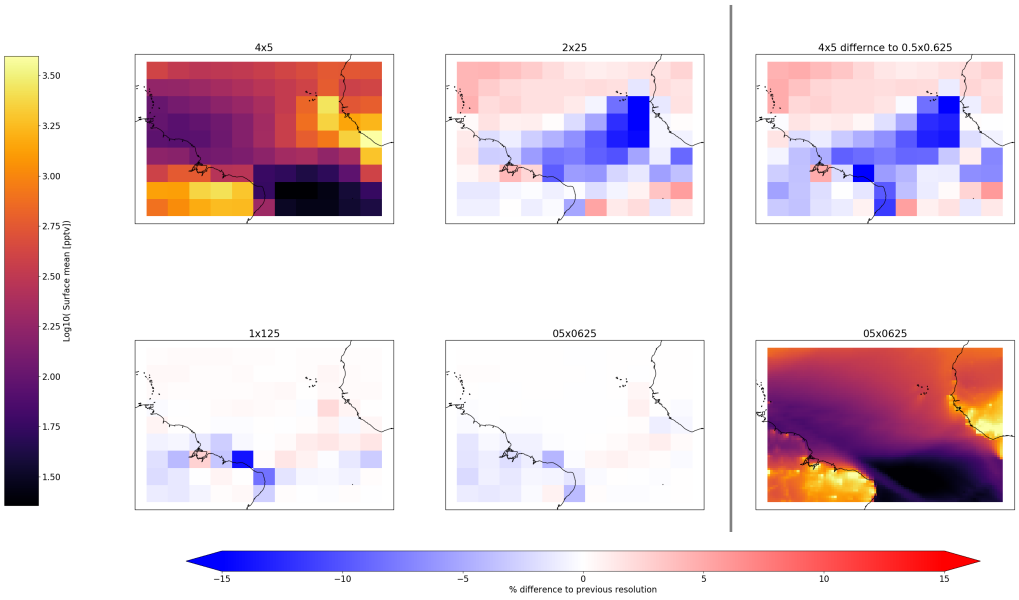

Figure 58: Average surface mixing ratio of ALK4 tracer within the nested domain for 4°x5° and 0.5°x0.625°. Percentage difference between 2°x2.5° and 4°x5°, percentage difference between 1°x1.25° and 2°x2.5°, percentage difference between 1°x1.25° and 0.5°x0.625°, and total percentage difference between 4°x5° and 0.5°x0.625°.

5.5.4 Aerosols and Sulfur Dioxide

DMS is important for both cloud formation and climate (section 1.2). The up-welling of ocean water between Cape Verde and the African coast (the Senegalo-Mauritanian up-welling) leads to high concentration of DMS around Cape Verde in the model, with lower concentration within the ITCZ and concentration picking back up on south side of the ITCZ. The largest area of positive change in surface DMS visible in both percentage and in the surface mixing ratios is the region between Cape Verde and coastal west Africa (figure 59) in the ITCZ. Offline DMS emissions are used with consistent emission resolution between model runs, hence this resolution dependence is not due to the emissions. Instead this appears to be linked to meteorological processes. Underestimates of DMS concentration are visible over the Sahara and Amazon. This is likely linked to the transport of very low concentrations of DMS in these regions.

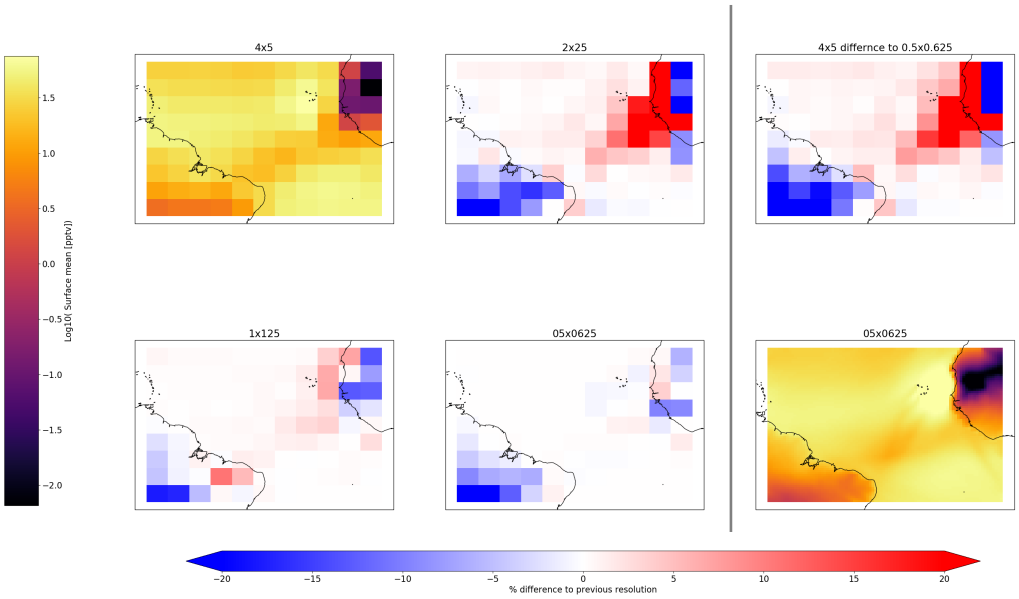

Figure 59: Average surface mixing ratio of DMS within the nested domain for 4°x5° and 0.5°x0.625°. Percentage difference between 2°x2.5° and 4°x5°, percentage difference between 1°x1.25° and 2°x2.5°, percentage difference between 1°x1.25° and 0.5°x0.625°, and total percentage difference between 4°x5° and 0.5°x0.625°.

Dust aerosol in the model is divided into 4 tracers, representing particles with radii of 0.7, 1.4, 2.4, and 4.5 μm. For comparison between model spatial resolution the tracer representing 0.7 μm is shown in figure 60. As dust emission is strongly correlated to meteorological conditions, this work uses resolution independent dust emissions. Dust is minimally reactive in the model hence error between resolution will have dependencies on wet deposition, dry deposition, and transport but not chemistry. Both wet deposition and transport have been shown to cause similar magnitude of error between spatial resolutions such as those observed in dust (section 5.4, $\sim$5-10%). The largest errors are found over Cape Verde on the north edge of the plume. This may be due to difficulties in representing the transport of dust through the boundary conditions and in managing the representation of the strong gradient within the plume. These differences are relatively small (10%) compared to the much larger differences seen for say DMS (20%).

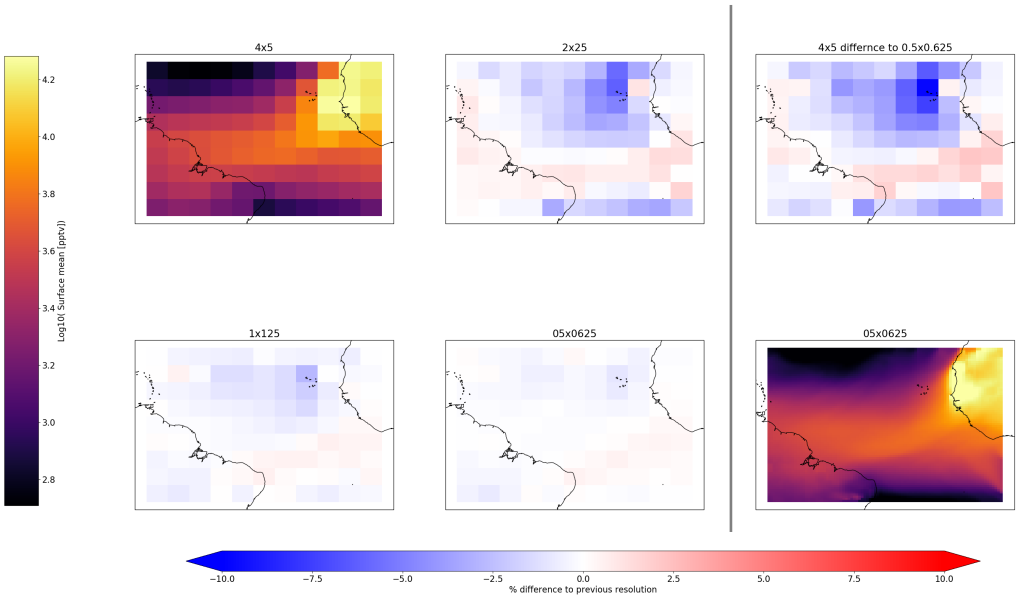

Figure 60: Average surface mixing ratio of dust within the nested domain for 4°x5° and 0.5°x0.625°. Percentage difference between 2°x2.5° and 4°x5°, percentage difference between 1°x1.25° and 2°x2.5°, percentage difference between 1°x1.25° and 0.5°x0.625°, and total percentage difference between 4°x5° and 0.5°x0.625°.

Highly structured emissions (and hence surface mixing ratios) are present for SO_2 (figure 61). Like NO_x, the ability to resolve point sources and shipping lanes is the main driving force in spatial resolution differences. Additionally the resolution change between 4°x5° and 2°x2.5° also represents the largest step change between spatial resolutions.

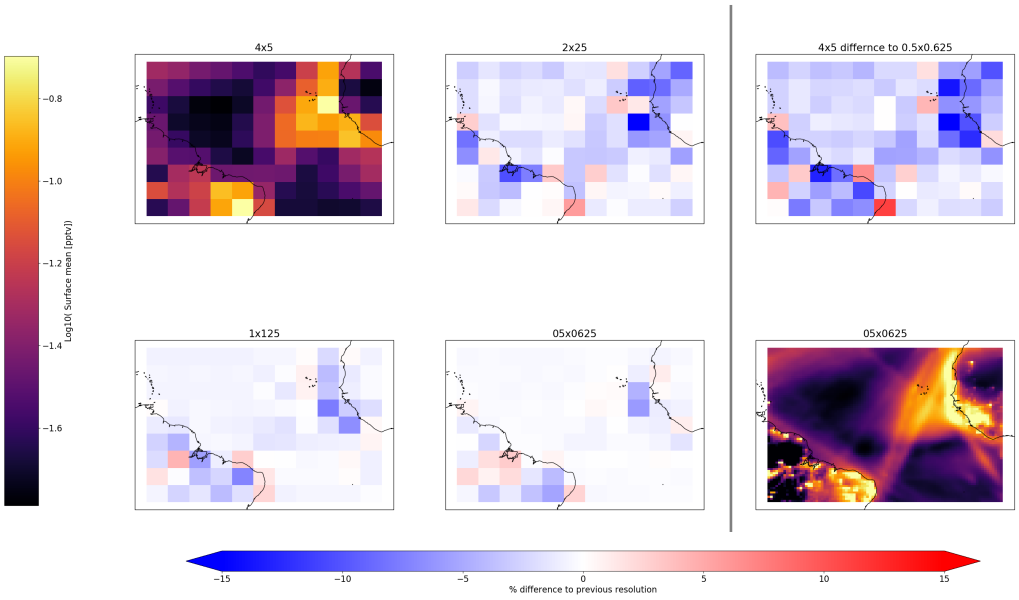

Figure 61: Average surface mixing ratio of SO_2 within the nested domain for 4°x5° and 0.5°x0.625°. Percentage difference between 2°x2.5° and 4°x5°, percentage difference between 1°x1.25° and 2°x2.5°, percentage difference between 1°x1.25° and 0.5°x0.625°, and total percentage difference between 4°x5° and 0.5°x0.625°.

The spatial variability in Ammonia, nitrate and sulfate aerosol are shown in figures 62 - 64. Both ammonia and nitrate aerosol show strong resolution dependence around coastal regions and along shipping lanes. The effects of the underlying structure of the emissions for the precursor species and subsequent chemistry compounds at different resolutions, becoming a likely explanation for this error.

Sulfate aerosol however does not share the strong spatial resolution dependence. Ultimately the SO_2 emitted into the model will, through chemistry, result as sulfate aerosol or be dry deposited. This mass conservation will contribute to the reduced error in sulfate aerosol. The error in sulfate aerosol ($\sim$ 5-10%) is likely fully or in part due to that of transport and convection, such as that observed in the idealised emission tracers (section 5.4).

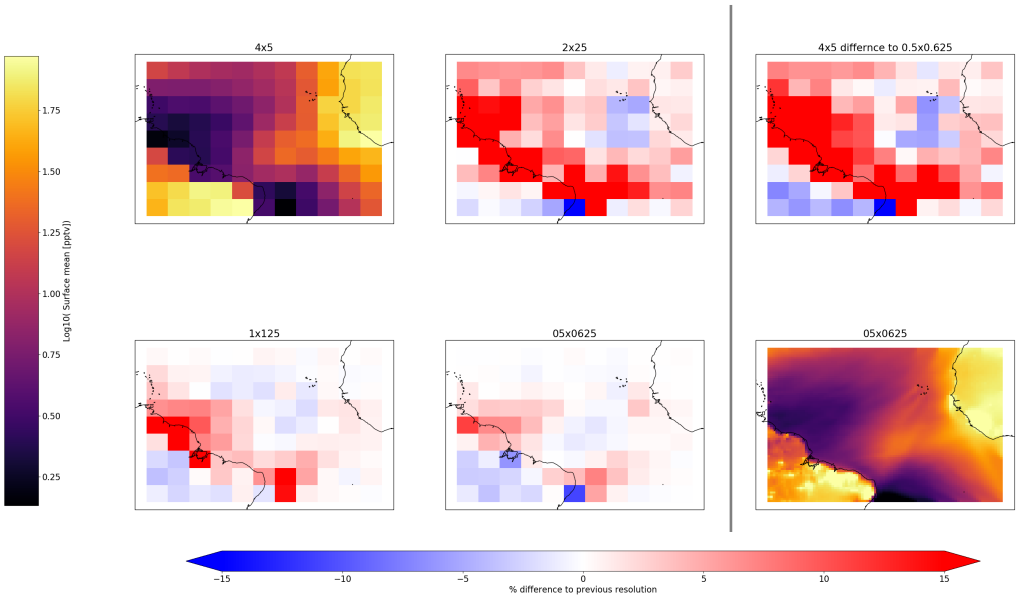

Figure 62: Average surface mixing ratio of Ammonia within the nested domain for 4°x5° and 0.5°x0.625°. Percentage difference between 2°x2.5° and 4°x5°, percentage difference between 1°x1.25° and 2°x2.5°, percentage difference between 1°x1.25° and 0.5°x0.625°, and total percentage difference between 4°x5° and 0.5°x0.625°.

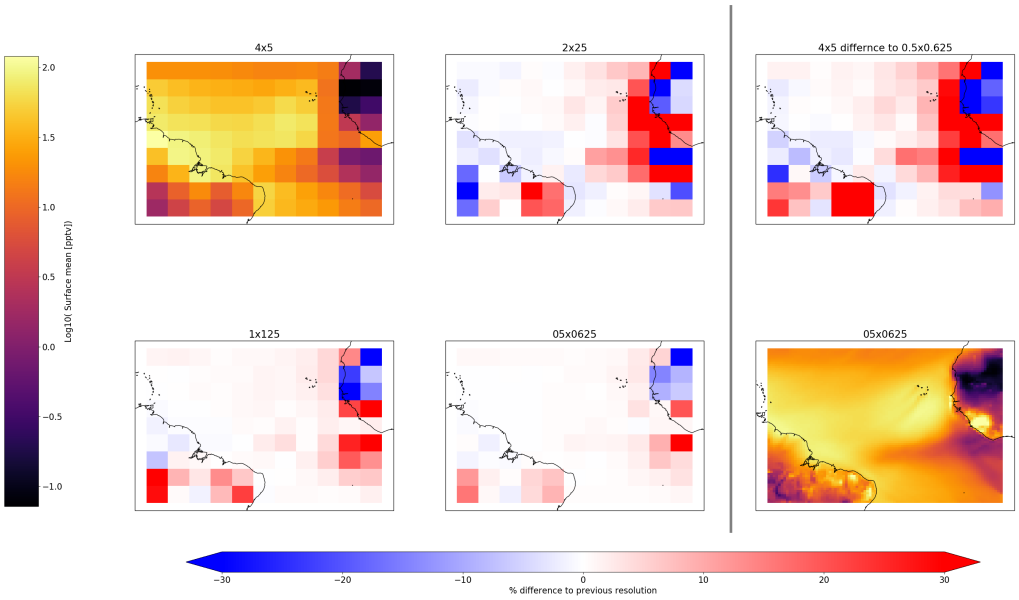

Figure 63: Average surface mixing ratio of nitrate aerosol within the nested domain for 4°x5° and 0.5°x0.625°. Percentage difference between 2°x2.5° and 4°x5°, percentage difference between 1°x1.25° and 2°x2.5°, percentage difference between 1°x1.25° and 0.5°x0.625°, and total percentage difference between 4°x5° and 0.5°x0.625°.

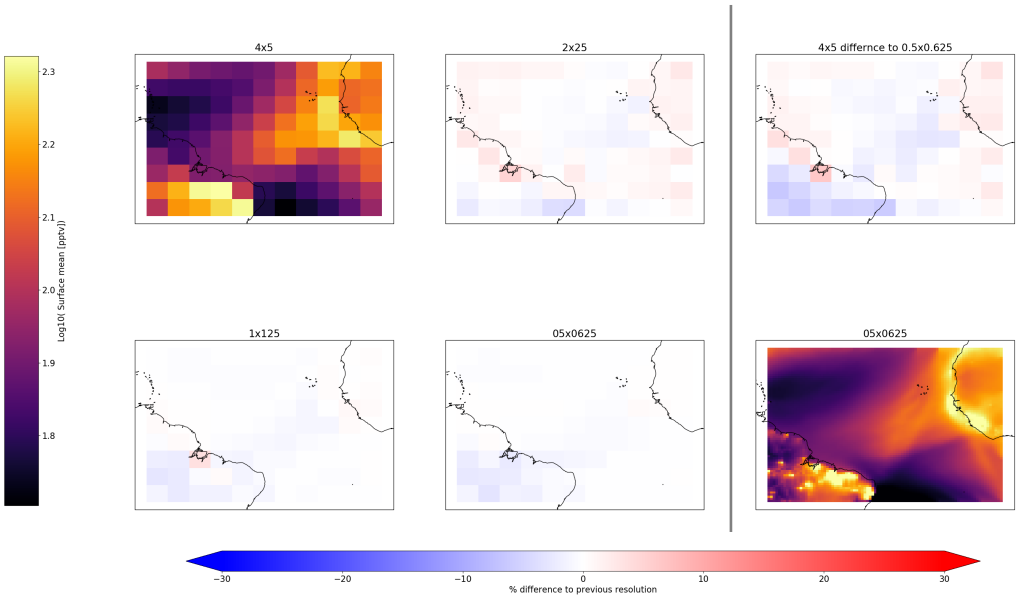

Figure 64: Average surface mixing ratio of sulfate aerosol within the nested domain for 4°x5° and 0.5°x0.625°. Percentage difference between 2°x2.5° and 4°x5°, percentage difference between 1°x1.25° and 2°x2.5°, percentage difference between 1°x1.25° and 0.5°x0.625°, and total percentage difference between 4°x5° and 0.5°x0.625°.

5.5.5 Summary of spatial resolution comparisons

Looking at the response of these different species to changes of resolution a number of conclusions can be made. Species most sensitive to spatial resolution are those with highly structured surface emissions, and relatively short atmospheric lifetimes. Species that can build up strong gradients between emission and sink regions can cause problems for the model.

5.6 Quantifying resolution differences on Tropsopheric mixing ratios

The average tropospheric burdens for both O_3 and OH are shown in table 9. There is a tendency for a small increase in O_3 burden and mean OH as resolution increases but surface OH appears almost unaffected. The greatest difference between resolutions is the increase between 4°x5° and 2°x2.5°. Following this

there remains differences between higher resolutions, however there are diminishing returns for each increase in spatial resolution. For example, the O_3 mean domain burden increases by 1.5% going from 4°x5° to 2°x2.5°, but around half of this (0.8%) going from 2°x2.5° to 1°x1.25° and then the difference roughly halves again (0.5%) going from 1x1.125 to 0.5°x0.625°. Average surface OH across the domain is more consistent across the spatial resolutions with the model predicting 15.6 x10^5 molec cm^{-3} within $\pm$ 0.3%. Thus the largest scale oxidants across the region are not significantly influenced by spatial resolution even if the concentration of some species show larger influences.

Resolution	O_3 mean domain burden Tg	OH troposphere mean x10^5 molec cm^{-3}	OH surface mean x10^5 molec cm^{-3}
4x5	12.47	16.05	15.60
2x2.5	12.66	16.23	15.65
1.1x25	12.76	16.37	15.61
0.5x0.625	12.82	16.48	15.58

Table 9: Mean tropsopheric burdens of ozone and mass weighted average OH concentration at each resolution for the nested domain. Troposphere taken between surface and 10km altitude (model level 28).

An alternative way to quantify the differences in model predictions between lowest (low, 4°x5°) and highest ($high$, 0.5°x0.625°) model resolution is the average relative root mean square error (RRMSE equation 44), where the number of timesteps is tt and the number of x and y spatial grid boxes is given by ii and jj.

$$RRMSE(t) = \frac{1}{ii * jj * tt} \sum_{t=1}^{tt} \sum_{i=1}^{ii} \sum_{j=1}^{jj} \sqrt{\frac{(high_{t,i,j} - low_{t,i,j})^2}{high_{t,i,j}^2}} \times 100 \qquad (44)$$

Figure 65 shows this for O_3, OH and HO_2 in the full domain and for only boxes over the ocean. As discussed earlier the resolution error between the highest and the lowest resolution is relatively small. It is substantially larger for grid boxes over the ocean. This may be due to the influence of ship plumes over the ocean. The errors in the HO_2 radical and surface O_3 concentrations are larger and comparable to each other. There is some difficulty in attribution of causality here, as

O_3 is the source of HO_2 but similarly HO_2 is necessary for O_3 production. The smaller error in OH compared to HO_2 and O_3 is unexpected but may be due to errors cancelling out due to OH chemistry.

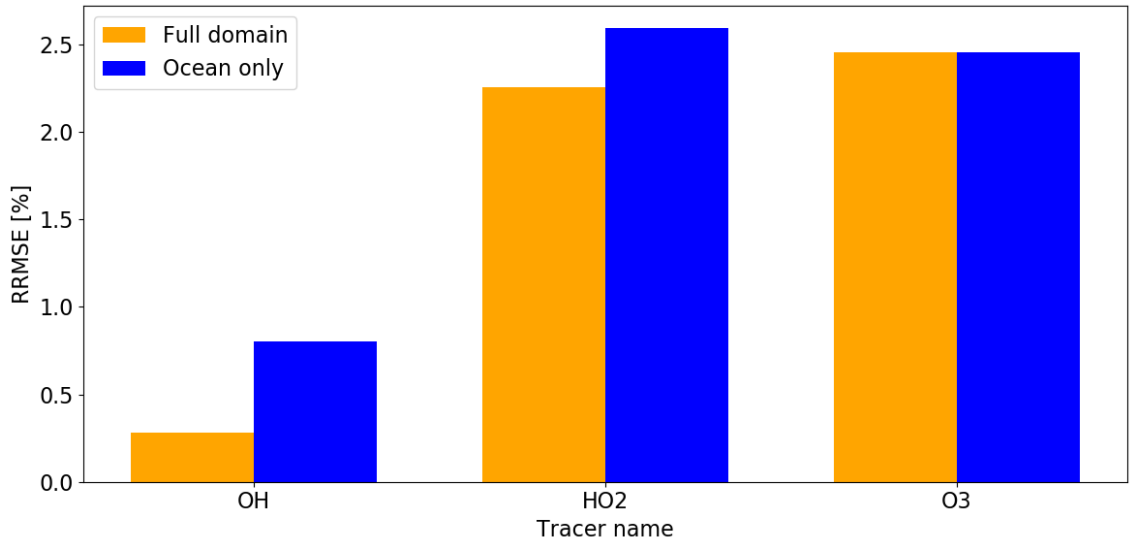

Figure 65: Average surface RRMSE, between 4°x5° and 0.5°x0.625°, of tracers produced from oxidation reactions across whole domain (orange) and above ocean only (blue) for ozone (O3), Hydroperoxyl radical (HO2), hydroxyl radical (OH).

RRMSE for primary emitted VOC's are shown in figure 66. CO has the longest lifetime and has the lowest values of RRMSE across the domain. As tropospheric lifetime decreases, the RRMSE for alkanes increases reaching a peak at around 20% for ALK4, which represents alkanes $\geq$C4. However this trend is not true for other VOCs. Isoprene, which has the shortest lifetime of species featured in figure 66, has one of the lowest values of RRMSE at 3%. The aromatics also don't follow the same pattern as alkanes, or that of the other VOCs. It is not known why there is different behaviours of resolution dependence for VOCs, instead some possible explanations for this behaviour are offered.

For long lived species (such as CO), spatial gradients are relatively small. Resolution related differences in the representation of transport are going to be less important. For short lived species (such as isoprene) transport is less important than oxidation for determining its concentration. OH concentration do not

seem to have much resolution dependence so there is likely little resolution dependence introduced by OH oxidation of these species. One possible explanation for the peak in resolution dependent error of ALK4 may be due to comparable atmospheric lifetime and transport timescales. With an atmospheric lifetime of approximately 2 days, the tracer is able to form gradients across the domain . A 500 km grid box (roughly the size of a 4°x5° gridbox) with a surface wind of 5 ms^{-1} (typical at Cape Verde) is crossed in 1.15 days. Species where this is the case may be particularly sensitive to forming strong gradients which are difficult to accurately represent at low resolutions. However it is worth noting that toluene, with an atmospheric lifetime of approximately 1.9 days does not show this enhancement of error. One possible explanation for this could be due to more localised and substantially smaller toluene emissions compared to ALK4 emissions, the same scale of gradients in the toluene tracer are not constructed, hence a smaller domain average error.

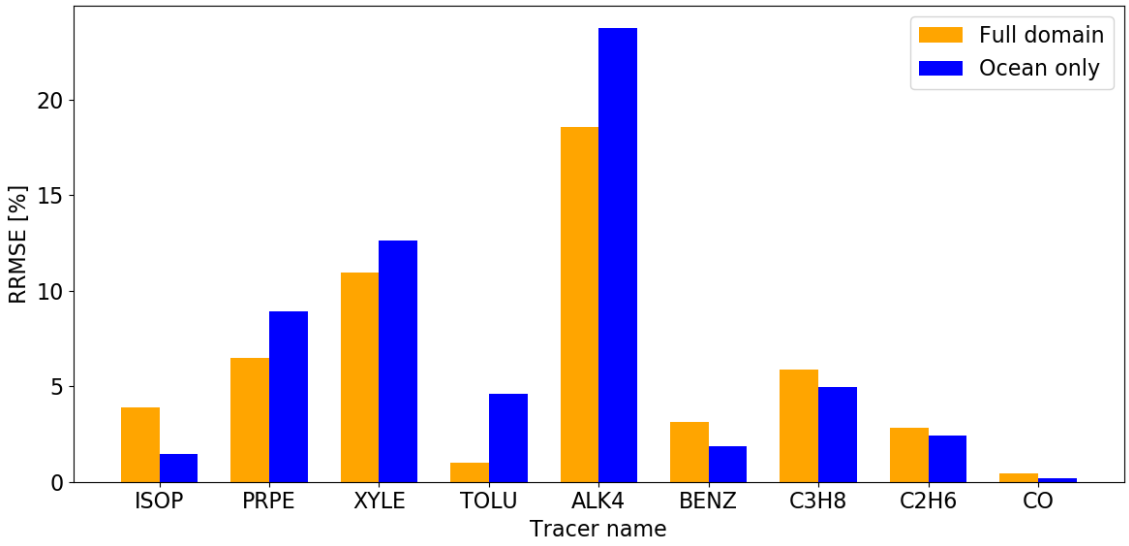

Figure 66: Average surface RRMSE, between 4°x5° and 0.5°x0.625°, of primarily emitted VOC's across whole domain (orange) and above ocean only (blue). Species in order of approximate atmospheric lifetime with shortest on left. Isoprene (ISOP), propene (PRPE), xylene (XYLE) toluene (TOLU), lumped butane and higher alkanes (ALK4), benzene (BENZ), propane (C3H8) ethane (C2H6), and carbon monoxide (CO).

Species that are the results of oxidation reactions are shown in figure 67. The largest error among these exists for H_2O_2, which is formed from the reactions be-

tween two HO_2 molecules, and hence goes as roughly the square of the error in HO_2 (error in HO_2 ~2.5%, error in HO_2 ~7%). The remaining species in figure 67 could be explained by the addition of errors between oxidants (OH and O_3) plus the error from the VOCs trying to maintain gradients.

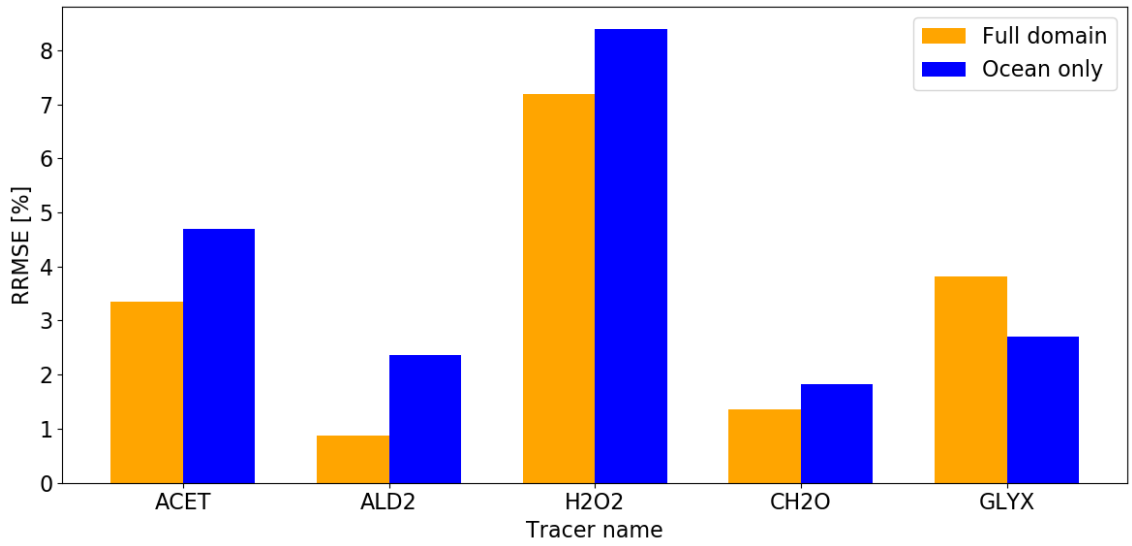

Figure 67: Average surface RRMSE, between 4°x5° and 0.5°x0.625°, of tracers produced from oxidation reactions across whole domain (orange) and above ocean only (blue). Acetone (ACET), acetaldehyde (ALD2), hydrogen peroxide (H2O2), formaldehyde (CH2O), and glyoxal (GLYX).

Error increases for NO_x and NO_y species through the chemical chain (figure 68). NO and NO_2 have the lowest errors as they are early in the chain and hence most dependent mainly on emissions and transport. Further down the oxidation chain the errors increase. The error in NO_3 will be dependent on errors in both O_3 and NO_2 concentrations and transport. This error will then be compounded again for N_2O_5 which is dependent on both NO_3 and NO_2. Hence the position of the NO_y species in the chain of chemistry is the controlling factor of error between resolutions.

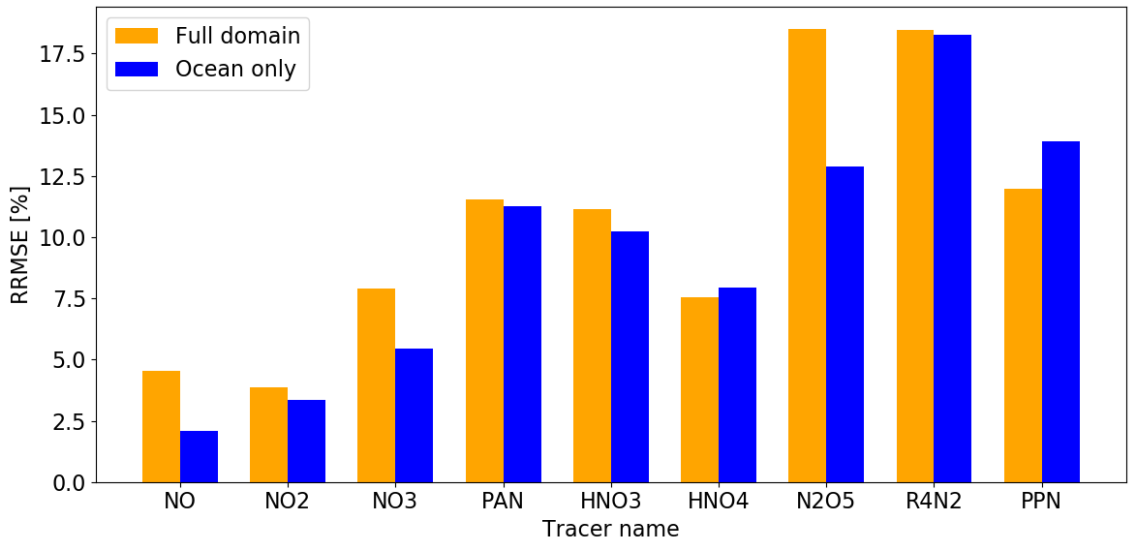

Figure 68: Average surface RRMSE, between 4°x5° and 0.5°x0.625°, of tracers from NO_x and NO_y families across whole domain (orange) and above ocean only (blue) for nitrogen oxide (NO), nitrogen dioxide (NO2), nitrate radical (NO3), Peroxyacetyl nitrate (PAN), nitric acid (HNO3), peroxynitric acid (HNO4), dinitrogen pentoxide (N2O5), lumped alkyl nitrate (R4N2), and lumped peroxypropionyl nitrate (PPN).

Errors between 4°x5° and 0.5°x0.625° for SO_2 (figure 69) is higher ($\sim$11%) than for NO_x and most of the VOCs. One explanation for this could be the dependence on H_2O_2 for uptake, hence the dependence on this species with a higher error translates to greater error in SO_2. Ultimately in the chemistry, all the sulfur emissions will result in loss through deposition or as sulfate aerosol, hence a relatively low error in this species compared to SO_2.

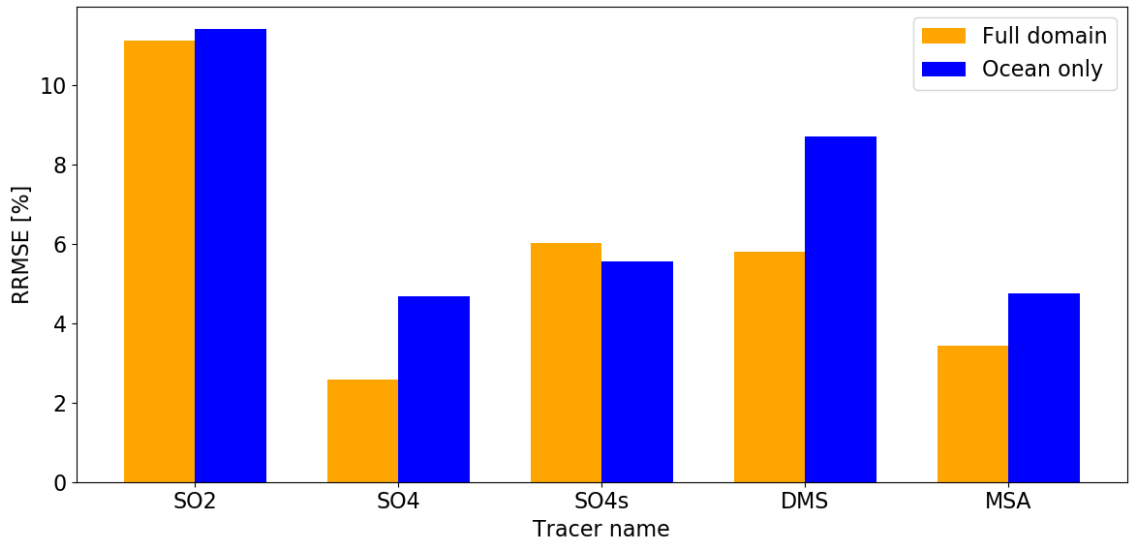

Figure 69: Average surface RRMSE, between 4°x5° and 0.5°x0.625°, of sulfur containing species across whole domain (orange) and above ocean only (blue) for sulfur dioxide (SO2), sulfate (SO4), sulfate on seasalt aerosol (SO4s), dimethylsulfide (DMS), and Methanesulfonic acid (MSA).

Finally, a selection of halogen tracers from GEOS-Chem are shown in figure 70. Error between spatial resolutions for iodine species are comparatively very low to bromine and chlorine species, including iodine species containing bromine or chlorine. The primary difference between iodine and the other halogens is the inorganic emissions (which represent the majority of emissions for all three species) of I_2 and HOI from the ocean rather from ocean emissions of seasalt aerosol, which is the case for chlorine and bromine. Resolution independent emissions for seasalt are used in this model (section 5.3), and relatively low error is present for sea salt aerosol (figure 71), however much larger errors are present for bromine sea salt aerosol species in the model which is likely the cause of errors in bromine. It is not known why this is the case.

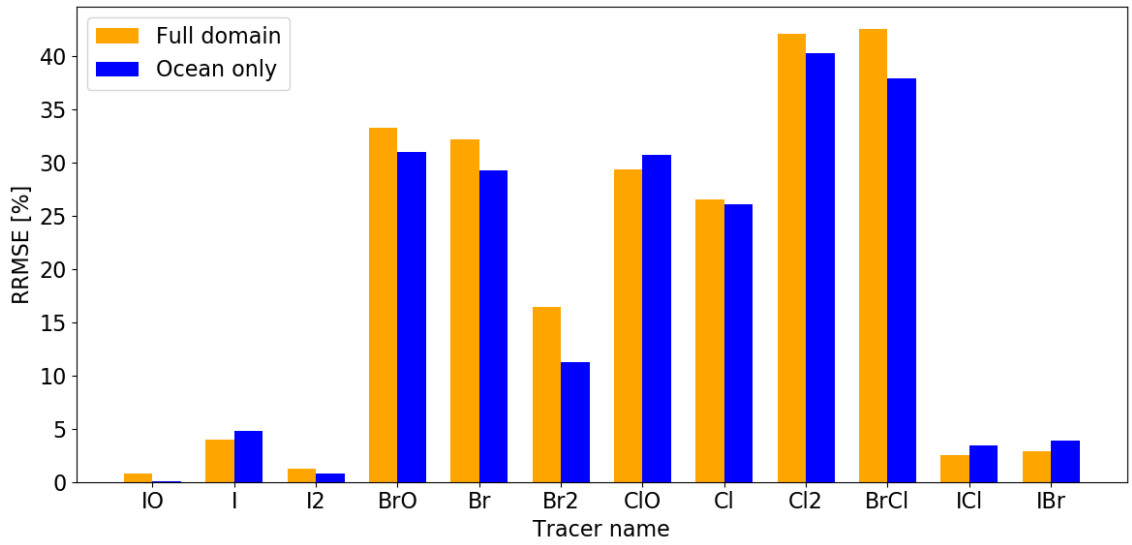

Figure 70: Average surface RRMSE, between 4°x5° and 0.5°x0.625°, of halogen species across whole domain (orange) and above ocean only (blue) for iodine monoxide (IO), iodine (I, I2), bromine monoxide (BrO), bromine (Br,Br2), chlorine monoxide (ClO), chlorine (Cl, Cl2), bromine chloride (BrCl), iodine chloride (ICl), and iodine bromide (IBr).

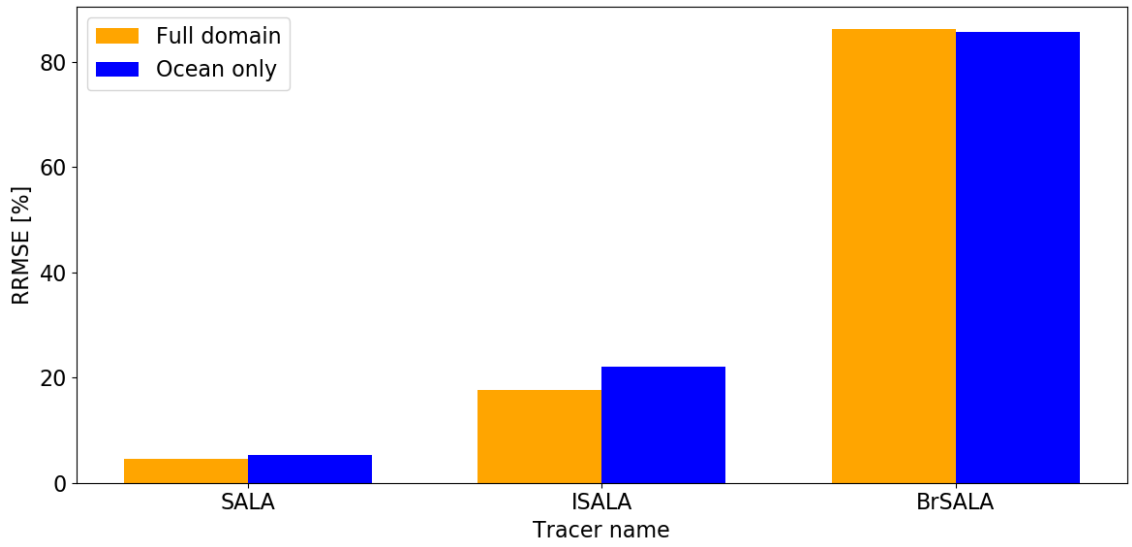

Figure 71: Average surface RRMSE, between 4°x5° and 0.5°x0.625°, of sea salt aerosol species across whole domain (orange) and above ocean only (blue) for fine sea salt aerosol (SALA), fine sea salt iodine (ISALA), and fine sea salt bromine (BrSALA).

5.6.1 Summary of quantifying differences between spatial resolutions

Key atmospheric oxidants show little sensitivity to resolution with errors of $< 1\%$ for OH and $< 3\%$ for O_3. Species with a lifetime large enough to be transported out of the grid box of emission, but short enough that steep gradients in mixing ratio exist are most susceptible to large differences between resolutions. Tracers

with longer lifetimes (such as CO) do not have the steep gradients in mixing ratio, equally tracers with very short lifetimes and steep gradients in mixing ratio (such as isoprene) are too short lived for effective transport away from emission source. These species have an error between spatial resolution similar to that of the oxidants OH and O_3. As reactions that a species depend on increase, so does their error as this compounds through the chain of chemical reactions of species, as demonstrated by NOy. SO_4 or loss to deposition is the end result of sulfur emitted into the model, as such SO_4 has much less error despite larger errors in primary species, as ultimately across the region the same total will be produced. Large errors are present for bromine and chlorine species in the model, this is likely due to large errors in the sea salt aerosol precursors, although the reason behind this is unknown.

5.7 Comparing low spatial resolution model predictions to observational data

Here the assessment of the importance of local emissions at different resolutions for ethene and propene is made (for the model setup described in 4). The observations made at CVAO are quality controlled to avoid any observation footprint containing local emissions, filtering for wind direction and flagging any data that may not meet the requirements of a true measurement of the background of the region.

To evaluate which spatial resolution for a global model run was most representative of the air mass observed at CVAO, three global model runs for the first six months of 2017 are run, each at different resolutions. The region around CVAO with the surface grid boxes for each resolution overlaid are shown in figure 72. The first two resolutions are the standard global spatial resolutions available in GEOS-Chem, 4°x5°, 2°x2.5° and 1°x1.25° is achieved using flexgrid. All three model runs use the emissions settings and meteorology described in section 4.2.

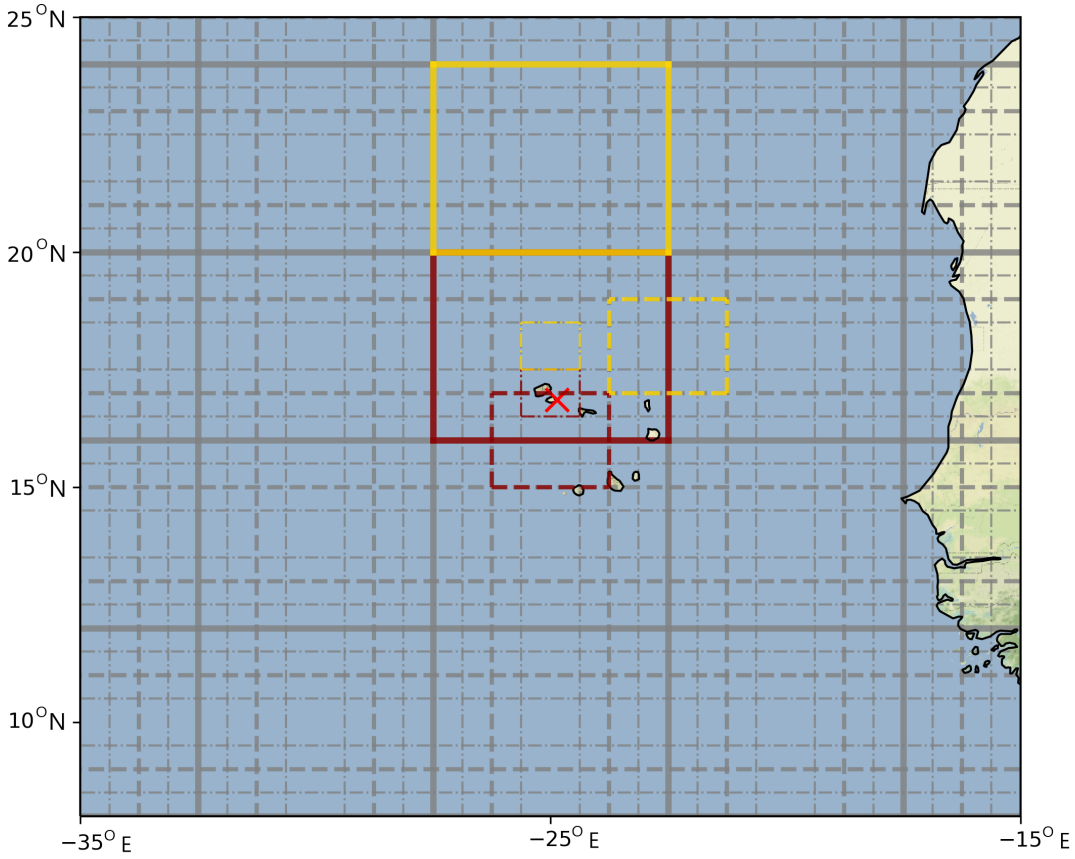

Figure 72: Local region surrounding CVAO (marked with red cross) with surface grid boxes for three model resolutions marked on, 4°x5° (solid line), 2°x2.5° (dashed line), and 1°x1.25° (dotted dashed line). Grid box over CVAO are marked with red edges. Grid box selected as most representative of CVAO observed airmass are marked with yellow edges.

Average surface mixing ratios for ethene and propene for the first six months of 2017 at 4°x5°, 2°x2.5°, and 1°x1.25° are shown in figure 73. Whilst all of the resolutions have similar features, a much more structured picture emerges as resolution increases. The most notable example of this is ethene at 1x1.25 where a distinct plume is now visible from Cape Verde, which is not the case in the coarser resolutions. The effects of local emissions becomes increasingly dominant for the model box containing CVAO as the resolution increases. This effect is most visible in propene where the 1°x1.25° grid box containing CVAO is now dominated by the local emissions from the islands in the grid box and is not representative of the marine background air mass that is observed at CVAO.

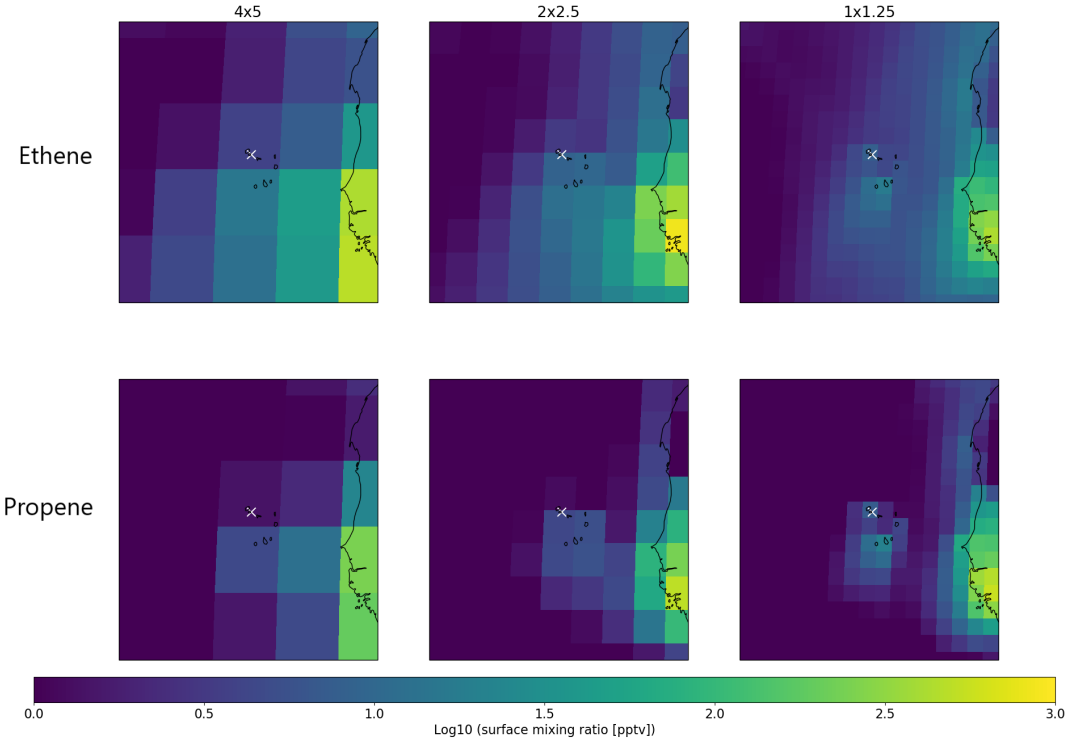

Figure 73: Log10 of the average surface mixing ratio from 2017-01-01 to 2017-07-01 for ethene and propene across three different model spatial resolutions (4°x5°, 2°x2.5°, and 1°x1.25°). The white cross marks the location of CVAO.

Whilst local anthroprogenic and biogenic emissions from Cape Verde islands are relatively small compared to cities and heavily forested areas, their low mixing ratios in marine air result in an increased effect. Local emissions become increasingly important for the model grid box containing CVAO as spatial resolution is increased. The larger volume of coarse resolution grid boxes (such as 4°x5°) mitigate to some extent the effect of local emissions from Cape Verde islands due to the percentage of the grid box surface representing land being much lower than that of higher resolutions (such as 2°x2.5° and 1°x1.25°). Furthermore the placement of grid boxes at each resolution will also impact the percentage of the surface grid box that is land. As shown in figure 73, 2°x2.5° and 1°x1.25° are affected by local emissions and become less representative of the marine airmass that is observed by CVAO. This is demonstrated in average model diurnal and timeseries at each resolution of the grid box directly over CVAO, figures 74 and 75.

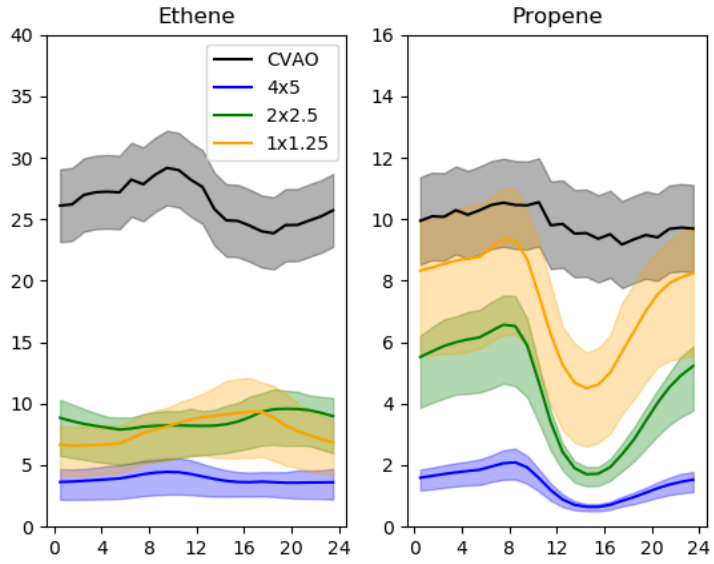

Figure 74: Average diurnal from 2017-01-01 to 2017-07-01 for ethene (left) and propene (right). Observations at CVAO (black), with shaded region representing average two sigma standard deviation. Model values taken from surface grid box containing CVAO at each resolution with shaded region representing 25^{th} - 75^{th} percentiles.

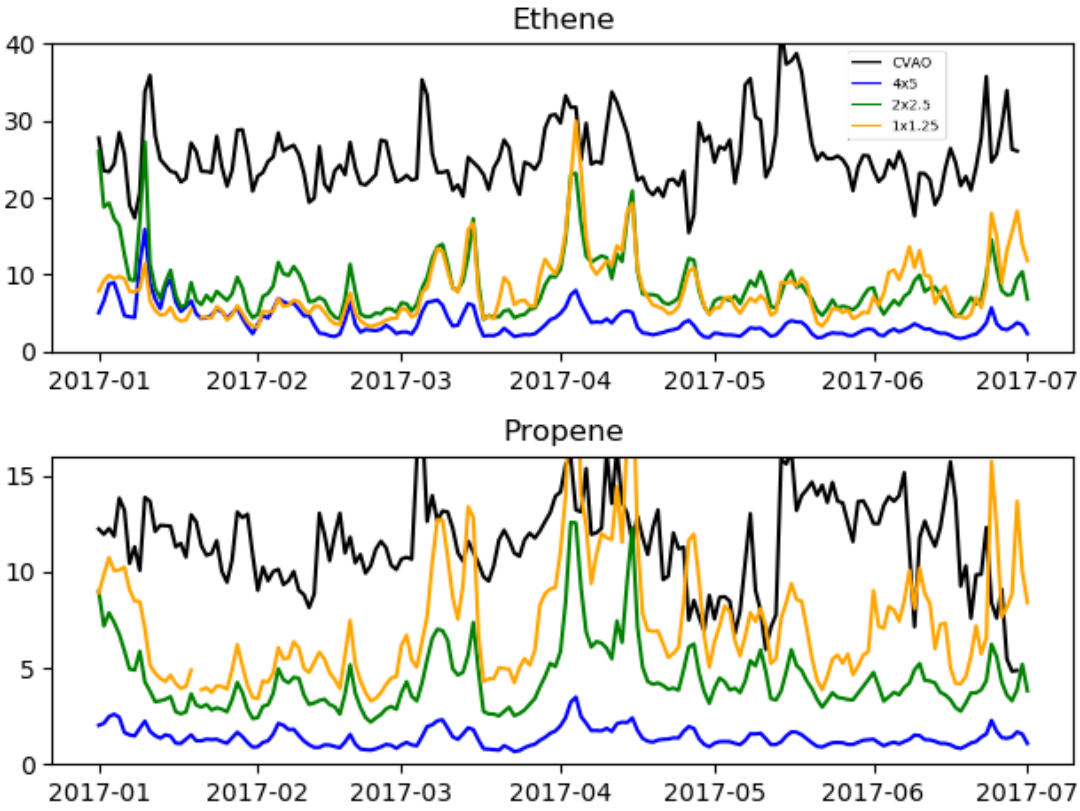

Figure 75: Daily average timeseries for ethene (top) and propene (bottom). Observations at CVAO (black). Model values taken from surface grid box containing CVAO.

5.7.1 Comparisons between resolutions for the CVAO region

As resolution increases, the ratio of island to ocean in the grid box over CVAO also increases. This results in the CVAO model grid box at higher resolutions experiencing greater land influence. An alternative to using the grid box containing the observations is to select a grid box near the observations that does not contain the islands. For 1°x1.25° this is a trivial process as by shifting one box north results in a grid box that contains no land but will be subject to the same meteorological conditions. This grid box is marked in yellow on figure 72.

Using this shifted 1°x1.25° grid box as the point of comparison, correlation plots for grid boxes at 2°x2.5° are shown in figure 76 and 4°x5° are shown in figure 77. The 2°x2.5° grid box containing CVAO is biased high compared to the 1°x1.25° reference box, this bias is reduced by shifting the grid box N. However a high bias remains due to a small portion of the Cape Verde islands being present in this grid box. The grid box north east of CVAO at 2°x2.5° has the best correlation with the 1°x1.25° reference box and contains none one the Cape Verde islands. At 4°x5°, the grid box containing CVAO is biased high, however to a lesser extent than the equivalent at 2°x2.5°. Shifting the comparison to the grid box north of CVAO results in a low bias compared to the 1°x1.25° reference box, however the spread in values for propene is greatly reduced. Comparing to the grid box west of CVAO at 4°x5° results in a substantially bias high without containing land, this is the result of this grid box containing the plume of emissions from the Cape Verde islands.

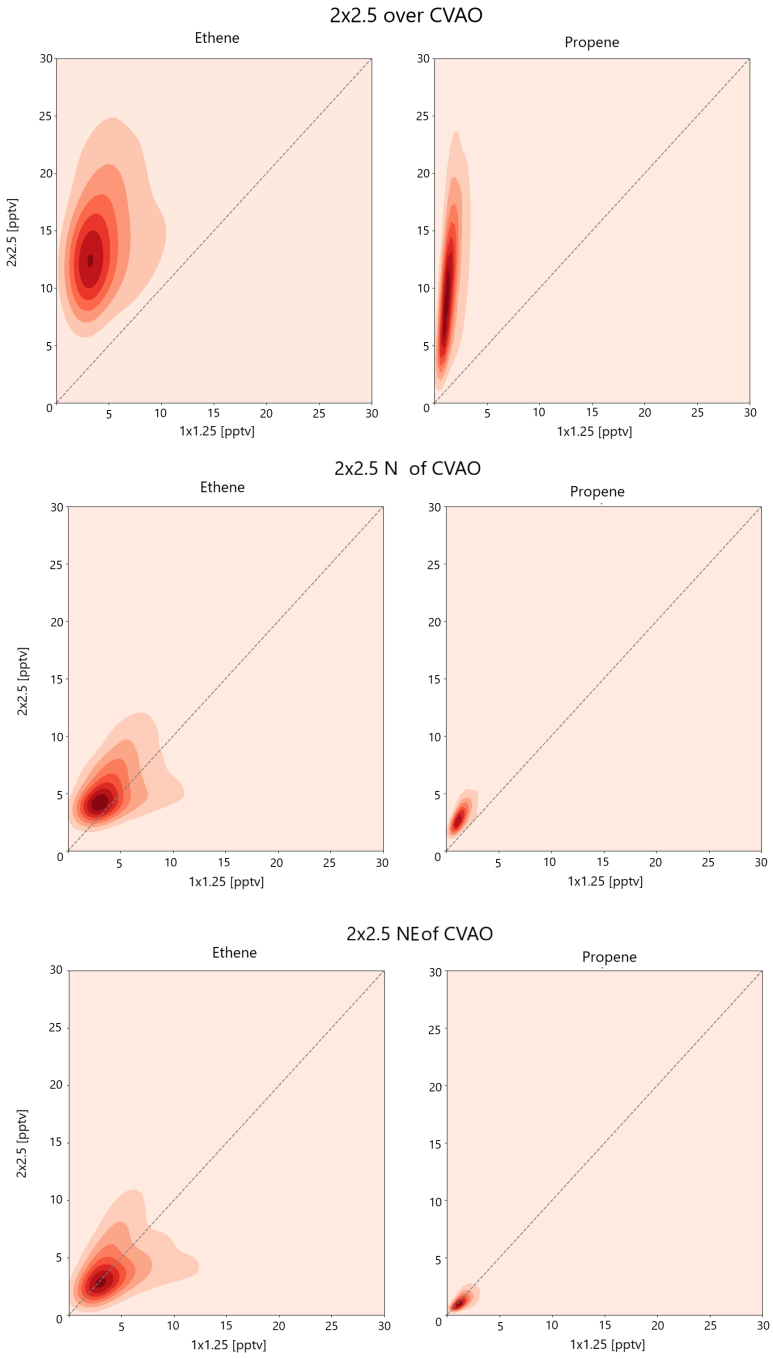

Figure 76: 2D probability density function for ethene (left column) and propene (right column) for the 2°x2.5° grid box over CVAO (top), the 2°x2.5° grid box North of CVAO (mid), the 2°x2.5° grid box north east of CVAO (bottom), and the 1°x1.25° box nearest CVAO that doesn't contain land.

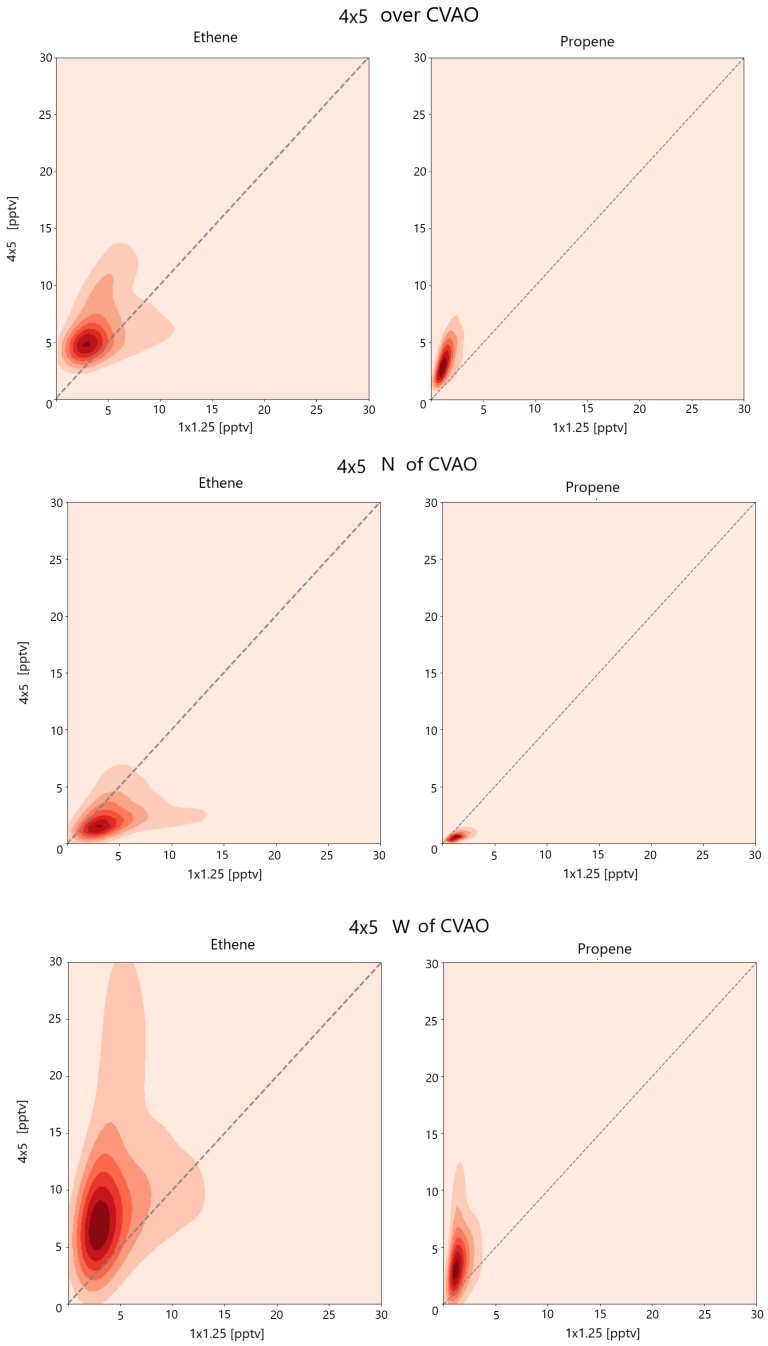

Figure 77: 2D probability density function for ethene (left column) and propene (right column) for the 4°x5° grid box over CVAO (top), the 4°x5° grid box North of CVAO (mid), the 4°x5° grid box west of CVAO (bottom), and the 1°x1.25° box nearest CVAO that doesn't contain land.

5.7.2 Comparisons of more representative model predictions at coarse resolution to observations

Reducing the effects of local anthroprogenic sources in these resolutions can be achieved by shifting the grid box used to represent CVAO. Model grid boxes marked in yellow on figure 72 were found in section 5.7.1 to be grid boxes that improved correlation between model spatial resolution by removing the influence of local island emissions. These boxes therefore are more representative of the marine background airmass observed at CVAO. Using the shifted grid boxes for average diurnal and timeseries (shown in figures 78 and 79 respectively) results in greater agreement between resolutions.

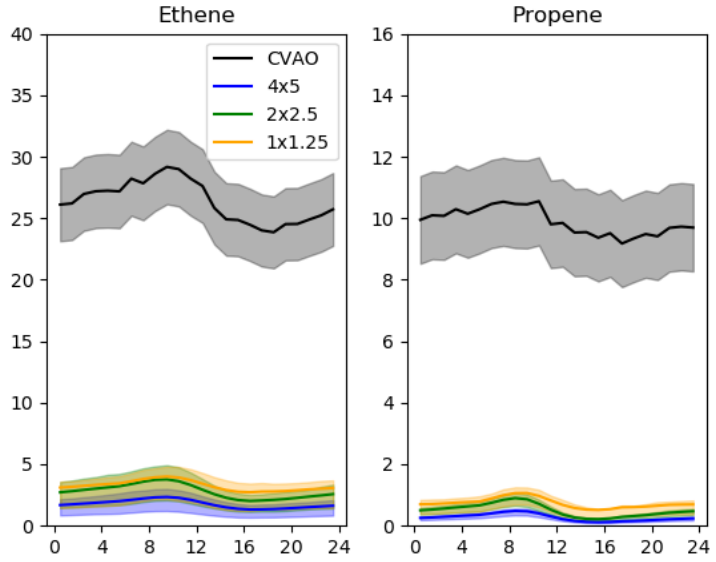

Figure 78: Average diurnal from 2017-01-01 to 2017-07-01 for ethene (left) and propene (right). Observations at CVAO (black), with shaded region representing average two sigma standard deviation. Model values taken from the grid boxes marked in yellow on figure 72 as more representative of the airmass observed at CVAO. Shaded region showing model 25^{th}-75^{th} percentiles.

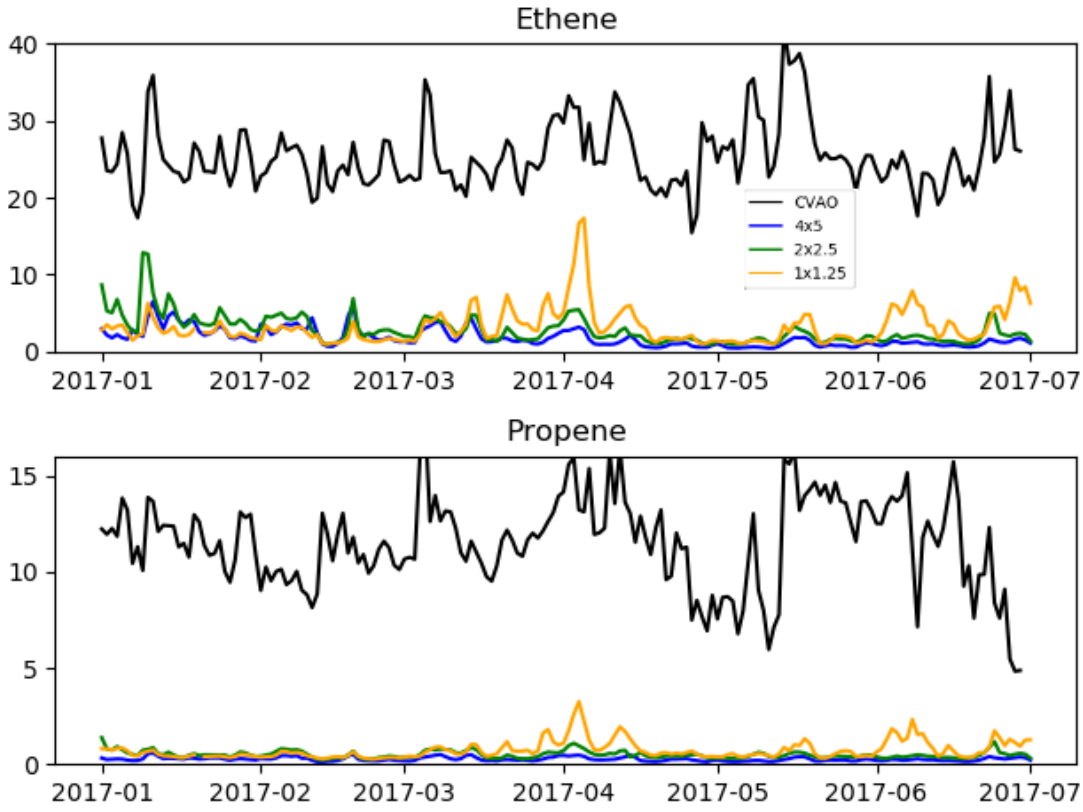

Figure 79: Daily average timeseries for ethene (top) and propene (bottom). Observations at CVAO (black). Model values taken from the grid boxes marked in yellow on figure 11 as more representative of the airmass observed at CVAO.

Using the shifted grid boxes (marked in yellow on figure 72), similar results are achieved across all resolutions meaning all could be suitable for comparisons to CVAO. There is a significant penalty to model run-time is incurred with increasing resolution, hence 2°x2.5° global resolution would be a suitable compromise as it a higher degree of structure to be represented in emissions and mixing ratios, represents the largest step difference between model spatial resolutions (as shown in section 5.5) without the more significant penalty to model run time incurred at 1°x1.25° and higher resolutions.

5.8 Summary of key findings for future model configurations

Based on the section 5.5, global model runs for analysis or publication should use a resolution no coarser than 2°x2.5°. This resolution is a direct and often substantial improvement on 4°x5° model results without the higher computational overheads of higher resolutions (1°x1.25° and higher). Table 10 recommends the spatial resolution to use for species of interest (based on results from section 5.5 and 5.6) which minimise differences between spatial resolutions whilst considering model run time incurred at higher spatial resolutions.

Using higher spatial resolution may be beneficial depending on the species considered or the aim of the model study, such as short lived trace gasses or studying plumes from specific locations. However there are significant overheads for increasing spatial resolution so assessing the most computational and time effective model spatial resolution using short trial model runs would allow for informed decisions to be made for future model analysis.

Comparisons between model predictions and observations (whether that be urban, rural or remote such as in section 5.7.1), considerations should be made for the composition of the grid box and its contents at that spatial resolution compared to the observed air-mass and conditions. The most representative grid box for the observational data-set may not be the model grid box that is over the observations but rather one that better represents the conditions of the observations (such as air-mass) or local emissions.

Table 10: Recommendations on appropriate model spatial resolution for model species analysed in section 5.5

Species	Recommended global resolution
OH	4°x5°
O_3	2°x2.5°
NO_x	1°x1.25°
Alkenes	1°x1.25°
Alkanes	2°x2.5°
Dust	2°x2.5°
DMS	2°x2.5°
SO_2	2°x2.5°
Ammonia	1°x1.25°
Nitrate	1°x1.25°
Sulfate	4°x5°

5.9 Conclusions

Idealised tracers show that in a nested domain all spatial resolutions share a common initialisation time of $\sim$10 days, and there is no bias caused by emissions. Error between spatial resolutions can be seen to be caused by transport and vertical mixing. At certain times, representation of distinct meteorological events can further increase differences. Transport and convection can contribute to differences of $\sim$10% between low (4°x5°) and high (0.5°x0.625°) spatial resolutions.

The representation of point sources and their plumes is highly dependent on model spatial resolution. For idealised tracers, differences between spatial resolutions grow as chemical lifetime decreases, hence species with shorter lifetimes ($\sim$1 hour) should be the most dependent on model spatial resolution. For idealised chemical tracers it can be also noted that as spatial resolution is increases the difference between the resolutions decreases, implying predictions will converge eventually although higher resolution model runs would be needed to verify this. For the wet deposition idealised tracers, not only is their some spatial resolution dependence present but also unexpected behaviour of domain averages exceeding the only source of the tracers. It is unknown if this behaviour also applies to other aerosol species in the model that also wet deposit and if so to what

extent the difference observed in aerosol species is derived from this.

Across the domain, species with strong gradients are susceptible to errors between resolutions. In marine environments this is most notable along shipping lanes, coastal regions and the ITCZ. Model predictions for aerosol display largest differences around coasts, apart from dust where transport from/near the boundary conditions is a large source of uncertainty. Representation of extremely low mixing ratios for species such as propene and NO_x in the clean marine boundary layer are also regions where model predictions have large percentage differences.

The increase in spatial resolution from 4°x5° to 2°x2.5° is the greatest single difference between spatial resolutions for almost all species in the model. Hence 2°x2.5° resolution model runs should be considered as the default for model runs to mitigate the larger differences that are found between 4°x5° and higher resolutions.

When transport time across a model grid box and species lifetime are approximately equal, the largest errors occur. In the conditions around CVAO at 4°x5° ALK4 and SO_2 approximately meet these conditions and have large errors, however this is a function of both species, transport time and lifetime hence should be considered for each model configurations.

The complex relationship between resolution based error and VOC species could be further explored with further idealised tracers with emissions within the domain like existing VOC species (such as ALK4 or aromatics) but with a range of specified lifetimes. This would allow for a definitive test of the hypothesis of increased error when atmospheric lifetime and transport timescales are similar, and could also be used to further explore the differences between error trends found in aromatic species compared to other VOC's.

There is small (0.5-3%) differences between spatial resolutions for key tropospheric oxidising species. Species that are the result of an oxidation reaction in the troposphere show higher variability between spatial resolution with this compounding with further oxidation reactions. Species that are a termination point in a chain of reactions (such as sulfate aerosol) present less spatial resolution dependence than species earlier in the chain. Bromine and chlorine species show very high spatial resolution dependence, whereas iodine species do not. These species however do not have resolution dependent emission. It is currently unclear why that may be the case.

Comparisons between model predictions and observation in marine environments should consider the contents of the model gridbox in relation to the observations and their airmass. Local emissions have greater impacts at high spatial resolutions for short lived atmospheric species. The large volume of coarse spatial resolutions mitigate this to some extent as local emissions make up a small percentage of the total volume, when compared to higher resolutions. However, moving the model box spatially away from the observatory, results in differences between model spatial resolutions decreasing. Hence the best model gridbox for making comparisons to remote observations, may not be the model gridbox that contains the location of those observations.

Considerations for error in model predictions from spatial resolution are important in marine environments where steep gradients exist because of local of shipping emissions, transitions from coastal to open ocean, meteorological convection zones such as the ITCZ, and transport across the model gridbox and species lifetime are approximately equal. Future developments in model spatial resolution that may be relevant to these findings are discussed in section 6.2.

6 Improving ocean-atmosphere exchange in global chemistry transport models

6.1 Summary of current ocean atmosphere interactions

This work has grown our understanding of ocean-atmosphere interactions by better constraining the deposition of O_3 through a more physically representative oceanic dry deposition scheme within the GEOS-Chem model, by developing an emission inventory for oceanic ethene and propene, and by developing some understanding of the influence of resolution on numerical simulations of the marine boundary layer.

The inclusion of a more physically and chemically representative loss mechanisms for O_3 to the ocean surface improved the models ability to simulate observations and reduced the oceanic depositions sink for O_3 by $\sim$45%. This increased the tropospheric O_3 burden by $\sim$1.2% but showed more significant increases in regions above and downwind of large ocean areas.

Oceanic emissions of ethene and propene are the dominant source of these species in many ocean regions, locally increasing concentrations many fold. However, tropospheric burdens are dominated by the terrestrial biogenic and anthropogenic sources, so global burdens only increase by $\sim$9% and $\sim$6% respectively. Despite this increase, the oceanic alkene emissions have minimal effect on tropospheric oxidative capacity.

This work has also shown that resolution considerations are important for marine environments. Some species show surprisingly large sensitivity to resolution, some of which is not currently well explained. Further, this work has also shown the complexity of comparing models to observations for some species within the marine boundary layer. When considering island and coastal observatory data, carefully consideration is necessary of which model grid box to compare to the

observations if model contamination by the island itself it to be avoided.

Although chapters 3 and 4 have advanced our knowledge of ocean-atmosphere exchange they exist as separate, prescribed functions. This presents two problems. Firstly in reality these processes are linked. The distribution of iodide and organic matter (and other important species such as DMS etc) in the ocean are driven by the same physical, chemical and biological processes. The current approach doesn't provide a consistent vision of the ocean atmosphere interface. Secondly it isn't clear how efficiently this piece-wise system would allow the model to make projections into the future for a warming ocean or better understand past ocean atmosphere interactions in the context of global atmospheric chemistry. Each separate function would require changes to parameters or inputs. Improving the representation of ocean-atmosphere exchange chemistry is discussed in Section 6.3.

6.2 Future of model spatial resolution

Chapter 5 highlighted the need to consider model resolution, even in regions such as the tropical marine boundary layer which may be considered relatively uniform and thus not especially susceptible to resolution issues. The spatial resolution of atmospheric chemistry models has increased (grid boxes have gotten smaller) over the decades. Increasing computer power allows for models with ever more complex physical, chemical and biological process representation to be run at higher spatial resolutions. Global simulations at 12.5km resolution now able to be produced for demonstration purposes (Hu et al., 2018). However, running at these resolutions globally is beyond the resources of most University computer facilities.

The work here used a nested offline approach to run higher resolution over an area of interest. This is approach is limited by the available offline meteorology.

Within the GEOS-Chem system, this is currently limited to the available offline 0.25°x0.3125° meteorology from the GEOS-FP system (Molod et al., 2012). Going to higher resolutions within that framework isn't possible.

Recent work has coupled the GEOS-Chem (GC) chemistry, emissions and deposition with the online weather research forecast (WRF) model (WRF-GC) (Lin et al., 2020; Feng et al., 2021). This online coupling allows for multiple layers of nested regions to be defined to reach the a model spatial resolution of 5km x 5km with WRF ultimately allowing for resolutions of as little as 1km x 1 km. This enhances the current nesting capacity within the model, allowing for very high resolution runs to capture increasingly fine structures associated with the ship plume, island emissions, convective processes etc inherent in the marine boundary layer. This approach may be able to provide case studies and understanding of processes within the marine boundary layer which are currently unavailable to the standard version of GEOS-Chem.

Achieving higher resolution of the model globally will require the use of more computationally capable platforms. A new version of the model, which allows for MPI as well as openMP message passing between computer cores provides some scope for this. GEOS-Chem High Performance (GCHP, Eastham et al. (2018)) has been designed to operate on massively parallel computing architectures allowing for increased model complexity and spatial resolution, without substantial increasing model runtime. The largest change made in GCHP is the implementation of the cubed-sphere spatial grid (Putman and Lin, 2007) which allows for greater accuracy and computational efficiency in simulating transport. Another interesting capacity of the cubed-sphere grid (Bindle et al., 2020) is the ability to apply stretch factors to the grid, increasing spatial resolution on one face of the cubed-sphere and decreasing spatial resolution on the opposite side of the grid. This allows for regions of interest to be studied in high spatial resolution (such as was the case of using a nested domain in chapter 5) but with the model

running globally. This would allow for increased spatial resolution in regions that are of interested and reduced resolution in those which are not. Comparisons between field observations and model predictions could be greatly enhanced by this development.

6.3 Alternative methods for representing ocean-atmosphere exchange

The representation of ocean-atmosphere exchange in offline chemistry transport models has often been a piecemeal approach, with modules being added on in an ad-hoc manner and without the necessity of internal consistency.

Earth system and climate models (such as SOCOLv4, Sukhodolov et al. (2021)) explicitly include the ocean by coupling ocean models with existing atmospheric model. In SOCOLv4, the representation of the ocean includes vertical mixing, horizontal transport and sea ice coverage of the ocean from the Max Planck Institute for meteorology coupled atmosphere–ocean general circulation model (MPIOM, Jungclaus et al. (2006, 2013), as well as biological and chemical processes within the water column are from the Hamburg ocean carbon cycle model (HAMOCC, Ilyina et al. (2013)). Although this allows for a fully interactive ocean-atmosphere coupling, uncertainties in ocean chemistry and biology still mean that marine emissions of trace gases are currently prescribed within the model rather than using those calculated by the coupled system.

There still remains a problem with this approach. Oceanic emissions and depositions (as discussed in chapters 1,3,4) occur at the ocean-atmosphere interface through the ocean surface microlayer. This layer is very much thinner than the top most level used in an ocean transport model. Hence coupling a full oceanic model into CTMs for the purpose of representing ocean-atmosphere exchange would not be efficient. Implementing an explicit treatment for the ocean surface microlayer to capture the chemical, physical and biological processes

mediating ocean-atmosphere exchange with a more simplistic treatment for bulk ocean might be a better way forwards.

One way to represent the ocean surface is with a two layer model, as described by (Liss and Slater, 1974). This system consists of a gas film and a liquid film either side of the ocean atmosphere interface with molecular diffusion between the two. The ocean surface below and atmosphere above their respective films are assumed to be well mixed. Whilst this is adequate for some species, the approach fails to capture observations for other species with more complex ocean-atmosphere interactions such as acetone (Marandino et al., 2005).

Cen-Lin and Tzung-May (2013) propose a three layer model for ocean-atmosphere exchange of VOCs, with a focus on acetone. This structure describes a gas film between the marine boundary layer and the ocean surface microlayer and a liquid film between the ocean surface microlayer and bulk ocean. Through the gas and liquid film molecular diffusion occurs between the layers. In the ocean surface microlayer physical, chemical and biological processes occur which lead to production or loss of species. Predictions for air-sea fluxes of acetone made using this three layer scheme are half that of predictions made using two layer models. However the calculations were highly sensitive to biological and photochemical properties of the surface microlayer, with flux direction reversing under some circumstances as is the case with observations.

Future work on ocean-atmosphere exchange within a CTM should focus a consistent treatment of the emissions and deposition from and to the ocean surface. They are currently treated as separate systems but they are in fact a coupled system. Figure 80 shows a proposed schematic of a 3 layer system with atmosphere (in this case the marine boundary layer [MBL]), ocean surface microlayer (sml) and bulk ocean layers. As is currently the case in the model transport, chemistry and photolysis will exist in the atmosphere. Mixing between the MBL

and ocean surface will be controlled by molecular diffusion, which can include the effects of surfactants (Goldman et al., 1988; Donaldson and Vaida, 2006). In the surface microlayer (SML), chemistry and photolysis will also occur. Additionally, the depth of the SML ranges between 1-1000 μm (Donaldson and Vaida, 2006) depending on turbulence caused by wind and chemical composition Cunliffe et al. (2013). The bulk ocean will also act as a reservoir for oceanic species (such as I^-) as well as loss of atmospheric species and products of reactions in SML to the ocean, mixing between these layers can also be controlled by molecular diffusion. The concentration of compounds such as DMS, iodide, and organics etc can be constrained in the bulk ocean from observed climatology's or bio-geo-chemical ocean models. Combining this with an ability to represent the oxidation chemistry within in the SML would allow for the emission of compounds such as I_2, HOI, alkenes, and oxygenates, with the deposition of species like O_3 to the ocean surface. Overall the development of an air-sea exchange scheme in a chemistry transport model should allow for a consistent representation of these important processes.

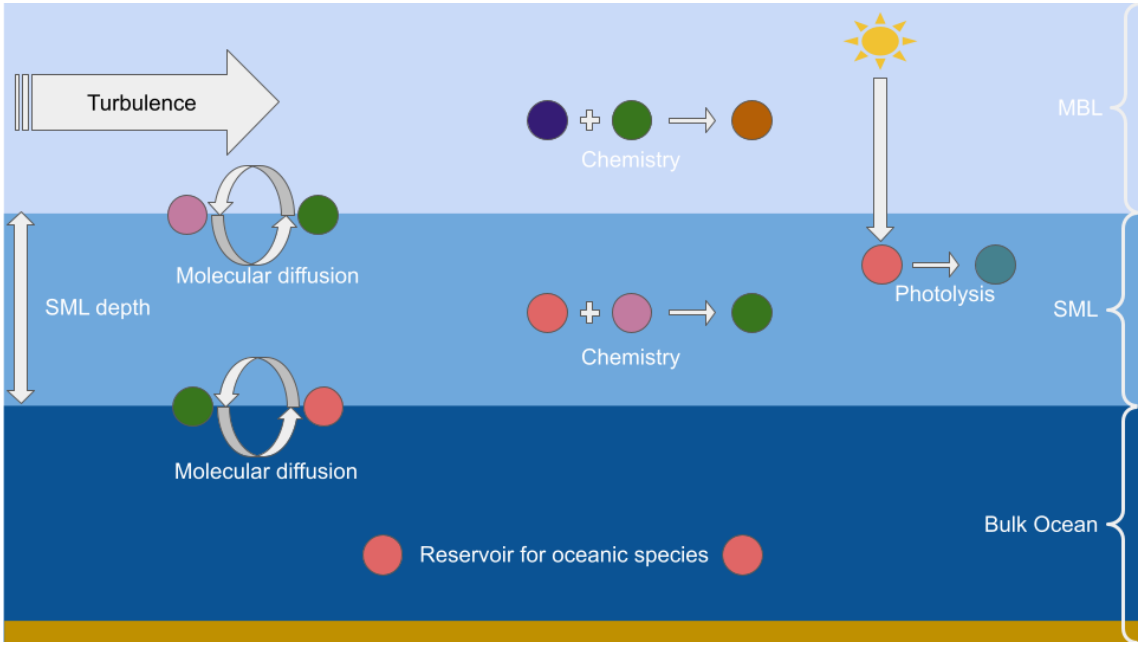

Figure 80: Proposed three layer system to couple oceanic emissions and depositions to represent the physical, chemical and biological processes at the ocean-atmosphere interface.

References

AMOF: Cape Verde Atmospheric Observatory (CVAO), URL https://amof.ac.uk/observatory/cape-verde-atmospheric-observatory-cvao/, the Atmospheric Measurement and Observation Facility, 2021.

Amos, H. M., Jacob, D. J., Holmes, C. D., Fisher, J. A., Wang, Q., Yantosca, R. M., Corbitt, E. S., Galarneau, E., Rutter, A. P., Gustin, M. S., Steffen, A., Schauer, J. J., Graydon, J. A., Louis, V. L. S., Talbot, R. W., Edgerton, E. S., Zhang, Y., and Sunderland, E. M.: Gas-particle partitioning of atmospheric Hg(II) and its effect on global mercury deposition, Atmospheric Chemistry and Physics, 12, 591–603, https://doi.org/10.5194/acp-12-591-2012, 2012.

Andersen, S. T., Carpenter, L. J., Nelson, B. S., Neves, L., Read, K. A., Reed, C., Ward, M., Rowlinson, M. J., and Lee, J. D.: Long-term NO_x measurements in the remote marine tropical troposphere, Atmospheric Measurement Techniques, 14, 3071–3085, https://doi.org/10.5194/amt-14-3071-2021, URL https://amt.copernicus.org/articles/14/3071/2021/, 2021.

Andreae, M. O. and Crutzen, P. J.: Atmospheric Aerosols: Biogeochemical Sources and Role in Atmospheric Chemistry, Science, 276, 1052–1058, https://doi.org/10.1126/science.276.5315.1052, 1997.

Archibald, A. T., O'Connor, F. M., Abraham, N. L., Archer-Nicholls, S., Chipperfield, M. P., Dalvi, M., Folberth, G. A., Dennison, F., Dhomse, S. S., Griffiths, P. T., Hardacre, C., Hewitt, A. J., Hill, R. S., Johnson, C. E., Keeble, J., Köhler, M. O., Morgenstern, O., Mulcahy, J. P., Ordóñez, C., Pope, R. J., Rumbold, S. T., Russo, M. R., Savage, N. H., Sellar, A., Stringer, M., Turnock, S. T., Wild, O., and Zeng, G.: Description and evaluation of the UKCA stratosphere–troposphere chemistry scheme (StratTrop vn 1.0) implemented in UKESM1, Geoscientific Model Development, 13, 1223–1266, https://doi.org/10.5194/gmd-13-1223-2020, URL https://gmd.copernicus.org/articles/13/1223/2020/, 2020.

Arnold, S. R., Spracklen, D. V., Williams, J., Yassaa, N., Sciare, J., Bonsang, B., Gros, V., Peeken, I., Lewis, A. C., Alvain, S., and Moulin, C.: Evaluation of the global oceanic isoprene source and its impacts on marine organic carbon aerosol, Atmospheric Chemistry and Physics, 9, 1253–1262, https://doi.org/10.5194/acp-9-1253-2009, URL https://acp.copernicus.org/articles/9/1253/2009/, 2009.

Arunachalam, S., Holland, A., Do, B., and Abraczinskas, M.: A quantitative assessment of the influence of grid resolution on predictions of future-year air quality in North Carolina, USA, Atmospheric Environment, 40, 5010–5026, https://doi.org/https://doi.org/10.1016/j.atmosenv.2006.01.024, URL https://www.sciencedirect.com/science/article/pii/S1352231006001117, 2006.

Atkinson, R.: Atmospheric chemistry of VOCs and NOx, Atmospheric Environment, 34, 2063–2101, https://doi.org/https://doi.org/10.1016/S1352-2310(99)00460-4, 2000.

Atkinson, R. and Arey, J.: Atmospheric Degradation of Volatile Organic Compounds, Chemical Reviews, 103, 4605–4638, https://doi.org/10.1021/cr0206420, URL https://doi.org/10.1021/cr0206420, pMID: 14664626, 2003.

Ayers, G. and Gillett, R.: DMS and its oxidation products in the remote marine atmosphere: implications for climate and atmospheric chemistry, Journal of Sea Research, 43, 275–286, https://doi.org/https://doi.org/10.1016/S1385-1101(00)00022-8, 2000.

Bacastow, R. B., Keeling, C. D., and Whorf, T. P.: Seasonal amplitude increase in atmospheric CO2 concentration at Mauna Loa, Hawaii, 1959–1982, Journal of Geophysical Research: Atmospheres, 90, 10 529–10 540, https://doi.org/https://doi.org/10.1029/JD090iD06p10529, 1985.

Bariteau, L., Helmig, D., Fairall, C. W., Hare, J. E., Hueber, J., and Lang, E. K.: Determination of oceanic ozone deposition by ship-borne eddy covariance

flux measurements, ATMOS MEAS TECH, 3, 441–455, https://doi.org/10.5194/amt-3-441-2010, URL https://www.atmos-meas-tech.net/3/441/2010/, 2010.

Barletta, B., Biggs, B., Blake, D., Blake, N., Hoffman, A., Hughes, S., Meinardi, S., Vieznor, N., and Woods, C.: ATom: L2 Halocarbons and Hydrocarbons from the UC-Irvine Whole Air Sampler (WAS), https://doi.org/10.3334/ORNLDAAC/1751, URL https://daac.ornl.gov/cgi-bin/dsviewer.pl?ds_id=1751, 2019.

Bates, K. H., Jacob, D. J., Wang, S., Hornbrook, R. S., Apel, E. C., Kim, M. J., Millet, D. B., Wells, K. C., Chen, X., Brewer, J. F., Ray, E. A., Commane, R., Diskin, G. S., and Wofsy, S. C.: The Global Budget of Atmospheric Methanol: New Constraints on Secondary, Oceanic, and Terrestrial Sources, Journal of Geophysical Research: Atmospheres, 126, https://doi.org/https://doi.org/10.1029/2020JD033439, 2021.

Behera, S., Sharma, M., Aneja, V., and Balasubramanian, R.: Ammonia in the atmosphere: a review on emission sources, atmospheric chemistry and deposition on terrestrial bodies, Environmental Science and Pollution Research, 20, 8092–8131, https://doi.org/10.1007/s11356-013-2051-9, 2013.

Bey, I., Jacob, D. J., Yantosca, R. M., Logan, J. A., Field, B. D., Fiore, A. M., Li, Q., Liu, H. Y., Mickley, L. J., and Schultz, M. G.: Global modeling of tropospheric chemistry with assimilated meteorology: Model description and evaluation, J GEOPHYS RES-ATMOS, 106, 23 073–23 095, https://doi.org/10.1029/2001JD000807, 2001.

Bian, H. and Prather, M.: Fast-J2: Accurate Simulation of Stratospheric Photolysis in Global Chemical Models, Journal of Atmospheric Chemistry, 41, 281–296, https://doi.org/https://doi.org/10.1023/A:1014980619462, 2002.

Bindle, L., Martin, R. V., Cooper, M. J., Lundgren, E. W., Eastham, S. D., Auer, B. M., Clune, T. L., Weng, H., Lin, J., Murray, L. T., Meng, J., Keller, C. A., Pawson, S., and Jacob, D. J.: Grid-Stretching Capability for the GEOS-Chem 13.0.0 Atmospheric Chemistry Model, Geoscientific Model Development

Discussions, 2020, 1–21, https://doi.org/10.5194/gmd-2020-398, URL https://gmd.copernicus.org/preprints/gmd-2020-398/, 2020.

Bongsang, B., Kanakidou, M., Lambert, G., and Monfray, P.: The Marine Source of C_2-C_6 Aliphatic Hydrocarbons, Journal of Atmospheric Chemistry, 6, 3–20, 1988.

Bongsang, B., Kanakidou, M., and Lambert, G.: NMHC in the Marine Atmosphere: Preliminary Results of Monitoring at Amsterdam Island, Journal of Atmospherie Chemistry, 11, 169–178, 1990.

Bouwman, A., Lee, D., Asman, W., Dentener, F., an Der Hoek, K., and Olivier, J.: A global high-resolution emission inventory for ammonia, Global Biogeochem. Cycles, 11(4), 561–587, 1997.

Breider, T. J., Mickley, L. J., Jacob, D. J., Ge, C., Wang, J., Payer Sulprizio, M., Croft, B., Ridley, D. A., McConnell, J. R., Sharma, S., Husain, L., Dutkiewicz, V. A., Eleftheriadis, K., Skov, H., and Hopke, P. K.: Multidecadal trends in aerosol radiative forcing over the Arctic: Contribution of changes in anthropogenic aerosol to Arctic warming since 1980, Journal of Geophysical Research: Atmospheres, 122, 3573–3594, https://doi.org/https://doi.org/10.1002/2016JD025321, 2017.

Broadgate, W. J., Liss, P. S., and Penkett, S. A.: Seasonal emissions of isoprene and other reactive hydrocarbon gases from the ocean, Geophysical Research Letters, 24, 2675–2678, 1997.

Canosa-Mas, C. E., Smith, S. J., Waygood, S. J., and Wayne, R. P.: -, J. Chem. Soc. Faraday Trans., 87, 1991.

Carpenter, L., Fleming, Z., Read, K., Lee, J. D., Moller, S. J., Hopkins, J. R., Purvis, R. M., Lewis, A. C., Müller, K., Heinold, B., Herrmann, H., Fomba, K. W., van Pinxteren, D., Müller, C., Tegen, I., Wiedensohler, A., Müller, T., Niedermeier, N., Achterberg, E. P., Patey, M. D., Kozlova, E. A., Heimann, M., Heard, D. E., Plane, J. M. C., Mahajan, A., Oetjen, H., Ingham, T., Stone,

D., Whalley, L. K., Evans, M. J., Pilling, M. J., Leigh, R. J., Monks, P. S., Karunaharan, A., Vaughan, S., Arnold, S. R., Tschritter, J., Pöhler, D., Frieß, U., Holla, R., Mendes, L. M., Lopez, H., Maria, B., Manning, A. J., and Wallace, D. W. R.: Seasonal characteristics of tropical marine boundary layer air measured at the Cape Verde Atmospheric Observatory, J Atmos Chem, 67, 87–140, https://doi.org/https://doi.org/10.1007/s10874-011-9206-1, 2010.

Carpenter, L., MacDonald, S., Shaw, M., Kumar, R., Saunders, R., Parthipan, R., Wilson, J., and Plane, J.: Atmospheric iodine levels influenced by sea surface emissions of inorganic iodine, NAT GEOSCI, 6, 108–111, https://doi.org/10.1038/ngeo1687, 2013.

Carpenter, L. J., Chance, R. J., Sherwen, T., Adams, T. J., Ball, S. M., Evans, M. J., Hepach, H., Hollis, L. D. J., Hughes, C., Jickells, T. D., Mahajan, A., Stevens, D. P., Tinel, L., and Wadley, M. R.: Marine iodine emissions in a changing world, Proceedings of the Royal Society A: Mathematical, Physical and Engineering Sciences, 477, 20200 824, https://doi.org/10.1098/rspa.2020.0824, URL https://royalsocietypublishing.org/doi/abs/10.1098/rspa.2020.0824, 2021.

Cen-Lin, H. and Tzung-May, F.: Air-Sea Exchange of Volatile Organic Compounds: A New Model with Microlayer Effects, Atmospheric and Oceanic Science Letters, 6, 97–102, https://doi.org/10.1080/16742834.2013.11447063, URL https://doi.org/10.1080/16742834.2013.11447063, 2013.

Chameides, W. L. and Davis, D. D.: Iodine: Its possible role in tropospheric photochemistry, Journal of Geophysical Research: Oceans, 85, 7383–7398, https://doi.org/https://doi.org/10.1029/JC085iC12p07383, 1980.

Chance, R., Tinel, L., Sherwen, T., Baker, A., Bell, T., Brindle, J., Campos, M., Croot, P., Ducklow, H., He, P., Hoogakker, B., Hopkins, F., Hughes, C., Jickells, T., Loades, D., Macaya, D., Mahajan, A., Malin, G., Phillips, D., Sinha, A., Sarkar, A., Roberts, I., Roy, R., Song, X., Winklebauer, H., Wuttig, K., Yang,

M., Zhou, P., and Carpenter, L.: Global sea-surface iodide observations, 1967-2018, SCI DATA, 6, https://doi.org/10.1038/s41597-019-0288-y, 2019.

Chang, W., Heikes, B., and Lee, M.: Ozone deposition to the sea surface:chemical enhancement and wind speed dependence, ATMOS ENVIRON, 38, 1053–1059, https://doi.org/10.1016/j.atmosenv.2003.10.050, 2004.

Charlson, R. J., Lovelock, J. E., Andreae, M. O., and Warren, S. G.: Oceanic phytoplankton, atmospheric sulphur, cloud albedo and climate, Nature, 326, 655,661, https://doi.org/10.1038/326655a0, 1987.

Charlton-Perez, C. L., Evans, M. J., Marsham, J. H., and Esler, J. G.: The impact of resolution on ship plume simulations with NO_x chemistry, Atmospheric Chemistry and Physics, 9, 7505–7518, https://doi.org/10.5194/acp-9-7505-2009, URL https://acp.copernicus.org/articles/9/7505/2009/, 2009.

Chen, Q., Schmidt, J. A., Shah, V., Jaeglé, L., Sherwen, T., and Alexander, B.: Sulfate production by reactive bromine: Implications for the global sulfur and reactive bromine budgets, Geophysical Research Letters, 44, 7069–7078, https://doi.org/https://doi.org/10.1002/2017GL073812, 2017.

Chin, M., Rood, R. B., Lin, S.-J., Müller, J.-F., and Thompson, A. M.: Atmospheric sulfur cycle simulated in the global model GOCART: Model description and global properties, Journal of Geophysical Research: Atmospheres, 105, 24 671–24 687, https://doi.org/https://doi.org/10.1029/2000JD900384, 2000.

Chipperfield, M. P., Cariolle, D., Simon, P., Ramaroson, R., and Lary, D. J.: A three-dimensional modeling study of trace species in the Arctic lower stratosphere during winter 1989–1990, Journal of Geophysical Research: Atmospheres, 98, 7199–7218, https://doi.org/https://doi.org/10.1029/92JD02977, 1993.

Cohan, D. S., Sturrock, G. A., Biazar, A. P., and Fraser, P. J.: Atmospheric Methyl Iodide at Cape Grim, Tasmania, from AGAGE Observations, Journal of Atmospheric Chemistry, 44, 131–150, https://doi.org/https://doi.org/10.1023/A:1022481516151, 2003.

Crawford, J., Cohen, D. D., Stelcer, E., and Atanacio, A. J.: Long term fine aerosols at the Cape Grim global baseline station: 1998 to 2016, Atmospheric Environment, 166, 34–46, https://doi.org/https://doi.org/10.1016/j.atmosenv.2017.07.012, 2017.

Crippa, M., Guizzardi, D., Muntean, M., Schaaf, E., Dentener, F., van Aardenne, J. A., Monni, S., Doering, U., Olivier, J. G. J., Pagliari, V., and Janssens-Maenhout, G.: Gridded emissions of air pollutants for the period 1970–2012 within EDGAR v4.3.2, Earth System Science Data, 10, 1987–2013, https://doi.org/10.5194/essd-10-1987-2018, URL https://essd.copernicus.org/articles/10/1987/2018/, 2018.

CSIRO: Cape Grim Observatory - History, URL https://research.csiro.au/acc/capabilities/cape-grim-baseline-air-pollution-station/, 2021.

Cunliffe, M., Engel, A., Frka, S., Gašparović, B., Guitart, C., Murrell, J. C., Salter, M., Stolle, C., Upstill-Goddard, R., and Wurl, O.: Sea surface microlayers: A unified physicochemical and biological perspective of the air–ocean interface, Progress in Oceanography, 109, 104–116, https://doi.org/https://doi.org/10.1016/j.pocean.2012.08.004, URL https://www.sciencedirect.com/science/article/pii/S0079661112000924, 2013.

Damian, V., Sandu, A., Damian, M., Potra, F., and Carmichael, G. R.: The kinetic preprocessor KPP-a software environment for solving chemical kinetics, Computers and Chemical Engineering, 26, 1567–1579, https://doi.org/https://doi.org/10.1016/S0098-1354(02)00128-X, 2002.

Del Vecchio, R. and Blough, N. V.: Spatial and seasonal distribution of chromophoric dissolved organic matter and dissolved organic carbon in the Middle Atlantic Bight, Marine Chemistry, 89, 169–187, https://doi.org/https://doi.org/10.1016/j.marchem.2004.02.027, URL https://www.sciencedirect.com/science/article/pii/S0304420304000878, 2004.

Derwent, R. G., Manning, A. J., Simmonds, P. G., Spain, T. G., and O'Doherty,

S.: Long-term trends in ozone in baseline and European regionally-polluted air at Mace Head, Ireland over a 30-year period, Atmospheric Environment, 179, 279–287, https://doi.org/https://doi.org/10.1016/j.atmosenv.2018.02.024, 2018.

Donaldson, D. and Vaida, V.: The Influence of Organic Films at the Air-Aqueous Boundary on Atmospheric Processes, Chemical Reviews, https://doi.org/10.1021/cr040367c, 2006.

Druffel, E. R. M., Williams, P. M., Bauer, J. E., and Ertel, J. R.: Cycling of dissolved and particulate organic matter in the open ocean, J. Geophys. Res., 15, 659, 1992.

Duce, R. A., LaRoche, J., Altieri, K., Arrigo, K. R., Baker, A. R., Capone, D. G., Cornell, S., Dentener, F., Galloway, J., Ganeshram, R. S., Geider, R. J., Jickells, T., Kuypers, M. M., Langlois, R., Liss, P. S., Liu, S. M., Middelburg, J. J., Moore, C. M., Nickovic, S., Oschlies, A., Pedersen, T., Prospero, J., Schlitzer, R., Seitzinger, S., Sorensen, L. L., Uematsu, M., Ulloa, O., Voss, M., Ward, B., and Zamora, L.: Impacts of Atmospheric Anthropogenic Nitrogen on the Open Ocean, Science, 320, 893–897, https://doi.org/10.1126/science.1150369, 2008.

Eastham, S. D., Weisenstein, D. K., and Barrett, S. R.: Development and evaluation of the unified tropospheric–stratospheric chemistry extension (UCX) for the global chemistry-transport model GEOS-Chem, Atmospheric Environment, 89, 52–63, https://doi.org/https://doi.org/10.1016/j.atmosenv.2014.02.001, 2014.

Eastham, S. D., Long, M. S., Keller, C. A., Lundgren, E., Yantosca, R. M., Zhuang, J., Li, C., Lee, C. J., Yannetti, M., Auer, B. M., Clune, T. L., Kouatchou, J., Putman, W. M., Thompson, M. A., Trayanov, A. L., Molod, A. M., Martin, R. V., and Jacob, D. J.: GEOS-Chem High Performance (GCHP v11-02c): a next-generation implementation of the GEOS-Chem chemical transport model for massively parallel applications, Geoscientific Model Development, 11, 2941–2953, https://doi.org/10.5194/gmd-11-2941-2018, URL https://gmd.copernicus.org/articles/11/2941/2018/, 2018.

Emmons, L. K., Schwantes, R. H., Orlando, J. J., Tyndall, G., Kinnison, D., Lamarque, J.-F., Marsh, D., Mills, M. J., Tilmes, S., Bardeen, C., Buchholz, R. R., Conley, A., Gettelman, A., Garcia, R., Simpson, I., Blake, D. R., Meinardi, S., and Pétron, G.: The Chemistry Mechanism in the Community Earth System Model Version 2 (CESM2), Journal of Advances in Modeling Earth Systems, 12, https://doi.org/https://doi.org/10.1029/2019MS001882, 2020.

Evans, M., Shallcross, D., Law, K., Wild, J., Simmonds, P., Spain, T., Berrisford, P., Methven, J., Lewis, A., McQuaid, J., Pilling, M., Bandy, B., Penkett, S., and Pyle, J.: Evaluation of a Lagrangian box model using field measurements from EASE (Eastern Atlantic Summer Experiment) 1996, Atmospheric Environment, 34, 3843–3863, https://doi.org/https://doi.org/10.1016/S1352-2310(00)00184-9, 2000.

Fairall, C. W., Helmig, D., Ganzeveld, L., and Hare, J.: Water-side turbulence enhancement of ozone deposition to the ocean, ATMOS CHEM PHYS, 7, 443–451, https://doi.org/10.5194/acp-7-443-2007, URL https://www.atmos-chem-phys.net/7/443/2007/, 2007.

Fairlie, T., Jacob, D. J., and Park, R. J.: The impact of transpacific transport of mineral dust in the United States, Atmospheric Environment, 41, 1251–1266, https://doi.org/https://doi.org/10.1016/j.atmosenv.2006.09.048, 2007.

Fenech, S., Doherty, R. M., Heaviside, C., Vardoulakis, S., Macintyre, H. L., and O'Connor, F. M.: The influence of model spatial resolution on simulated ozone and fine particulate matter for Europe: implications for health impact assessments, Atmospheric Chemistry and Physics, 18, 5765–5784, https://doi.org/10.5194/acp-18-5765-2018, URL https://acp.copernicus.org/articles/18/5765/2018/, 2018.

Feng, X., Lin, H., Fu, T.-M., Sulprizio, M. P., Zhuang, J., Jacob, D. J., Tian, H., Ma, Y., Zhang, L., Wang, X., and Chen, Q.: WRF-GC (v2.0): online two-way coupling of WRF (v3.9.1.1) and GEOS-Chem (v12.7.2) for modeling regional atmospheric chemistry-meteorology interactions, Geoscientific Model Devel-

opment Discussions, 2021, 1–48, https://doi.org/10.5194/gmd-2020-441, URL https://gmd.copernicus.org/preprints/gmd-2020-441/, 2021.

Fischer, E., Jacob, D., Millet, D., Yantosca, R., and Mao, J.: The role of the ocean in the global atmospheric budget of acetone, Geophys. Res. Lett., 39, L01 807, 2012.

Fischer, E. V., Jacob, D. J., Yantosca, R. M., Sulprizio, M. P., Millet, D. B., Mao, J., Paulot, F., Singh, H. B., Roiger, A., Ries, L., Talbot, R. W., Dzepina, K., and Pandey Deolal, S.: Atmospheric peroxyacetyl nitrate (PAN): a global budget and source attribution, Atmospheric Chemistry and Physics, 14, 2679–2698, https://doi.org/10.5194/acp-14-2679-2014, 2014.

Fisher, J. A., Jacob, D. J., Wang, Q., Bahreini, R., Carouge, C. C., Cubison, M. J., Dibb, J. E., Diehl, T., Jimenez, J. L., Leibensperger, E. M., Lu, Z., Meinders, M. B., Pye, H. O., Quinn, P. K., Sharma, S., Streets, D. G., van Donkelaar, A., and Yantosca, R. M.: Sources, distribution, and acidity of sulfate–ammonium aerosol in the Arctic in winter–spring, Atmospheric Environment, 45, 7301–7318, https://doi.org/https://doi.org/10.1016/j.atmosenv.2011.08.030, 2011.

Fisher, J. A., Jacob, D. J., Travis, K. R., Kim, P. S., Marais, E. A., Chan Miller, C., Yu, K., Zhu, L., Yantosca, R. M., Sulprizio, M. P., Mao, J., Wennberg, P. O., Crounse, J. D., Teng, A. P., Nguyen, T. B., St. Clair, J. M., Cohen, R. C., Romer, P., Nault, B. A., Wooldridge, P. J., Jimenez, J. L., Campuzano-Jost, P., Day, D. A., Hu, W., Shepson, P. B., Xiong, F., Blake, D. R., Goldstein, A. H., Misztal, P. K., Hanisco, T. F., Wolfe, G. M., Ryerson, T. B., Wisthaler, A., and Mikoviny, T.: Organic nitrate chemistry and its implications for nitrogen budgets in an isoprene- and monoterpene-rich atmosphere: constraints from aircraft (SEAC^{4}RS) and ground-based (SOAS) observations in the Southeast US, Atmospheric Chemistry and Physics, 16, 5969–5991, https://doi.org/10.5194/acp-16-5969-2016, 2016.

Fomba, K. W., Müller, K., van Pinxteren, D., Poulain, L., van Pinxteren, M., and Herrmann, H.: Long-term chemical characterization of tropical and ma-

rine aerosols at the Cape Verde Atmospheric Observatory (CVAO) from 2007 to 2011, Atmospheric Chemistry and Physics, 14, 8883–8904, https://doi.org/10.5194/acp-14-8883-2014, URL https://acp.copernicus.org/articles/14/8883/2014/, 2014.

Fountoukis, C. and Nenes, A.: ISORROPIA II: a computationally efficient thermodynamic equilibrium model for K^+, Ca^{2+}, Mg^{2+}, NH_4^+, Na^+, SO_4^{2-}, NO_3^-,Cl^-, H_2O aerosols, Atmospheric Chemistry and Physics, 7, 4639–4659, https://doi.org/10.5194/acp-7-4639-2007, URL https://acp.copernicus.org/articles/7/4639/2007/, 2007.

Fraser, P. J., Khalil, M. A. K., Rasmussen, R. A., and Crawford, A. J.: Trends of atmospheric methane in the southern hemisphere, Geophysical Research Letters, 8, 1063–1066, https://doi.org/https://doi.org/10.1029/GL008i010p01063, URL https://agupubs.onlinelibrary.wiley.com/doi/abs/10.1029/GL008i010p01063, 1981.

Gantt, B., Meskhidze, N., and Kamykowski, D.: A new physically-based quantification of marine isoprene and primary organic aerosol emissions, Atmospheric Chemistry and Physics, 9, 4915–4927, URL www.atmos-chem-phys.net/9/4915/2009/, 2009a.

Gantt, B., Meskhidze, N., and Kamykowski, D.: A new physically-based quantification of marine isoprene and primary organic aerosol emissions, Atmospheric Chemistry and Physics, 9, 4915–4927, https://doi.org/10.5194/acp-9-4915-2009, URL https://acp.copernicus.org/articles/9/4915/2009/, 2009b.

Ganzeveld, L., Helmig, D., Fairall, C., Hare, J., and Pozzer, A.: Atmosphere-ocean ozone exchange: A global modeling study of biogeochemical, atmospheric, and waterside turbulence dependencies, GLOBAL BIOGEOCHEM CY, 23, https://doi.org/10.1029/2008GB003301, 2009.

Garland, J. A. and Curtis, H.: Emission of iodine from the sea surface in the pres-

ence of ozone, J GEOPHYS RES-OCEANS, 86, 3183–3186, https://doi.org/10.1029/JC086iC04p03183, 1981.

Garland, J. A., Elzerman, A. W., and Penkett, S. A.: The mechanism for dry deposition of ozone to seawater surfaces, J GEOPHYS RES-OCEANS, 85, 7488–7492, https://doi.org/10.1029/JC085iC12p07488, URL https://agupubs.onlinelibrary.wiley.com/doi/abs/10.1029/JC085iC12p07488, 1980.

Garraway, S.: Measurement and modelling of volatile organic compounds in a tropical rainforest environment, URL http://etheses.whiterose.ac.uk/21337/, thesis, 2018.

GC12.1.1: geoschem/geos-chem: GEOS-Chem 12.1.1, https://doi.org/10.5281/zenodo.2249246, URL https://doi.org/10.5281/zenodo.2249246, Please see the LICENSE.txt and AUTHORS.txt files in the root folder for the GEOS-Chem license description (based on the MIT license) and a complete list of authors. For more information about GEOS-Chem in general, please see www.geos-chem.org and wiki.geos-chem.org., 2018.

GC12.6.0: geoschem/geos-chem: GEOS-Chem 12.6.0, https://doi.org/10.5281/zenodo.3507501, URL https://doi.org/10.5281/zenodo.3507501, Please see the LICENSE.txt and AUTHORS.txt files in the root folder for the GEOS-Chem license description (based on the MIT license) and a complete list of authors. For more information about GEOS-Chem in general, please see www.geos-chem.org and wiki.geos-chem.org., 2019.

Gelaro, R., McCarty, W., Suárez, M. J., Todling, R., Molod, A., Takacs, L., Randles, C. A., Darmenov, A., Bosilovich, M. G., Reichle, R., Wargan, K., Coy, L., Cullather, R., Draper, C., Akella, S., Buchard, V., Conaty, A., da Silva, A. M., Gu, W., Kim, G.-K., Koster, R., Lucchesi, R., Merkova, D., Nielsen, J. E., Partyka, G., Pawson, S., Putman, W., Rienecker, M., Schubert, S. D., Sienkiewicz, M., and Zhao, B.: The Modern-Era Retrospective Analysis for Research and Applications, Version 2 (MERRA-2), Journal of Climate, 30, 5419–5454, https://doi.org/10.1175/JCLI-D-16-0758.1, 2017.

GEOS-Chem Steering Committee: Narrative Description (and how to cite GEOS-Chem, URL http://acmg.seas.harvard.edu/geos/geos_chem_narrative.html, 2021.

Giglio, L., Randerson, J. T., and van der Werf, G. R.: Analysis of daily, monthly, and annual burned area using the fourth-generation global fire emissions database (GFED4), Journal of Geophysical Research: Biogeosciences, 118, 317–328, https://doi.org/https://doi.org/10.1002/jgrg.20042, 2013.

Goldman, J. C., Dennett, M. R., and Frew, N. M.: Surfactant effects on air-sea gas exchange under turbulent conditions, Deep Sea Research Part A. Oceanographic Research Papers, 35, 1953–1970, https://doi.org/https://doi.org/10.1016/0198-0149(88)90119-7, 1988.

Goldstein, A. H., Fan, S. M., Goulden, M. L., Munger, J. W., and Wofsy, S. C.: Emissions of ethene, propene, and 1-butene by a midlatitude forest, Journal of Geophysical Research: Atmospheres, 101, 9149–9157, https://doi.org/https://doi.org/10.1029/96JD00334, 1996.

Guenther, A. B., Jiang, X., Heald, C. L., Sakulyanontvittaya, T., Duhl, T., Emmons, L. K., and Wang, X.: The Model of Emissions of Gases and Aerosols from Nature version 2.1 (MEGAN2.1): an extended and updated framework for modeling biogenic emissions, Geoscientific Model Development, 5, 1471–1492, https://doi.org/10.5194/gmd-5-1471-2012, URL https://gmd.copernicus.org/articles/5/1471/2012/, 2012.

Hardacre, C., Wild, O., and Emberson, L.: An evaluation of ozone dry deposition in global scale chemistry climate models, ATMOS CHEM PHYS, 15, 6419–6436, https://doi.org/10.5194/acp-15-6419-2015, URL https://www.atmos-chem-phys.net/15/6419/2015/, 2015.

Harris, J. M. and Oltmans, S. J.: Variations in tropospheric ozone related to transport at American Samoa, Journal of Geophysical Research: Atmospheres, 102, 8781–8791, https://doi.org/https://doi.org/10.1029/97JD00238, 1997.

Hayase, S., Yabushita, A., Kawasaki, M., Enami, S., Hoffmann, M. R., and Colussi, A. J.: Heterogeneous Reaction of Gaseous Ozone with Aqueous Iodide in the Presence of Aqueous Organic Species, J PHYS CHEM A, 114, 6016–6021, https://doi.org/10.1021/jp101985f, 2010.

Haywood, J. and Boucher, O.: Estimates of the direct and indirect radiative forcing due to tropospheric aerosols: A review, Reviews of Geophysics, 38, 513–543, https://doi.org/https://doi.org/10.1029/1999RG000078, URL https://agupubs.onlinelibrary.wiley.com/doi/abs/10.1029/1999RG000078, 2000.

Heard, D. E., Read, K. A., Methven, J., Al-Haider, S., Bloss, W. J., Johnson, G. P., Pilling, M. J., Seakins, P. W., Smith, S. C., Sommariva, R., Stanton, J. C., Still, T. J., Ingham, T., Brooks, B., De Leeuw, G., Jackson, A. V., McQuaid, J. B., Morgan, R., Smith, M. H., Carpenter, L. J., Carslaw, N., Hamilton, J., Hopkins, J. R., Lee, J. D., Lewis, A. C., Purvis, R. M., Wevill, D. J., Brough, N., Green, T., Mills, G., Penkett, S. A., Plane, J. M. C., Saiz-Lopez, A., Worton, D., Monks, P. S., Fleming, Z., Rickard, A. R., Alfarra, M. R., Allan, J. D., Bower, K., Coe, H., Cubison, M., Flynn, M., McFiggans, G., Gallagher, M., Norton, E. G., O'Dowd, C. D., Shillito, J., Topping, D., Vaughan, G., Williams, P., Bitter, M., Ball, S. M., Jones, R. L., Povey, I. M., O'Doherty, S., Simmonds, P. G., Allen, A., Kinnersley, R. P., Beddows, D. C. S., Dall'Osto, M., Harrison, R. M., Donovan, R. J., Heal, M. R., Jennings, S. G., Noone, C., and Spain, G.: The North Atlantic Marine Boundary Layer Experiment(NAMBLEX). Overview of the campaign held at Mace Head, Ireland, in summer 2002, Atmospheric Chemistry and Physics, 6, 2241–2272, https://doi.org/10.5194/acp-6-2241-2006, 2006.

Helmig, D., Lang, E. K., Bariteau, L., Boylan, P., Fairall, C. W., Ganzeveld, L., Hare, J. E., Hueber, J., and Pallandt, M.: Atmosphere-ocean ozone fluxes during the TexAQS 2006, STRATUS 2006, GOMECC 2007, GasEx 2008, and AMMA 2008 cruises, J GEOPHYS RES-ATMOS, 117, https://doi.org/10.1029/2011JD015955, 2012.

Henrot, A.-J., Stanelle, T., Schröder, S., Siegenthaler, C., Tarabor-

relli, D., and Schultz, M.: Implementation of the MEGAN (v2.1) biogenic emission model in the ECHAM6-HAMMOZ chemistry climate model, Geoscientific Model Development, 10, 903–926, https://doi.org/10.5194/gmd-10-903-2017, URL https://www.scopus.com/inward/record.uri?eid=2-s2.0-85014013407&doi=10.5194%2fgmd-10-903-2017&partnerID=40&md5=fb8bb3b08bcce10bea9b0782347032c6, 2017.

Hoesly, R. M., Smith, S. J., Feng, L., Klimont, Z., Janssens-Maenhout, G., Pitkanen, T., Seibert, J. J., Vu, L., Andres, R. J., Bolt, R. M., Bond, T. C., Dawidowski, L., Kholod, N., Kurokawa, J.-I., Li, M., Liu, L., Lu, Z., Moura, M. C. P., O'Rourke, P. R., and Zhang, Q.: Historical (1750–2014) anthropogenic emissions of reactive gases and aerosols from the Community Emissions Data System (CEDS), Geoscientific Model Development, 11, 369–408, https://doi.org/10.5194/gmd-11-369-2018, URL https://gmd.copernicus.org/articles/11/369/2018/, 2018.

Holmes, C. D., Prather, M. J., Søvde, O. A., and Myhre, G.: Future methane, hydroxyl, and their uncertainties: key climate and emission parameters for future predictions, Atmospheric Chemistry and Physics, 13, 285–302, https://doi.org/10.5194/acp-13-285-2013, URL https://acp.copernicus.org/articles/13/285/2013/, 2013.

Holmes, C. D., Prather, M. J., and Vinken, G. C. M.: The climate impact of ship NO_x emissions: an improved estimate accounting for plume chemistry, Atmospheric Chemistry and Physics, 14, 6801–6812, https://doi.org/10.5194/acp-14-6801-2014, 2014.

Hu, J. H., Shi, Q., Davidovits, P., Worsnop, D. R., Zahniser, M. S., and Kolb, C. E.: Reactive Uptake of Cl2(g) and Br2(g) by Aqueous Surfaces as a Function of Br- and I- Ion Concentration: The Effect of Chemical Reaction at the Interface, J. Phys. Chem., 99, 8768–8776, https://doi.org/10.1021/j100021a050, 1995.

Hu, L., Millet, D. B., Baasandorj, M., Griffis, T. J., Turner, P., Helmig, D., Curtis, A. J., and Hueber, J.: Isoprene emissions and impacts over an

ecological transition region in the U.S. Upper Midwest inferred from tall tower measurements, Journal of Geophysical Research: Atmospheres, 120, 3553–3571, https://doi.org/https://doi.org/10.1002/2014JD022732, URL https://agupubs.onlinelibrary.wiley.com/doi/abs/10.1002/2014JD022732, 2015.

Hu, L., Keller, C. A., Long, M. S., Sherwen, T., Auer, B., Da Silva, A., Nielsen, J. E., Pawson, S., Thompson, M. A., Trayanov, A. L., Travis, K. R., Grange, S. K., Evans, M. J., and Jacob, D. J.: Global simulation of tropospheric chemistry at 12.5 km resolution: performance and evaluation of the GEOS-Chem chemical module (v10-1) within the NASA GEOS Earth system model (GEOS-5 ESM), Geoscientific Model Development, 11, 4603–4620, https://doi.org/10.5194/gmd-11-4603-2018, URL https://gmd.copernicus.org/articles/11/4603/2018/, 2018.

Hudman, R. C., Moore, N. E., Mebust, A. K., Martin, R. V., Russell, A. R., Valin, L. C., and Cohen, R. C.: Steps towards a mechanistic model of global soil nitric oxide emissions: implementation and space based-constraints, Atmospheric Chemistry and Physics, 12, 7779–7795, https://doi.org/10.5194/acp-12-7779-2012, URL https://acp.copernicus.org/articles/12/7779/2012/, 2012.

Huebert, B. J., Blomquist, B. W., Hare, J. E., Fairall, C. W., Johnson, J. E., and Bates, T. S.: Measurement of the sea-air DMS flux and transfer velocity using eddy correlation, Geophysical Research Letters, 31, https://doi.org/https://doi.org/10.1029/2004GL021567, 2004.

Huijnen, V., Williams, J., van Weele, M., van Noije, T., Krol, M., Dentener, F., Segers, A., Houweling, S., Peters, W., de Laat, J., Boersma, F., Bergamaschi, P., van Velthoven, P., Le Sager, P., Eskes, H., Alkemade, F., Scheele, R., Nédélec, P., and Pätz, H.-W.: The global chemistry transport model TM5: description and evaluation of the tropospheric chemistry version 3.0, Geoscientific Model Development, 3, 445–473, https://doi.org/10.5194/gmd-3-445-2010, URL https://gmd.copernicus.org/articles/3/445/2010/, 2010.

Ilyina, T., Wolf-Gladrow, D., Munhoven, G., and Heinze, C.: Assessing the potential of calcium-based artificial ocean alkalinization to mitigate rising atmospheric CO2 and ocean acidification, Geophysical Research Letters, 40, 5909–5914, https://doi.org/https://doi.org/10.1002/2013GL057981, URL https://agupubs.onlinelibrary.wiley.com/doi/abs/10.1002/2013GL057981, 2013.

[IPCC], Team], C. W., Pachauri, R., and Meyer, L.: Climate Change 2014: Synthesis Report. Contribution of Working Groups I, II and III to the Fifth Assessment Report of the Intergovernmental Panel on Climate Change, IPCC, Geneva, Switzerland, 2014.

IPCC Stocker, T., Qin, D., Plattner, G., Tignor, M., Allen, S., Boschung, J., Nauels, A., Xia, Y., Bex, V., and Midgley, P.: Climate Change 2013: The Physical Science Basis. Contribution of Working Group I to the Fifth Assessment Report of the Intergovernmental Panel on Climate Change, IPCC, p. 1535, 2013.

IUPAC: IUPAC Development Version Evaluated Kinetic Data, URL http://iupac-dev.ipsl.jussieu.fr/index.html, task Group on Atmospheric Chemical Kinetic Data Evaluation, 2021.

Jacob, D.: Introduction to Atmospheric Chemistry, Princeton University Press, 1999.

Jaeglé, L., Quinn, P. K., Bates, T. S., Alexander, B., and Lin, J.-T.: Global distribution of sea salt aerosols: new constraints from in situ and remote sensing observations, Atmospheric Chemistry and Physics, 11, 3137–3157, https://doi.org/10.5194/acp-11-3137-2011, URL https://acp.copernicus.org/articles/11/3137/2011/, 2011.

Johnson, P. N. and Davis, R. A.: Diffusivity of Ozone in Water, J CHEM ENG DATA, 41, 1485–1487, https://doi.org/10.1021/je9602125, 1996.

JPL: JPL Publication 15-10, URL https://jpldataeval.jpl.nasa.gov, 2015.

Jungclaus, J. H., Keenlyside, N., Botzet, M., Haak, H., Luo, J.-J., Latif, M., Marotzke, J., Mikolajewicz, U., and Roeckner, E.: Ocean Circulation and Trop-

ical Variability in the Coupled Model ECHAM5/MPI-OM, Journal of Climate, 19, 3952 – 3972, https://doi.org/10.1175/JCLI3827.1, URL https://journals.ametsoc.org/view/journals/clim/19/16/jcli3827.1.xml, 2006.

Jungclaus, J. H., Fischer, N., Haak, H., Lohmann, K., Marotzke, J., Matei, D., Mikolajewicz, U., Notz, D., and von Storch, J. S.: Characteristics of the ocean simulations in the Max Planck Institute Ocean Model (MPIOM) the ocean component of the MPI-Earth system model, Journal of Advances in Modeling Earth Systems, 5, 422–446, https://doi.org/https://doi.org/10.1002/jame.20023, URL https://agupubs.onlinelibrary.wiley.com/doi/abs/10.1002/jame.20023, 2013.

Kaiser, J. C., Hendricks, J., Righi, M., Jöckel, P., Tost, H., Kandler, K., Weinzierl, B., Sauer, D., Heimerl, K., Schwarz, J. P., Perring, A. E., and Popp, T.: Global aerosol modeling with MADE3 (v3.0) in EMAC (based on v2.53): model description and evaluation, Geoscientific Model Development, 12, 541–579, https://doi.org/10.5194/gmd-12-541-2019, URL https://gmd.copernicus.org/articles/12/541/2019/, 2019.

Keller, C. A., Long, M. S., Yantosca, R. M., Da Silva, A. M., Pawson, S., and Jacob, D. J.: HEMCO v1.0: a versatile, ESMF-compliant component for calculating emissions in atmospheric models, Geoscientific Model Development, 7, 1409–1417, https://doi.org/10.5194/gmd-7-1409-2014, 2014.

Kieber, R. J., Zhou, X., and Mopper, K.: Formation of carbonyl compounds from UV-induced photodegradation of humic substances in natural waters: Fate of riverine carbon in the sea, Limnology and Oceanography, 35, 1503–1515, https://doi.org/https://doi.org/10.4319/lo.1990.35.7.1503, 1990.

Kim, P. S., Jacob, D. J., Fisher, J. A., Travis, K., Yu, K., Zhu, L., Yantosca, R. M., Sulprizio, M. P., Jimenez, J. L., Campuzano-Jost, P., Froyd, K. D., Liao, J., Hair, J. W., Fenn, M. A., Butler, C. F., Wagner, N. L., Gordon, T. D., Welti, A., Wennberg, P. O., Crounse, J. D., St. Clair, J. M., Teng, A. P., Millet,

D. B., Schwarz, J. P., Markovic, M. Z., and Perring, A. E.: Sources, seasonality, and trends of southeast US aerosol: an integrated analysis of surface, aircraft, and satellite observations with the GEOS-Chem chemical transport model, Atmospheric Chemistry and Physics, 15, 10 411–10 433, https://doi.org/10.5194/acp-15-10411-2015, URL https://acp.copernicus.org/articles/15/10411/2015/, 2015.

Kley, D.: Tropospheric Chemistry and Transport, Science, 276, 1043–1044, https://doi.org/10.1126/science.276.5315.1043, 1997.

Kloster, S., Feichter, J., Maier-Reimer, E., Six, K. D., Stier, P., and Wetzel, P.: DMS cycle in the marine ocean-atmosphere system; a global model study, Biogeosciences, 3, 29–51, https://doi.org/10.5194/bg-3-29-2006, URL https://bg.copernicus.org/articles/3/29/2006/, 2006.

Koppmann, R., Bauer, R., Johnen, F. J., Plass, C., and Rudolph, J.: The Distribution of Light Nonmethane Hydrocarbons over the Mid-Atlantic: Results of the Polarstern Cruise ANT VIIII, Journal of Atmospheric Chemistry, 15, 215–234, 1992.

Krishnamurthy, A., Moore, J. K., Zender, C. S., and Luo, C.: Effects of atmospheric inorganic nitrogen deposition on ocean biogeochemistry, Journal of Geophysical Research: Biogeosciences, 112, https://doi.org/https://doi.org/10.1029/2006JG000334, 2007.

Lana, A., Bell, T. G., Simó, R., Vallina, S. M., Ballabrera-Poy, J., Kettle, A. J., Dachs, J., Bopp, L., Saltzman, E. S., Stefels, J., Johnson, J. E., and Liss, P. S.: An updated climatology of surface dimethlysulfide concentrations and emission fluxes in the global ocean, Global Biogeochemical Cycles, 25, https://doi.org/https://doi.org/10.1029/2010GB003850, 2011.

Langner, J. and Rodhe, H.: A global three-dimensional model of the tropospheric sulfur cycle, J Atmos Chem, 13, 225–263, https://doi.org/https://doi.org/10.1007/BF00058134, 1991.

Lewis, A. C., Carpenter, L. J., and J., P. M.: Nonmethane hydrocarbons in Southern Ocean boundary layer air, Journal of Geophysical Research, 106, 4987–4994, 2001.

Lewis, A. C., Hopkins, J. R., Carpenter, L. J., Stanton, J., Read, K. A., and Pilling, M. J.: Sources and sinks of acetone, methanol, and acetaldehyde in North Atlantic marine air, Atmospheric Chemistry and Physics, 5, 1963–1974, https://doi.org/10.5194/acp-5-1963-2005, 2005.

Li, J., Cunnold, D. M., Wang, H.-J., Weiss, R. F., Miller, B. R., Harth, C., Salameh, P., and Harris, J. M.: Halocarbon emissions estimated from Advanced Global Atmospheric Gases Experiment measured pollution events at Trinidad Head, California, J. Geophys. Res., 110, https://doi.org/doi:10.1029/2004JD005739, 2005.

Li, M., Zhang, Q., Streets, D. G., He, K. B., Cheng, Y. F., Emmons, L. K., Huo, H., Kang, S. C., Lu, Z., Shao, M., Su, H., Yu, X., and Zhang, Y.: Mapping Asian anthropogenic emissions of non-methane volatile organic compounds to multiple chemical mechanisms, Atmospheric Chemistry and Physics, 14, 5617–5638, https://doi.org/10.5194/acp-14-5617-2014, URL https://acp.copernicus.org/articles/14/5617/2014/, 2014.

Lin, H., Feng, X., Fu, T.-M., Tian, H., Ma, Y., Zhang, L., Jacob, D. J., Yantosca, R. M., Sulprizio, M. P., Lundgren, E. W., Zhuang, J., Zhang, Q., Lu, X., Zhang, L., Shen, L., Guo, J., Eastham, S. D., and Keller, C. A.: WRF-GC (v1.0): online coupling of WRF (v3.9.1.1) and GEOS-Chem (v12.2.1) for regional atmospheric chemistry modeling – Part 1: Description of the one-way model, Geoscientific Model Development, 13, 3241–3265, https://doi.org/10.5194/gmd-13-3241-2020, URL https://gmd.copernicus.org/articles/13/3241/2020/, 2020.

Lin, J.-T. and McElroy, M. B.: Impacts of boundary layer mixing on pollutant vertical profiles in the lower troposphere: Implications to satellite remote sens-

ing, Atmospheric Environment, 44, 1726–1739, https://doi.org/https://doi.org/10.1016/j.atmosenv.2010.02.009, 2010.

Lin, S.-J. and Rood, R.: Multidimensional flux form semi-Lagrangian transport schemes, Mon. Wea. Rev., pp. 2046–2070, https://doi.org/https://doi.org/10.1175/1520-0493(1996)124⟨2046:MFFSLT⟩2.0.CO;2, 1996.

Liss, P. and Slater, P.: Flux of gases across the air-sea interface, Nature, 247, 181–184, https://doi.org/10.1038/247181a0, 1974.

Liu, H., Jacob, D. J., Bey, I., and Yantosca, R. M.: Constraints from 210Pb and 7Be on wet deposition and transport in a global three-dimensional chemical tracer model driven by assimilated meteorological fields, Journal of Geophysical Research: Atmospheres, 106, 12 109–12 128, https://doi.org/https://doi.org/10.1029/2000JD900839, 2001a.

Liu, Q., Schurter, L. M., Muller, C. E., Aloisio, S., Francisco, J. S., and Margerum, D. W.: Kinetics and Mechanisms of Aqueous Ozone Reactions with Bromide, Sulfite, Hydrogen Sulfite, Iodide, and Nitrite Ions, INORG CHEM, 40, 4436–4442, https://doi.org/10.1021/ic000919j, 2001b.

Liu, S., Liu, C.-C., Froyd, K. D., Schill, G. P., Murphy, D. M., Bui, T. P., Dean-Day, J. M., Weinzierl, B., Dollner, M., Diskin, G. S., Chen, G., and Gao, R.-S.: Sea spray aerosol concentration modulated by sea surface temperature, Proceedings of the National Academy of Sciences, 118, https://doi.org/10.1073/pnas.2020583118, 2021.

Logan, J. A.: Tropospheric ozone: Seasonal behavior, trends, and anthropogenic influence, Journal of Geophysical Research: Atmospheres, 90, 10 463–10 482, https://doi.org/https://doi.org/10.1029/JD090iD06p10463, URL https://agupubs.onlinelibrary.wiley.com/doi/abs/10.1029/JD090iD06p10463, 1985.

Logan, J. A., Prather, M. J., Wofsy, S. C., and McElroy, M. B.: Tropospheric chemistry: A global perspective, Journal of Geophysical Research: Oceans, 86, 7210–7254, https://doi.org/https://doi.org/10.

1029/JC086iC08p07210, URL https://agupubs.onlinelibrary.wiley.com/doi/abs/10.1029/JC086iC08p07210, 1981.

Luhar, A. K., Galbally, I. E., Woodhouse, M. T., and Thatcher, M.: An improved parameterisation of ozone dry deposition to the ocean and its impact in a global climate-chemistry model, ATMOS CHEM PHYS, 17, 3749–3767, https://doi.org/10.5194/acp-17-3749-2017, 2017.

Luhar, A. K., Woodhouse, M. T., and Galbally, I. E.: A revised global ozone dry deposition estimate based on a new two-layer parameterisation for air–sea exchange and the multi-year MACC composition reanalysis, ATMOS CHEM PHYS, 18, 4329–4348, https://doi.org/10.5194/acp-18-4329-2018, URL https://www.atmos-chem-phys.net/18/4329/2018/, 2018.

Ma, X., von Salzen, K., and Li, J.: Modelling sea salt aerosol and its direct and indirect effects on climate, Atmospheric Chemistry and Physics, 8, 1311–1327, https://doi.org/10.5194/acp-8-1311-2008, URL https://acp.copernicus.org/articles/8/1311/2008/, 2008.

MacDonald, S. M., Gómez Martín, J. C., Chance, R., Warriner, S., Saiz-Lopez, A., Carpenter, L. J., and Plane, J. M. C.: A laboratory characterisation of inorganic iodine emissions from the sea surface: dependence on oceanic variables and parameterisation for global modelling, ATMOS CHEM PHYS, 14, 5841–5852, https://doi.org/10.5194/acp-14-5841-2014, URL https://www.atmos-chem-phys.net/14/5841/2014/, 2014.

Magi, L., Schweitzer, F., Pallares, C., Cherif, S., Mirabel, P., and George, C.: Investigation of the Uptake Rate of Ozone and Methyl Hydroperoxide by Water Surfaces, J PHYS CHEM A, 101, 4943–4949, https://doi.org/10.1021/jp970646m, 1997.

Mahowald, N., Scanza, R., Brahney, J., Goodale, C., Hess, P., Moore, J., and Neff, J.: Aerosol Deposition Impacts on Land and Ocean Carbon Cycles, Current

Climate Change Reports, 3, 16–31, https://doi.org/10.1007/s40641-017-0056-z, 2017.

Malley, C. S., Henze, D. K., Kuylenstierna, J. C., Vallack, H. W., Davila, Y., Anenberg, S. C., Turner, M. C., and Ashmore, M. R.: Updated Global Estimates of Respiratory Mortality in Adults $\geq$ 30 Years of Age Attributable to Long-Term Ozone Exposure, ENVIRON HEALTH PERSP, 125, 087 021, https://doi.org/10.1289/EHP1390, 2017.

Mannino, A., Russ, M., and Hooker, S.: Algorithm development and validation for satellite-derived distributions of DOC and CDOM in the U.S. Middle Atlantic Bight, Journal of Geophysical Research, 113, https://doi.org/10.1029/2007JC004493, 2008.

Mao, J., Jacob, D. J., Evans, M. J., Olson, J. R., Ren, X., Brune, W. H., Clair, J. M. S., Crounse, J. D., Spencer, K. M., Beaver, M. R., Wennberg, P. O., Cubison, M. J., Jimenez, J. L., Fried, A., Weibring, P., Walega, J. G., Hall, S. R., Weinheimer, A. J., Cohen, R. C., Chen, G., Crawford, J. H., McNaughton, C., Clarke, A. D., Jaeglé, L., Fisher, J. A., Yantosca, R. M., Le Sager, P., and Carouge, C.: Chemistry of hydrogen oxide radicals (HO_x) in the Arctic troposphere in spring, Atmospheric Chemistry and Physics, 10, 5823–5838, https://doi.org/10.5194/acp-10-5823-2010, 2010.

Marais, E. A. and Wiedinmyer, C.: Air Quality Impact of Diffuse and Inefficient Combustion Emissions in Africa (DICE-Africa), Environmental Science & Technology, 50, 10 739–10 745, https://doi.org/10.1021/acs.est.6b02602, URL https://doi.org/10.1021/acs.est.6b02602, 2016.

Marais, E. A., Jacob, D. J., Jimenez, J. L., Campuzano-Jost, P., Day, D. A., Hu, W., Krechmer, J., Zhu, L., Kim, P. S., Miller, C. C., Fisher, J. A., Travis, K., Yu, K., Hanisco, T. F., Wolfe, G. M., Arkinson, H. L., Pye, H. O. T., Froyd, K. D., Liao, J., and McNeill, V. F.: Aqueous-phase mechanism for secondary organic aerosol formation from isoprene: application to the southeast United States and co-benefit of SO_2 emission controls, Atmospheric Chemistry and

Physics, 16, 1603–1618, https://doi.org/10.5194/acp-16-1603-2016, URL https://acp.copernicus.org/articles/16/1603/2016/, 2016.

Marandino, C. A., De Bruyn, W. J., Miller, S. D., Prather, M. J., and Saltzman, E. S.: Oceanic uptake and the global atmospheric acetone budget, Geophysical Research Letters, 32, https://doi.org/https://doi.org/10.1029/2005GL023285, 2005.

Martino, M., Lézé, B., Baker, A., and Liss, P.: Chemical controls on ozone deposition to water, Geophys. Res. Lett., 39, L05 809, https://doi.org/10.1029/2011GL050282., 2012.

McGillis, W. R., Edson, J. B., Hare, J. E., and Fairall, C. W.: Direct covariance air-sea CO2 fluxes, Journal of Geophysical Research: Oceans, 106, 16 729–16 745, https://doi.org/https://doi.org/10.1029/2000JC000506, 2001.

McLinden, C. A., Olsen, S. C., Hannegan, B., Wild, O., Prather, M. J., and Sundet, J.: Stratospheric ozone in 3-D models: A simple chemistry and the cross-tropopause flux, Journal of Geophysical Research: Atmospheres, 105, 14 653–14 665, https://doi.org/https://doi.org/10.1029/2000JD900124, 2000.

Menut, L., Bessagnet, B., Briant, R., Cholakian, A., Couvidat, F., Mailler, S., Pennel, R., Siour, G., Tuccella, P., Turquety, S., and Valari, M.: The CHIMERE v2020r1 online chemistry-transport model, Geoscientific Model Development Discussions, 2021, 1–50, https://doi.org/10.5194/gmd-2021-96, URL https://gmd.copernicus.org/preprints/gmd-2021-96/, 2021.

Mertens, M., Kerkweg, A., Grewe, V., Jöckel, P., and Sausen, R.: Are contributions of emissions to ozone a matter of scale? – a study using MECO(n) (MESSy v2.50), Geoscientific Model Development, 13, 363–383, https://doi.org/10.5194/gmd-13-363-2020, URL https://gmd.copernicus.org/articles/13/363/2020/, 2020.

Mikaloff Fletcher, S. E., Gruber, N., Jacobson, A. R., Doney, S. C., Dutkiewicz, S., Gerber, M., Follows, M., Joos, F., Lindsay, K., Menemenlis, D., Mouchet, A.,

Müller, S. A., and Sarmiento, J. L.: Inverse estimates of anthropogenic CO2 uptake, transport, and storage by the ocean, Global Biogeochemical Cycles, 20, https://doi.org/https://doi.org/10.1029/2005GB002530, 2006.

Millet, D. B., Goldstein, A. H., Allan, J. D., Bates, T. S., Boudries, H., Bower, K. N., Coe, H., Ma, Y., McKay, M., Quinn, P. K., Sullivan, A., Weber, R. J., and Worsnop, D. R.: Volatile organic compound measurements at Trinidad Head, California, during ITCT 2K2: Analysis of sources, atmospheric composition, and aerosol residence times, Journal of Geophysical Research: Atmospheres, 109, https://doi.org/https://doi.org/10.1029/2003JD004026, 2004.

Millet, D. B., Guenther, A., Siegel, D. A., Nelson, N. B., Singh, H. B., de Gouw, J. A., Warneke, C., Williams, J., Eerdekens, G., Sinha, V., Karl, T., Flocke, F., Apel, E., Riemer, D. D., Palmer, P. I., and Barkley, M.: Global atmospheric budget of acetaldehyde: 3-D model analysis and constraints from in-situ and satellite observations, Atmospheric Chemistry and Physics, 10, 3405–3425, https://doi.org/10.5194/acp-10-3405-2010, URL https://acp.copernicus.org/articles/10/3405/2010/, 2010.

Millet, D. B., Baasandorj, M., Farmer, D. K., Thornton, J. A., Baumann, K., Brophy, P., Chaliyakunnel, S., de Gouw, J. A., Graus, M., Hu, L., Koss, A., Lee, B. H., Lopez-Hilfiker, F. D., Neuman, J. A., Paulot, F., Peischl, J., Pollack, I. B., Ryerson, T. B., Warneke, C., Williams, B. J., and Xu, J.: A large and ubiquitous source of atmospheric formic acid, Atmospheric Chemistry and Physics, 15, 6283–6304, https://doi.org/10.5194/acp-15-6283-2015, 2015.

Molod, A., Takacs, L., Suarez, M., Bacmeister, J., Song, I., and Eichmann, A.: The GEOS-5 Atmospheric General Circulation Model: Mean Climate and Development from MERRA to Fortuna, Technical Report Series on Global Modeling and Data Assimilation, NASA GMAO, Goddard Space Flight Center, Greenbelt, MD, 28, URL https://gmao.gsfc.nasa.gov/pubs/docs/tm28.pdf, 2012.

Monks, P. S., Carpenter, L. J., Penkett, S. A., Ayers, G. P., Gillett, R. W., Galbally, I. E., and (Mick) Meyer, C.: Fundamental ozone photochemistry in the remote

marine boundary layer: the soapex experiment, measurement and theory, Atmospheric Environment, 32, 3647–3664, https://doi.org/https://doi.org/10.1016/S1352-2310(98)00084-3, 1998.

Moreno, C. G., Gálvez, O., López-Arza Moreno, V., Espildora-García, E. M., and Baeza-Romero, M. T.: A revisit of the interaction of gaseous ozone with aqueous iodide. Estimating the contributions of the surface and bulk reactions, Phys. Chem. Chem. Phys., 20, 27 571–27 584, https://doi.org/10.1039/C8CP04394A, URL http://dx.doi.org/10.1039/C8CP04394A, 2018.

Morris, J.: The aqueous solubility of ozone - A review, Ozone news, 1, 14–16, 1988.

Murray, L. T., Jacob, D. J., Logan, J. A., Hudman, R. C., and Koshak, W. J.: Optimized regional and interannual variability of lightning in a global chemical transport model constrained by LIS/OTD satellite data, Journal of Geophysical Research: Atmospheres, 117, https://doi.org/https://doi.org/10.1029/2012JD017934, 2012.

NCAS, Carpenter, L., Hopkins, J., Lewis, A., Neves, L., Moller, S., Pilling, M., Read, K., Young, T., and Lee, J.: Continuous Cape Verde Atmospheric Observatory Observations, https://doi.org/http://catalogue.ceda.ac.uk/uuid/81693aad69409100b1b9a247b9ae75d5, 2010.

Nemecek-Marshall, M., Wojciechowski, C., Kuzma, J., Silver, G. M., and Fall, R.: Marine Vibrio species produce the volatile organic compound acetone, Applied and Environmental Microbiology, 61, 44–47, https://doi.org/10.1128/aem.61.1.44-47.1995, 1995.

NOAA: Mauna Loa site description and Dataset, URL https://gml.noaa.gov/dv/site/MLO.html, 2021.

NOAA: Observation Sites, The Samoa Observatory, URL https://gml.noaa.gov/dv/site/SMO.html?stacode=SMO, 2021.

NOAA: Trinidad Head site description and Dataset, URL https://gml.noaa.gov/dv/site/THD.html, 2021.

O'Dowd, C. D. and de Leeuw, G.: Marine aerosol production: a review of the current knowledge, Philosophical Transactions of the Royal Society A: Mathematical, Physical and Engineering Sciences, 365, 1753–1774, https://doi.org/10.1098/rsta.2007.2043, 2007.

Oltmans, S. J., Lefohn, A. S., Harris, J. M., and Shadwick, D. S.: Background ozone levels of air entering the west coast of the US and assessment of longer-term changes, Atmospheric Environment, 42, 6020–6038, https://doi.org/https://doi.org/10.1016/j.atmosenv.2008.03.034, 2008.

Ordóñez, C., Lamarque, J.-F., Tilmes, S., Kinnison, D. E., Atlas, E. L., Blake, D. R., Sousa Santos, G., Brasseur, G., and Saiz-Lopez, A.: Bromine and iodine chemistry in a global chemistry-climate model: description and evaluation of very short-lived oceanic sources, Atmospheric Chemistry and Physics, 12, 1423–1447, https://doi.org/10.5194/acp-12-1423-2012, URL https://acp.copernicus.org/articles/12/1423/2012/, 2012.

Pai, S. J., Heald, C. L., Pierce, J. R., Farina, S. C., Marais, E. A., Jimenez, J. L., Campuzano-Jost, P., Nault, B. A., Middlebrook, A. M., Coe, H., Shilling, J. E., Bahreini, R., Dingle, J. H., and Vu, K.: An evaluation of global organic aerosol schemes using airborne observations, Atmospheric Chemistry and Physics, 20, 2637–2665, https://doi.org/10.5194/acp-20-2637-2020, URL https://acp.copernicus.org/articles/20/2637/2020/, 2020.

Park, R. J., Jacob, D. J., Field, B. D., Yantosca, R. M., and Chin, M.: Natural and transboundary pollution influences on sulfate-nitrate-ammonium aerosols in the United States: Implications for policy, Journal of Geophysical Research: Atmospheres, 109, https://doi.org/https://doi.org/10.1029/2003JD004473, 2004.

Parrella, J. P., Jacob, D. J., Liang, Q., Zhang, Y., Mickley, L. J., Miller, B., Evans, M. J., Yang, X., Pyle, J. A., Theys, N., and Van Roozendael, M.:

Tropospheric bromine chemistry: implications for present and pre-industrial ozone and mercury, Atmospheric Chemistry and Physics, 12, 6723–6740, https://doi.org/10.5194/acp-12-6723-2012, URL https://acp.copernicus.org/articles/12/6723/2012/, 2012.

Philip, S., Martin, R. V., and Keller, C. A.: Sensitivity of chemistry-transport model simulations to the duration of chemical and transport operators: a case study with GEOS-Chem v10-01, Geoscientific Model Development, 9, 1683–1695, https://doi.org/10.5194/gmd-9-1683-2016, 2016.

Plass-Dulmer, C., Khedim, A., Koppmann, R., Jobhen, F. J., Rudolph, J., and Kuosa, H.: Emissions of light non-methane hydrocarbons from the Atlantic into the atmosphere, Global Biogeochemical Cycles, 7, 211–228, 1993.

Plass-Dulmer, C., Koppmann, R., Ratte, M., and Rudolph, J.: Light non-methane hydrocarbons in seawater, Global Biogeochemical Cycles, 9, 79–100, 1995.

Pound, R. J., Sherwen, T., Helmig, D., Carpenter, L. J., and Evans, M. J.: Influences of oceanic ozone deposition on tropospheric photochemistry, Atmospheric Chemistry and Physics, 20, 4227–4239, https://doi.org/10.5194/acp-20-4227-2020, URL https://acp.copernicus.org/articles/20/4227/2020/, 2020.

Putman, W. M. and Lin, S.-J.: Finite-volume transport on various cubed-sphere grids, Journal of Computational Physics, 227, 55–78, https://doi.org/https://doi.org/10.1016/j.jcp.2007.07.022, URL https://www.sciencedirect.com/science/article/pii/S0021999107003105, 2007.

Pye, H. O. T., Chan, A. W. H., Barkley, M. P., and Seinfeld, J. H.: Global modeling of organic aerosol: the importance of reactive nitrogen (NO_x and NO_3), Atmospheric Chemistry and Physics, 10, 11 261–11 276, https://doi.org/10.5194/acp-10-11261-2010, URL https://acp.copernicus.org/articles/10/11261/2010/, 2010.

Ratte, M., Bujok, O., Spitzy, A., and Rudolph, J.: Photochemical alkene formation in seawater from dissolved organic carbon: Results from laboratory experiments, Journal of Geophysical Research, 103, 5707–5717, 1998.

Read, K. A., Lewis, A. C., Salmon, R. A., Jones, A. E., and Bauguitte, S.: OH and halogen atom influence on the variability of non-methane hydrocarbons in the Antarctic Boundary Layer, Chemical and Physical Meteorology, 59, 22–38, https://doi.org/10.1111/j.1600-0889.2006.00226.x, 2007.

Read, K. A., Mahajan, A. S., Carpenter, L. J., Evans, M. J., Faria, B. V. E., Heard, D. E., Hopkins, J. R., Lee, J. D., Moller, S. J., Lewis, A. C., Mendes, L., McQuaid, J. B., Oetjen, H., Saiz-Lopez, A., Pilling, M. J., and Plane, J. M. C.: Extensive halogen-mediated ozone destruction over the tropical Atlantic Ocean, Nature, 453, 1232–1235, https://doi.org/10.1038/nature07035, 2008.

Roberts, J. M. and Bertman, S. B.: The thermal decomposition of peroxyacetic nitric anhydride (PAN) and peroxymethacrylic nitric anhydride (MPAN), International Journal of Chemical Kinetics, 24, 297–307, https://doi.org/https://doi.org/10.1002/kin.550240307, URL https://onlinelibrary.wiley.com/doi/abs/10.1002/kin.550240307, 1992.

Roshan, S. and DeVries, T.: Efficient dissolved organic carbon production and export in the oligotrophic ocean, NAT COMMUN, 8, 2036, https://doi.org/10.1038/s41467-017-02227-3, 2017.

Sabine, C. L., Feely, R. A., Gruber, N., Key, R. M., Lee, K., Bullister, J. L., Wanninkhof, R., Wong, C. S., Wallace, D. W. R., Tilbrook, B., Millero, F. J., Peng, T.-H., Kozyr, A., Ono, T., and Rios, A. F.: The Oceanic Sink for Anthropogenic CO2, Science, 305, 367–371, https://doi.org/10.1126/science.1097403, URL https://science.sciencemag.org/content/305/5682/367, 2004.

Safieddine, S. A. and Heald, C. L.: A Global Assessment of Dissolved Organic Carbon in Precipitation, Geophysical Research Letters, 44, 11,672–11,681, https://doi.org/https://doi.org/10.1002/2017GL075270, 2017.

Saito, T., Yokouchi, Y., and Kawamura, K.: Distributions of C_2-C_6 hydrocarbons over the western North Pacific and eastern Indian Ocean, Atmospheric Environment, 34, 4373–4381, 2000.

Saiz-Lopez, A., Lamarque, J.-F., Kinnison, D. E., Tilmes, S., Ordóñez, C., Orlando, J. J., Conley, A. J., Plane, J. M. C., Mahajan, A. S., Sousa Santos, G., Atlas, E. L., Blake, D. R., Sander, S. P., Schauffler, S., Thompson, A. M., and Brasseur, G.: Estimating the climate significance of halogen-driven ozone loss in the tropical marine troposphere, Atmospheric Chemistry and Physics, 12, 3939–3949, https://doi.org/10.5194/acp-12-3939-2012, URL https://acp.copernicus.org/articles/12/3939/2012/, 2012.

Sakamoto, Y., Yabushita, A., Kawasaki, M., and Enami, S.: Direct Emission of I2 Molecule and IO Radical from the Heterogeneous Reactions of Gaseous Ozone with Aqueous Potassium Iodide Solution, J PHYS CHEM A, 113, 7707–7713, https://doi.org/10.1021/jp903486u, 2009.

Sander, R.: Compilation of Henry's law constants (version 4.0) for water as solvent, Atmospheric Chemistry and Physics, 15, 4399–4981, https://doi.org/10.5194/acp-15-4399-2015, 2015.

Sarwar, G., Kang, D., Foley, K., Schwede, D., and Gantt, B.: Technical note: Examining ozone deposition over seawater, ATMOS ENVIRON, 141, 255–262, https://doi.org/10.1016/j.atmosenv.2016.06.072, 2016.

Saunders, S. M., Jenkin, M. E., Derwent, R. G., and Pilling, M. J.: Protocol for the development of the Master Chemical Mechanism, MCM v3 (Part A): tropospheric degradation of non-aromatic volatile organic compounds, Atmospheric Chemistry and Physics, 3, 161–180, https://doi.org/10.5194/acp-3-161-2003, URL http://mcm.york.ac.uk, 2003.

Schmidt, J. A., Jacob, D. J., Horowitz, H. M., Hu, L., Sherwen, T., Evans, M. J., Liang, Q., Suleiman, R. M., Oram, D. E., Le Breton, M., Percival, C. J., Wang, S., Dix, B., and Volkamer, R.: Modeling the observed tropospheric BrO back-

ground: Importance of multiphase chemistry and implications for ozone, OH, and mercury, J GEOPHYS RES-ATMOS, 121, 11,819–11,835, https://doi.org/10.1002/2015JD024229, 2016.

SciPy community: scipy.optimize.curve_fit, URL \url{https://docs.scipy.org/doc/scipy/reference/generated/scipy.optimize.curve_fit.html}, 2021.

Seinfeld, J. H. and Pandis, S. N.: Atmospheric Chemistry and Physics: From Air Pollution to Climate Change, Wiley-Interscience, 2. aufl. edn., 2012.

Shaw, G.: Bio-controlled thermostasis involving the sulfur cycle., Climatic Change 5, p. 297–303, https://doi.org/https://doi.org/10.1007/BF02423524, 1983.

Shaw, M. D. and Carpenter, L. J.: Modification of Ozone Deposition and I_2 Emissions at the Air-Aqueous Interface by Dissolved Organic Carbon of Marine Origin, ENVIRON SCI TECHNOL, 47, 10 947–10 954, https://doi.org/10.1021/es4011459, 2013.

Shaw, S., Gantt, B., and Meskhidze, N.: Production and Emissions of Marine Isoprene and Monoterpenes: A Review, Advances in Meteorology, https://doi.org/10.1155/2010/408696, 2010.

Shaw, S. L., Chisholm, S. W., and Prinn, R. G.: Isoprene production by Prochlorococcus, a marine cyanobacterium, and other phytoplankton, Marine Chemistry, 80, 227–245, 2003.

Sheng, J.-X., Weisenstein, D. K., Luo, B.-P., Rozanov, E., Stenke, A., Anet, J., Bingemer, H., and Peter, T.: Global atmospheric sulfur budget under volcanically quiescent conditions: Aerosol-chemistry-climate model predictions and validation, Journal of Geophysical Research: Atmospheres, 120, 256–276, https://doi.org/https://doi.org/10.1002/2014JD021985, 2015.

Sherwen, T., Evans, M. J., Carpenter, L. J., Andrews, S. J., Lidster, R., Dix, B., Koenig, T. K., Sinreich, R., Ortega, I., Volkamer, R., Saiz-Lopez, A., Prados-Roman, C., Mahajan, A. S., and Ordóñez, C.: Iodine's impact on tropospheric oxidants: a global model study in GEOS-Chem, ATMOS CHEM

PHYS, 16, 1161–1186, https://doi.org/10.5194/acp-16-1161-2016, URL https://www.atmos-chem-phys.net/16/1161/2016/, 2016a.

Sherwen, T., Schmidt, J. A., Evans, M. J., Carpenter, L. J., Großmann, K., Eastham, S. D., Jacob, D. J., Dix, B., Koenig, T. K., Sinreich, R., Ortega, I., Volkamer, R., Saiz-Lopez, A., Prados-Roman, C., Mahajan, A. S., and Ordóñez, C.: Global impacts of tropospheric halogens (Cl, Br, I) on oxidants and composition in GEOS-Chem, ATMOS CHEM PHYS, 16, 12 239–12 271, https://doi.org/10.5194/acp-16-12239-2016, URL https://www.atmos-chem-phys.net/16/12239/2016/, 2016b.

Sherwen, T., Chance, R. J., Tinel, L., Ellis, D., Evans, M. J., and Carpenter, L. J.: A machine-learning-based global sea-surface iodide distribution, EARTH SYST SCI DATA, 11, 1239–1262, https://doi.org/10.5194/essd-11-1239-2019, URL https://www.earth-syst-sci-data.net/11/1239/2019/, 2019.

Shindell, D. T., Grenfell, J. L., Rind, D., Grewe, V., and Price, C.: Chemistry-climate interactions in the Goddard Institute for Space Studies general circulation model: 1. Tropospheric chemistry model description and evaluation, Journal of Geophysical Research: Atmospheres, 106, 8047–8075, https://doi.org/https://doi.org/10.1029/2000JD900704, 2001.

Silva, S. J. and Heald, C. L.: Investigating Dry Deposition of Ozone to Vegetation, J GEOPHYS RES-ATMOS, 123, 559–573, https://doi.org/10.1002/2017JD027278, 2018.

Simmonds, P., Derwent, R., Manning, A., Fraser, P., Krummel, P., O'Doherty, S., Prinn, R., Cunnold, D., Miller, B.R. abd Wang, H., Ryall, D., Porter, L., R.F., W., and Salameh, P.: AGAGE Observations of Methyl Bromide and Methyl Chloride at Mace Head, Ireland, and Cape Grim, Tasmania, 1998–2001, Journal of Atmospheric Chemistry, 47, 243–269, https://doi.org/https://doi.org/10.1023/B:JOCH.0000021136.52340.9c, 2004.

Simó, R. and Dachs, J.: Global ocean emission of dimethylsulfide predicted

from biogeophysical data, Global Biogeochemical Cycles, 16, 26–1–26–10, https://doi.org/https://doi.org/10.1029/2001GB001829, 2002.

Sinha, V., Williams, J., Meyerhöfer, M., Riebesell, U., Paulino, A. I., and Larsen, A.: Air-sea fluxes of methanol, acetone, acetaldehyde, isoprene and DMS from a Norwegian fjord following a phytoplankton bloom in a mesocosm experiment, Atmospheric Chemistry and Physics, 7, 739–755, https://doi.org/10.5194/acp-7-739-2007, URL https://acp.copernicus.org/articles/7/739/2007/, 2007.

Sohrin, R. and Sempéré, R.: Seasonal variation in total organic carbon in the northeast Atlantic in 2000–2001, Journal of Geophysical Research: Oceans, 110, https://doi.org/https://doi.org/10.1029/2004JC002731, 2005.

Solomon, S.: Stratospheric ozone depletion: A review of concepts and history, Reviews of Geophysics, 37, 275–316, https://doi.org/https://doi.org/10.1029/1999RG900008, 1999.

Sommariva, R., Haggerstone, A.-L., Carpenter, L. J., Carslaw, N., Creasey, D. J., Heard, D. E., Lee, J. D., Lewis, A. C., Pilling, M. J., and Zádor, J.: OH and HO_2 chemistry in clean marine air during SOAPEX-2, Atmospheric Chemistry and Physics, 4, 839–856, https://doi.org/10.5194/acp-4-839-2004, URL https://acp.copernicus.org/articles/4/839/2004/, 2004.

Spracklen, D. V., Pringle, K. J., Carslaw, K. S., Chipperfield, M. P., and Mann, G. W.: A global off-line model of size-resolved aerosol microphysics: I. Model development and prediction of aerosol properties, Atmospheric Chemistry and Physics, 5, 2227–2252, https://doi.org/10.5194/acp-5-2227-2005, URL https://acp.copernicus.org/articles/5/2227/2005/, 2005.

Stettler, M., Eastham, S., and Barrett, S.: Air quality and public health impacts of UK airports. Part I: Emissions, Atmospheric Environment, 45, 5415 – 5424, https://doi.org/https://doi.org/10.1016/j.atmosenv.2011.07.012, URL http://www.sciencedirect.com/science/article/pii/S135223101100728X, 2011.

Stock, Z. S., Russo, M. R., Butler, T. M., Archibald, A. T., Lawrence, M. G., Telford, P. J., Abraham, N. L., and Pyle, J. A.: Modelling the impact of megacities on local, regional and global tropospheric ozone and the deposition of nitrogen species, Atmospheric Chemistry and Physics, 13, 12 215–12 231, https://doi.org/10.5194/acp-13-12215-2013, URL https://acp.copernicus.org/articles/13/12215/2013/, 2013.

Stock, Z. S., Russo, M. R., and Pyle, J. A.: Representing ozone extremes in European megacities: the importance of resolution in a global chemistry climate model, Atmospheric Chemistry and Physics, 14, 3899–3912, https://doi.org/10.5194/acp-14-3899-2014, URL https://acp.copernicus.org/articles/14/3899/2014/, 2014.

Sukhodolov, T., Egorova, T., Stenke, A., Ball, W. T., Brodowsky, C., Chiodo, G., Feinberg, A., Friedel, M., Karagodin-Doyennel, A., Peter, T., Vattioni, S., and Rozanov, E.: Atmosphere-Ocean-Aerosol-Chemistry-Climate Model SOCOLv4.0: description and evaluation, Geoscientific Model Development Discussions, 2021, 1–58, https://doi.org/10.5194/gmd-2021-35, URL https://gmd.copernicus.org/preprints/gmd-2021-35/, 2021.

The Royal Society: Ground-level ozone in the 21st century: future trends, impacts and policy implications, Policy Document, 2008.

Thomas, C., Cauwet, G., and Minster, J.-F.: Dissolved organic carbon in the equatorial Atlantic Ocean, Marine Chemistry, 49, 155–169, https://doi.org/https://doi.org/10.1016/0304-4203(94)00061-H, 1995.

Thoning, K. W., Tans, P. P., and Komhyr, W. D.: Atmospheric carbon dioxide at Mauna Loa Observatory: 2. Analysis of the NOAA GMCC data, 1974–1985, Journal of Geophysical Research: Atmospheres, 94, 8549–8565, https://doi.org/https://doi.org/10.1029/JD094iD06p08549, 1989.

Travis, K. R., Jacob, D. J., Fisher, J. A., Kim, P. S., Marais, E. A., Zhu, L., Yu, K., Miller, C. C., Yantosca, R. M., Sulprizio, M. P., Thompson, A. M., Wennberg,

P. O., Crounse, J. D., St. Clair, J. M., Cohen, R. C., Laughner, J. L., Dibb, J. E., Hall, S. R., Ullmann, K., Wolfe, G. M., Pollack, I. B., Peischl, J., Neuman, J. A., and Zhou, X.: Why do models overestimate surface ozone in the Southeast United States?, Atmospheric Chemistry and Physics, 16, 13 561–13 577, https://doi.org/10.5194/acp-16-13561-2016, 2016.

Travis, K. R., Heald, C. L., Allen, H. M., Apel, E. C., Arnold, S. R., Blake, D. R., Brune, W. H., Chen, X., Commane, R., Crounse, J. D., Daube, B. C., Diskin, G. S., Elkins, J. W., Evans, M. J., Hall, S. R., Hintsa, E. J., Hornbrook, R. S., Kasibhatla, P. S., Kim, M. J., Luo, G., McKain, K., Millet, D. B., Moore, F. L., Peischl, J., Ryerson, T. B., Sherwen, T., Thames, A. B., Ullmann, K., Wang, X., Wennberg, P. O., Wolfe, G. M., and Yu, F.: Constraining remote oxidation capacity with ATom observations, Atmospheric Chemistry and Physics, 20, 7753–7781, https://doi.org/10.5194/acp-20-7753-2020, URL https://acp.copernicus.org/articles/20/7753/2020/, 2020.

Tripathi, N., Sahu, L. K., Singh, A., Yadav, R., Patel, A., Patel, K., and Meenu, P.: Elevated levels of biogenic non-methane hydrocarbons in the marine boundary layer of the Arabian Sea during the inter-monsoon, Journal of Geophysical Research: Atmospheres, n/a, e2020JD032 869, https://doi.org/10.1029/2020JD032869, URL https://agupubs.onlinelibrary.wiley.com/doi/abs/10.1029/2020JD032869, 2020.

Tzompa-Sosa, Z. A., Mahieu, E., Franco, B., Keller, C. A., Turner, A. J., Helmig, D., Fried, A., Richter, D., Weibring, P., Walega, J., Yacovitch, T. I., Herndon, S. C., Blake, D. R., Hase, F., Hannigan, J. W., Conway, S., Strong, K., Schneider, M., and Fischer, E. V.: Revisiting global fossil fuel and biofuel emissions of ethane, Journal of Geophysical Research: Atmospheres, 122, 2493–2512, https://doi.org/https://doi.org/10.1002/2016JD025767, 2017.

van Donkelaar, A., Martin, R. V., Leaitch, W. R., Macdonald, A. M., Walker, T. W., Streets, D. G., Zhang, Q., Dunlea, E. J., Jimenez, J. L., Dibb, J. E., Huey, L. G., Weber, R., and Andreae, M. O.: Analysis of aircraft and satellite mea-

surements from the Intercontinental Chemical Transport Experiment (INTEX-B) to quantify long-range transport of East Asian sulfur to Canada, Atmospheric Chemistry and Physics, 8, 2999–3014, https://doi.org/10.5194/acp-8-2999-2008, URL https://acp.copernicus.org/articles/8/2999/2008/, 2008.

Vinken, G. C. M., Boersma, K. F., Jacob, D. J., and Meijer, E. W.: Accounting for non-linear chemistry of ship plumes in the GEOS-Chem global chemistry transport model, Atmospheric Chemistry and Physics, 11, 11 707–11 722, https://doi.org/10.5194/acp-11-11707-2011, 2011.

von Glasow, R., von Kuhlmann, R., Lawrence, M. G., Platt, U., and Crutzen, P. J.: Impact of reactive bromine chemistry in the troposphere, Atmospheric Chemistry and Physics, 4, 2481–2497, https://doi.org/10.5194/acp-4-2481-2004, URL https://acp.copernicus.org/articles/4/2481/2004/, 2004.

Wang, Q., Jacob, D. J., Spackman, J. R., Perring, A. E., Schwarz, J. P., Moteki, N., Marais, E. A., Ge, C., Wang, J., and Barrett, S. R. H.: Global budget and radiative forcing of black carbon aerosol: Constraints from pole-to-pole (HIPPO) observations across the Pacific, Journal of Geophysical Research: Atmospheres, 119, 195–206, https://doi.org/https://doi.org/10.1002/2013JD020824, 2014.

Wang, S., Apel, E. C., Schwantes, R. H., Bates, K. H., Jacob, D. J., Fischer, E. V., Hornbrook, R. S., Hills, A. J., Emmons, L. K., Pan, L. L., Honomichl, S., Tilmes, S., Lamarque, J.-F., Yang, M., Marandino, C. A., Saltzman, E. S., de Bruyn, W., Kameyama, S., Tanimoto, H., Omori, Y., Hall, S. R., Ullmann, K., Ryerson, T. B., Thompson, C. R., Peischl, J., Daube, B. C., Commane, R., McKain, K., Sweeney, C., Thames, A. B., Miller, D. O., Brune, W. H., Diskin, G. S., DiGangi, J. P., and Wofsy, S. C.: Global Atmospheric Budget of Acetone: Air-Sea Exchange and the Contribution to Hydroxyl Radicals, Journal of Geophysical Research: Atmospheres, 125, https://doi.org/https://doi.org/10.1029/2020JD032553, 2020.

Wang, Y., Jacob, D. J., and Logan, J. A.: Global simulation of tropospheric O3-NO

x -hydrocarbon chemistry: 1. Model formulation, J GEOPHYS RES-ATMOS, 103, 10 713–10 725, https://doi.org/10.1029/98JD00158, 1998.

Wang, Y. X., McElroy, M. B., Jacob, D. J., and Yantosca, R. M.: A nested grid formulation for chemical transport over Asia: Applications to CO, Journal of Geophysical Research: Atmospheres, 109, https://doi.org/https://doi.org/10.1029/2004JD005237, 2004.

Waterman, L. S., Nelson, D. W., Komhyr, W. D., Harris, T. B., Thoning, K. W., and Tans, P. P.: Atmospheric carbon dioxide measurements at Cape Matatula, American Samoa, 1976–1987, Journal of Geophysical Research: Atmospheres, 94, 14 817–14 829, https://doi.org/https://doi.org/10.1029/JD094iD12p14817, 1989.

Weng, H., Lin, J., Martin, R., Millet, D., Jaegle, L., Ridley, D., Keller, C., Li, C., Du, M., and Meng, J.: Global high-resolution emissions of soil NOx, sea salt aerosols, and biogenic volatile organic compounds, Scientific Data, 7, https://doi.org/10.1038/s41597-020-0488-5, 2020.

Wesely, M.: Parameterization of surface resistances to gaseous dry deposition in regional-scale numerical models, ATMOS ENVIRON, 23, 1293–1304, 1989.

Wesely, M. and Hicks, B.: Some Factors that Affect the Deposition Rates of Sulfur Dioxide and Similar Gases on Vegetation, Journal of the Air Pollution Control Association, 27, 1110–1116, https://doi.org/10.1080/00022470.1977.10470534, 1977.

WHO: World health statistics 2019: monitoring health for the SDGs, sustainable development goals, World Health Organization, 2019.

WMO-GAW: GAW stations network and other measurements, URL `http://community.wmo.int/activity-areas/gaw/research-infrastructure/gaw-stations`, 2021.

Wofsy, S. and ATom Science Team: ATom: Aircraft Flight Track and Navigational

Data, https://doi.org/10.3334/ORNLDAAC/1613, URL https://daac.ornl.gov/cgi-bin/dsviewer.pl?ds_id=1613, 2018.

Woodhouse, M. T., Carslaw, K. S., Mann, G. W., Vallina, S. M., Vogt, M., Halloran, P. R., and Boucher, O.: Low sensitivity of cloud condensation nuclei to changes in the sea-air flux of dimethyl-sulphide, Atmospheric Chemistry and Physics, 10, 7545–7559, https://doi.org/10.5194/acp-10-7545-2010, URL https://acp.copernicus.org/articles/10/7545/2010/, 2010.

Wu, X., Deng, L., Song, X., Vettoretti, G., Peltier, W. R., and Zhang, G. J.: Impact of a modified convective scheme on the Madden-Julian Oscillation and El Niño–Southern Oscillation in a coupled climate model, Geophysical Research Letters, 34, https://doi.org/https://doi.org/10.1029/2007GL030637, 2007.

Xiao, Y., Logan, J. A., Jacob, D. J., Hudman, R. C., Yantosca, R., and Blake, D. R.: Global budget of ethane and regional constraints on U.S. sources, Journal of Geophysical Research: Atmospheres, 113, https://doi.org/https://doi.org/10.1029/2007JD009415, 2008.

Yang, M., Huebert, B. J., Blomquist, B. W., Howell, S. G., Shank, L. M., McNaughton, C. S., Clarke, A. D., Hawkins, L. N., Russell, L. M., Covert, D. S., Coffman, D. J., Bates, T. S., Quinn, P. K., Zagorac, N., Bandy, A. R., de Szoeke, S. P., Zuidema, P. D., Tucker, S. C., Brewer, W. A., Benedict, K. B., and Collett, J. L.: Atmospheric sulfur cycling in the southeastern Pacific – longitudinal distribution, vertical profile, and diel variability observed during VOCALS-REx, Atmospheric Chemistry and Physics, 11, 5079–5097, https://doi.org/10.5194/acp-11-5079-2011, 2011.

Young, P., Naik, V., Fiore, A., Gaudel, A., Guo, J., Lin, M., Neu, J., Parrish, D., Rieder, H., Schnell, J., Tilmes, S., Wild, O., Zhang, L., Ziemke, J., Brandt, J., Delcloo, A., Doherty, R., Geels, C., Hegglin, M., Hu, L., Im, U., Kumar, R., Luhar, A., Murray, L., Plummer, D., Rodriguez, J., Saiz-Lopez, A., Schultz, M., Woodhouse, M., and Zeng, G.: Tropospheric Ozone Assessment Report: Assessment of global-scale model performance for global and regional ozone

distributions, variability, and trends., Elem Sci Anth, 6(1), 10, https://doi.org/http://doi.org/10.1525/elementa.265, 2018.

Young, P. J., Archibald, A. T., Bowman, K. W., Lamarque, J.-F., Naik, V., Stevenson, D. S., Tilmes, S., Voulgarakis, A., Wild, O., Bergmann, D., Cameron-Smith, P., Cionni, I., Collins, W. J., Dalsøren, S. B., Doherty, R. M., Eyring, V., Faluvegi, G., Horowitz, L. W., Josse, B., Lee, Y. H., MacKenzie, I. A., Nagashima, T., Plummer, D. A., Righi, M., Rumbold, S. T., Skeie, R. B., Shindell, D. T., Strode, S. A., Sudo, K., Szopa, S., and Zeng, G.: Pre-industrial to end 21st century projections of tropospheric ozone from the Atmospheric Chemistry and Climate Model Intercomparison Project (ACCMIP), ATMOS CHEM PHYS, 13, 2063–2090, https://doi.org/10.5194/acp-13-2063-2013, URL https://www.atmos-chem-phys.net/13/2063/2013/, 2013.

Yu, K., Jacob, D. J., Fisher, J. A., Kim, P. S., Marais, E. A., Miller, C. C., Travis, K. R., Zhu, L., Yantosca, R. M., Sulprizio, M. P., Cohen, R. C., Dibb, J. E., Fried, A., Mikoviny, T., Ryerson, T. B., Wennberg, P. O., and Wisthaler, A.: Sensitivity to grid resolution in the ability of a chemical transport model to simulate observed oxidant chemistry under high-isoprene conditions, Atmospheric Chemistry and Physics, 16, 4369–4378, https://doi.org/10.5194/acp-16-4369-2016, URL https://acp.copernicus.org/articles/16/4369/2016/, 2016.

Yu, K., Keller, C. A., Jacob, D. J., Molod, A. M., Eastham, S. D., and Long, M. S.: Errors and improvements in the use of archived meteorological data for chemical transport modeling: an analysis using GEOS-Chem v11-01 driven by GEOS-5 meteorology, Geoscientific Model Development, 11, 305–319, https://doi.org/10.5194/gmd-11-305-2018, URL https://gmd.copernicus.org/articles/11/305/2018/, 2018.

Zhang, L., Gong, S., Padro, J., and Barrie, L.: A size-segregated particle dry deposition scheme for an atmospheric aerosol module, Atmospheric Environment, 35, 549–560, https://doi.org/https://doi.org/10.1016/S1352-2310(00)00326-5, 2001.

Zhou, X. and Mopper, K.: Photochemical production of low-molecular-weight carbonyl compounds in seawater and surface microlayer and their air-sea exchange, Marine Chemistry, 56, 201–213, https://doi.org/https://doi.org/10.1016/S0304-4203(96)00076-X, 1997.

Zweng, M., Reagan, J., Antonov, J., Locarnini, R., Mishonov, A., Boyer, T., Garcia, H., Baranova, O., Johnson, D., D.Seidov, and Biddle, M.: World Ocean Atlas 2013 Volume 2: Salinity, NOAA Atlas NESDIS 74, p. 39, 2013.